THÈSE PRÉSENTÉE

POUR OBTENIR LE GRADE DE

DOCTEUR
DE L'UNIVERSITÉ DE BORDEAUX

ECOLE DOCTORALE SCIENCES PHYSIQUES ET DE L'INGENIEUR

LASERS, MATIERE, NANOSCIENCE

Par **Rohit MANGALWEDHEKAR**

Diffusion de nanotubes de carbone unidimensionnels dans un environnement complexe de matière molle

Sous la direction de : **Laurent COGNET et Stéphane BANCELIN**

Soutenue le 06 Octobre 2026

Membres du jury :

M. Ignacio IZEDDIN	Maître de conférences	ESPCI	Examinateur
M. Jean-Baptiste MASSON	Directeur de Recherche	CNRS	Rapporteur
M. David HOLCMAN	Directeur de Recherche	CNRS	Rapporteur
M. Jean-Pierre DELVILLE	Directeur de Recherche	CNRS	Président
M. Stéphane BANCELIN	Chargé de Recherche	CNRS	Co-directeur
M. Laurent COGNET	Directeur de Recherche	CNRS	Directeur

THÈSE PRÉSENTÉE

POUR OBTENIR LE GRADE DE

DOCTEUR
DE L'UNIVERSITÉ DE BORDEAUX

ECOLE DOCTORALE SCIENCES PHYSIQUES ET DE L'INGENIEUR

LASERS, MATIERE, NANOSCIENCE

Par **Rohit MANGALWEDHEKAR**

Diffusion de nanotubes de carbone unidimensionnels dans un environnement complexe de matière molle

Sous la direction de : **Laurent COGNET et Stéphane BANCELIN**

Soutenue le 06 Octobre 2026

Membres du jury :

M. Ignacio IZEDDIN	Maître de conférences	ESPCI	Examinateur
M. Jean-Baptiste MASSON	Directeur de Recherche	CNRS	Rapporteur
M. David HOLCMAN	Directeur de Recherche	CNRS	Rapporteur
M. Jean-Pierre DELVILLE	Directeur de Recherche	CNRS	Président
M. Stéphane BANCELIN	Chargé de Recherche	CNRS	Co-directeur
M. Laurent COGNET	Directeur de Recherche	CNRS	Directeur

To Amma and Appa, and to the first book on science they bought me

Acknowledgements

I would like to take this opportunity to express my sincere appreciation to all those who have supported me throughout my journey in completing this PhD. The past three years have been exciting, rewarding, and most importantly deeply memorable, and I am very grateful to all those who have been a part of this journey.

I will begin by taking this opportunity to thank members of my jury. I am deeply grateful to the members of my jury for their time, their thoughtful questions, and for the stimulating discussions that have enriched this work.

First and foremost, I would like to extend my deepest gratitude to Laurent and Stephane for their unwavering guidance and support throughout my three years. Laurent, your mentorship through our various discussions are lessons I will carry forward throughout my career, for this I cannot thank you enough. Stephane, thank you for your guidance and always lending an ear to my ideas, our countless discussions have strongly shaped how I approach problems and solutions. Together, their encouragement and advice have played a pivotal role in shaping this research project and my academic growth.

A big thanks to Marc for all the help with the microscopy. I had a great time working alongside you to set up, align, and test microscopes. I could always count on you to help me with the optics, and for this I cannot thank you enough.

I would like to acknowledge the GPR LIGHT program, the University of Bordeaux, CNRS, and the Institut d'Optique Graduate School for funding this research, as well as all the collaborators whose expertise and contributions helped bring this project to life.

I would like to thank Theo for being such a gentle friend and colleague, I am so happy to have worked alongside you. To Nathan, thank you for being a wonderful colleague and friend. I hope our paths cross again, hopefully over masala dosa and filter coffee. I also thank JB for his kindness throughout our time in the lab together.

To Somen, Benjamin, and Rossana, thank you. In addition to being wonderful friends and colleagues, you were the ones that I could always trust to have and understand carbon nanotubes. Limeng, you have been an excellent friend and an even better colleague to collaborate on projects with. Thank you, it has been super fun to work with you.

Hanna, Blanca, Anirban and Naveen, you were among the first friends I had in the lab and in Bordeaux, thank you for making it a wonderful time throughout these years. Hanna, thank you very much for a wonderful time in the lab and outside. From surfing, to skiing, to getting beers, and for always showing up, my time in the lab and Bordeaux would not have been the same without you guys.

To Nasim and Sourath, from our late night walks, to discussing everything and nothing,

to having masala chai, you made sure I kept a piece of home always with me, thank you very very much. Roopa, for all the reminiscing and nostalgia of Rajajinagar, Malleshwara, and Bengaluru, and most importantly for keeping me well fed during the writing of my thesis, thank you very very much.

A very big thanks to Yara for always having time for coffee breaks, for introducing me to incredible food, and for always making the lab a happier and cheerful place. To Sanjana, thank you very much. We may have overlapped very briefly in the lab (unfortunately), but I am incredibly lucky and thankful for all the time spent together. I cannot wait for our paths to cross again.

I am also grateful to all the members of LP2N, both past and present, for creating such a welcoming and stimulating environment. Whether through scientific discussions, technical help, or simply sharing coffee breaks and lunches, each of you has contributed to making these years enjoyable.

I also would like to take this opportunity to thank Deepak, who has been a constant support and source of inspiration in my career from the very beginning. I also wish to thank KRR who introduced me to research and scientific methods.

To Akanksha, Jahnavi, and Vivek, you guys have been nothing short of family in Bordeaux. It is difficult to articulate how much you have influenced my life here. You were and are my home away from home, and I only have the deepest gratitude to you three.

To Flanish, Adithya, Vighnaraj, Uday, Spoorthi, Tanmayee, Malvika, and Niharika my time at Manipal would not have been the same without you all. From our late night beach trips to watching bioluminescence, the time I spent with you guys still inspires me.

Anish, Aishwarya, Agneya, Sanjana, Suhas, Sneha, Sushma, Malvika, Lavanya, Soumya, Naveena, Abhijna, and Harini, thank you all very very much. You guys have been a constant source of encouragement, inspiration, and support. I am incredibly lucky to have this circle of friends to lean on.

Shama, thank you very very very much for your support and always believing in me. Between wordle, references, and Azul, you ensured that even the most difficult days have been easier.

Saving the best for last, my deepest appreciation goes to Amma, Appa, and Ashrit. I have received everything from constant encouragement and support to insightful questions and discussions regarding my work. You have been the driving force behind my achievements. Thank you for always being there and for instilling in me the importance of perseverance and determination.

In conclusion, this journey would not have been possible without the support of each and every one of you. Your contributions, whether big or small, have made a significant

impact on my life and academic pursuits. This thesis is as much a testament to all your support as it is to my work. From the bottom of my heart, thank you for believing in me and for being a part of this incredible chapter of my life.

Abstract

The transport of nanoscale objects in complex structured environments underpins a wide range of processes, from biomolecular activity in the extracellular spaces of tissues to fluid transport through filters, catalysts, and metal-organic frameworks. Understanding how particle geometry interacts with local architecture to influence diffusion and escape dynamics remains a fundamental challenge in complex biological and soft matter systems. While the anomalous diffusion of spherical probes in heterogeneous environments is well established, far less is known about how anisotropic, one-dimensional molecules explore confined microenvironments, or how their length influences residence times and escape through narrow passages.

In my thesis, I investigated the diffusion of anisotropic carbon nanotubes in a complex soft matter system. Nanotubes functionalized with color centers (CCNTs), which enhance their infrared luminescence, were used. As a biophysical model system, densely packed emulsion droplets were prepared: the aqueous interstitial regions between the droplets reproduce complex soft matter environments such as the brain extracellular spaces (ECS). Using a near-infrared single-molecule microscopy setup operating over an extended depth of field and in three dimensions, I then imaged individual CCNTs of two distinct size scales, differing by an order of magnitude, diffusing in aqueous medium within the biophysical model. Having observed subdiffusive and antipersistent motion for nanotubes of both size scales, we extended our analysis to understand the nature of diffusion in local geometries and to better characterize the scaling of diffusion properties with particle length. To connect local dynamics with global diffusion, escape from confined chambers was investigated. Surprisingly, despite a tenfold increase in particle length, long CCNTs require only about 1.4 times longer to escape than short CCNTs. Moreover, this weak dependence contrasts sharply with simple theoretical predictions, which suggest that escape times should scale approximately linearly with particle length. To understand this discrepancy, we implemented Single Particle Orientation Tracking (SPoT) microscopy to directly measure the azimuthal and polar orientations of the particle. These measurements reveal that long CCNTs become rotationally constrained and aligned within narrow channels, reducing their orientational freedom while facilitating their transport through the network.

Taken together, these results identify geometric frustration as a fundamental mechanism underlying anomalous transport in continuous structured environments. Even in the absence of binding interactions or discrete trapping sites, geometry alone is sufficient to generate subdiffusive and antipersistent dynamics through repeated wall-mediated interactions and intermittent confinement. Furthermore, particle anisotropy determines how this geometric frustration is resolved, enabling confinement-induced alignment to facil-

itate rather than hinder transport. These findings establish general physical principles governing the diffusion of anisotropic objects in complex media and provide insight into transport processes in biological, porous, and soft matter systems.

The principles identified in this thesis provide a foundation for future investigations of transport in increasingly realistic complex environments. Beyond rigid carbon nanotubes, future studies may employ flexible and deformable nanoscale probes to determine how mechanical properties such as bending and conformational fluctuations influence diffusion under confinement. In parallel, more sophisticated model systems incorporating flow gradients, biomolecular interactions, and gel-like matrices could bridge the gap between simplified soft matter architectures and biological extracellular spaces. Such a bottom-up approach offers a promising route toward understanding the combined roles of particle geometry, mechanics, and environmental complexity in governing nanoscale transport.

Résumé

Le transport d'objets à l'échelle nanométrique dans des environnements structurés complexes sous-tend un large éventail de processus, allant de l'activité biomoléculaire dans les espaces extracellulaires des tissus au transport de fluides à travers des filtres, des catalyseurs et des réseaux métallo-organiques. Comprendre comment la géométrie des particules interagit avec l'architecture locale pour influencer la diffusion et la dynamique d'échappement demeure un défi fondamental dans les systèmes biologiques complexes et la matière molle. Si la diffusion anormale de sondes sphériques dans des environnements hétérogènes est bien établie, on connaît beaucoup moins bien la manière dont les molécules anisotropes, unidimensionnelles, explorent les microenvironnements confinés, ni comment leur longueur influence les temps de résidence et l'échappement à travers des passages étroits.

Dans ma thèse, j'ai étudié la diffusion de nanotubes de carbone anisotropes dans un système complexe de matière molle. Des nanotubes fonctionnalisés par des centres colorés (CCNT), qui renforcent leurs propriétés de luminescence infrarouge, ont été utilisés. Comme système modèle biophysique, des gouttelettes d'émulsion densément empilées ont été préparées : les régions interstitielles aqueuses entre les gouttelettes reproduisent les environnements complexes de matière molle, tels que les espaces extracellulaires (ECS) du cerveau. À l'aide d'un montage de microscopie de molécules uniques dans le proche infrarouge opérant sur une profondeur de champ étendue et en trois dimensions, j'ai alors imagé des CCNT individuels appartenant à deux échelles de taille distinctes, différant d'un ordre de grandeur, en train de diffuser en milieu aqueux dans le modèle biophysique. Ayant observé un mouvement sous-diffusif et anti-persistant pour les nanotubes des deux échelles de taille, nous avons étendu notre analyse afin de comprendre la nature de la diffusion dans les géométries locales, et de mieux appréhender la mise à l'échelle des propriétés de diffusion en fonction de la longueur des particules.

Pour relier la dynamique locale à la diffusion globale, l'échappement depuis des chambres confinées a été étudié. De façon surprenante, malgré une augmentation de la longueur des particules d'un facteur dix, les longs CCNT ne mettent qu'environ 1,4 fois plus de temps à s'échapper que les CCNT courts. En outre, cette faible dépendance contraste fortement avec les prédictions théoriques simples, qui suggèrent que les temps d'échappement devraient croître de façon approximativement linéaire avec la longueur des particules. Pour comprendre cet écart, nous avons mis en œuvre la microscopie de suivi de l'orientation de particules uniques (Single Particle Orientation Tracking, SPoT) afin de mesurer directement les orientations azimutale et polaire de la particule. Ces mesures révèlent que les longs CCNT deviennent contraints en rotation et s'alignent au sein des canaux étroits, réduisant leur liberté d'orientation tout en facilitant leur transport à travers le réseau.

Dans leur ensemble, ces résultats identifient la frustration géométrique comme un mécanisme fondamental sous-tendant le transport anormal dans les environnements structurés continus. Même en l'absence d'interactions de liaison ou de sites de piégeage discrets, la géométrie seule suffit à générer une dynamique sous-diffusive et anti-persistante, par le biais d'interactions répétées médiées par les parois et d'un confinement intermittent. De plus, l'anisotropie des particules détermine la manière dont cette frustration géométrique est résolue, permettant à l'alignement induit par le confinement de faciliter le transport plutôt que de l'entraver. Ces résultats établissent des principes physiques généraux régissant la diffusion d'objets anisotropes dans les milieux complexes, et apportent un éclairage sur les processus de transport dans les systèmes biologiques, poreux et de matière molle. Les principes identifiés dans cette thèse constituent une base pour de futures recherches sur le transport dans des environnements complexes de plus en plus réalistes. Au-delà des nanotubes de carbone rigides, des études futures pourraient employer des sondes nanométriques flexibles et déformables afin de déterminer comment des propriétés mécaniques telles que la flexion et les fluctuations conformationnelles influencent la diffusion en situation de confinement. Parallèlement, des systèmes modèles plus sophistiqués intégrant des gradients d'écoulement, des interactions biomoléculaires et des matrices de type gel pourraient combler l'écart entre les architectures simplifiées de matière molle et les espaces extracellulaires biologiques. Une telle approche ascendante (bottom-up) ouvre une voie prometteuse vers la compréhension des rôles combinés de la géométrie des particules, de la mécanique et de la complexité environnementale dans la régulation du transport à l'échelle nanométrique.

Résumé étendu

Le transport d'objets à l'échelle nanométrique dans des environnements complexes, structurés et poreux est à la base d'un large éventail de processus, allant de l'activité biomoléculaire dans les espaces extracellulaires des tissus à la diffusion de fluides à travers des filtres, des catalyseurs ou des réseaux métallo-organiques. Comprendre comment la géométrie des objets interagit avec l'architecture de l'environnement pour influencer la diffusion et la dynamique d'échappement reste une question fondamentale pour la diffusion dans les environnements biologiques complexes. L'étude des nanoparticules anisotropes dans de tels milieux est en particulier essentielle pour prédire le transport dans les systèmes biologiques et dans la matière molle complexe. Si la diffusion anormale de nano-objets sphériques dans des environnements complexes est bien établie, on en sait beaucoup moins sur la manière dont les nanoparticules unidimensionnelles explorent les microenvironnements confinés. On ne sait notamment pas encore clairement comment la longueur de la particule affecte son temps de séjour dans le confinement, ni sa cinétique de sortie à travers des passages étroits.

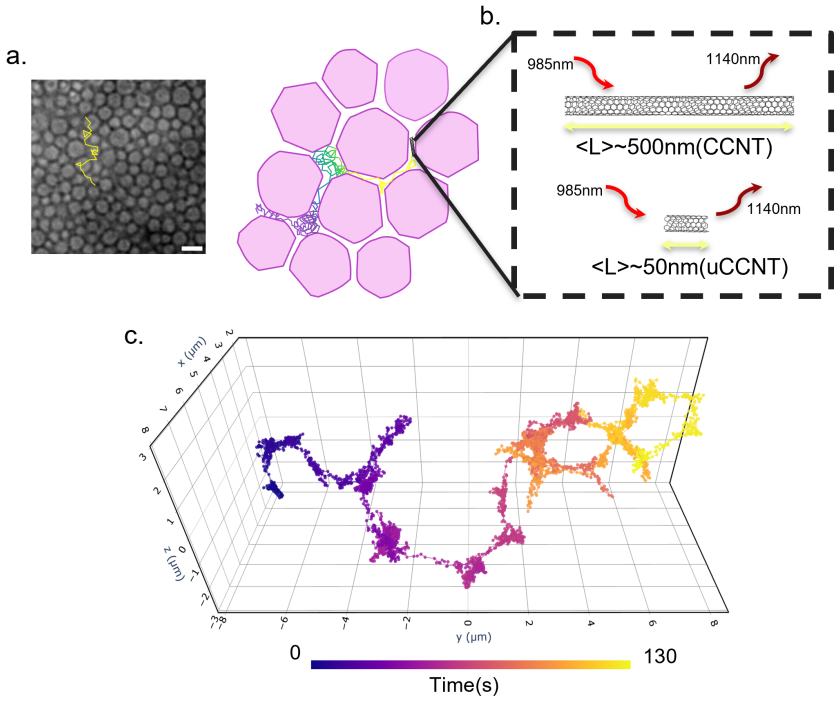

Figure 1: Suivi de particules uniques de nanotubes de carbone individuels dans un modèle biophysique a. Image en lumière blanche de gouttelettes compactes servant de modèle biophysique avec un schéma d'une trajectoire (en jaune). b. Représentation schématique de nanotubes de carbone longs et ultracourts utilisés pour étudier la dépendance en longueur de la diffusion dans une matière molle complexe. c. Tracé représentatif d'une trajectoire longue unique d'un nanotube de carbone diffusant dans le modèle de gouttelettes compactes.

Nous proposons ici un système de matière molle composé de gouttelettes d'émulsion

densément agencées, servant de modèle biophysique des tissus : il reproduit les espaces extracellulaires et permet de remettre en question les modèles de diffusion actuels applicables à la matière molle complexe. Ce modèle offre un réseau continu, enchevêtré et complexe d'espaces interstitiels, constitué de chambres et de passages à géométrie convexe. Nous l'explorons grâce au suivi 3D de particules individuelles : des nanotubes de carbone à paroi simple (CCNT) très brillants, actifs dans l'infrarouge et dotés de centres colorés. Afin d'étudier le rôle de la longueur des particules unidimensionnelles sur la diffusion, des CCNTs de deux échelles de taille distinctes, différant d'un ordre de grandeur, ont été analysés, la plus grande taille étant comparable aux dimensions typiques de l'environnement (Figure 1).

Nous constatons d'abord que la diffusion des CCNTs longs et courts dans le modèle biophysique présente un comportement de diffusion anormale aux échelles de temps où les particules explorent plusieurs chambres et passages. Aux échelles de temps intermédiaires, les nanotubes présentent un mouvement antipersistant dans les chambres, correspondant à une diffusion entravée par des interactions répétées avec les parois plutôt qu'à un piégeage discret (Figure 2). En revanche, dans les passages reliant les chambres, la diffusion est proche du mouvement brownien selon l'axe du passage, accompagnée d'un alignement progressif des nanotubes les plus longs sur cet axe.

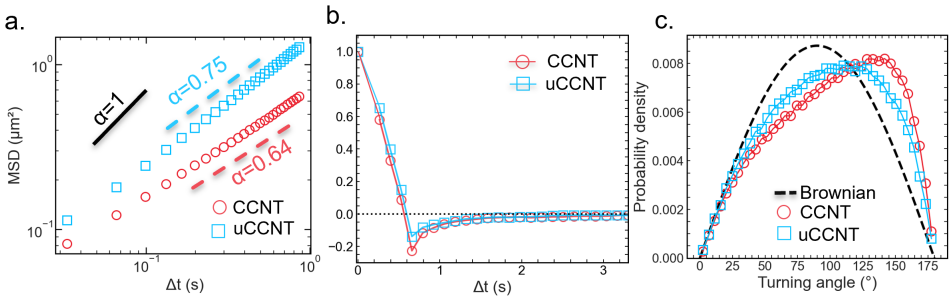

Figure 2: La diffusion des CNTs dans le modèle biophysique est anormale a. Le déplacement quadratique moyen (MSD) est sous-linéaire pour les nanotubes de carbone courts (uCCNTs) et longs (CCNTs). b. La VACF montre une motion anticorrélée marquée, avec une antipersistance plus forte pour les nanotubes longs que pour les courts. Les distributions des angles de retournement sont décalées vers la droite vers des angles plus grands, indiquant un effet de "rebond" vers l'espace interstitiel dû à des collisions répétées. Ce décalage est plus important pour les CNTs longs que pour les CNTs courts. La ligne noire en pointillés représente la diffusion brownienne dans un environnement libre.

Les nanotubes courts présentent un mouvement de type brownien à temps courts, accompagné par de fréquentes collisions avec les parois de la chambre. Leur diffusion rotationnelle reste principalement libre, et leur dynamique de sortie dépend de leur capacité à explorer efficacement l'espace exploré disponible. Ce comportement s'inscrit conceptuellement dans le cadre d'un problème de premier passage, où l'échappement

dépend de la probabilité d'atteindre une ouverture par exploration aléatoire (Figure 3).

Les nanotubes longs se comportent différemment, car leur longueur est comparable aux dimensions caractéristiques des chambres de confinement. Il en résulte une diffusion rotationnelle frustrée, leur géométrie allongée les contraignant à s'aligner sur les axes spatiaux disponibles. Ils ont ainsi tendance à s'aligner par avance le long des passages reliant les chambres, ce qui favorise un transport vers la sortie selon des directions préférentielles, plutôt que de dépendre de rares fluctuations isotropes (Figure 3).

Dans les passages de liaison, les nanotubes courts présentent une diffusion tridimensionnelle au sein d'un environnement anisotrope et allongé. Les nanotubes longs, quant à eux, passent d'un piégeage transitoire et d'un mouvement confiné à l'intérieur des chambres à un transport guidé par les passages. À l'intérieur de ces derniers, la dynamique des angles de virage devient progressivement bimodale : la distribution des angles présente deux pics distincts, correspondant à l'alignement et à l'anti-alignement le long de l'axe du passage (Figure 3).

De manière surprenantes, nous observons que, malgré une longueur multipliée par dix, les nanotubes longs ne présentent qu'une augmentation d'environ 1,4 fois du temps de séjour moyen dans les chambres par rapport aux nanotubes courts. Les modèles classiques décrivant l'échappement de particules browniennes anisotropes hors d'environnements confinés prédisent une dépendance à la longueur bien plus forte, car l'allongement de la tige réduit considérablement la diffusion, tant translationnelle que rotationnelle (Figure 4). La faible dépendance observée expérimentalement démontre que l'échappement n'est pas limité par la seule réorientation diffusive ni par la seule exploration aléatoire. Nous identifions au contraire deux modes d'échappement distincts : les nanotubes courts s'échappent par un échantillonnage quasi isotrope de l'espace vide, tandis que les nanotubes longs subissent un alignement induit par le confinement qui facilite leur transport le long des passages de raccordement, compensant partiellement leur mobilité réduite (Figure 5).

Nos travaux révèlent que les nanotubes courts explorent aisément leur environnement : ils se déplacent rapidement et efficacement, entrent fréquemment en collision avec les parois, tout en conservant une distribution complète des orientations. Dans des architectures convexes continues composées de chambres et de passages interconnectés, ils présentent une diffusion quasi libre à court terme, mais un comportement anormal et entravé aux temps longs en raison du confinement spatial. Leur mouvement reste rapide et aléatoire, seulement légèrement influencé par des interactions avec les parois qui ne restreignent que faiblement leur liberté d'orientation. À l'inverse, lorsque la longueur des nanotubes s'approche des dimensions caractéristiques de l'environnement, la diffusion reste efficace mais devient plus lente et plus dirigée. Dans ce régime, la géométrie elle-même facilite la

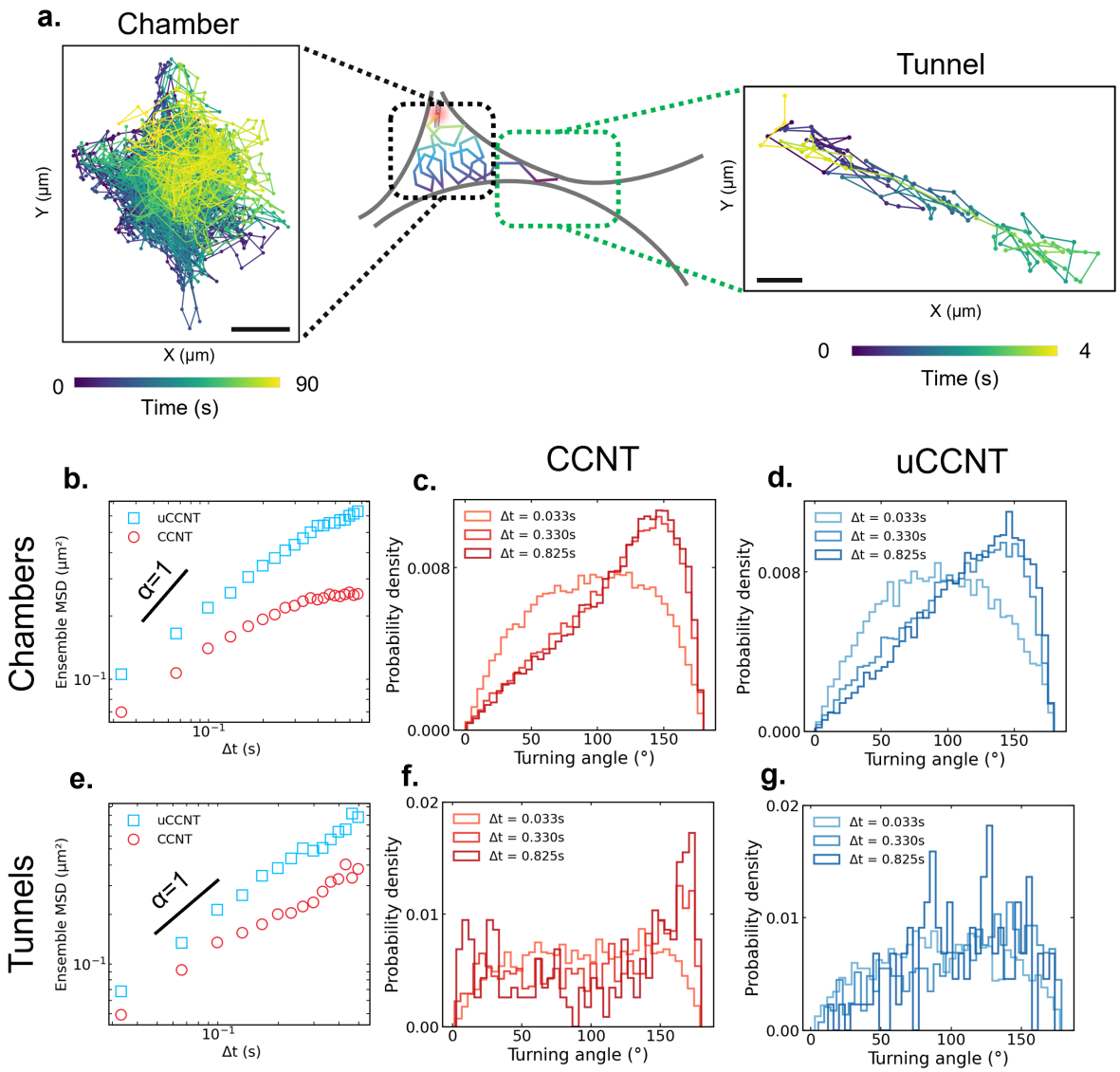

Figure 3: La diffusion des nanotubes est influencée par la géométrie locale : a. Schéma d'une trajectoire de nanotube dans le système modèle, montrant les deux topologies environnementales distinctes, avec des trajectoires représentatives dans les chambres (barre d'échelle : 500 nm) et dans les tunnels (barre d'échelle : 200 nm), segmentées manuellement sur CloudCompare. b. Le MSD en fonction du temps de retard pour les CCNTs montre un piégeage transitoire dans les chambres, tandis que les uCCNTs présentent un comportement fortement sous-diffusif aux temps de retard plus longs. c, d. La distribution des angles de retournement dans les chambres montre une exploration proche de la diffusion brownienne au premier intervalle de temps, mais un décalage vers la droite vers des angles plus grands aux temps plus longs, confirmant un comportement fortement sous-diffusif pour les CCNTs et les uCCNTs. e. Le MSD en fonction du temps de retard pour les CCNTs et les uCCNTs révèle une diffusivité presque brownienne dans les régions de type tunnel. f, g. La distribution des angles de retournement dans les tunnels est fortement parallèle ou antiparallèle, avec une sous-représentation marquée des angles intermédiaires en raison des contraintes géométriques et stériques aux temps longs pour les nanotubes longs. À l'inverse, les nanotubes ultra-courts continuent de montrer des angles décalés vers la droite à différents temps de retard, indiquant une diffusion entravée mais brownienne.

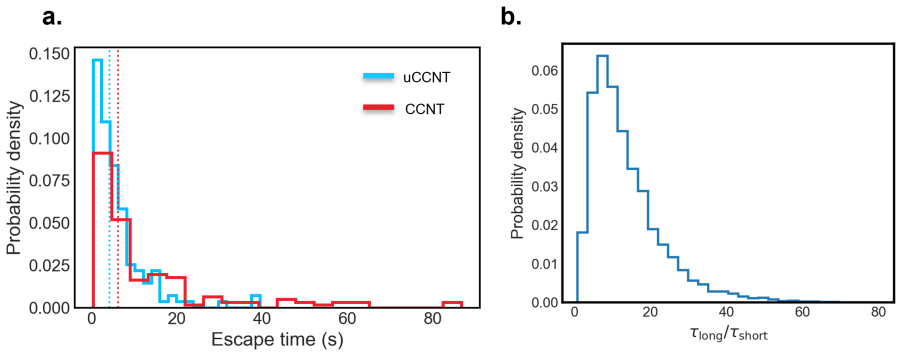

Figure 4: Dépendance de la longueur sur les temps d'échappement des chambres a. La distribution des temps de résidence des uCCNTs et des CCNTs révèle un temps médian d'échappement d'environ 3,3 s et 5 s, respectivement. Ainsi, le rapport des temps d'échappement entre particules longues et courtes est de 1,38. Une simulation de balayage paramétrique de type Monte Carlo a été utilisée pour prédire théoriquement le rapport des temps d'échappement pour une diffusion brownienne de particules anisotropes confinées, et la valeur médiane obtenue est d'environ 10.

sortie du confinement : les interactions fréquentes avec les parois entravent la diffusion rotationnelle et alignent les nanotubes le long des passages disponibles, ce qui conduit à un mouvement guidé, à une probabilité d'échappement plus élevée et à une réduction du temps de séjour global.

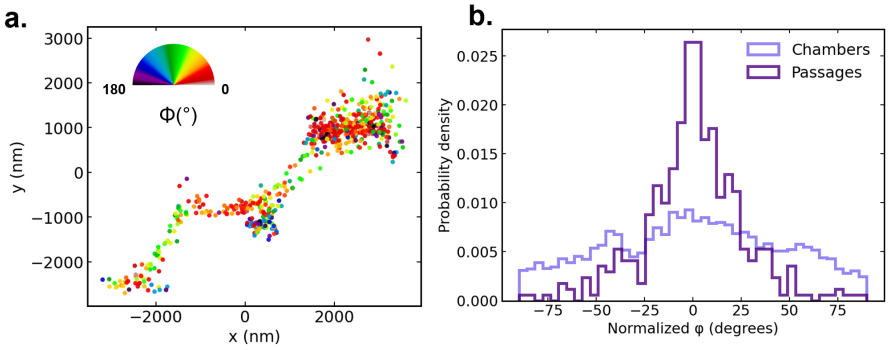

Figure 5: La diffusion géométriquement frustrée induit une sortie facilitée a. La distribution spatiale de l'angle plan (ϕ) d'une trajectoire représentative d'un CCNT explorant les chambres et les tunnels dans le modèle biophysique révèle des hétérogénéités spatiales dans l'orientation des particules. b. La distribution normalisée des angles dans les chambres et les tunnels révèle une forte conformité orientelle dans les tunnels. En revanche, dans les chambres, les particules explorent l'ensemble du spectre des angles afin de s'orienter.

Nos résultats révèlent que la frustration géométrique est à l'origine fondamentale du transport anormal dans un environnement continu et structuré. Malgré l'absence de fuites par les pores ou de pièges de liaison, l'architecture convexe des chambres et des passages interconnectés suffit à elle seule à générer une dynamique antipersistante et subdiffusive. Cette origine géométrique de la diffusion anormale ne nécessite ni piégeage marqué ni

alignement persistant, puisque les nanotubes, courts comme longs, présentent tous un comportement de diffusion anormal. L'anomalie résulte au contraire de l'interaction avec une géométrie continue et hétérogène, où les collisions contre les parois et le confinement intermittent façonnent progressivement les statistiques de transport. La longueur des particules module alors la manière dont cette frustration géométrique est résolue : par une exploration isotrope pour les nanotubes courts, ou par un alignement induit par le confinement et un échappement facilité pour les nanotubes longs. Nous montrons ainsi que l'interaction entre la géométrie des objets et l'architecture locale peut faciliter, plutôt qu'entraver, le transport à travers des environnements confinés.

Les principes développés dans cette thèse établissent un cadre pour de futures études sur le transport dans des environnements complexes de plus en plus réalistes. Au-delà des nanotubes de carbone rigides, les travaux futurs pourraient explorer des sondes nanométriques souples et déformables afin d'étudier comment les propriétés mécaniques, telles que la rigidité à la flexion et les fluctuations conformationnelles, influencent la diffusion en conditions de confinement. Parallèlement, des systèmes modèles plus avancés intégrant des gradients d'écoulement, des interactions biomoléculaires et des matrices de type gel pourraient contribuer à combler le fossé entre les architectures simplifiées de matière molle et les environnements extracellulaires biologiques. Dans son ensemble, une telle stratégie ascendante offre une voie prometteuse pour comprendre comment la géométrie des particules, leurs propriétés mécaniques et la complexité de l'environnement régissent collectivement le transport à l'échelle nanométrique.

ಸಾರಾಂಶ

ವಿಸರಣವು (Diffusion) ಪ್ರಕೃತಿಯಲ್ಲಿ ಕಾಣುವ ಅತ್ಯಂತ ಮೂಲಭೂತ ಪ್ರಕ್ರಿಯೆಗಳಲ್ಲಿ ಒಂದಾಗಿದೆ. ಈ ಪ್ರಕ್ರಿಯೆಯಲ್ಲಿ ಅಣುಗಳು ಮತ್ತು ಕಣಗಳು ತಮ್ಮ ಸುತ್ತಲಿನ ಪರಿಸರದೊಂದಿಗೆ ನಡೆಯುವ ನಿರಂತರ ಪರಸ್ಪರ ಕ್ರಿಯೆಗಳ ಪರಿಣಾಮವಾಗಿ ಯಾದೃಚ್ಛಿಕವಾಗಿ ಚಲಿಸುತ್ತವೆ. ಪರಿಸರವು ಏಕರೂಪವಾಗಿದ್ದರೆ, ಈ ಚಲನೆಯು ಬ್ರೌನಿಯನ್ ಚಲನೆ ಎಂದು ಕರೆಯಲಾಗುವ ಸರಳ ಯಾದೃಚ್ಛಿಕ ಚಲನೆಯನ್ನು ಅನುಸರಿಸುತ್ತದೆ. ಆದರೆ ಪ್ರಕೃತಿಯಲ್ಲಿನ ಪರಿಸರಗಳು ಬಹಳ ಅಪರೂಪವಾಗಿ ಮಾತ್ರ ಸರಳವಾಗಿರುತ್ತವೆ. ಸಾಮಾನ್ಯವಾಗಿ ಕಣಗಳ ಚಲನೆಯು ಪರಿಸರದ ಸಂಕೀರ್ಣ ರಚನೆಗಳು, ಭೌತಿಕ ಮತ್ತು ರಾಸಾಯನಿಕ ಪರಸ್ಪರ ಕ್ರಿಯೆಗಳು ಹಾಗೂ ದ್ರವ ಹರಿವುಗಳಂತಹ ಅನೇಕ ಅಂಶಗಳಿಂದ ಪ್ರಭಾವಿತವಾಗುತ್ತದೆ. ಈ ಪ್ರಕ್ರಿಯೆಯು ಜೀವಕೋಶಗಳು, ವಸ್ತುಗಳು, ಶೋಧನಾ ವ್ಯವಸ್ಥೆಗಳು ಹಾಗೂ ಅನೇಕ ದೈನಂದಿನ ಮತ್ತು ವೈಜ್ಞಾನಿಕ ವ್ಯವಸ್ಥೆಗಳಲ್ಲಿ ಪ್ರಮುಖ ಪಾತ್ರ ವಹಿಸುತ್ತದೆ. ಹಲವಾರು ವರ್ಷಗಳಿಂದ ನಮ್ಮ ಸಂಶೋಧನಾ ತಂಡವು ಮೆದುಳಿನ ಜೀವಕೋಶಗಳ ನಡುವಿನ ಹೊರಕೋಶೀಯ ಪ್ರದೇಶಗಳಲ್ಲಿ ನಡೆಯುವ ವಿಸರಣವನ್ನು ಅರ್ಥಮಾಡಿಕೊಳ್ಳಲು ಪ್ರಯತ್ನಿಸುತ್ತಿದೆ. ಈ ಪ್ರದೇಶಗಳನ್ನು ಹೊರಕೋಶೀಯ ಸ್ಥಳ (Extracellular Space ಅಥವಾ ECS) ಎಂದು ಕರೆಯಲಾಗುತ್ತದೆ. ಇದಕ್ಕಾಗಿ ನಾವು ಏಕ ಕಣ ಅನುಸರಣೆ (Single Particle Tracking ಅಥವಾ SPT) ಸೂಕ್ಷ್ಮದರ್ಶಕ ತಂತ್ರಜ್ಞಾನವನ್ನು ಬಳಸಿ, ಫೋಟೋಲ್ಯೂಮಿನೆಸೆಂಟ್ ಅಲ್ಟ್ರಾ ಬ್ರೈಟ್ ಕಲರ್ ಸೆಂಟರ್ ಕಾರ್ಬನ್ ನ್ಯಾನೋಟ್ಯೂಬ್ಗಳ (CCNT) ಚಲನೆಯನ್ನು ನೇರವಾಗಿ ಅನುಸರಿಸಿ ಅಧ್ಯಯನ ಮಾಡಿದ್ದೇವೆ. CCNT ಗಳು ಉದ್ದವಾದ ಕೊಳವೆಯಾಕಾರದ ಇಂಗಾಲದ ನ್ಯಾನೋಕಣಗಳಾಗಿದ್ದು, ಬೆಳಕಿನ ಪ್ರಭಾವದಿಂದ ಪ್ರತಿದೀಪ್ತಿಯನ್ನು (fluorescence) ಹೊರಸೂಸುತ್ತವೆ. ಈ ಗುಣಲಕ್ಷಣವು ಅವುಗಳನ್ನು ಪ್ರತ್ಯೇಕವಾಗಿ ಗುರುತಿಸಲು ಮತ್ತು ಅವುಗಳ ಚಲನೆಯನ್ನು ದೀರ್ಘಕಾಲದವರೆಗೆ ಅನುಸರಿಸಲು ಸಾಧ್ಯವಾಗಿಸುತ್ತದೆ. ಈ ಹಿಂದಿನ ಅಧ್ಯಯನಗಳು ECS ನಲ್ಲಿನ ಬದಲಾಗುವ ಸಾಂದ್ರತೆ, ಅದರ ಸಂಕೀರ್ಣ ಆಕಾರ ಮತ್ತು ಗಾತ್ರಗಳು, ಹಾಗೂ ಕಾಲಾನಂತರದಲ್ಲಿ ಸಂಭವಿಸುವ ಬದಲಾವಣೆಗಳ ಬಗ್ಗೆ ಮಹತ್ವದ ತಿಳುವಳಿಕೆಯನ್ನು ನೀಡಿವೆ.

ಆದರೆ ಇಂತಹ ಸಂಕೀರ್ಣ ಜೀವಕೋಶೀಯ ಪರಿಸರಗಳಲ್ಲಿ ಆಕಾರ ಮತ್ತು ಗಾತ್ರದ ಬದಲಾವಣೆ, ಭೌತಿಕ ಮತ್ತು ರಾಸಾಯನಿಕ ಪರಸ್ಪರ ಕ್ರಿಯೆಗಳು, ಜೆಲ್-ಸಮಾನ ಮಾಧ್ಯಮಗಳು ಹಾಗೂ ದ್ರವ ಹರಿವುಗಳಂತಹ ಅನೇಕ ಅಂಶಗಳು ವಿಸರಣವನ್ನು ಪ್ರಭಾವಿತಗೊಳಿಸುತ್ತವೆ. ಈ ಅಧ್ಯಯನದಲ್ಲಿ ನಾವು ದಟ್ಟವಾಗಿ ಕೂಡಿಕೊಂಡಿರುವ ಎಮಲ್ಶನ್ (emulsion) ವ್ಯವಸ್ಥೆಯನ್ನು ಮಾದರಿ ಸಾಫ್ಟ್ ಮ್ಯಾಟರ್ (soft matter) ಪರಿಸರವಾಗಿ ಬಳಸಿದ್ದೇವೆ. ಎಮಲ್ಶನ್ ಎಂದರೆ ನೀರಿನೊಳಗೆ ಎಣ್ಣೆ ಹನಿಗಳು ಅಥವಾ ಎಣ್ಣೆಯೊಳಗೆ ನೀರಿನ ಹನಿಗಳು ವಿತರಣೆಯಾಗಿರುವ ಮಿಶ್ರಣ ವ್ಯವಸ್ಥೆ. ಇದರ ಮೂಲಕ CCNT ವಿಸರಣವನ್ನು ಅಧ್ಯಯನ ಮಾಡಲಾಗಿದೆ. ಇದರ ಜೊತೆಗೆ ಕಣದ ಉದ್ದ ಮತ್ತು ಅನಿಸೋಟ್ರೋಪಿ (anisotropy) ವಿಸರಣದ ಮೇಲೆ ಹೇಗೆ ಪರಿಣಾಮ ಬೀರುತ್ತವೆ ಎಂಬುದನ್ನು ಅರ್ಥಮಾಡಿಕೊಳ್ಳಲಾಗಿದೆ. ಜೈವಿಕ ಅನ್ವಯಗಳ ಹೊರತಾಗಿಯೂ, ಅನಿಸೋಟ್ರೋಪಿಕ್ ಕಣಗಳು ಸಂಕೀರ್ಣ ಪರಿಸರಗಳಲ್ಲಿ ಹೇಗೆ ಚಲಿಸುತ್ತವೆ ಎಂಬ ಮೂಲಭೂತ ಭೌತಿಕ ತತ್ವಗಳು ಇನ್ನೂ ಪ್ರಯೋಗಾತ್ಮಕವಾಗಿ ಸಂಪೂರ್ಣವಾಗಿ ಅರ್ಥವಾಗಿಲ್ಲ.

ಈ ಅಧ್ಯಯನದಲ್ಲಿ ನಾವು ಉದ್ದವಾದ 500 nm ಮತ್ತು ಚಿಕ್ಕ 50 nm CCNTs ಎಮಲ್ಶನ್ ಹನಿಗಳ ನಡುವೆ ರೂಪುಗೊಳ್ಳುವ ಸಂಕೀರ್ಣ ಜಾಲದಂತಹ ಪರಿಸರದಲ್ಲಿ ಹೇಗೆ ಚಲಿಸುತ್ತವೆ ಎಂಬುದನ್ನು ಅಧ್ಯಯನ ಮಾಡಿದ್ದೇವೆ. ಇಂತಹ ಪರಿಸರಗಳಲ್ಲಿ ಅವುಗಳ ಚಲನೆ ಸರಳವಾಗಿ ನಡೆಯುವುದಿಲ್ಲ; ಬದಲಾಗಿ ಸುತ್ತಲಿನ ರಚನೆಯಿಂದ ಬಹಳವಾಗಿ ಪ್ರಭಾವಿತವಾಗುತ್ತದೆ. ಕಣಗಳ ಪಥಗಳನ್ನು ವಿಶ್ಲೇಷಿಸುವ ಮೂಲಕ ಅವುಗಳ ವಿಸರಣದ ಸ್ವಭಾವ ಮತ್ತು ಪರಿಸರದ ಪರಿಣಾಮವನ್ನು ಅರ್ಥಮಾಡಿಕೊಳ್ಳಲು ಪ್ರಯತ್ನಿಸಲಾಗಿದೆ.

ಆರಂಭಿಕವಾಗಿ ನಾವು ಕಂಡುಕೊಂಡಿದ್ದು, ಉದ್ದವಾದ ಮತ್ತು ಚಿಕ್ಕ CCNT ವಿಸರಣವು ಸರಳ ಬ್ರೌನಿಯನ್ ಚಲನೆಯಾಗಿರದೆ ಅನಿಯಮಿತ ಹಾಗೂ ಕುಂಠಿತ ಸ್ವಭಾವವನ್ನು ತೋರಿಸುತ್ತದೆ. ಮಧ್ಯಮ ಕಾಲಮಾಪಕಗಳಲ್ಲಿ ಅವು ಹಿಂದಕ್ಕೆ ತಿರುಗುವ ಪ್ರವೃತ್ತಿಯನ್ನು ತೋರಿಸುತ್ತವೆ ಹಾಗೂ ದೊಡ್ಡ ಕೋನಗಳನ್ನು ಹೆಚ್ಚಾಗಿ ಆಯ್ಕೆಮಾಡುವ ಮೂಲಕ ಅನಿಯಮಿತ ಉಪವಿಸರಣದ ಸ್ಪಷ್ಟ ಲಕ್ಷಣಗಳನ್ನು ಪ್ರದರ್ಶಿಸುತ್ತವೆ. ನಿರೀಕ್ಷಿಸಿದಂತೆ, ಉದ್ದವಾದ CCNT ಗಳು ಚಿಕ್ಕ ಕಣಗಳಿಗಿಂತ ಹೆಚ್ಚು ಕುಂಠಿತ ಚಲನೆಯನ್ನು ತೋರಿಸುತ್ತವೆ.

ಮುಂದಾಗಿ, ಸ್ಥಳೀಯ ಜ್ಯಾಮಿತಿಗಳಲ್ಲಿ ವಿಸರಣ ಹೇಗೆ ನಡೆಯುತ್ತದೆ ಎಂಬುದನ್ನು ಅರ್ಥಮಾಡಿಕೊಳ್ಳಲು ನಾವು ಎರಡು ಪ್ರದೇಶಗಳನ್ನು ವಿಭಾಗಿಸಿದ್ದೇವೆ: ದೊಡ್ಡ ಕೋಣೆಯಂತಹ ಕೊಠಡಿಗಳು (Chambers) ಮತ್ತು ಸಣ್ಣ ಕೊಳವೆ-ಸಮಾನ ಮಾರ್ಗಗಳು (tunnels). ಕೊಠಡಿಗಳಲ್ಲಿ ಉದ್ದವಾದ CCNT ಗಳ ವಿಸರಣವು ಕಾಲದೊಂದಿಗೆ ಹೆಚ್ಚಾಗಿ ಅವುಗಳನ್ನು ಆ ಕೋಣೆಯೊಳಗೆ ಸೀಮಿತಗೊಳಿಸಿತು; ಆದರೆ ಚಿಕ್ಕ CCNT ಗಳು ಕುಂಠಿತವಾಗಿದ್ದರೂ ಸಂಪೂರ್ಣವಾಗಿ ಬಂಧಿತವಾಗಲಿಲ್ಲ. ಇದಕ್ಕೆ ವಿರುದ್ಧವಾಗಿ, ಕೊಳವೆಗಳೊಳಗಿನ ವಿಸರಣವನ್ನು ನೋಡಿದಾಗ ಉದ್ದ ಮತ್ತು ಚಿಕ್ಕ CCNT ಗಳು ಎರಡೂ ಸರಳ ಬ್ರೌನಿಯನ್ ಚಲನೆಯಂತೆಯೇ ನೇರವಾಗಿ ಚಲಿಸುವಂತೆ ಕಂಡವು. ಆದರೆ ಸೂಕ್ಷ್ಮವಾಗಿ ಪರಿಶೀಲಿಸಿದಾಗ ಕಣಗಳ ತಿರುಗುವ ಸ್ವಭಾವವು ಎರಡು ಗಾತ್ರಗಳ ನಡುವೆ ಸ್ಪಷ್ಟವಾಗಿ ಭಿನ್ನವಾಗಿರುವುದು ಕಂಡುಬಂತು. ಚಿಕ್ಕ CCNT ಗಳು ಗೋಡೆಗಳಿಗೆ ನಿರಂತರವಾಗಿ ಡಿಕ್ಕಿ ಹೊಡೆಯುತ್ತಾ ಬಹುತೇಕ ಯಾದೃಚ್ಛಿಕ ಚಲನೆಯನ್ನು ಮುಂದುವರೆಸಿದವು.ಇದಕ್ಕೆ ವಿರುದ್ಧವಾಗಿ ಉದ್ದವಾದ CCNT ಗಳು ಕಾಲದೊಂದಿಗೆ ಎರಡು-ಸ್ಥಿತಿಯ ತಿರುಗುವ ಸ್ವಭಾವವನ್ನು ತೋರಿಸಿದವು; ಅಂದರೆ ಅವು ಕೊಳವೆಯ ದಿಕ್ಕಿಗೆ ಕ್ರಮವಾಗಿ ಹೊಂದಿಕೊಳ್ಳುತ್ತಾ ಮುಂದೆ ಅಥವಾ ಹಿಂದೆ ಚಲಿಸುವ ದಿಶಾವಿನ್ಯಾಸಿತ ಚಲನೆಯನ್ನು ಪ್ರದರ್ಶಿಸಿದವು.

ಸ್ಥಳೀಯ ವಿಸರಣ ಗತಿಶಾಸ್ತ್ರವು ದೀರ್ಘ-ಅಂತರದ ಜಾಗತಿಕ ವಿಸರಣವನ್ನು ಹೇಗೆ ಪ್ರಭಾವಿಸುತ್ತದೆ ಎಂಬುದನ್ನು ಅರ್ಥಮಾಡಿಕೊಳ್ಳಲು ನಾವು ಕಣಗಳು ಕೊಠಡಿಯೊಳಗಿಂದ ಹೊರಬರುವ ಸಮಯವನ್ನು ವಿಶ್ಲೇಷಿಸಿದ್ದೇವೆ. ಇಲ್ಲಿ ನಾವು ಕಂಡಿದ್ದು, ಉದ್ದವಾದ CCNT ಚಿಕ್ಕ CCNT ಸುಮಾರು 1.4 ಪಟ್ಟು ಹೆಚ್ಚು ಸಮಯ ತೆಗೆದುಕೊಳ್ಳುತ್ತವೆ. ಆದರೆ ಅತ್ಯಂತ ಆಶ್ಚರ್ಯಕರವಾದ ವಿಷಯವೆಂದರೆ, ಉದ್ದದಲ್ಲಿ 10 ಪಟ್ಟು ಹೆಚ್ಚಳವಾಗಿದ್ದರೂ ಹೊರಬರುವ ಸಮಯದಲ್ಲಿ ಕೇವಲ 1.4 ಪಟ್ಟು ಬದಲಾವಣೆ ಮಾತ್ರ ಕಂಡುಬಂದಿತು. ಇದನ್ನು ಅರ್ಥಮಾಡಿಕೊಳ್ಳಲು ನಾವು ಸಿದ್ಧಾಂತಾತ್ಮಕವಾಗಿ ಸರಳ ಯಾದೃಚ್ಛಿಕ ವಿಸರಣವನ್ನು ಆಧರಿಸಿದ ಮಾದರಿಯನ್ನು ನಿರ್ಮಿಸಿ, ಸಣ್ಣರಂಧ್ರದ ಮೂಲಕ ಹೊರಬರುವ CCNT ಗಳ ವರ್ತನೆಯನ್ನು ಅನುಕರಣೆ ಮಾಡಿದ್ದೇವೆ. ಗಣಿತಾತ್ಮಕವಾಗಿ ನೋಡಿದರೆ, 10 ಪಟ್ಟು ಉದ್ದವಾದ ಕಣವು ಹೊರಬರುವ ಸಮಯವೂ ಸುಮಾರು 10 ಪಟ್ಟು ಹೆಚ್ಚಾಗಬೇಕು ಎಂಬ ನಿರೀಕ್ಷೆ ಇದೆ.

ಮುಂದಾಗಿ ನಾವು SPoT (Single Particle Orientation Tracking) ಸೂಕ್ಷ್ಮದರ್ಶಕವನ್ನು ಬಳಸಿದ್ದು, ಇದು ನ್ಯಾನೋನಳಿಕೆಗಳ ದಿಕ್ಕಿನ (orientation) ಮಾಹಿತಿಯನ್ನು ಪಡೆಯಲು ಸಹಾಯಕವಾದ ತಂತ್ರವಾಗಿದೆ. SPoT ಸೂಕ್ಷ್ಮದರ್ಶಕದ ಮೂಲಕ ನಾವು ಕೊಠಡಿಗಳಲ್ಲಿಯೂ ಮತ್ತು ಕೊಳವೆಗಳಲ್ಲಿಯೂ CCNT ಗಳ ತಿರುಗುವ ವರ್ತನೆಯನ್ನು ಅಧ್ಯಯನ ಮಾಡಿದ್ದೇವೆ. ಕೊಠಡಿಗಳಲ್ಲಿ ಉದ್ದವಾದ CCNT ಗಳು ಮುಕ್ತವಾಗಿ ತಿರುಗುತ್ತಿದ್ದು, ಎಲ್ಲಾ ಕೋನಗಳಲ್ಲಿಯೂ ದಿಕ್ಕು ಬದಲಾಯಿಸಲು ಸಾಧ್ಯವಾಗುತ್ತಿತ್ತು. ಆದರೆ ಕೊಳವೆಗಳಲ್ಲಿ ಅವು ರಚನೆಯೊಂದಿಗೆ ಹೊಂದಿಕೊಂಡು ದಿಕ್ಕು ನಿರ್ಬಂಧಿತವಾಗಿದ್ದರಿಂದ ತಿರುಗುವಿಕೆ ಬಹಳವಾಗಿ ಕುಂಠಿತವಾಗಿತ್ತು; ಇದರಿಂದಾಗಿ ಅವು ಮುಖ್ಯವಾಗಿ ಕೊಳವೆಯೊಳಗೆ ಮುಂದೆ ಮತ್ತು ಹಿಂದೆ ಮಾತ್ರ ಚಲಿಸುತ್ತಿದ್ದವು. ಚಿಕ್ಕ CCNT ಗಳಿಗೆ ಅವುಗಳ ಸಣ್ಣ ಗಾತ್ರದ ಕಾರಣದಿಂದ ತಿರುಗುವಿಕೆ ಅತ್ಯಂತ ವೇಗವಾಗಿ ನಡೆಯುತ್ತಿದ್ದು, ನಾವು ಅವುಗಳ ದಿಕ್ಕನ್ನು ಸ್ಪಷ್ಟವಾಗಿ ನಿರ್ಣಯಿಸಲು ಸಾಧ್ಯವಾಗಲಿಲ್ಲ; ಇದು ಅವುಗಳ ಎರಡೂ ಪರಿಸರಗಳಲ್ಲಿ ಮುಕ್ತ ವರ್ತನೆಯನ್ನು ಸೂಚಿಸುತ್ತದೆ.

ನಮ್ಮ ಫಲಿತಾಂಶಗಳು ನಿರಂತರ ಮತ್ತು ರಚನಾತ್ಮಕ ಪರಿಸರದಲ್ಲಿ ಕಾಣುವ ಅನಿಯಮಿತ ವಿಸರಣದ ಮೂಲ

ಕಾರಣವಾಗಿ ಜ್ಯಾಮಿತೀಯ ನಿರ್ಬಂಧವನ್ನು (geometric frustration) ಸೂಚಿಸುತ್ತವೆ. ರಂಧ್ರಾಧಾರಿತ (porous) ನಿರ್ಗಮನ ಅಥವಾ ಬಂಧನಾತ್ಮಕ ತೊಡಕುಗಳಿಲ್ಲದಿದ್ದರೂ ಸಹ, ಪರಸ್ಪರ ಸಂಪರ್ಕಗೊಂಡ ಕೊಠಡಿಗಳು ಮತ್ತು ಮಾರ್ಗಗಳ ವಕ್ರ ಜ್ಯಾಮಿತಿಯೇ ಅನಿಯಮಿತ ಹಾಗೂ ಹಿಂದಕ್ಕೆ ತಿರುಗುವ ಚಲನೆಯನ್ನು ಉಂಟುಮಾಡಲು ಸಾಕು ಎಂಬುದು ಕಂಡುಬಂತು. ಇಂತಹ ಅನಿಯಮಿತ ವಿಸರಣವು ಬಲವಾದ ಬಂಧನಗಳು ಅಥವಾ ನಿರಂತರ ದಿಕ್ಕಿನ ಹೊಂದಾಣಿಕೆಯಿಂದ ಉಂಟಾಗುವುದಿಲ್ಲ; ಬದಲಾಗಿ ಇದು ನಿರಂತರ ಆದರೆ ಅಸಮಾನವಾದ ಜ್ಯಾಮಿತಿಯೊಂದಿಗೆ ಕಣಗಳ ಪರಸ್ಪರ ಕ್ರಿಯೆಯಿಂದ ಉದ್ಭವಿಸುತ್ತದೆ. ಇಲ್ಲಿ ಗೋಡೆಗಳೊಂದಿಗೆ ಆಗುವ ಘರ್ಷಣೆಗಳು ಮತ್ತು ಮಧ್ಯಂತರ ಸೀಮಿತಗೊಳಿಸುವಿಕೆಗಳು ಕಾಲಕ್ರಮೇಣ ವಿಸರಣದ ಗುಣಲಕ್ಷಣಗಳನ್ನು ರೂಪಿಸುತ್ತವೆ. ಕಣದ ಉದ್ದವು ಈ ಜ್ಯಾಮಿತೀಯ ನಿರ್ಬಂಧ ಹೇಗೆ ಪರಿಹಾರವಾಗುತ್ತದೆ ಎಂಬುದನ್ನು ನಿರ್ಧರಿಸುತ್ತದೆ — ಚಿಕ್ಕ ನ್ಯಾನೋನಳಿಕೆಗಳಲ್ಲಿ ಇದು ಸಮಸಮಾನ ಅನ್ವೇಷಣೆಯಾಗಿ ಕಾಣಿಸಿಕೊಂಡರೆ, ಉದ್ದವಾದ ನ್ಯಾನೋನಳಿಕೆಗಳಲ್ಲಿ ಸೀಮಿತಗೊಳಿಸುವಿಕೆಯಿಂದ ಉಂಟಾಗುವ ಹೊಂದಾಣಿಕೆ ಮತ್ತು ಸುಗಮ ನಿರ್ಗಮನದ ಮೂಲಕ ಕಾಣಿಸುತ್ತದೆ. ಆದ್ದರಿಂದ, ಕಣದ ಆಕಾರ ಮತ್ತು ಸ್ಥಳೀಯ ರಚನೆಯ ನಡುವಿನ ಪರಸ್ಪರ ಕ್ರಿಯೆಯು ಸೀಮಿತ ಪರಿಸರಗಳಲ್ಲಿ ವಿಸರಣವನ್ನು ತಡೆಯುವುದಕ್ಕಿಂತ ಹೆಚ್ಚಾಗಿ ಸುಗಮಗೊಳಿಸಬಹುದು ಎಂಬುದನ್ನು ನಾವು ತೋರಿಸುತ್ತೇವೆ.

Contents

1 Introduction **1**

1.1 Brownian motion in free environments 1

1.2 Langevin formalization of Brownian motion 2

1.3 Experimental approaches to diffusion 4

1.3.1 Nuclear magnetic resonance 5

1.3.2 Dynamic light scattering 5

1.3.3 Fluorescence recovery after photobleaching 6

1.3.4 Fluorescence correlation spectroscopy 6

1.3.5 Heterogeneity and the ensemble averaging problem 7

1.3.6 The power of single particle approaches 7

1.4 Diffusion in complex environments 8

1.4.1 Opallic, crowded, and porous structures 8

1.4.2 Hydrogels 10

1.4.3 The brain extracellular space 11

1.5 The curious case of anistropic particles 13

1.5.1 Diffusion in a free environment 13

1.5.1.1 Experimental validation of Perrin's model 16

1.5.1.2 Perrin's diffusion model for an ellipsoid 16

1.5.2 Diffusion in a complex environment 18

2 Quantifying and modeling diffusion **21**

2.1 Statistical descriptors of diffusion dynamics 21

2.1.1 Mean Square Displacement 21

2.1.2 van Hove correlation . . . 25
2.1.3 Velocity autocorrelation function . . . 26
2.1.4 Distribution of turning angles . . . 28
2.1.5 Non Gaussianity parameter . . . 30
2.1.6 Asphericity . . . 31
2.1.7 Escape time . . . 32
2.2 Stochastic models of diffusion . . . 32
2.2.1 Brownian motion . . . 32
2.2.2 Fractional Brownian Motion . . . 34
2.2.3 Continuous time random walk (CTRW) . . . 35
2.2.4 Obstructed Diffusion . . . 36

3 Single particle tracking of anisotropic carbon nanotubes 39
3.1 Single particle tracking Microscopy . . . 39
3.1.1 Classical microscopes . . . 39
3.1.2 Point spread function . . . 40
3.1.3 The diffraction limit . . . 40
3.1.4 Localization from the PSF . . . 41
3.1.5 From localization to single particle tracking . . . 43
3.2 Isotropic fluorescent probes . . . 44
3.3 Single Walled Carbon Nanotubes . . . 45
3.3.1 Physical and electronic properties . . . 45
3.3.2 Excitonic and optical properties . . . 48
3.3.3 Tuning optical properties: The CCNT . . . 50
3.3.4 Length tunability: The uCCNT . . . 51
3.4 Presentation of the 3D single particle tracking setup . . . 54
3.4.1 The setup . . . 54
3.4.1.1 PSF engineering for 3D tracking . . . 55
3.4.1.2 Phase retrieval . . . 56
3.4.1.3 The role of localization precision . . . 57

3.5 Diffusion of (u)CCNTs in a brownian fluid 59
3.5.1 Experimental constraints and measurement artefacts 59
3.5.1.1 Truncation of trajectories 61
3.5.1.2 Effect of refractive index matching 63
3.5.2 True Brownian motion in bulk homogeneous liquid 64

4 Packed emulsion droplets: a novel diffusion landscape 68
4.1 Packed emulsions as model systems 68
4.2 Characterizing droplets packing: HiLo optical sectioning 70
4.3 Assembling the biophysical system for single particle studies 74
4.3.1 Index matching of droplets 74
4.4 Packing of droplets 75
4.4.1 Preparation of samples for imaging 76
4.4.2 Sample imaging 76
4.4.3 Optimizing imaging conditions for the biophysical model 76
4.5 Segmentation of droplets and interstitial spaces 78
4.6 Introduction of CCNTs in the biophysical model 79
4.7 Role of nanotube surfactants 82
4.8 Optimizing packing of droplets 83
4.9 Characterization of local geometries 85

5 Obstructed diffusion of nanoparticles in a liquid labyrinth 87
5.1 Ensemble diffusion in the biophysical model 88
5.1.1 Anomalous subdiffusive scaling of MSD 88
5.1.2 Anticorrelated dynamics reveal memory effects 89
5.1.3 Particle wall interactions skew Brownian statistics 90
5.1.4 Non-gaussianity validates obstructed diffusion 90
5.2 Geometric characterization of the interstitial space 91
5.2.1 Segmentation and characterization of the interstitial space from trajectories 93

5.2.1.1 Size characterization of chambers . . . 93
5.2.1.2 Size characterization of tunnels . . . 94
5.2.2 Local geometry governs diffusion of nanotubes . . . 96
5.2.2.1 Diffusion in Chambers . . . 96
5.2.2.2 Diffusion in tunnels . . . 98
5.3 From local to global transport . . . 100
5.3.1 Distribution of escape time from chambers . . . 100
5.3.2 Simulating Brownian escape of anisotropic particles . . . 101
5.4 Rotational diffusion explains anisotropic escape . . . 104
5.4.1 The mean square angular dispacement . . . 107
5.4.2 Local geometry influences orientational memory . . . 107
5.4.3 Alignment induced escape of CCNTs . . . 108
5.5 The effect of particle (an)isotropy on diffusion in the biophysical model: Preliminary results . . . 111
5.5.1 Ensemble statistics of HiQ particles in the biophysical model . . . 112
5.5.2 The effect of local geometry on diffusion of isotropic particles . . . 114

6 Conclusion 117

7 Perspectives 120

7.1 Novel single particle probes . . . 120
7.1.1 Fluorescent worms . . . 120
7.1.2 Gold nanoparticles . . . 122
7.1.3 Nunchaku SWCNTs . . . 123
7.2 Novel environments . . . 124
7.2.1 Opallic structures . . . 124
7.2.2 Bottom up approach to building ECS environments . . . 126

A Paper-I: Orientational frustration drives enhanced diffusion of anisotropic particles in a liquid labyrinth 128

B Paper-II: Click'n ROPISA: One-pot synthesis of ultrabright fluorescent

nanoparticles made of polypeptides **170**

C Protocols for biophysical model with nanotubes **194**

Chapter 1

Introduction

The evolution of stochastic motion over time is the premise to understand diffusive processes. These processes form the cornerstone in understanding transport in nature, governing the movement of particles, molecules, and information across a vast range of length scales. From the transport of nutrients and signaling molecules in living tissues to the migration of pollutants in the environment and the operation of filtration and energy-storage technologies, the ability of objects to explore their surroundings through random motion underpins countless physical, chemical, and biological phenomena. Yet, real environments are rarely simple. Complex geometries with constrictions, confinements, and dead-ends, coupled with crowding, physical, and chemical interactions, can strongly influence transport. Moreover, the shape and size of these nanoscale objects and their interactions with their surroundings particularly influence diffusion. Understanding how particle anisotropy and environmental complexity together govern diffusion therefore remains a central challenge. To address this, simplified and well-controlled model systems provide a powerful approach, allowing individual physical mechanisms to be isolated and studied before progressing toward the complexity of real biological environments.

However, before we address transport in complex systems, it becomes imperative to consider the simplest and most fundamental diffusive process: the random motion of a particle suspended in a fluid. This phenomenon, known as Brownian motion, provides the foundation upon which modern theories of stochastic transport are built.

1.1 Brownian motion in free environments

In 1827, while studying pollen grains suspended in water under a microscope, the Scottish botanist Robert Brown observed they performed a continuous and random motion. Initially, suspecting biological origins, Brown conducted a series of experiments, with

variety of organic and inorganic materials, such as dust and finely powdered minerals. He noticed that this irregular motion persisted, irrespective of the source of particles indicating that the phenomenon was not unique to life. Although Brown was unable to identify the physical origin of this motion, his observations laid the foundation for one of the most important developments in statistical physics and the erratic and seemingly random motion he discovered was coined *Brownian motion* [1].

Until the early twentieth century, there seemed to be no satisfactory arguments for the origin of Brownian motion and the subject remained a matter of debate. In 1905, Einstein proposed that the continuous motion of fluid molecules was related to thermal fluctuations which would impart countless random impulses to suspended particles, causing them to execute observable stochastic trajectories. By linking the microscopic molecular dynamics of the fluid to the measurable motion of colloidal particles, Einstein described a framework to quantify connected macroscopic observations with the atomic nature of matter [2].

Soon, in 1908, Jean Perrin was able to experimentally validate Einstein's predictions. Through a series of experiments with Chaudesaigues and Dabrowski, Perrin manually tracked suspended colloidal particles using a microscope, at time intervals of 30 s for over 3000 timepoints (cumulatively 25 hours!). These measurements, apart from providing evidence for Brownian motion as a consequence of molecular agitation, also validated the atomic theory of matter. Additionally, their work also enabled an independent measurement of Avogadro's number, further linking the microscopic world with the macroscopic observations [3].

While the works of Einstein and Perrin have been seminal in describing Brownian motion, they still did not explicitly address the transient dynamics of a particle subjected to the repeated collisions of the fluid molecules or the effect of fluid viscosity in such scenarios. Paul Langevin then introduced an equation of motion that incorporates both deterministic and random forces [4]. The Langevin formalism remains one of the fundamental frameworks for describing Brownian motion and forms the basis of many modern theories of stochastic transport that we will look at in the next section.

1.2 Langevin formalization of Brownian motion

Let us consider a spherical object or particle of radius R and mass m, moving with velocity $\mathbf{v}$. The fundamental equation of motion can be defined as:

$$m\frac{\partial \mathbf{v}}{\partial t} = -m\alpha_v \mathbf{v} + \mathbf{F}_{\text{ext}} + \mathbf{F}_{\text{stoch}}. \tag{1.1}$$

The term $-m\alpha_v \mathbf{v}$ corresponds to the viscous friction acting between the surface of the

sphere and the surrounding fluid, opposing the motion of the particle. This force depends on the radius of the particle R and the fluid viscosity η. By Stokes' law we have:

$$-m\alpha_v \mathbf{v} = -6\pi\eta R\mathbf{v}, \tag{1.2}$$

where α_v is the relaxation rate of the particle. This expression is derived as a solution of the Navier–Stokes equations for a sphere in a homogeneous Newtonian fluid given that the fluid is in laminar flow with the assumption that fluid particles do not interact among themselves. The term $\mathbf{F_{ext}}$ corresponds to an external force acting on the particle and could represent drifts, convections, or gravity. In the absence of flow, this term is set to zero. This assumption is valid for isolated systems, as gravitational effects are negligible compared to viscous forces ($\sim 10^9$ stronger than gravity in such systems). $\mathbf{F_{stoch}}$ is the stochastic force describing collisions between fluid molecules and the particle. It is responsible for Brownian motion. It is characterized by:

$$\langle \mathbf{F}_{\text{stoch}} \rangle = 0, \tag{1.3}$$

$$\langle \mathbf{F}_{\text{stoch}}(t)\mathbf{F}_{\text{stoch}}(t+\tau) \rangle = 2\Gamma_f m^2 \delta(\tau), \tag{1.4}$$

where $\delta(\tau)$ is the Dirac delta function and Γ_f is the velocity fluctuation parameter. The vanishing average simply points to the absence of directed motion in equilibrium and the Dirac delta implies that stochastic forces are uncorrelated in time.

We now proceed to plug in the initial conditions $\mathbf{v}(0) = \mathbf{v}_0$ in Equation 1.1, and the velocity evolves as:

$$\mathbf{v}(t) = \mathbf{v}_0 e^{-\alpha_v t} + \frac{1}{m}\int_0^t \mathbf{F}_{\text{stoch}}(t')e^{-\alpha_v(t-t')}dt'. \tag{1.5}$$

Integrating once more with initial position $\mathbf{r}(0) = \mathbf{r}_0$, the particle position is:

$$\mathbf{r}(t) = \mathbf{r}_0 + \mathbf{v}_0\frac{1-e^{-\alpha_v t}}{\alpha_v} + \frac{1}{m}\int_0^t \mathbf{F}_{\text{stoch}}(t')\frac{1-e^{-\alpha_v(t-t')}}{\alpha_v}dt'. \tag{1.6}$$

Here, we define the average area explored by the particle over a given time interval τ by the mean squared displacement (MSD) as:

$$\text{MSD}(\tau) = \left\langle (\mathbf{r}(t+\tau) - \mathbf{r}(t))^2 \right\rangle. \tag{1.7}$$

The MSD remains a widely used metric to study diffusion statistics which we will visit

again later in Chapter 2. Inserting Equation (1.5) into (1.6), the MSD can be written as:

$$\mathrm{MSD}(\tau) = \frac{2\Gamma_f}{\alpha_v^2}\,\tau, \qquad \text{for } \tau \gg \alpha_v^{-1}. \tag{1.8}$$

We consider simply the overdamped regime since the relaxation time α_v^{-1} is generally in the order of tens of picoseconds, far too small for experimental timescales and therefore negligible. For scale, our experiments are in the order of tens of seconds.

The fluctuation parameter Γ_f depends on both particle and fluid properties. Using the equipartition property of energy:

$$\langle E \rangle = \frac{1}{2} m \langle \mathbf{v}^2 \rangle = \frac{3}{2} k_B T. \tag{1.9}$$

where k_B is Boltzmann's constant and T is the absolute temperature.

From here, we derive:

$$\Gamma_f = \frac{3 k_B T \alpha_v}{m}. \tag{1.10}$$

The diffusion coefficient D_∞, defined as the long-time limit of the mean squared displacement per unit time, is:

$$D_\infty = \frac{\Gamma_f}{\alpha_v^2}. \tag{1.11}$$

Using Stokes' law, the diffusion coefficient of a spherical particle becomes:

$$D_\infty = \frac{k_B T}{6\pi\eta R}. \tag{1.12}$$

Thus, the MSD in 3D can be written as:

$$\mathrm{MSD}(\tau) \approx 6 D_\infty \tau, \qquad \text{for } \tau \gg \alpha_v^{-1}. \tag{1.13}$$

1.3 Experimental approaches to diffusion

While the diffusion theory had been established for long time, experimental characterization beyond the works of Perrin remained significantly challenging especially at more micrsocopic scales. Over the years, a wide range of techniques have been developed to quantify transport processes across different length and time scales. Early experimental-

ists mostly relied on ensemble measurements, in which the dynamics of a large population of particles are averaged to extract global transport properties in order to validate theoretical descriptions.

1.3.1 Nuclear magnetic resonance

In 1950, Hahn's discovery of spin echos [5, 6], where the application of a 180° radiofrequency pulse led to the spin magnetization being refocused into an experimentally measurable signal in the scale of tens of milliseconds. This macroscopic signal is a direct result of the local clusters of nuclei, and thus represents the properties of the ensemble. Thus, Hahn found the attenuation of such a macroscopic signal is directly influenced by the free diffusion under steady magnetic fields. This direct experimental access to the diffusion coefficient through NMR was further improved by Das and Saha in 1954 [7]. Beyond the standardization of diffusion and the extraction of diffusion coefficients from Brownian fluids, a group led by Woessner measured the attenuation of NMR signals for water molecules in geological cores and in a suspension of silica spheres [8]. He termed the coefficient so retrieved, as spin-echo diffusion coefficent, which we now call "effective or apparent diffusion coefficient".

1.3.2 Dynamic light scattering

Yet another method to understand diffusion was using dynamic light scattering (DLS). The works of Pecora, Cummins, and Pike (among many others) between 1965 to 1980 towards determing diffusion led to the development of the DLS system [9, 10]. The DLS system works by illuminating a steady state aqueous solution at a constant temperature with a visible laser. Upon irradiation, a small fraction of the light is scattered, and this scattered intensity fluctuates in a time-dependent manner due to the continuously changing distance between the particles, leading to constructive and destructive interferences. The fluctuations in intensity observed in DLS provide information on the timescale of motion of the scattering elements. Using autocorrelation, one can measure the diffusion coefficient of the particles, and therefore their dimensions. One characteristic of simple Brownian motion in a steady solution is that molecular motion is size dependent, with larger molecules moving more slowly as compared to smaller molecules which would perform rapid Brownian motion.

1.3.3 Fluorescence recovery after photobleaching

With the arrival of more powerful optical microscopy systems such as the confocal or spinning disk, the use of fluorescence to study diffusion seemed promising. Fluorescence recovery after photobleaching (FRAP) is a method standardized to study the dynamics of lipids and proteins on the cell membrane (or on artifical membranes) using fluorescence microscopy [11]. A small region of a surface containing mobile fluorophescent molecules is exposed to an intense illumination briefly so as to photobleach the fluorescence completely and irreversibly. Owing to the mobility of the fluorophores, however, the fluorescence is recovered. Using the rate at which the fluoroscence returns directly determines the mobility of the particles and is used to determine diffusion coefficients with knowledge of the bleached area [12]. This has been especially useful in studying the anomalous transport in crowded cells in biology [13]. Figure 1.1 represents a schematic of the FRAP process where the fluorescence is bleached upon strong illumination (blue arrow), and the fluorescence gradually recovers over time.

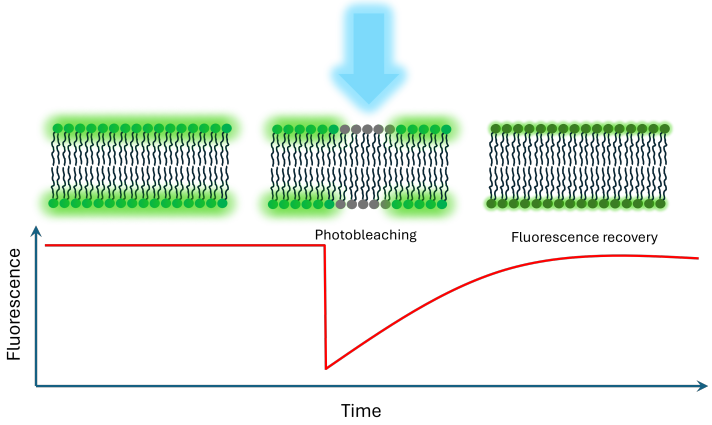

Figure 1.1: Fluorescence recovery after photobleaching: The mechanism of fluorescence recovery after photobleaching involves exciting mobile fluorophores such as on a bilipid membrane, followed by an intense pulse of excitation (shown as blue arrow) that irreversibly photobleaches the fluorophores, thus, turning them ”off” in predetermined region. Due to the motility of the particles, unbleached fluorophores then diffuse into the region thus recovering the fluorescence signal.

1.3.4 Fluorescence correlation spectroscopy

Fluorescence correlation spectroscopy (FCS) is yet another powerful technique for studying molecular diffusion and dynamics at very low concentrations. By analyzing temporal fluctuations in fluorescence intensity arising from molecules entering and leaving a small observation volume, FCS can extract characteristic diffusion times, diffusion coefficients, and molecular concentrations [14, 15]. Due to its high sensitivity and compatibility with

biological systems, FCS has been widely applied to investigate diffusion in solutions, living cells, and complex soft matter environments [16]. FCS has also been applied to identifying molecules even at the single particle level [17, 18]

While these approaches (among others that have not been discussed here) vary widely in terms of working principles, the common goal was to infer molecular motion through collective behavior at the microscopic scale. Consequently, while the measurements achieved through these techniques allow us to determine diffusion coefficients, they are still probed on the ensemble scale.

1.3.5 Heterogeneity and the ensemble averaging problem

The diffusion coefficient obtained from ensemble measurements typically determines the properties of the system as a whole at a given time scale by averaging over a given length scale and diffusing objects. While this poses no problem to homogeneous environments such as brownian fluids, or fairly homogeneous cell membranes, the method is restricted to samples that show statistically equivalent environments. A simpler example of this limitation is to consider a system with two distinct subpopulations of particles with very different diffusion coefficients. An ensemble experiment will accurately determine the average transport dynamics of the population as a whole, and yet it may fail to capture the true picture of heterogeneity. Generally, different microscopic processes can produce similar ensemble-averaged observables, making the interpretation of diffusion measurements inherently ambiguous. However, many natural and engineered systems exhibit significant spatial and temporal heterogeneity. Some examples of such systems are zeolitic and metal organic frameworks, biological cells, porous materials, polymer networks, and crowded extracellular environments, in which local transport properties may vary substantially even in microscale domains [19–22].

Thus, ensemble-averaged measurements act as a global characterization of the dynamics. Different particles experiencing distinct local environments, or even a single particle faced with diffusing through varying environments tend to get averaged over a potentially broad range of diffusion. As a consequence, important features such as confinement, transient trapping, directed transport, or local variations in viscosity or tortuosity may remain hidden within the ensemble average.

1.3.6 The power of single particle approaches

The arrival of single molecule techniques in optical microscopy shifted the paradigm of diffusion studies towards single molecule and single particle tracking (SPT) [16, 23, 24]. The SPT techniques which enabled the reconstruction of molecular motion at nanoscale

precisions allowed for probing the heterogeneities at this scale. Unlike methods we discussed so far, we can now probe heterogeneous environments for variations in diffusive properties spatially as well as temporally. SPT also offers a fundamentally different perspective by resolving the stochastic trajectories of individual probes, thereby accessing distributions of diffusivities and even rare events that are averaged out in ensemble measurements. In principle, we can trace the conceptual roots of the method to the earliest observations and quantification of Brownian motion by Perrin. This shift from ensemble averages to trajectory-resolved statistics has been particularly transformative in complex biological and soft matter environments, where local structure and temporal fluctuations play a dominant role in transport. As the core experimental technique used in this work, we will discuss the complete concept and functionality of SPT and single molecule microscopy in the next chapter.

1.4 Diffusion in complex environments

Real world environments in which diffusion occurs are often far more complex than what occurs in standard Brownian fluids considered in classical descriptions so far. Molecules and particles frequently encounter obstacles, trapping, interfaces, changes in viscosity among many other heterogeneities [19, 20, 25–28]. As a result, transport in such environments is strongly coupled to the underlying structure, forces, molecular activity of other species, all of which results in dynamics that is substantially different from static, unbound solution [22, 29–31]. Characterizing diffusion under such conditions has therefore become a central topic across disciplines ranging from soft matter physics and materials science to biology and medicine [28, 32–35]. In the following subsections, I discuss three relevant examples of SPT investigations in different complex environments which will be relevant in Chapter 3.

1.4.1 Opallic, crowded, and porous structures

The team of Schwartz at the University of Colorado studied spherical, fluorescent beads of polystyrene diffusing in a complex inverse opal structures which consist of a network of cavities interconnected by pores forming a ”pore-cavity-pore” structure. The network is hexagonally close packed and each cavity is connected to 12 adjacent cavities via circular holes. By analyzing 3 dimensional SPT (3D-SPT) trajectories, they first show that the diffusion in such environments are constricting and show trapped behavior [36]. Furthermore, they demonstrated a mechanism of how Brownian diffusion of these particles leads to escape from local trapping environments through a pore. They infer from experiments and theoretical calculations that escape under Brownian statistics is barrier controlled

rather than diffusion controlled as shown in Figure 1.2.

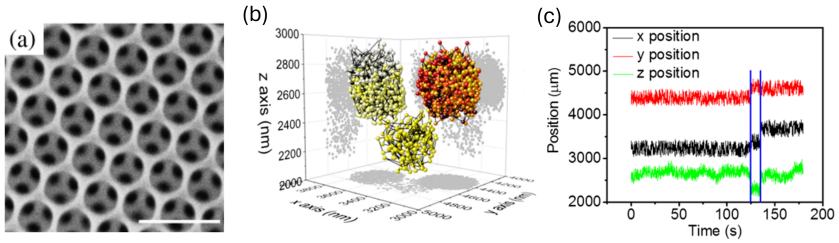

Figure 1.2: Diffusive escape in inverse opals: a. Representative scanning electron microscope image of the inverse opals structure b. Representation of a single trajectory of a fluorescent particle exploring three cavities c. The x, y, and z coordinates of a single particle over time as it explores the inverse opal cavities. The blue lines indicate an escape event from one cavity to another. (Adapted from [36]).

This led to a decreased escape probability with a stronge size based exclusion factor that was larger than expected from just pore-size dependence. Importantly, they emphasize the application of residence and escape times to analyze stochastic processes that show confinement. We will discuss these statistics in more detail in the next chapter.

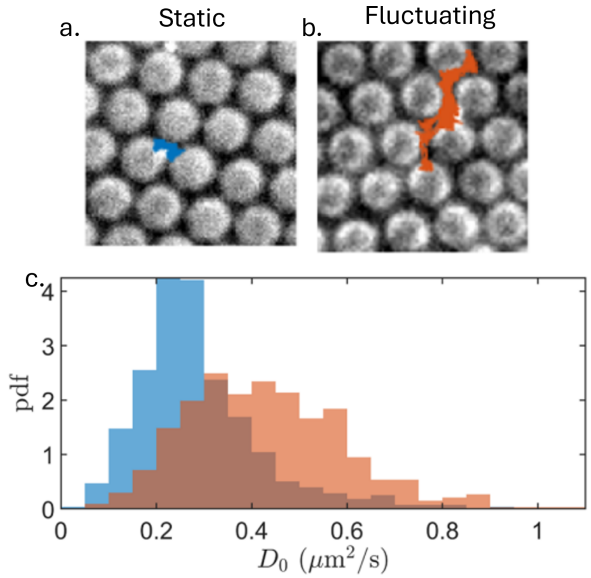

Figure 1.3: Diffusion in static and fluctuating crowded media: a. Single particle trajectory(in blue) of a fluorescent probe diffusing in a static field of packed silica spheres. b. Single particle trajectory(in orange) of a fluorescent probe diffusing in a fluctuating field of silica spheres. c.Frequency distribution demonstrating that the diffusion coefficient is higher in fluctuating porous environments as opposed to static packed media. (Adapted from [29]).

Subsequent work from the same team has also shown the facilitation of diffusion using thermal fluctuation of the crowding environment [29]. Assembling two independent layers of static and fluctuating layers of closely packed silica spheres, the team revealed the

action of fluctuations and their influence on diffusion. By performing SPT of fluorescent spherical tracers in static and fluctuating layers independently, they showed the ability of the flucutuating medium to enhance the diffusive process by transiently opening escape routes for the tracers leading to increases in the range of 50% 1.3.

1.4.2 Hydrogels

Yet another popular diffusive playground are hydrogels. Their complex structure of interwoven gel-mesh network coupled with their transparency makes them an ideal environment to study nanoscale transport. One such recent work by Lin *et al.* [25] uses a high-speed 3D active feedback system to achieve 3D localization and tracking at the nanoscale. They report the diffusion of single spherical fluorescent tracers between distinct cavities within the gel matrix. Owing to the high sampling rate of the setup, they uncover a hopping behavior of the particle between different confinement regions. By studying the dwell time of a particle in each cavity, they uncover the thermodynamic mechanism that underlies such hopping mechanism showing that it is entirely governed by entropic difference between the pores. They further showed that this entropic barrier is determined by pore size, and have quantified and given an expression for the difference in free energy in terms of the two adjacently involved confinements (Figure 1.4).

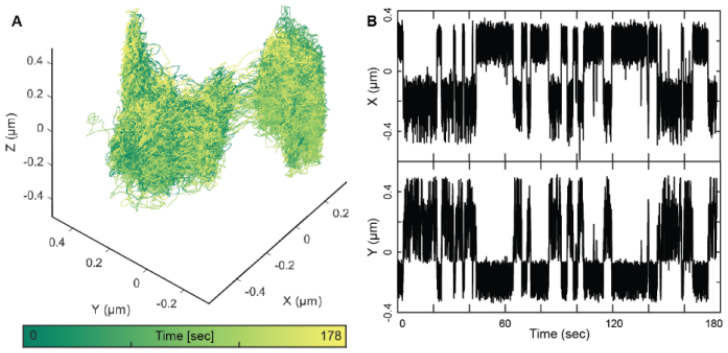

Figure 1.4: Hopping diffusion in hydrogel networks: a. Single particle trajectory reveals a hopping diffusion between two distinct confining compartments within the hydrogel. b. The x and y coordinates of a single particle demonstrates the two nature of the two state process of the hopping between two compartments (Adapted from [25]).

Lee *et al.* have recently worked with single particle tracking of quantum dots in polyacrylamid gels [37]. They observe a subdiffusive mean square displacement along with non-Gaussian step sizes indicating hindrances to normal diffusive behavior of such tracer molecules. A range of cross-linkers were used to modify the gel to vary caging events by controlling the density of the network. Using the distribution of caging times could be explained by simple random trap models with an exponential distribution of trapping

energies which could range from 1 to 3 times that of the thermal energy with increased cross-link density (Figure 1.5).

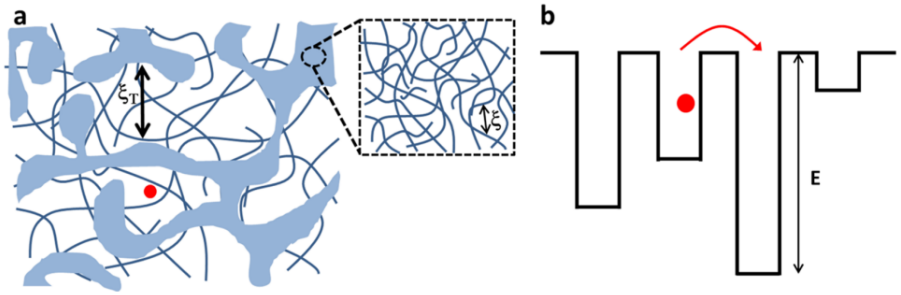

Figure 1.5: Diffusion of QDs in polyacrylamide gels:a. Representation of QD diffusing in a meshwork of polyacrylamid gels with "caging". b. Schematic representing the caging behavior in terms of a array of 1D traps with random energy barriers. (Adapted from [37]).

1.4.3 The brain extracellular space

One of the direct applications of diffusion studies has been in the health and biology sector, where both ensemble as well as SPT observations have led to significant progress in understanding health and disease. Here, to illustrate such progress, we consider the case of extracellular space in the brain [38, 39], a region which is actively studied in our group.

The extracellular space (ECS) in the brain accounts for approximately a quarter of the volume. Apart from forming intricate structures of networks between the cells, these regions also exhibit dynamic heterogeneities with regard to age, health and development [40, 41]. Furthermore, these regions are also microenvironments for diffusion of biomolecules such as neurotransmitters, nutrients, proteins, and signaling molecules. While the ECS had been mapped previously through cryo-EM imaging of fixed tissues, little was known about the diffusive behavior of molecules in these regions, especially with regard to live tissues [40] (Figure 1.6). Needless to say, the exploration of brain ECS using diffusing nanoparticles has gained significant interest in recent years with respect to health and disease [42–44].

While some of the earliest experiments probing this region was achieved using ensemble techniques and hence provided spatially and temporally coarse data, methods using ionophoresis and radiotracers were able to estimate volume fractions and tortuosity as a measure of hindrance to simple diffusion [45, 46]. More recently, the exploration of the ECS has shifted focus towards SPT. Over the years, studies from our team have explored and progressed in the study of diffusion in the ECS owing to the application of single walled carbon nanotubes (SWCNTs) as single molecule probes that have been engineered

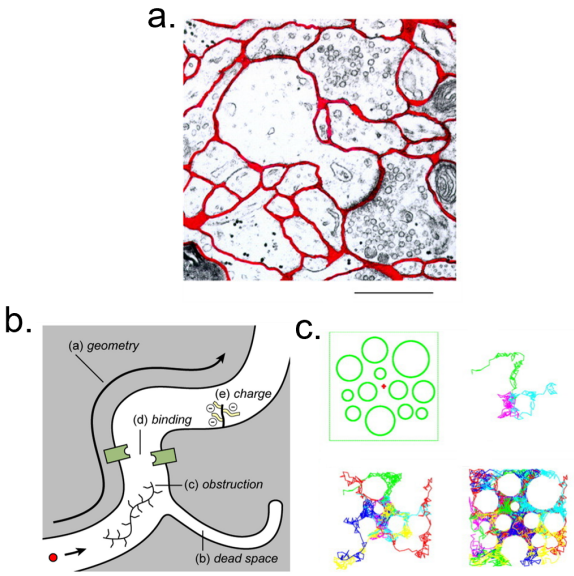

Figure 1.6: Diffusion in the brain ECS a. Cryo-EM imaging reveals the continuous structure of the brain ECS (in red) Scale bar: 1 µm b. Schematic representation of the ECS showing the complexity with charged regions, dead-ends, fluxes, and binding sites adding to the already complex geometry. c. Schematic representation to understand the diffusion in ECS involves modelling diffusion in the ECS as particles diffusing through a crowded environment full of obstacles (Not to scale, ECS sizes exaggerated) (Adapted from [40, 42])

for size, optical, and biological compatibility. The earliest use of SWCNTs for SPT in the ECS was led by Godin *et al.* [47]. Taking advantage of the overlap of the biologically transparent optical and the emission of SWCNTs, the work showed that single particles of SWCNTs could be tracked diffusing inside the ECS of acute rat brain tissues at depths of upto 100 μm with a resolution of 40nm. The tracking demonstrates the interconnected compartmentalization of the ECS even at the nanoscale with signatures of specific rheological properties [41, 48, 49]. The work further revealed that diffusion in the ECS is heterogeneous, and instantaneous maps of the diffusion coefficients showed spatial variations in viscosities. Chemical alterations before the introduction of the SWCNTs also demonstrated the rheological properties of the ECS are locally affected. Such SPT also reveals the physical nanoscale dimensions of the ECS. SWCNTs have also been used to study other domains of health and disease, including the demonstration of variation in diffusion in the interstitial spaces of healthy and fibrosed liver tissues [50].

More recently with the progress of chemically engineering SWCNTs to have increased intensities as well as engineering the physical size of the nanotubes, 3D-SPT of nanotubes diffusing in mouse organotypic slices have revealed previously unknown architectures within the ECS [51]. Furthermore, with the advancements of optics, using a polarization sensitive microscopy technique, Ruan *et al.* [52] have demonstrated that apart from heterogeneity in translational diffusion, there exists inhomogeneity in local rotational

diffusion in the ECS. In this thesis, I will show the application of such microscopy in unravelling escape mechanisms of SWCNTs from trapped environments. The team further showed that by modulating the structure of the extracellular matrix scaffolding, the translational and rotational diffusion dynamics of SWCNTs are affected.

1.5 The curious case of anistropic particles

Although the diffusion of spherical particles provides an important foundation for understanding stochastic transport, relatively few objects encountered in nature possess truly spherical symmetry. Naturally occurring particles such as proteins, biopolymers, filamentous structures, viruses, and many engineered nanomaterials instead exhibit elongated or otherwise anisotropic geometries. Such particles interact with their surroundings with an added degree of freedom pertaining to their rotation, resulting in transport properties that differ fundamentally from those of spheres. Before considering the influence of confining, complex and heterogeneous diffusion architectures, it becomes important to evaluate the effect of the shape of the particle on diffusion. Single-walled carbon nanotubes (SWCNTs), as used by our team to probe the extracellular space, fall into the category of anisotropic particles due to their effectively one-dimensional structure. Naturally, this raises the question of how such 1D objects diffuse in complex environments which I address in this thesis.

1.5.1 Diffusion in a free environment

As discussed above, the earliest explanations and mathematical formalization for Brownian motion was provided by Einstein in 1905 [2]. Subsequently, several experiments have been conducted with direct videoimaging of isotropic particles exploring homogeneous and complex environments [29, 36, 53–55]. On the other hand, such direct detection of observation of rotational Brownian motion have remained fairly untested for long. F. Perrin's work first discussed the role of coupling of rotational and translation motion for anisotropic particles and their influence on diffusion [56].

First, an anisotropic particle with a single axis (rod-like or ellisoidal) is defined by anistropic hydrodynamic frictional forces whose coefficients are defined by γ_a (along the axis of the particle) and γ_b (perpendicular to the particle axis). The translational diffusion of such a particular independently along the two directions considering no rotation, gives diffusion coefficients $D_a = k_B T/\gamma_a$ and $D_b = k_B T/\gamma_b$ along the respective directions referred to as body frame. Here k_B is Boltzmann's constant and T is the absolute temperature. The general notion is $\gamma_a < \gamma_b$ resulting in $D_a > D_b$.

However, when rotation is allowed in 2D for example, the rotational diffusion is now characterized by the diffusion coefficient D_θ and the characteristic timescale of this rotation is given by $\tau_\theta = 1/2D_\theta$. The rotation and the associated diffusion time τ_θ define the the window over which the particle loses memory of its orientation. This leads to the crossover from anisotropic diffusion at shorter time windows to isotropic diffusion when the timescales are relatively larger compared to τ_θ and D_a converge with D_b. Additionally, the coupling between translational and rotational motion gives rise to non-Gaussian displacement distributions. The mathematical formulation of this is given by Perrin model of ellipsoid diffusion as below.

We first write the hydrodynamic friction terms as follows:

$$\gamma_{a,b} = 3\pi\eta L G_{a,b} \tag{1.14}$$

and G_a and G_b are the Perrin geometric factors that depend on the aspect ratio of the particle and are defined as:

$$G_a = \frac{8}{3}\left[\frac{2\phi}{1-\phi^2} + \frac{2\phi^2-1}{(1-\phi^2)^{3/2}}\ln\left(\frac{\phi+\sqrt{\phi^2-1}}{\phi-\sqrt{\phi^2-1}}\right)\right]^{-1}, \tag{1.15}$$

$$G_b = \frac{8}{3}\left[\frac{\phi}{\phi^2-1} + \frac{2\phi^2-3}{(\phi^2-1)^{3/2}}\ln\Big(\phi+\sqrt{\phi^2-1}\Big)\right]^{-1}. \tag{1.16}$$

From here, the two diffusion coefficients D_a and D_b can be written as:

$$D_a = \frac{k_B T ln(2\phi)}{2\pi\eta L} \tag{1.17}$$

and

$$D_b = \frac{k_B T ln(2\phi)}{4\pi\eta L} \tag{1.18}$$

where $\phi = L/d$ is the aspect ratio of the particle for length L and diameter d and $\phi >> 1$. The fact that the axial diffusion D_a is twice as large as the perpendicular diffusion D_b is natural consequence of the ellipsoid having two perpendicular axes and only one parallel axis.

To study the mean square displacement along these two directions we have:

$$MSD_a(\Delta t) = 2D_a(\Delta t) \tag{1.19}$$

and,

$$MSD_b(\Delta t) = 4D_b(\Delta t) \tag{1.20}$$

In a given 3D volume space (x,y,z), the MSD for the general case is written as:

$$MSD = 6D_t\Delta t \tag{1.21}$$

where D_t is the effective translational diffusion coefficient. For the anisotropic case, the diffusion along the parallel and perpendicular direction through equipartition results in:

$$D_t = \frac{D_a + 2D_b}{3}. \tag{1.22}$$

Then, using the Einstein's relation,

$$D_a = \frac{k_B T}{\gamma_a}\ , \qquad D_b = \frac{k_B T}{\gamma_b} \tag{1.23}$$

Here, we write the friction coefficients as:

$$\gamma_a = 6\pi\eta V\, G_a\ , \qquad \gamma_b = 6\pi\eta V\, G_b \tag{1.24}$$

For a particle with a large aspect ratio ϕ, the orientationally averaged translational diffusion coefficient is approximated to:

$$D_t \simeq \frac{k_B T}{3\pi\eta L}\ln(2\phi). \tag{1.25}$$

and the rotational diffusion is described by:

$$D_r = \frac{k_B T}{\gamma_r}, \tag{1.26}$$

for rotational diffusion coefficient D_r with the rotational friction coefficient γ_r as:

$$\gamma_r = 6\eta V G_r, \tag{1.27}$$

and G_r is the rotational geometric factor and V is the volume of the ellipsoid $V = \frac{4}{6}\pi L\frac{d^2}{4}$ and:

$$G_r = \frac{2}{3}\frac{\phi^4 - 1}{\phi}\left[\frac{2\phi^2 - 1}{\sqrt{\phi^2 - 1}}\ln\left(\phi + \sqrt{\phi^2 - 1}\right) - \phi\right]^{-1}. \tag{1.28}$$

Again, for large aspect ratio particles, this equation can be reduced to:

$$D_r \simeq \frac{3k_B T \ln(2\phi)}{\pi\eta L^3}. \tag{1.29}$$

For rotational diffusion in 3D with two independent axes that are perpendicular to the particle axis, the Mean Square Angular Displacement is then defined as:

$$\langle MSAD(\Delta t)\rangle = 4D_r\,\Delta t \tag{1.30}$$

1.5.1.1 Experimental validation of Perrin's model

The first direct observation and validation of Perrin's model with rod like ellisoidal particles diffusing in 2D was demonstrated by Han *et al.* in 2006 [57]. In their experiments, they studied ellipsoidal PMMA (polymethyl methacrylate) molecules diffusing in a quasi-2-dimensional cell allowing for in-plane imaging (Figure 1.7). The 3D MSD and MSAD derived by Perrin can be reduced to 2D as follows:

$$MSD_{xy} = 4D_{xy}(\Delta t) \tag{1.31}$$

and,

$$MSAD_\theta = 2D_\theta(\Delta t) \tag{1.32}$$

1.5.1.2 Perrin's diffusion model for an ellipsoid

The diffusion of the particles were considered in two perspectives. The first being the lab frame, where the initial orientation of the particle was considere to be zero and diffusion in the lab frame was defined as D_{xx} and D_{yy} along the x and y directions given by:

$$D_{xx} = \frac{\langle[\Delta x(t)^2]\rangle_0}{2t} \tag{1.33}$$

and,

$$D_{yy} = \frac{\langle[\Delta y(t)^2]\rangle_0}{2t} = \frac{\langle[\Delta x(t)^2]\rangle_{\frac{\pi}{2}}}{2t} \tag{1.34}$$

where x and y are the coordinate directions and t represents time. The angles 0 and $\pi/2$ written as subscripts represent the orthognality of the two axes.

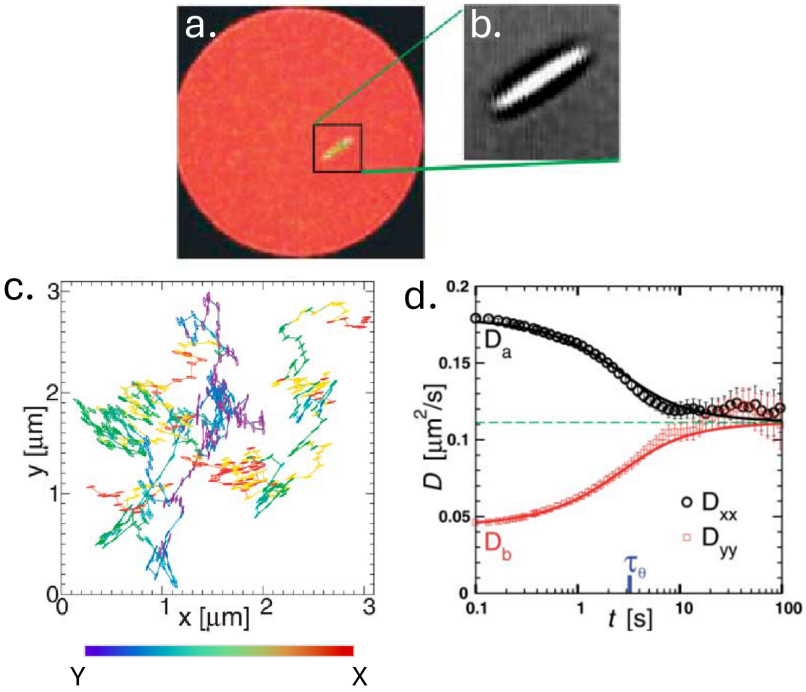

Figure 1.7: Brownian motion of an ellipsoid: a. True color image of an anisotropic particle diffusing in 2D with b. image of a single ellipsoidal PMMA (polymethyl methacrylate) molecule. c. The 2D trajectory of a single ellipsoidal particle performing Brownian motion.n The color scale represents orientation with bluer colors representing diffusion along the Y-axis, and red colors representing diffusion along the X-axis. d. The diffusion coefficient D in the lab frame with initial orientation set to zero demonstrates the decoherence time τ_θ beyond which the anisotropic nature of the diffusion crosses over to isotropic diffusion (Adapted from [57]).

By analyzing the diffusion of the particles in the lab frame (D_{xx} and D_{yy}) and comparing it to the diffusion of the particle in body frame (D_a and D_b), they were able to experimentally verify the notion of anisotropic diffusion at early timescales that, beyond the diffusion time window τ_θ, converge to isotropic diffusion due to loss of orientational memory. That is, for $t << \tau_\theta$:

$$D_{xx} = D_a \tag{1.35}$$

and

$$D_{yy} = D_b \tag{1.36}$$

However, when $t >> \tau_\theta$:

$$D_{xx} = D_a = D_{yy} = D_b = \overline{D} \tag{1.37}$$

Apart from directly visualising the coupling between rotational and translational diffusion, their work also experimentally demonstrated the non-Gaussian effects for anisotropic particles when $D_a >> D_b$, followed by describing that the experimental limit below which non-Gaussianity was lost is $D_a/D_b < 2.5$.

1.5.2 Diffusion in a complex environment

As we have seen in the previous section, the anisotropic nature of 1D molecules gives rise to interesting diffusion phenomena. Now, when we couple this anisotropy with restrictions in diffusion caused by crowded media such as gels and packed collides, the underlying behavior of the particle under constrained spaces strongly influences the diffusion properties. I highlight two such experiments here.

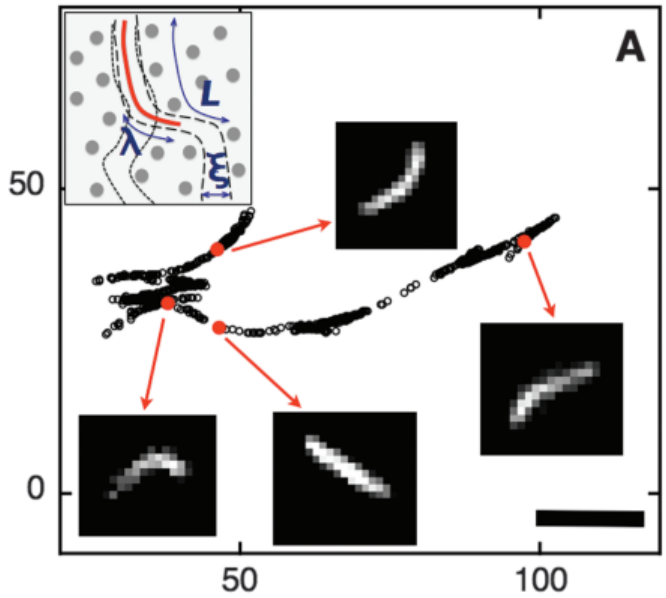

Figure 1.8: Diffusion of an SWCNT in a complex environment: The two-dimensional center-of-mass trajectories of a SWCNT performing a reptating behavior in 1.5 % agarose gel. The insets are representative NIR images showing the bending nature of the tubes. The scale bar represents $5\mu m$ (Adapted from [58]).

Using SWCNTs diffusing in 1.5% agarose gel, Fakhri *et al.* [58] showed the mechanisms of interplay between crowding and thermal bending in 1D molecules. SWCNTs, as stiff 1D molecules, show different time domains of diffusion along translation and perpendicular directions. As the nanotubes explore their rotational freedom by repeatedly reptating in and out of pores, the rotational and translational get strongly coupled (which is true even in Brownian fluids). At short time windows, the diffusion of nanotubes in such

crowded environments is anisotropic. The diffusion along the length of the nanotube is significantly faster than in the perpendicular direction. Beyond this timescale, defined by the diffusion crosses over to the isotropic regime owing to the later timescales that show superdiffusive behavior along the perpendicular axis. The results show how the coupling between translation and rotation result in specific probing mechanisms for long molecules in complex crowded environments and by extension, biological media (Figure 1.8).

In yet another study from our team, the reptation dynamics of SWCNTs were studied in a porous structure formed from the interstitial spaces of packed monodispersed colloids [59]. Using videomicroscopy to visualize diffusing SWCNTs in packed colloidal media, it was shown that their diffusion influenced by the environment. The pore shape and pore structure strongly affected the mobility of the SWCNTs, with the environment strongly controlling the reorientation. The work reveals how in packed structures SWCNTs diffuse along straight pores and bend across pores, while on the other hand, in gel-like material, the SWCNTs consistently diffuse in curved pores, displaying faster parallel motion. Finally, it was seen that in both types of complex media, the finite stiffness of the SWCNT enhanced rotation diffusion that ultimately prevents the jamming of the particle (Figure 1.9).

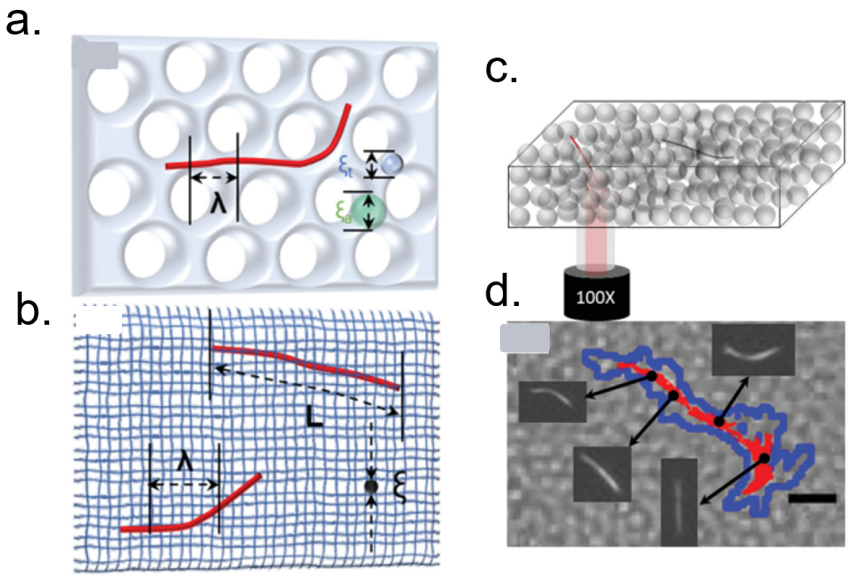

Figure 1.9: Reptation dynamics of SWCNTs in complex environments: a. Representative image of an SWCNT(in red) diffusing in randomly ordered packed colloidal particles. b. Representative image of SWCNTs diffusing in an agarose gel mesh. L, λ, and ξ represent the length, deflection length of the nanotube, and the pore size respectively. c. Experminetal single molecule microscopy setup showing semi-flexible SWCNTs diffusing in complex environments. d. SWCNT image overlapping on brightfield image of the complex environment with the trajectory in red, and area explored in blue. The insets show the various orientations and bending of SWCNTs through their diffusion [59].

To address the question of diffusion of stiff SWCNTs that are used in studying the ECS,

there is a need to understand diffusion of SWCNTs in a model system that closely resembles the ECS. In this regard, hydrogels and opal like structures, while representative of complex diffusion environments, describe pore-mediated transport and thus do not truly represent the continuous geometry as seen in the ECS. Thus, this work introduces a model system that closely represents the continuous geometries that are seen in the ECS.

In this chapter, we have introduced the key concepts that form the basis of the work presented in this thesis. From the diffusion of isotropic and anisotropic particles to the challenges posed by complex environments, we have seen how transport can be influenced by both particle properties and the surrounding medium. We also highlighted the role of single-particle tracking as a powerful tool for probing these dynamics and highlighted the applications of SWCNTs as a 1D probe in complex environments as well as brain tissues. With this background in place, we now turn to the methods and models used to characterize diffusion before applying them to a range of experimental systems.

Chapter 2

Quantifying and modeling diffusion

Having introduced the theoretical foundations of Brownian diffusion in both isotropic and anisotropic particles, together with the advantages of single-particle tracking over ensemble techniques, we now turn to the statistical framework used to characterize diffusion. In this chapter, we introduce the principal analytical tools used to quantify diffusion and discuss the different physical models under which diffusive motion can be classified.

2.1 Statistical descriptors of diffusion dynamics

Single-particle tracking (SPT) provides direct access to the stochastic trajectories of individual particles, enabling the quantitative characterization of their transport dynamics across multiple spatial and temporal scales [60, 61]. To quantify diffusion from these trajectories, a range of statistical descriptors can be employed to probe different aspects of the underlying motion, including spatial exploration, temporal correlations, confinement, and directional persistence. These descriptors are not limited to SPT experiments alone, but constitute general analytical tools widely used in the study of diffusive and stochastic processes across soft matter, biological, and statistical physics systems [62–64]. In this section, I describe these statistical measures and their application to characterize the diffusion of single particles in different environments that we will later apply to our own experimental datasets.

2.1.1 Mean Square Displacement

The most familiar measure to study diffusion of single particles is the mean square displacement(MSD) [4, 65, 66]. The MSD is a popular parameter to describe the explorative capacity of a particle in an environment and is defined by the exploration area against the timescale of exploration [62]. A common method to calculate the MSD is the ensemble-

averaged MSD (eaMSD), which is the squared of the displacements for a given lag time that are averaged over all the trajectories that are available. Thus, mathematically, one can define the MSD for a specific time as:

$$\langle r^2(\Delta t)\rangle = \frac{1}{M}\sum_{i=1}^{M}\left(\mathbf{r}_{j+k}^{(i)} - \mathbf{r}_{j}^{(i)}\right)^2 \tag{2.1}$$

where $\langle r^2(\Delta t)\rangle$ is the mean squared displacement (MSD) for a lag time Δt, M is the total number of displacement intervals considered, $\mathbf{r}_j^{(i)}$ is the particle position at time index j for the ith trajectory segment, and $\mathbf{r}_{j+k}^{(i)}$ is the position after a time lag corresponding to k frames. A schematic representation is shown in Figure 2.1.

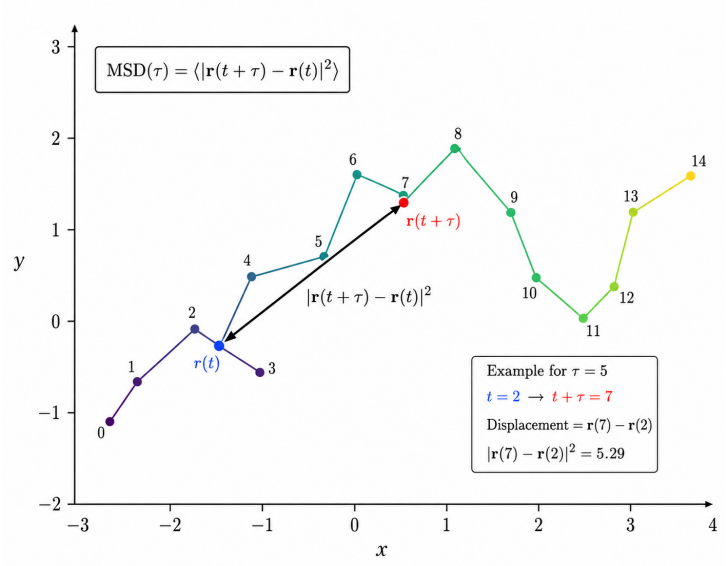

Figure 2.1: Calculating the mean square displacement: The MSD of a trajectory is calculated by averaging the squares of the displacements at each time lag

Alternatively, the time averaged MSD (taMSD) could be calculated for each trajectory in order to get a distribution of MSDs. Obtaining such distribution of individual MSDs allows us to look at heterogeneities in diffusion, which could potentially be helpful in complex environments or biological tissues to spatially correlate diffusion behaviors. However, care must be taken when interpreting the taMSD at long lag times. As the lag time increases, the number of independent displacement measurements decreases, resulting in larger statistical fluctuations and reduced reliability of the calculated taMSD [66]. The taMSD is mathematically defined as below:

$$\langle r^2(\Delta t)\rangle_i = \frac{1}{N-k}\sum_{j=1}^{N-k}\left(\mathbf{r}_{j+k}^{(i)} - \mathbf{r}_{j}^{(i)}\right)^2 \tag{2.2}$$

where $\langle r^2(\Delta t)\rangle_i$ is the time-averaged mean squared displacement (MSD) for trajectory i

at lag time Δt, N is the total number of frames in the trajectory, k is the lag expressed in number of frames, and $\mathbf{r}_j^{(i)}$ and $\mathbf{r}_{j+k}^{(i)}$ are the particle position vectors at frames j and $j+k$, respectively.

We next come across the possibility of combining the previous two flavors of MSDs available to us, thereby arriving at a time averaged ensemble MSD (teaMSD). The teaMSD is mathematically defined as below:

$$\left\langle r^2(\Delta t)\right\rangle_{t,E} = \frac{1}{M}\sum_{i=1}^{M}\left\langle r^2(\Delta t)\right\rangle_t^{(i)} \tag{2.3}$$

where $\langle r^2(\Delta t)\rangle_{t,E}$ is the time ensemble averaged mean squared displacement (teaMSD) at lag time Δt, M is the total number of trajectories included in the averaging, and $\langle r^2(\Delta t)\rangle_t^{(i)}$ is the time-averaged MSD calculated for the ith trajectory. This quantity represents the average of the individual trajectory taMSDs over the ensemble of particles. Due to the averaging of multiple trajectories, the teaMSD sufficiently smoothens out the fluctuations that one would expect in taMSD. However, we must ensure that the trajectories that are used to calculate the teaMSD explore similar regimes. Large flucutations in the explorative capabilities of the individual trajectories would lead to a less reliable teaMSD [66]. Figure 2.2 shows an example of the teaMSD (blue), eaMSD(red), and the individual taMSDs calculated from trajectories of CCNTs diffusing in homogeneous solution.

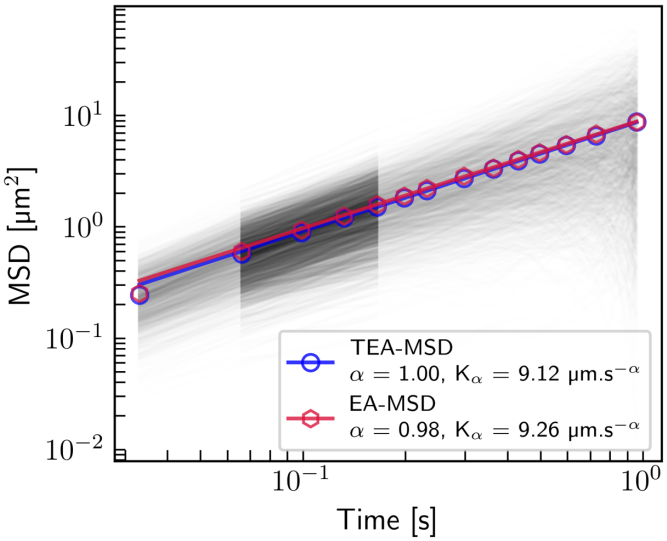

Figure 2.2: Mean squared displacement for CCNTs in bulk liquid: The EA-MSD and TEA-MSD as calculated from SPT of CCNTs diffusing in a bulk solution shows ergodic behavior with the ensemble α significantly less than unity. Each background gray line reveals the MSD of individual trajectories in the ensemble.

All three means of calculating the MSD follow a common power law given by the following mathematical expression:

$$\left\langle r^2(t) \right\rangle_i = 2dK_\alpha t^\alpha \tag{2.4}$$

In the above equation, d is the spatial dimension of the environment where the random walk occurs (d = 3 for 3D-SPT), α is the scaling exponent (often referred to as 'anomaly exponent'), and K_α is the generalized diffusion coefficient. When the diffusion is in a bulk liquid for example, normal Brownian motion is achieved trivially by setting $\alpha = 1$ and identifying $K_\alpha = D$. This generalized scenario allows for the value of K_α to be the diffusion coefficient that yields the analogy of rate of exploration of the underlying stochastic process. On the other hand, the term alpha determines scaling of diffusion as: $\alpha = 1$ indicating normal Brownian diffusion characterized by true random walks, with the cases of $\alpha < 1$ and $1 < \alpha < 2$ are termed sub- and superdiffusion, respectively (Figure 2.3). Thus, the two parameters, the scaling exponent α with the diffusion coefficient K_α, indicate whether a particle is impeded in its diffusion (e.g. by obstacles or the viscoelasticity of the surrounding medium) or rather is actively driven (e.g. by molecular motors or an ambient flow). Given that the generalized diffusion coefficient K_α is only equivalent to the standard diffusion constant for α=1, we must be careful not to interpret it as a rate of region explored when $\alpha < 1$, since when $\alpha < 1$, K_α has irrational units of area per fractional time. This in turn makes straightforward comparisons of K_α meaningless if the exponent α varies between trajectories and/or ensembles. However, as a rough estimate to the case of normal diffusion constants, one could use the values of K_α at different α can be interpreted as the typical area that is explored within one second, although this neglects the multi-scale nature of the diffusion process. Additionally, one could also employ MSD values at smaller and/or larger times for a simple quantitative comparison when facing different α. Finally, ballistic motion is characterized by $\alpha = 2$ with K_α having dimensions equivalent to the square of the velocity of the particle being tracked [65] [66]. In this thesis, I have chosen to graphically represent these power laws in a double logarithmic plot, thus representing growing MSDs as simple straight lines. The representation of the same MSD plots in linear styles would lead to strongly curved lines as a linear plot basically visualizes only the largest order of magnitude. These methods of representation become less meaningful or important for short trajectories that can only yield MSD values within an order of magnitude in lag time.

Apart from MSDs being a first insight into single-particle tracking data, MSDs also help determine the fundamentals of underlying statistical mechanics [67]. For example, a significant deviation between the eaMSD and taMSDs (or even teaMSD) demonstrate ergodicity breaking [66]. Here, ergodicity is the property of equivalence (or even conver-

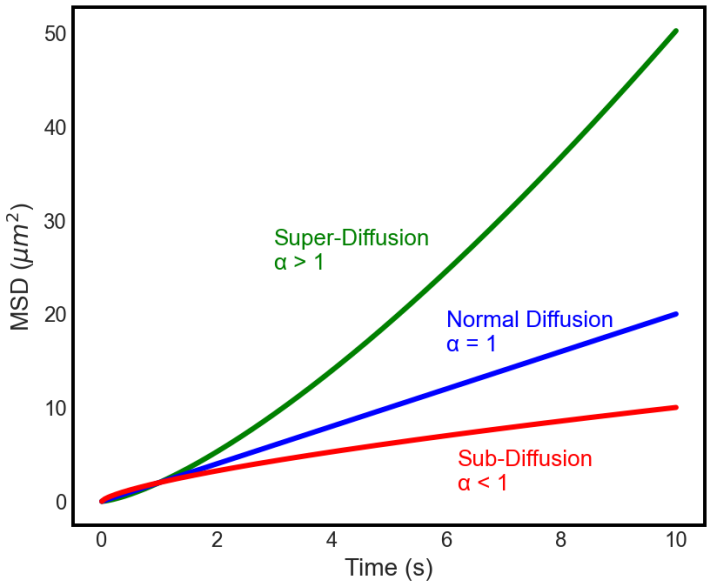

Figure 2.3: Scaling of diffusion regimes Simulated trajectories of superdiffusive, brownian, and subdiffusive motions show the scaling of MSD with lagtime.

gence sometimes) between time-averaged and ensemble-averaged observables in stochastic processes. In a system that is ergodic, statistical measurables computed along a single sufficiently long trajectory will be equivalent or converge to the same measurables calculated by averaging over many independent realizations(Figure 2.2). For diffusion processes, this is often probed by comparing taMSD and the eaMSD. For example, classical Brownian motion and fractional Brownian motion (FBM) (which will be introduced in the next section) are ergodic, that is, their time averaged and ensemble averaged MSDs coincide at longer time scales. In contrast, other processes such as continuous time random walk having heavy-tailed waiting time distributions exhibit ergodicity breaking, where significant trajectory-to-trajectory variability persists even for long observation times. This non-ergodic behavior is often accompanied by material and diffusion properties such as aging, where measured quantities depend on the total measurement duration. In SPT, assessing ergodicity is an important step in identifying the underlying diffusion model, since different mechanisms of anomalous diffusion can produce similar MSD scaling despite originating from fundamentally different physical processes. In this regard, the MSD has been a vital tool to study diffusion properties in the cytoplasm of cells, structured environments, as well as the brain ECS in our team [13, 19, 20, 32, 46, 55]. As we will see in chapter 4, I use MSD as the fundamental basis for my own analysis.

2.1.2 van Hove correlation

Now we introduce another estimator called the probability density function (PDF) of displacements. Also called the van Hove correlation, this measure probes the distribution

of step sizes sampled by the single particle. Simple Brownian motion leads to smooth Gaussian PDFs which reminiscent of true random steps taken in a homogenous medium. On the contrary, more complex environments can lead to heavy tailed functions of the distribution as a result of intermittent big "jumps" or architectural heterogeneity [66,68]. The van Hove correlation function provides a statistical description of particle displacements over a given time lag. This measure acts complementary to the MSD. In SPT, the van Hove function, $G_s(\Delta r, \Delta t)$, is commonly used and corresponds to the probability distribution of displacements over a time interval Δt:

$$G_s(\Delta r, \Delta t) = \langle \delta(\Delta r - |r(t + \Delta t) - r(t)|) \rangle \tag{2.5}$$

This quantity captures the full distribution of step sizes, providing information that is particularly useful for identifying deviations from Gaussian steps. For the standard case of Brownian motion, the van Hove function takes a Gaussian form, owing to the central limit theorem and the uncorrelated mechanism of random walk. In such a case, the distribution widens with time lag, however, always maintaing the Gaussian shape of the distribution. The extent of widening then is characterized by the diffusion coefficient signifying the explorative "speed" of the particle.

On the contrary, complex systems tend to exhibit non-Gaussian distributions, even if the MSD were to demonstrate simple scaling in the power law. Such deviations point to changing heterogeneity arising from a changing environment [69, 70]. Additionally, different diffusion models can bring about distinct distributions in this distribution, thus the van Hove PDF also acts as a fingerprint to distinguish between certain diffusion models [65].

2.1.3 Velocity autocorrelation function

While a nonlinear scaling in the MSD shows the exponential scaling of the diffusivity and provides some interpretations on the speed of exploration, it yet does not determine the diffusive model that the transport process follows [65]. To simplify, multiple diffusive processes can yield similar MSD scalings, thereby making them indistinguishable from each other if one were to look at the MSD alone as a diffusion parameter. Hence, we now look at an additional parameter to study diffusive processes that drive particle motion. The velocity autocorrelation function (VACF) is a quantifier to precisely probe memory between successive steps in particle motion within a trajectory [66]. We first extract the steps between localizations within the trajectory at a chosen time lag. Next, we calculate instantaneous velocity, demonstrating how the particle would jump between these frames neglecting the localizations in-between. Pairs of these velocities are correlated

in a temporal span Δt which ultimately determines the "memory" between successive steps. Standard Brownian motion shows no memory, meaning that successive steps are truly random, and thus uncorrelated (Figure 2.4 orange). However, various scenarios in diffusive processes allow for the correlation to be persistent or antipersistent, at which point the VACF yields a non zero correlation. Briefly, when particle steps are such that the particle tends to have persistence in its motion in a certain direction, the correlation tends towards positivity (Figure 2.4 green).

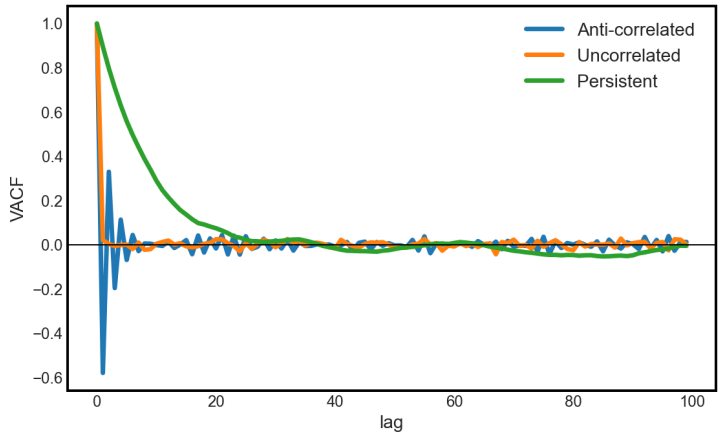

Figure 2.4: Trajectory memory effects probed by VACF: Simulated trajectories with persistent, antipersistent and uncorrelated (Brownian) steps as distinguished using VACF. The noise in the curves is a result of the VACF being calculated on single long trajectory of varying lengths with localization errors. Thus, VACF is ofted calculated on ensemble scale.

On the contrary, when a particle tends to "bounce back" or experience hindrances resulting in retracing its step, the correlation tends towards negativity(Figure 2.4 blue). To investigate the existence of a potential memory kernel for a single particle, the VACF can be mathematically formulated as:

$$c_t^{(i)}(\Delta t) = \frac{\langle v(t)\, v(t+\Delta t)\rangle_t}{\langle v(t)^2\rangle_t} = \frac{\sum_{j=1}^{N-k} v_{j+k}^{(i)} v_j^{(i)}}{\sum_{j=1}^{N-k} \left[v_j^{(i)}\right]^2} \tag{2.6}$$

where $c_t^{(i)}(\Delta t)$ is the normalized velocity autocorrelation function (VACF) for trajectory i at lag time Δt, $v_j^{(i)}$ is the velocity at time index j for trajectory i, N is the total number of velocity points in the trajectory, and k is the lag index corresponding to the lag time $\tau = k\Delta t$, where Δt is the experimental time step. The notation $\langle \cdots \rangle_t$ denotes averaging over time. However, the length of a single trajectory is often too short to yield a sufficiently smooth correlation function. Therefore, we tend to calculate a smoother

ensemble-averaged VACF as given below:

$$C(\Delta t) = \langle c_t(\Delta t) \rangle_E = \frac{1}{M} \sum_{i=1}^{M} c_t^{(i)}(\Delta t) \tag{2.7}$$

where $C(\Delta t)$ is the ensemble-averaged normalized velocity autocorrelation function (VACF) at lag time Δt, $c_t^{(i)}(\Delta t)$ is the normalized VACF of trajectory i, M is the total number of trajectories in the ensemble, and $\langle \cdots \rangle_E$ denotes averaging over the ensemble of trajectories.

In SPT analysis, the evolution of the VACF demonstrates the nature of transport occurring. The VACF of true random motion, such as brownian diffusion oscillates around zero demonstrating the absence of correlation between steps. A positive correlation in contrast, may arise from active, directed transport or propulsion. Negative correlations meanwhile, indicate antipersistence where particles have a strong tendency to retrace their steps. Experimentally, these different regimes manifest distinctly in the VACF curves [65–67]. Persistent dynamics show positive correlations at early lag times before gradually decaying toward zero, whereas antipersistent motion is characterized by a strong negative dip in the VACF. The magnitude and decay timescale of these correlations therefore provide important information regarding memory effects and the extent to which environmental structure influences particle transport. The VACF of some simulated trajectories were plotted to show anticorrelated, uncorrellated, and positively correlated dynamics (Figure 2.4).

2.1.4 Distribution of turning angles

The distribution of turning angle statistics provides an additional approach to diffusion studies by directly probing the directional correlations between successive displacements in a trajectory. For a discrete trajectory $r(t_i)$, the turning angle θ_i is defined as the angle between two consecutive displacement vectors:

$$\theta_i = cos^{-1}((\Delta r_i . \Delta r_{i+1})/(|\Delta r_i||\Delta r_{i+1}|)) \tag{2.8}$$

where $\Delta r_i = r(t_{i+1}) - r(t_i)$. The distribution of turning angles provides direct insight into step-to-step correlations that may not be reflected purely by the MSD. In the case of Brownian motion, displacements are uncorrelated, resulting in a uniform turning angle distribution in two dimensions and a positive sinusoidal curve in 3D, reflecting isotropic random motion, given by the relation:

$$P(\theta) \propto \sin\theta \tag{2.9}$$

Deviations from such uniform behavior indicate the presence of structural constraints or correlations in steps.

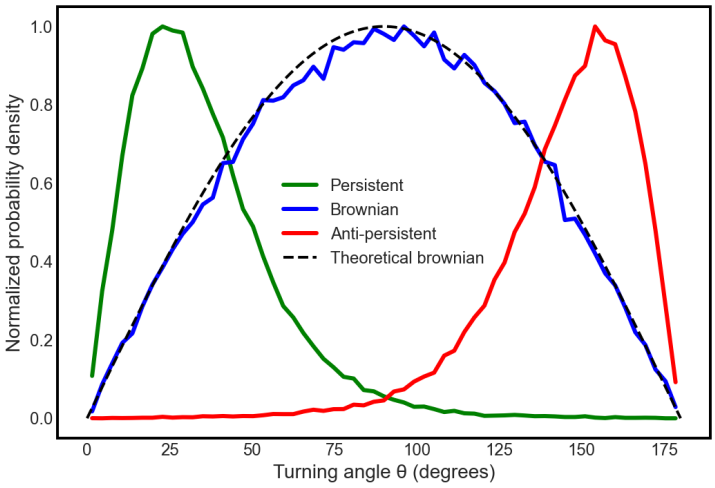

Figure 2.5: Distribution of turning angles: The distribution of turning angles from simulated trajectories of persistent, antipersistent and brownian motions show the shifts in distribution of turning angles towards smaller angles (alignment due to persistence) and larger angles due to collisions.

In subdiffusive systems, turning angle statistics are particularly useful for distinguishing between different physical mechanisms. For instance, diffusion processes that exhibit memory also often exhibit anti-correlated steps, leading to an increased probability of turning angles near π (*i.e.* retracing of steps) [71]. This manifests as a right shifted peak in the turning angle distribution at large angles and shows consistency with a negative VACF. Meanwhile, a left shifted peak signifies persistence in motion or directionality to the diffusive process. The three cases have been simulated as an example (Figure 2.5). Turning angle distributions are also sensitive to geometrical confinement and anisotropy. In structured environments, trajectories may exhibit preferred directions or frequent reflections at boundaries, leading to characteristic peaks in the angular distribution. For example, confinement can induce an excess of large turning angles due to repeated encounters with barriers, while directed or persistent motion leads to an accumulation of small turning angles [65].

Importantly, turning angle statistics are robust to localization noise and short trajectory lengths, making them a valuable tool in experimental SPT where data may be limited. When combined with MSD and VACF analysis, they provide a more complete characterization of the underlying stochastic process, enabling discrimination between competing diffusion models that would otherwise appear similar based on MSD scaling alone [71,72].

2.1.5 Non Gaussianity parameter

Given that the parameters so far described such as the MSD, VACF and distribution of turning angles quantify the dynamics of single particle tracking, we now turn to an estimator that quantifies diffusion in a geometric perspective of trajectories [65, 73]. In diffusive model, it turns out that the application of only dynamic parameters of MSD, VACF, etc can sometimes be inadequate quantities to discriminate certain subdiffusive processes. A prime example for this is diffusion in a viscoelastic medium (often defined by FBM) from subdiffusion in a fractal percolation or in mazes (often called obstructed diffusion (OD) model) [34, 74]. In their recent work, Metzler and Weiss derive two such parameters, the non-Gaussianity parameter (NGP) and the asphericity. The NGP acts as a versatile tool to quantify time variant geometrical aspects of the trajectories and is mathematically described by:

$$g(t) = \frac{3\langle r^4(t)\rangle}{5\langle r^2(t)\rangle^2} - 1, \tag{2.10}$$

where $r(t)$ is the 3D displacement of the particle over lag time t, defined as

$$r^2(t) = x^2(t) + y^2(t) + z^2(t), \tag{2.11}$$

$\langle r^2(t)\rangle$ denotes the ensemble-averaged mean squared displacement, and $\langle r^4(t)\rangle$ is the ensemble-averaged fourth moment of the displacement distribution. The prefactor 3/5 arises from the isotropic normalization in three-dimensional space (Figure 2.6).

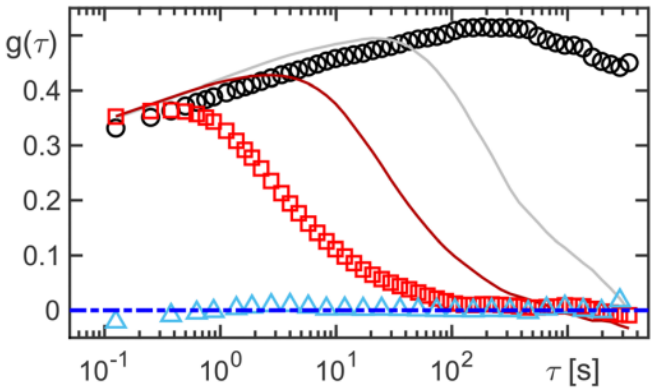

Figure 2.6: NGP of trajectories: The non- Gaussianity for OD strongly deviates from zero (black circles). For OD among mobile obstacles, the NGP converges to zero at long timescales (red squares, red and grey lines). FBM shows a constant zero NGP (blue line and triangles) (Adapated from [74]).

Simply put, the NGP is a parameter that tests the independence of the fourth and second moments of the increment statistic with regard to the time scale t. Metzler and Weiss [74], through numerical simulations show that the NGP for OD in a static maze shows strong

deviations from zero, demonstrating non-Gaussian nature of this transport process. On the other hand, they show that brownian and FBM models result in a vanishing NGP (discussed more in detail in Chapter 5). Thus, the Gaussianity of trajectories, becomes a powerful tool in discriminating diffusion models.

2.1.6 Asphericity

Yet another geometric descriptor for the trajectory is asphericity. To put simply, this measures how close to spherical (or away from it) a trajectory's shape is. A simple example is that Brownian motion trajectories encompass elliptical shapes in two dimensions diverging from more circular explorations [34, 74]. In the same work, Metzler and Weiss showed that asphericity provides a robust method to distinguish between FBM and OD, thus allowing for better interpretation of the diffusion environment. In two-dimensions, the asphericity parameter is mathematically defined as:

$$A_{2D} = \frac{\left\langle \left(R_1^2 - R_2^2\right)^2 \right\rangle}{\left\langle \left(R_1^2 + R_2^2\right)^2 \right\rangle} \tag{2.12}$$

where R_1^2 and R_2^2 are the eigenvalues of the 2D gyration tensor of the trajectory, ordered such that $R_1^2 \geq R_2^2$, and $\langle \cdot \rangle$ denotes an ensemble average over trajectories or time windows. Narrow and long trajectories have asphericity values close to 1, while more circular (or

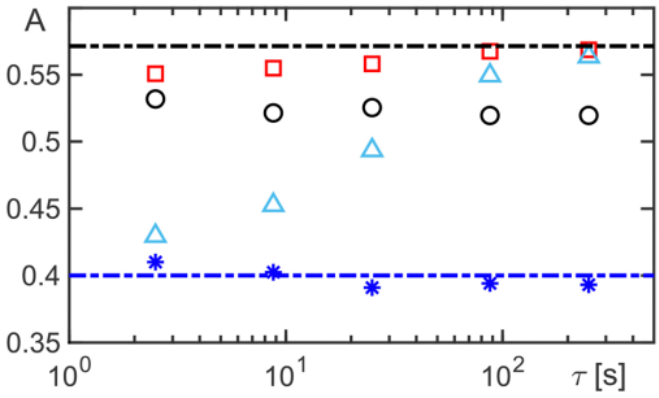

Figure 2.7: Asphericity as a test for diffusion model The asphericity parameter of trajectories display the contrast of FBMs and ODs. The asphericity of diffusion follows $A_{FBM\approx 0.4}$ for pure FBM with $\alpha = 0.7$ (blue dash-dot line and asterisks) and $A_o = 4/7$ for Brownian motion (black dash dot line). For OD (open black circles:static and red squares:mobile) the asphericity is around A_o (Adapted from [74]).

spherical) shaped trajectories result in A=0. Mathematically, Brownian motion can be shown to result in A = 4/7 in two dimensions [74]. Thus, the asphericity of a trajectory

is an accessible estimator to differentiate between diffusive processes that can otherwise seem to be identical (Figure 2.7).

2.1.7 Escape time

Finally, another useful quantity for characterizing transport in confined or heterogeneous environments is the escape time. Broadly, the escape time corresponds to the time required for a particle to leave a defined region of space, such as a cavity, or compartment through. Unlike measures such as the MSD, which quantify the extent of particle spreading, escape times provide direct information on how long particles remain trapped within local environments. From a theoretical perspective, this concept is closely related to the mean first-passage time (MFPT), which describes the average time required for a stochastic process to reach an arbitrary threshold for the first time [75–77]. In the simplest case of Brownian motion in homogeneous media, MFPTs can be derived analytically and scale predictably with system size and dimensionality [78]. However, in complex or confined geometries, the MFPT becomes highly sensitive to boundary structure, heterogeneity, and the presence of obstacles, often leading to broad or non-trivial distributions of first-passage events. As a result, escape times are particularly sensitive to confinement, geometrical constraints, and particle–environment interactions [27,79]. In complex media, escape time distributions can reveal the presence of barriers, preferential pathways, or transient trapping events that may not be readily apparent from ensemble-averaged diffusion metrics [80–82]. Consequently, escape times and MFPT-based frameworks serve as powerful complementary tools for understanding transport processes in crowded, porous, and heterogeneous systems especially to understand how local constraints act as bottlenecks influencing global diffusion rates [81, 82]. Practically, this allows us to understand and define trapping in biological compartments in cells or tissues, binding activity and release, or molecular motion through structured environments [83]. In our work, we will particularly use it to understand how anisotropic particles can escape through nanoscaled domains in tissue-like environments [84].

2.2 Stochastic models of diffusion

2.2.1 Brownian motion

Classical Brownian motion describes the true random motion of particles arising from thermal fluctuations in a homogeneous fluid and serves as the fundamental reference model for diffusion [2,3,65]. It is marked by a Gaussian, Markovian, and ergodic process, characterized by independent and identically distributed increments with no memory

kernel [66]. Brownian motion is defined by the linear scaling of the mean squared displacement (MSD) with time:

$$\langle r^2(\Delta t)\rangle = 2dD\Delta t \tag{2.13}$$

where $\langle r^2(\Delta t)\rangle$ is the mean squared displacement of the particle over lag time Δt, $r^2 = x^2+y^2$ in two dimensions and $r^2 = x^2+y^2+z^2$ in three dimensions, Δt is the lag time over which displacements are evaluated, d is the dimensionality of the system, and D is the diffusion coefficient characterizing the rate of spatial spreading of the particle ensemble.

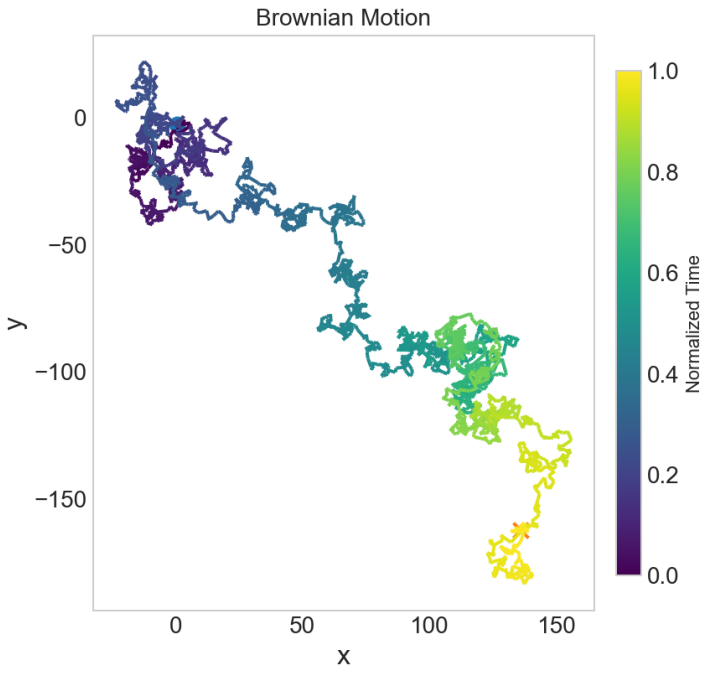

Figure 2.8: Brownian motion: Simulated single trajectory performing brownian motion. The scale is in µm

This linear dependence reflects the absence of temporal correlations and indicates that particle spreading is purely driven by random thermal forces. The statistics of Brownian motion are well defined. Particle step-sizes follow a Gaussian distribution through varying timescales. Additionally, owing to memoryless exploration of their surroundings, the particle trajectories show successive displacements that are uncorrelated, resulting in an uncorrelated VACF at nonzero time. Similarly, turning angle statistics are uniformly distributed, in 2D, they represent equal probability for all angles, while in 3D, due to projections, the distribution takes the shape of the positive half wave of a sinusoidal curve with the peak at 90 degrees [65, 66]. Experimentally, Brownian motion is observed in bulk fluids or dilute systems where interactions and environmental constraints are minimal. Deviations from Brownian behavior such as non-linear MSD scaling, non-Gaussian displacement distributions, or the presence of temporal correlations indicate the influence of additional physical, chemical, or biological mechanisms, including viscoelasticity, trapping, or geometrical constraints [13, 62, 72]. As such, classical Brownian motion serves

not only as a model of diffusion in its own right but also as a reference framework for diagnosing and interpreting more complex stochastic dynamics in heterogeneous environments [55, 60, 85]. An example of a Brownian trajectory is shown in Figure 2.8.

2.2.2 Fractional Brownian Motion

Fractional Brownian motion (FBM) is the generalized form of the classical Brownian motion that incorporates temporal correlations between successive displacements. While Brownian motion is characterized by a truly random walk, thereby making it a memoryless Markovian process, FBM is non-Markovian arising typically from viscoelastic interactions [65]. That is to say, the direction (and magnitude) of the particle's trajectory is dependent on its past motion. However, interestingly, despite displaying memory, FBM remains a Gaussian and ergodic process [74], distinguishing it from other anomalous diffusion models such as continuous-time random walks (CTRW). The power law of the FBM model features a typically anomalous scaling of the mean squared displacement (MSD), given by:

$$\langle r^2(\Delta t)\rangle \sim \Delta t^{\alpha} \tag{2.14}$$

where the anomalous exponent α reflects the nature of temporal correlations. For $\alpha < 1$, the motion is subdiffusive and characterized by anti-persistent behavior, in which successive steps tend to reverse direction. For $\alpha > 1$, the motion becomes superdiffusive, with persistent correlations leading to directed-like trajectories. These correlations aris-

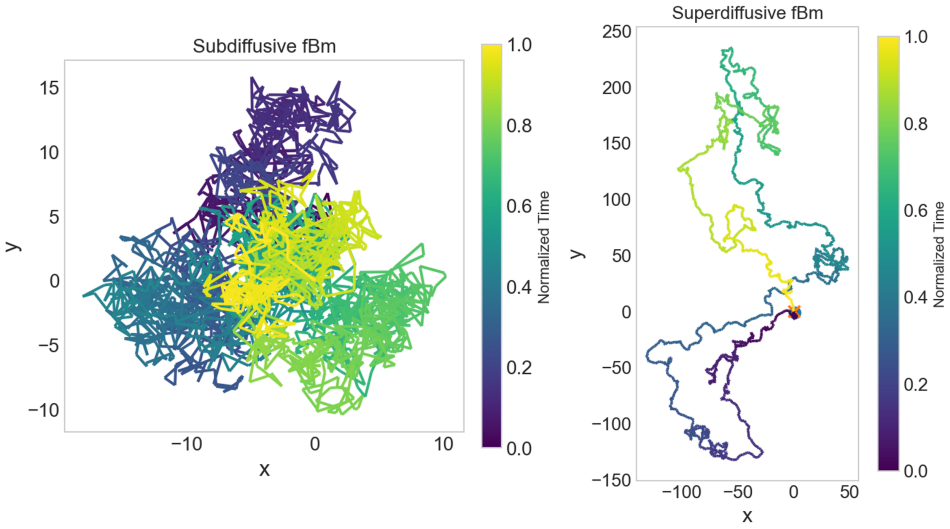

Figure 2.9: Fractional brownian motion: Simulated individual trajectories of particles performing subdiffusive (left) and superdiffusive (right) fractional Brownian motion. The scale is in µm

ing from the non-Markovian nature of the diffusive process are directly reflected in the

VACF, thus making VACF a prime indicator to identify FBM. In the subdiffusive regime, FBM exhibits a negative VACF, indicating that forward motion is likely to be followed by backward motion [65, 74]. This tendency to retrace steps is a hallmark of motion in viscoelastic or even in crowded environments, where the surrounding medium exerts restoring forces or induces memory effects.

Distinguishing FBM from other subdiffusive models requires the use of observables beyond MSD. In particular, the presence of temporal correlations (e.g., non-zero VACF) and the absence of ergodicity breaking are key indicators of FBM dynamics [65–67]. Additionally, turning angle statistics often show an increased probability of large angles in the subdiffusive regime, as expected with anti-persistent motion.

Overall, FBM captures the essential features of diffusion in systems where memory effects and viscoelasticity dominate, making it a central model for interpreting correlated stochastic motion in complex environments. Examples of trajectories performing subdiffusive and superdiffusive FBM are shown in Figure 2.9.

2.2.3 Continuous time random walk (CTRW)

The continuous-time random walk (CTRW) framework extends the classical Brownian random walk by introducing a random waiting times along with random steps between successive displacements [65, 66]. This definition results in a natural description of stochastic processes involving trapping or intermittency. A particle diffusing in the CTRW model takes a series of steps that are separated by waiting times that are also taken from a probability distribution $\psi(t)$. When this distribution exhibits a heavy tail, given by $\psi(t) \sim t^{(-1-\alpha)}$with $0 < \alpha < 1$, the mean waiting time turns divergent, thus converging to anomalous diffusion. The consequence of such a mechanism of subdiffusive behavior, when characterized by a mean squared displacement (MSD) is given by:

$$\langle r^2(t) \rangle \sim t^{\alpha}, 0 < \alpha < 1 \tag{2.15}$$

Thus, here, the anomalous behavior in CTRW arises from long periods of immobilization or wait times between the random jumps. One of the defining features of CTRW used to distinguish it from other models is its non-ergodic nature [65]. Non ergodic process, as discussed earlier shows a divergence between eaMSD and taMSD (or even teaMSD). Practically, a significant variation arises between individual trajectories, which is physically interpreted as longterm trapping or binding interactions with the surroundings. Furthermore, CTRW diffusion also displays ageing, a property where statistical estimators depend explicitly on the length of observation. An example of a particle showing CTRW is shown in Figure 2.10.

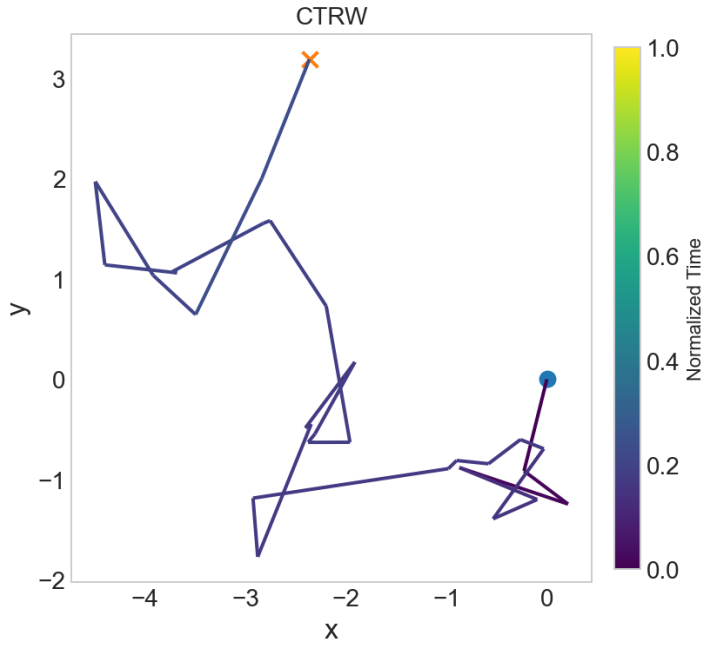

Figure 2.10: Continuous time random walk: Simulated single trajectory performing CTRW with randomized wait times. The scale is in µm

In single-particle tracking experiments, CTRW behavior is typically associated with environments where particles undergo binding, caging, or transient immobilization, such as in crowded or heterogeneous media [86]. This manifests as trajectories with visible pauses or localized segments. While CTRW can produce MSD scaling similar to other anomalous diffusion models, the model generally exhibits no temporal correlations between successive displacements, a signature that can be interpreted by studying the VACF. Additionally, the van Hove PDF often shows a pronounced peak at small displacements due to the prevalence of waiting events along with heavy tails due to jumps between localized events. Overall, the CTRW framework provides a physically intuitive model for stochastic processes dominated by intermittency and trapping arising from biophysical binding activity [86].

2.2.4 Obstructed Diffusion

Obstructed diffusion models diffusion processes of particles in environments where their trajectories are hindered by static physical constraints in environental geometry, such as obstacles, barriers, maze-like patterns, or confining structures [21, 22, 28, 34, 60]. Unlike models such as CTRW or FBM, where anomalous behavior arises from temporal effects (such as waiting times or memory for example), obstructed diffusion is governed by the spatial organization of the medium.

In such systems, particles undergo Brownian motion locally at short time scales but expe-

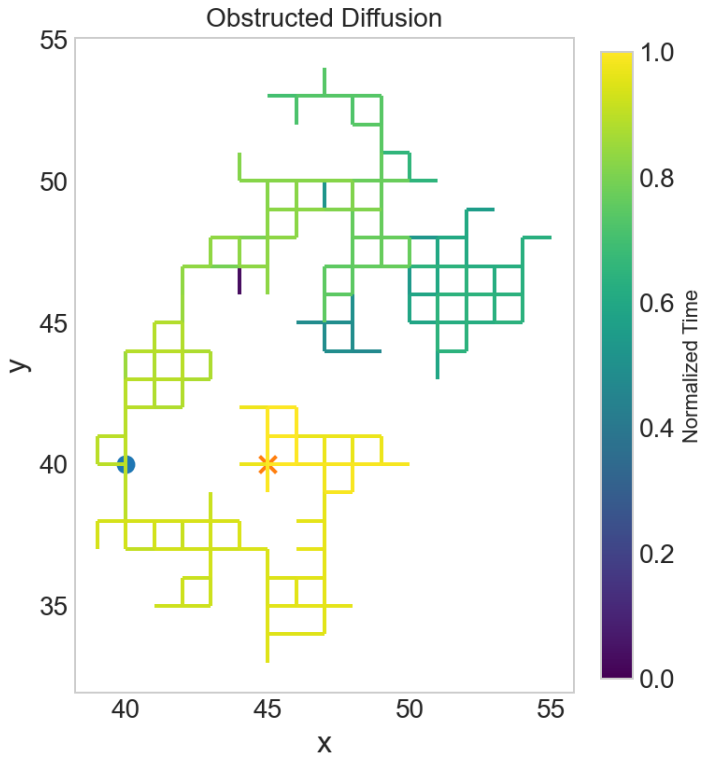

Figure 2.11: Obstructed diffusion model: Simulated single trajectory experiencing obstructed diffusion in a 2D maze. The scale is in µm.

rience frequent interactions with boundaries, leading to deviations from free diffusion at larger time scales. This typically results in subdiffusive behavior, where the mean squared displacement (MSD) scales as $\langle r^2(t) \rangle \sim t^\alpha$ with $\alpha < 1$ [74]. At short times, motion may appear approximately Brownian as particles explore their vicinity without interacting strongly with the boundaries or obstacles. On the contrary, at longer times, the cumulative effect of interactions with obstacles and boundaries leads to reduced transport efficiency.

One of the defining features in OD is the presence of temporary confinement regimes or transient trapping along with tortuosity. Particles may become temporarily (or sometimes even permanently) restricted within local compartments. In such cases, the progression of transport between regions occurs by "escape" processes [36, 80]. These escape processes prove to be a bottleneck between diffusion and exploration of local environments and diffusion at more global scales [25]. This leads to heterogenous trajectories, as well as heterogeneities within single long trajectories that explore multiple different regions and compartments as diffusion now becomes a combination of local exploration as well as transitioning between distinct regions. In SPT, OD models can be identified with several characteristic signatures. Primarily, as mentioned earlier, the MSD scales sublinearly with time.

The turning angle distribution often shows an excess of large angles, reflecting frequent

reflections or redirections at boundaries. Similarly, the VACF exhibits negative correlations at short time scales due to collisions with obstacles. However, it is important to note that the anomalous scaling of the MSD, the negative VACF, and mostly Gaussian PDFs are reminiscent of other models as well, chiefly the FBM [65, 74]. While the estimators of diffusion models tend to be similar, the underlying process of diffusion is fundamentally different. The dynamics of OD are generated from the environment and not by temporal correlations. As a result, distinguishing obstructed diffusion from other anomalous processes requires combining multiple observables, including trajectory morphology, directional statistics, and spatial mapping of particle motion. Finally, the NGP as well as the asphericity of the trajectory here acts as a true distinguishing feature between FBM and OD. OD displays strongly aspheric and non-Gaussian behaviors while on the other hand, FBM models tend to follow more Gaussian and spherical behaviors, especially converging to spherical and Gaussian statistics at longer time scales [74]. Thus, OD provides an intuitive framework to interpret diffusion in complex environments that are maze-like, structure, or porous obstructed diffusion where spatial constraints are the dominant hindrances to diffusion. Figure 2.11 represents a single trajectory performing OD in a maze like pattern.

Two other very interesting diffusion models worth mentioning are the Levy walks and Levy flights. Characterized by a long tail distribution of van Hove PDFs, such diffusion is seldom seen in relevance to cellular, or biological contexts and are instead more relevant in understanding diffusion at macroscales while investigating animal behavior with regard to migration or food search [87].

In the following chapter, we will look at the theoretical and experimental techniques involved in carrying out 3D-SPT that will allow us to obtain diffusion metrics and infer diffusion models.

Chapter 3

Single particle tracking of anisotropic carbon nanotubes

Having introduced the statistical descriptors used to characterize and classify diffusion, we now turn to the experimental methods employed to study diffusion at the single-molecule level. This chapter begins with the principles of localizing and tracking single molecules in two dimensions before extending these concepts to three-dimensional single-particle tracking. I then discuss the commonly used fluorescent probes for SPT and highlight the advantages of using CCNTs as near-infrared, photostable probes. Finally, I describe the experimental setup used throughout this work, together with the associated experimental constraints. The chapter concludes with the characterization and validation of both the experimental and analytical pipelines through measurements of CCNT and uCCNT diffusion in a homogeneous Brownian medium.

3.1 Single particle tracking Microscopy

3.1.1 Classical microscopes

Optical microscopy is a powerful imaging technique that utilizes visible light and lenses to observe and analyze microscopic structures and objects. It has played a pivotal role in the advancement of various fields of science, but has been especially instrumental in our understanding of health, wellness, and disease at fundamental levels. Apart from biological applications, optical microscopy continues to be applied in the fields of material sciences and nanotechnology.

3.1.2 Point spread function

Let us consider the case of a single point emitting light. As a consequence of diffraction, a point emitter cannot be imaged as an infinitely localized point in a microscope. Instead, the emitted light is spatially distributed in the image plane into a characteristic diffraction pattern known as the point spread function (PSF). The PSF therefore represents the fundamental response or an impulse response of an optical imaging system to an ideal point source and ultimately determines the spatial resolution achievable in microscopy.

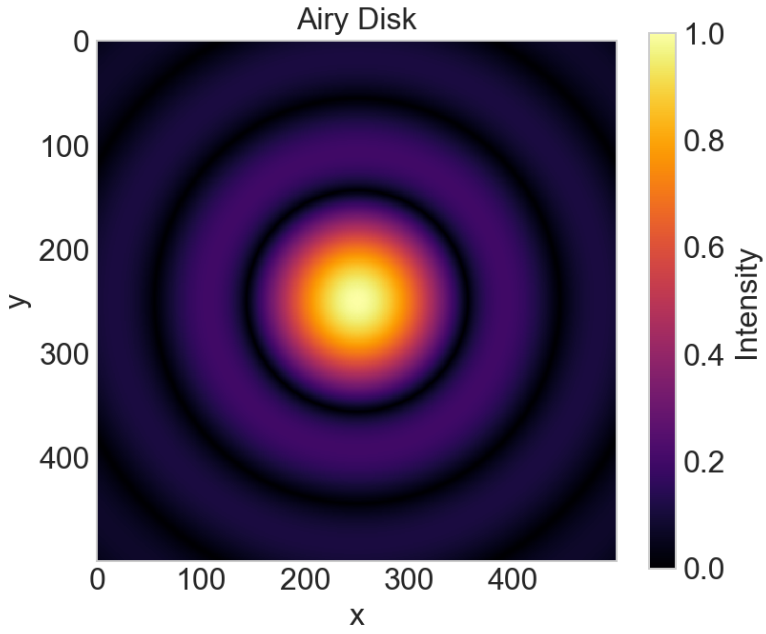

Figure 3.1: 2 dimensional profile of an airy disc: Simulation of the Airy diffraction pattern generated by a point emitter in a diffraction-limited optical system. This diffraction-limited spot forms the basis of the point spread function used for particle localization in fluorescence microscopy.

For circular apertures for example, the diffraction limit manifests itself as the characteristic intensity profile of Airy disks as described by Airy [88]. Figure 3.1 shows an Airy disc pattern simulated from a Bessel function.

3.1.3 The diffraction limit

The quality and resolution of the image formed by a microscope is determined by the Abbe criterion or Abbe's diffraction limit. Given by Ernst Abbe in the 19th century, this criteria defines a limiting factor on the resolution of microscopes, and that this minimum resolvable distance (d) between any two objects under an optical microscope can be mathematically described by [89]:

$$d = \frac{\lambda}{2\,\mathrm{NA}} \tag{3.1}$$

where d is the Abbe diffraction limit corresponding to the minimum resolvable distance between two point sources, λ is the wavelength of the detected light, and NA is the numerical aperture of the objective lens, defined as:

$$\mathrm{NA} = n \sin\theta, \tag{3.2}$$

with n being the refractive index of the imaging medium and θ the half-angle of the maximum cone of light collected by the objective. The Abbe criterion defines the fundamental diffraction-limited spatial resolution achievable in a conventional optical microscope.

3.1.4 Localization from the PSF

While imaging single particle emitters in 2D, only the point emitters in the focal plane (with a small non zero width) are being imaged [90]. The PSF of these particles show a spread that can be fitted using a Gaussian approximation. To know the precise location of each indivdual emitter, the simplest and one of the earliest methods was to indeed perform least square fitting on each of the PSF or intensity spreads with a Gaussian function [91–94].

Briefly, the least square fit used in 2D was one of the first localization algorithms considered to be unbiased and is still widely accepted and used in localization microscopy. When single particle emitters are imaged onto a 2D digital sensor array such as a camera sensor, the PSF is convoluted due to noize and pixelization. Using the least square method, we can minimize the squared error between the PSF model (so Gaussian if it is in 2D) and the observed pixelated image. Mathematically, it is described as:

$$S = \sum_{i=1}^{N} \left[n_i - \mu_i(\theta)\right]^2 \tag{3.3}$$

where S is the objective function minimized during the fitting procedure, N is the total number of data points or pixels included in the fit, n_i is the experimentally measured intensity at pixel or data point i, and $\mu_i(\theta)$ is the model-predicted intensity at the same point, parameterized by the fitting parameters θ. The term $\left[n_i - \mu_i(\theta)\right]^2$ represents the squared residual between the experimental measurement and the fitted model.

While this method is fairly robust, the caveat still remains that it is truly functional based on certain statistical assumptions that every pixel value is influenced by identical

noise, and the noise is described by a normal and independent statistics. More commonly, a Gaussian fitting is supplemented with a constant background to account for the background noise which can be described through the following equation:

$$I(u,v) \approx \frac{N_p}{2\pi\delta^2} \exp\left(-\frac{(x-x_0)^2+(y-y_0)^2}{2\delta^2}\right) + N_{\text{bg}} \tag{3.4}$$

where $I(u,v)$ is the measured intensity distribution at image coordinates (u,v), N_p is the total number of detected photons emitted by the particle, (x_0, y_0) denotes the center position of the emitter in the image plane, and δ is the standard deviation of the Gaussian point spread function, characterizing its spatial width. The exponential term describes the spatial decay of intensity away from the emitter center, while N_{bg} represents the background intensity arising from detector noise, autofluorescence, or background light from out of focus elements.

Now, knowing the intensity profiles and the least square fit, we next look at experimentally measuring the precision of a microscope to localize a point emitter. In our experimental framework, a common and simple method of measuring the localization precision is to image single fluorophores directly immobilized over several hundred frames. Next, we fit the PSFs in each frame with a Gaussian function to retrieve the distribution of position estimations. The spread of this distribution, measured by the standard deviation would then define the localization precision. For single particle microscopy techniques, this value is around 10 nm to 20 nm.

Further work from Thompson and Mortensen theoretically predict a precision given that the system apart from background noise, also has a photon shot noise [93]. Additionally, they account for the noise amplication brought about by internal gains, such as the ones present in EMCCD cameras. Their work mathematically describes such a precision as follows:

$$\left\langle (\Delta x)^2 \right\rangle = \frac{\delta^2 + \frac{a^2}{12}}{N_p} \left(\frac{16}{9} + \frac{8\pi N_{\text{bg}} \left(\delta^2 + \frac{a^2}{12}\right)}{N_p a^2} \right) \tag{3.5}$$

where $\langle (\Delta x)^2 \rangle$ is the variance of the localization error in the x-direction, δ is the standard deviation of the PSF, a is the pixel size of the detector, N_p is the total number of detected photons from the emitter, and N_{bg} is the background photon count per pixel. The term $\delta^2 + \frac{a^2}{12}$ accounts for the combined effects of the optical PSF width and finite pixelation, while the remaining terms quantify the degradation of localization precision due to photon noise and background intensity.

Yet another method that addresses the challenges of achieving the best localization pre-

cision for any arbitrary PSF is Maximum Likelihood Estimation (MLE). MLE, through a statisitcal framework, estimates the underlying parameters that optimally describes the experimental data, while also accounting for noise characterizations and PSF model [95]. The idea is then to maximize the MLE function, to achieve the most probable parameters. The mathematical representation of this concept would be:

$$\mathcal{L}(\boldsymbol{\theta}) \equiv p(\mathbf{n} \mid \mu, \boldsymbol{\theta}) = p(n_1, n_2, \ldots, n_N \mid \mu, \boldsymbol{\theta}) \tag{3.6}$$

where $\mathcal{L}(\boldsymbol{\theta})$ is the likelihood function of the parameter set θ, $\mathbf{n} = (n_1, n_2, \ldots, n_N)$ denotes the set of experimentally observed data points, μ represents the corresponding model predictions, and $p(\cdot)$ is the joint probability of observing the data given the model and its parameters. Ultimately, the objective would be to maximize μ.

3.1.5 From localization to single particle tracking

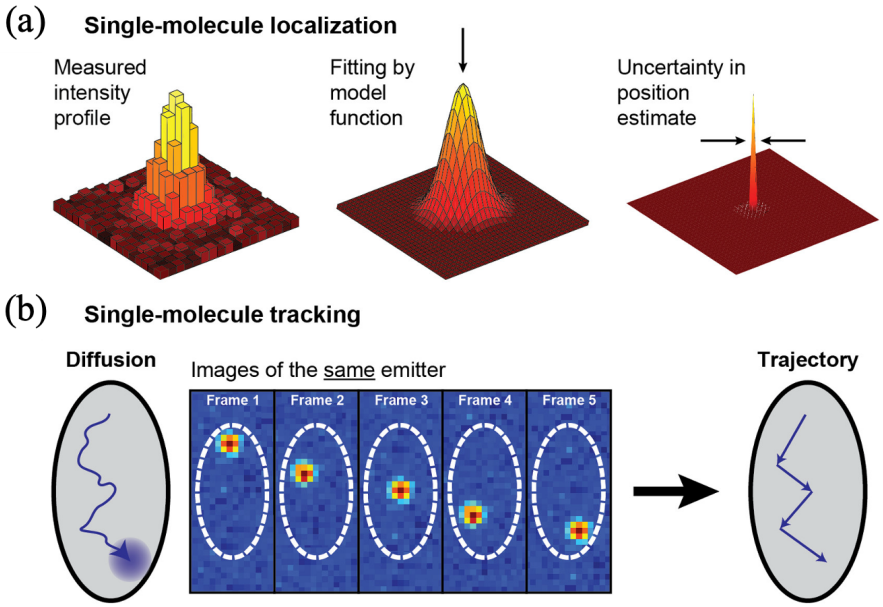

Figure 3.2: Single molecule localization and tracking: a. A schematic describing single molecule localization by fitting the intensity profile with a gaussian and estimating the uncertainty in the position. b. Schematic representation of single molecule localizations of a diffusing molecule used to reconstruct the trajectory of molecular motion (Adapted from [96]).

Once the rules of single molecule localization were well established, and localizing single molecules with precisions of under 20 nm was possible, the natural progression for microscopists was towards single particle tracking, where the same particle is localized across subsequent frames as it moves to retrieve the overall motion of the molecule [97].

A simplified protocol is graphically represented in Figure 3.2. Individual particles are first

localized as described previously in all the frames as the particle moves. The localizations in each frame can be linked to each other primarily based on two parameters. The first is the search radius, which defines the region within which the next localization associated with the same particle is searched for. The second parameter is the memory, which determines the number of consecutive frames for which a particle can remain undetected before the trajectory is terminated. This accounts for temporary losses of localization arising from noise, blinking events, or transient motion out of the focal plane [97]. These two linking parameters must be optimized to avoid both false positives and false negatives. Thus, successive localizations are linked to reconstruct trajectories of diffusing particles. These reconstructed trajectories can be further analyzed to retrieve statistical quantifiers of diffusion as described in the first chapter.

3.2 Isotropic fluorescent probes

While theoretical and experimental protocols are now established to achieve 2D and 3D single particle tracking with precisions under 10 nm, we must next look at the choice of probe or fluorophore for these applications. Fluorophores exhibit distinct optical properties that determine both their suitability and specificity for single-molecule applications.

Undoubtedly, brightness of the fluorophore is one of the chief parameters that governs the suitability of a molecule to be localized at the single particle level. Quantum yield (QY) and lifetime of a fluorescent probe directly determine the number of photons emitted (and therefore detected) and thus strongly influences localization precision [93,98]. Bright emitters also allow for shorter acquisition windows and enable faster frame rates on the camera, and improved tracking even in noisy environments. However, intensity of the particle is not enough to classify a molecule as a good probe.

Apart from being bright, a particle used for SPT also requires good photostability. Fluorescent molecules can irreversibly lose their ability to emit under strong and continuous illumination. In conventional SPT, especially in cellular and biological experiments, photobleaching is a key issue due to the limited photostability of many biological fluorophores [99]. While organic dyes and fluorescent proteins have been engineered to achieve high localization precision, their finite photon budget often limits trajectory duration and overall observation time. Thus, photostability becomes a critical factor when selecting an appropriate probe. On the other hand, probes such as quantum dots (QDs), while very bright, exhibit blinking behavior, intermittently switching off their fluorescence before turning back on, which can strongly complicate trajectory reconstruction [100, 101].

Finally, an important consideration is the spectral range of excitation and emission. Conventional fluorophores and most QDs operate primarily in the 400–700 nm UV–visible

window [54]. However, this is also the range where biological materials such as tissues and cells exhibit strong autofluorescence, scattering, and absorption, thereby limiting imaging depth and signal-to-noise ratio.

Some standard fluorescent molecules that are used in SMLM and SPT are small organic molecules, fluorescent tagged proteins, QDs, and fluorescent beads. While most of these standardized probes are designed to be very bright, they still tend to photobleach over time. Fluorescent proteins and organic small molecules especially, bleach quite fast (around 1 s or lesser) making long trajectories particularly difficult to reconstruct. Meanwhile, fluorescent beads and QDs can be bright and photostable allowing for longer trajectories (several seconds). Additionally fluorescent beads are highly monodispersed and often used as fiducial markers or calibrations for STORM and PALM [24, 102, 103]. However, most of these particles, except for a few QDs, are restricted to the visible spectrum, far outside the biological transparent window. Furthermore, all particles discussed so far are spherical or isotropic in shape, or are so small that they are often approximated to point particles.

Thus, given that most classical fluorophores are active only in the visible spectrum, and show photobleaching, there was a need for a photostable and IR active probe. SWCNTs, as we have seen in the first chapter, are an interesting solution to overcome these drawbacks with visible probes. In the following sections, we will focus on understanding the electronic structure that give SWCNTs their unique optical properties that allow for emission in the SWIR. Furthermore, we will discuss methods for chemically and physically tailoring their physical and optical properties to better suit our imaging requirements.

3.3 Single Walled Carbon Nanotubes

Given the widespread use of photoluminescent carbon nanotubes as probes for studying diffusion at the single-particle level in biological tissues and complex environments [58,59], it is important to understand the unique electronic and optical properties that underpin their utility. We will also look at how SWCNTs are being engineered to further optimize their application as probes.

3.3.1 Physical and electronic properties

Carbon nanotubes gained significant notice based on the production of hollow graphite-like tubes in the nanometer scale by Iijima in 1991 [104]. Carbon nanotubes are an allotrope of carbon that form a tubular shape in the nanoscale. Here, a carbon nanotube could be composed of a single rolled up graphene sheet, or several layers, thus distinguish-

ing the single walled carbon nanotube (SWCNT) from the multiwalled carbon nanotube (MWCNT) [104, 105]. SWCNTs can be described as rolled-up sheets of graphene, forming a hollow cylindrical structure with a regular hexagonal lattice. In this lattice, each vertex is occupied by a carbon atom, and the strong covalent bonds between them are preserved due to the underlying periodicity of the structure [106, 107]. As a result, the tube maintains a fairly constant diameter along its length, typically on the order of a few nanometers. In contrast, the length of carbon nanotubes can vary widely, ranging from a few hundred nanometers to several micrometers [106–108].

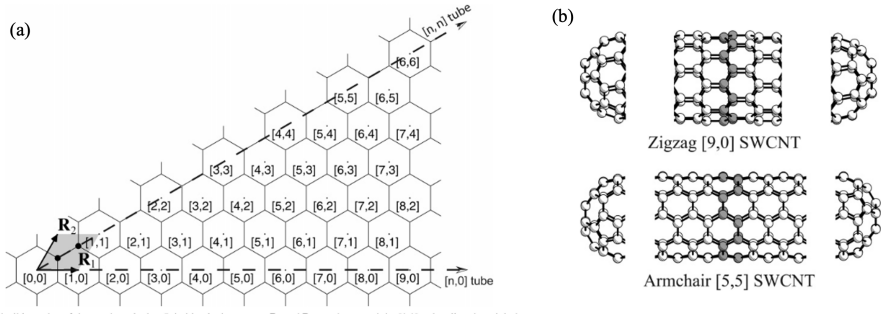

Figure 3.3: Physical structure of single walled carbon nanotubes: a. A schematic representation of roll-up of graphene sheet to form SWCNTs of different chiralities given by the basis vectors. b. Two example structures of SWCNTs with hemispheric fullerene caps on both ends of the nanotubes showing zigzag (above) and armchair conformations (Adapted from [109]).

The angle in which a graphene sheet is rolled to form the SWCNT is called the "roll-up" angle and plays a primarily role in it's electronic structure, and therefore the optical properties of SWCNTs [107]. Based on the "roll-up" angle, a nanotube acquires a specific chirality, denoted by *(n,m)*, which defines the orientation and magnitude of the wrapping (circumference) vector on the graphene lattice (Figure 3.3) [107, 110]. This rolling direction not only determines the nanotube geometry, but also strongly influences the quantization of its electronic states [106, 111, 112]. Mathematically, it is defined by the basis vectors of the graphene lattice:

$$\mathbf{C}_h = n\mathbf{a}_1 + m\mathbf{a}_2 \tag{3.7}$$

where $\mathbf{C}_h$ is the chiral vector defining the rolling direction of the graphene sheet into a nanotube, n and m are integer chiral indices, and $\mathbf{a}_1$ and $\mathbf{a}_2$ are the primitive lattice vectors of graphene. On the basis of these "roll-up" vectors, SWCNTs can be classified as chiral or achiral. Due to their surface symmetry, achiral SWCNTs, can be either armchair (n, n) or zigzag $(n, 0)$ types. The chirality of an SWCNT determines its fundamental physical properties, including helicity and diameter, which in turn govern its electronic structure. This electronic structure ultimately dictates whether the nanotube behaves

metallic or semiconducting [113].

To understand the electronic properties of SWCNTs, it is necessary to first consider the atomic structure of graphene [110, 113, 114]. In graphene, each carbon atom is sp^2-hybridized and forms covalent σ-bonds with three neighboring carbon atoms arranged in a hexagonal lattice. The remaining valence electron occupies a p_z-orbital oriented perpendicular to the graphene plane. The overlap of these p_z-orbitals across the lattice gives rise to delocalized π- and π^*-electronic bands, which are responsible for the material's electronic transport properties [110, 114].

The resulting band structure can be more conveniently described in reciprocal space. Here, the valence and conduction bands meet at six symmetry points located at the edges of the Brillouin zone, known as the Dirac points and conventionally labeled K and K' [110, 114, 115]. In the vicinity of these points, the energy dispersion becomes linear, producing the characteristic conical features known as Dirac cones. Consequently, pristine graphene possesses no intrinsic band gap and behaves as a semimetal, or equivalently a zero-band-gap semiconductor (Figure 3.4a).

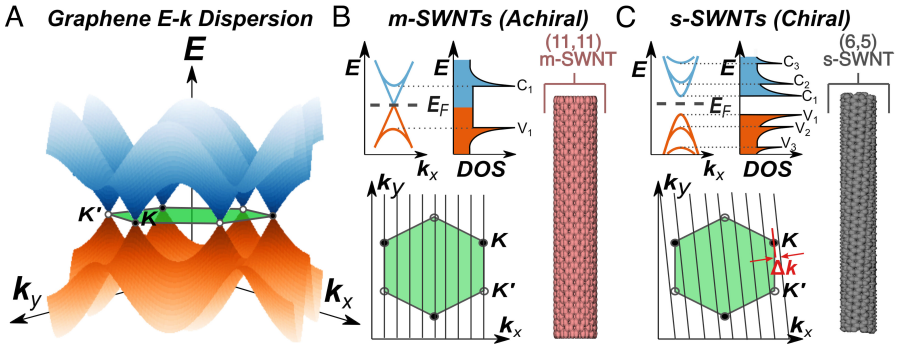

Figure 3.4: Electronic band structure of graphene and its evolution into metallic and semiconducting SWCNTs: a. Energy–wavevector dispersion relation of graphene showing the Dirac cones at the K and K' points of the Brillouin zone, where the conduction and valence bands meet. b. Formation of an achiral metallic SWNT ((11,11)) by quantization of the graphene wavevector around the nanotube circumference. One allowed k-state passes through the K point, resulting in zero bandgap and metallic behavior. The corresponding one-dimensional density of states (DOS) exhibits van Hove singularities associated with the first conduction (C1) and valence (V1) subbands. c. Formation of a chiral semiconducting SWNT ((6,5)). Quantization lines are shifted by Δk from the K point, opening an electronic bandgap between the valence and conduction bands. The DOS shows discrete van Hove singularities corresponding to multiple conduction and valence subbands (Adapted from [116]).

When graphene is rolled into a nanotube, the allowed electronic wavevectors become quantized around the nanotube circumference due to periodic boundary conditions based on the structure. Depending on how these quantized states intersect the Dirac cones of graphene, the nanotube may behave metallically (no band gap), or develop a finite band

gap and behave as a semiconductor (Figure 3.4 b,c). In general, nanotubes satisfying the condition $(n - m) = 3q$, where q is an integer, exhibit metallic or near-metallic behavior, while all other chiralities are semiconducting [106, 114]. This transition from a 2D sheet to a 1D nanotube also strongly modifies the electronic density of states. Unlike the continuous band structure of graphene, which exhibits a continuous electronic band structure, the confinement due to the circumference in SWCNTs narrows down the allowed electronic states into discrete 1D sub-bands [114]. The resulting density of states (DOS) develops a series of sharp peaks known as van Hove singularities, which are characteristic of one-dimensional systems (Figure 3.4 c).

3.3.2 Excitonic and optical properties

The semiconducting properties and DOS of SWCNTs result in unique and interesting optical phenomena with nanotubes.

When a photon is incident on a SWCNT, a valence (2p) or core electron (1s, 2s) electron is excited to the conduction band. The van Hove singularities now behave similar to the discrete orbitals allowing for sharp spectral features based on the energy differences. The initial occupancy of the photo-excited electron becomes unoccupied upon photon absorption in a valence band, and creates a positive "hole" that behaves like a particle. The Coulombic forces between the electron and hole result in them pairing upto form a bound state called an exciton. Next, the exciton, can also be scattered by emitting phonons through exciton-phonon or electron-phonon interactions and these excitations can decay to the bottom of the conduction band (or to the top of the valence band). At this point, the electron-hole pair recombine in a timespan ranging from 10 ps to a few 100 ps resulting in the spontaneous emission of a photon by a process termed photoluminescence [110, 114]. The transitions are represented by E^s_{ij} for transitions from i to j, where $i = j$ to conserve angular momentum. Following Kasha's rule, fluorescence in SWCNTs mainly arises from the lowest energy spin-conserving transition, i.e, E^s_{11} (in the 900-1600 nm), while other transitions such as E^s_{22} (550-900 nm) and E^s_{33} (400-600 nm) are not observed [105, 117] (Figure 3.5).

We now turn to another important aspect of excitonic states in SWCNTs arising from spin and valley symmetry. Owing to the honeycomb lattice inherited from graphene, carbon nanotubes possess two inequivalent sub-lattices, conventionally labeled A and B, as well as two inequivalent valleys located at the K and K' points of the Brillouin zone [113, 115]. As a result, optical transitions in SWCNTs are influenced not only by the electronic energy states, but also by the spin and valley quantum numbers associated with the charge carriers, leading to doubly degenerate conduction and valence bands. The combined effect of spin and valley degeneracy ultimately gives rise to 16 possible

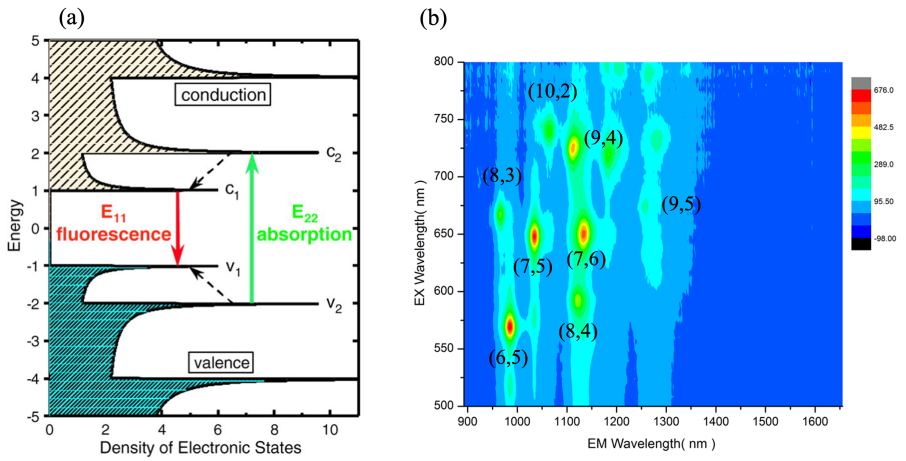

Figure 3.5: Optical properties of SWCNTs arise from band structure: a. The electronic band structure of an SWCNT showing allowed transitions from van Hove singularities with E_{11}^{*} being the only photoluminescing state b. The PL map of different chiralities of SWCNTs demonstrating the dependence of electronic structure and optical properties on the roll-up angle (Adapted from [118])

excitonic states [106, 112]. Among these excitonic configurations, the spin symmetry of the electron-hole pair plays a particularly important role in determining the optical activity of the exciton [106, 110].

The spin state of an exciton is given by the combined spin configuration of the excited electron and the corresponding hole (formed on excitation) in the valence band. Owing to the conservation of spin in an optical dipole transition, excitation of an electron does not alter spin. As a consequence, the electron-hole pair forms a spin-singlet exciton ($S = 0$), which is an optically allowed state that interacts with photons readily. On the other hand, magnetic interactions or electron-electron exchange interactions could lead to spin flipping, forming spin-triplet excitons ($S = 1$) [106, 114, 119]. However, triplet excitons are forbidden states under selection rules and are thus called dark excitons.

Thus, the overall strong Coulombic forces and 1D nature of the particle combined with the complex nature of electronic states and allowed (and disallowed) transitions coupled with the lead to the existence of bright and dark excitonic states which strongly dictates the optical response and photoluminescence quantum yield (PLQY) of semiconducting SWCNTs. Thus, in pristine semiconducting SWCNTs, emission primarily arises from the bright E_{11} exciton following relaxation from higher-energy excitonic states such as E_{22} [112,113]. Based on these excitation and emission energies, certain chiralities are preferred and more widely used as per the required application [119]. In our work similarly, we have chosen the $(6, 5)$ chiralities of nanotubes to achieve emission in the short-wave infrared regime.

Laslty, we look at a parameter that contributes to the low PLQY of SWCNTs comes from

the diffusion of excitons along the length of the nanotube before quenching. Excitons are significantly mobile on pristine nanotubes, and exhibit diffusion lengths of several hundreds of nanometers [51]. As a consequence, the excitons are also more likely to be quenched non-radiatively towards the ends of the nanotubes or structural defects of the lattice, thus hindering recombination and emission. Furthermore, the diffusion length of excitons defines a restriction on the lower limit of the length of photoluminescent nanotubes. Short lifetimes of SWCNT lifetimes along with direct single molecule experiments on the stepwise quenching of nanotubes further support the notion of low PLQY due rapid quenching [106, 119]. However, semiconducting SWCNTs remained as some of the brightest emitters in the near-infrared (Figure 3.6), allowing for single particle tracking studies deep into tissues [41].

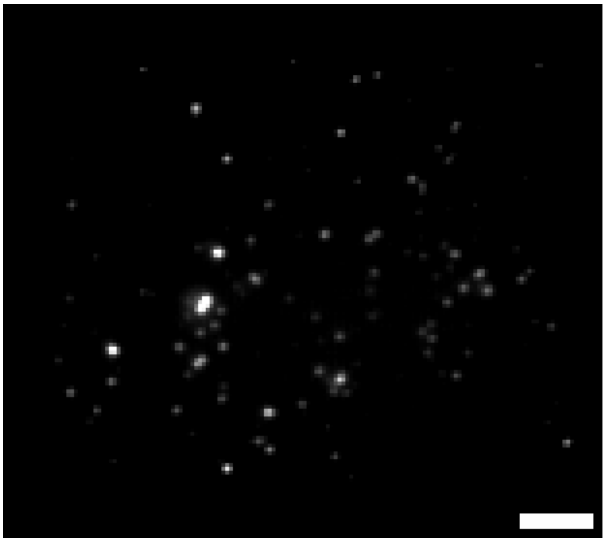

Figure 3.6: Widefield image of spincoated SWCNTs: Widefield image of sparsely dispersed individual SWCNTs excited at 568 nm. The emission was collected through a 900nm longpass filter. The scale bar represents 5µm.

3.3.3 Tuning optical properties: The CCNT

The application of NIR active SWCNTs at the single molecule level, especially in depth in thick tissue samples despite a low PLQY garnered enough attention to revisit efforts on improving the PLQY.

Addressing this problem immediately begs the question of how one must engineering SWCNTs to achieve higher PLQY. Having understood the low PLQY of SWCNTS results from the presence of dark excitonic states and nonradiative decay stemming from diffusion of excitons along the length of the tube, this challenge was addressed by the introduction of quantum defects. This field of research to improve PLQY remains very active with many possible applications in nanomaterials and biology.

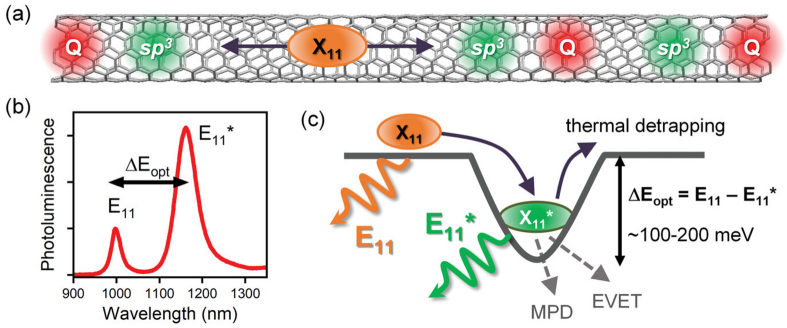

Figure 3.7: Defect-induced exciton localization in an sp^3-functionalized single-walled carbon nanotube: (a) Schematic representation of a nanotube containing covalent sp^3 defects that act as localized trapping sites for mobile X_{11} excitons. (b) Photoluminescence spectrum showing the emergence of a red-shifted defect-state emission (E_{11}^*) relative to the intrinsic excitonic transition (E_{11}), separated by an optical energy shift ΔE_{opt}. (c) Energy diagram illustrating exciton trapping at a defect site, radiative emission from both the intrinsic and defect-bound excitonic states, and thermally activated detrapping of the localized exciton. Figure adapted from [120].

By introducing covalent defects through chemical functionalization, semiconducting SWCNTs can be modified into structures that resemble conventional semiconductor doping (Figure 3.9 [121, 122]). The addition of such chemical molecules forms sites on the surface of the tube where the sp^2 hybridization is coverted to sp^3 allowing for the "defect" molecule to be accommodated (Figure 3.7). This change in hybridization breaks π conjugates that allow for new optically excitable exitonic states [51, 123]. Termed E_{11}^*, these new states behave as energy traps for diffusing excitons. The excitons are confined limiting their ability to decay nonradiatively, leading to increased PLQY(Figure 3.8). These sites of enhanced brightness are termed "color centers"(CCs), and by extension the SWCNTs containing CCs are called color center nanotubes (CCNTs). While the addition of suitable color centers remains an active area of research, in our team we work with oxygen and aryl defects (Figure 3.9) [51]. The bulk of the experiments in this thesis have been carried out with aryl defects on the nanotubes.

While the concentration of CCs is crucial to the enhancement of PLQY and is still the subject of further study at the single particle level, from ensemble studies, it is known that achieving optimally high PLQY requires fairly low CC concentration. PLQY is strongly sensitive to the number of defects, and further increase in concentration of CCs quickly extinguishes the fluorescence of nanotubes degrading the delocalized sp^2 lattice [51].

3.3.4 Length tunability: The uCCNT

While SWCNTs have shown to be great single particle probes for studying tissue rheology and extracellular spaces, and that CCNTs would further bolster their capabilities

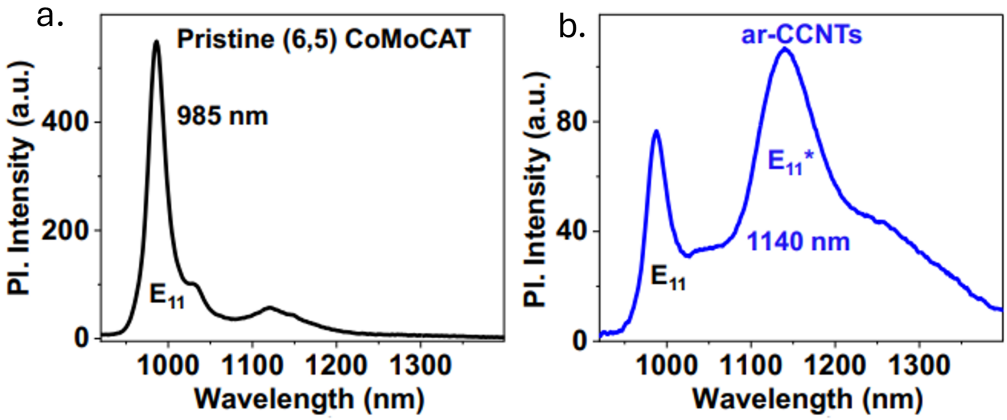

Figure 3.8: Spectral confirmation of color-center formation: a. The emission spectrum of pristine (6, 5) SWCNTs showing the pristine peak at 985 nm corresponding to the E_{11} transition, and b. the emission spectra after defect formation shows a lowered E_{11} peak relative to a strong emission at 1140 nm corresponding to E_{11}^{*} transition brought about by color-centers (Adapted from [51])

as a single molecule probe, the caveat of size would potentially still remain. While their nanoscale diameters and high aspect ratio allow access into complex structures that remain restricted for isotropic probes, their lengths extending to several hundred nanometers are not the most optimal to serve as a universal imaging probe due to rotational hindrances arising purely due to their length.

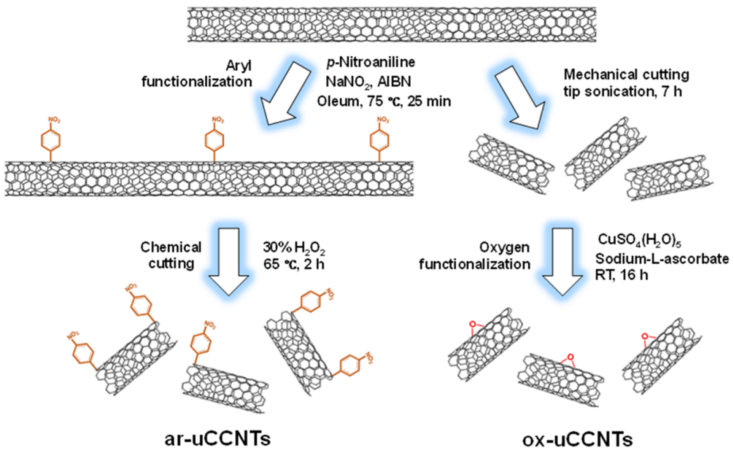

Figure 3.9: Schematic representation of preparation of CCNTs and uCCNTs Ar-CCNTs are first produced using diazonium chemistry, followed by chemical peroxide cutting (left). To produce, ox-uCCNTs, first the pristine naotubes are physically cut using tip sonication which is then followed by oxygenation through fenton reactions (Adapted from [51]).

With the advent of CCNTs, the possibility of shorter nanotubes, no longer limited by the diffusion length of excitons were soon realized in our group [51]. Without going into detail, I will now quickly discuss two types of CCNTs and ultrashort CCNTs (uCCNTs)

(about 50 nm in length) based on the color centers or defects doped onto the tubes as seen in Figure 3.9 and 3.10. These nanotubes have been central to the experiments conducted in this thesis.

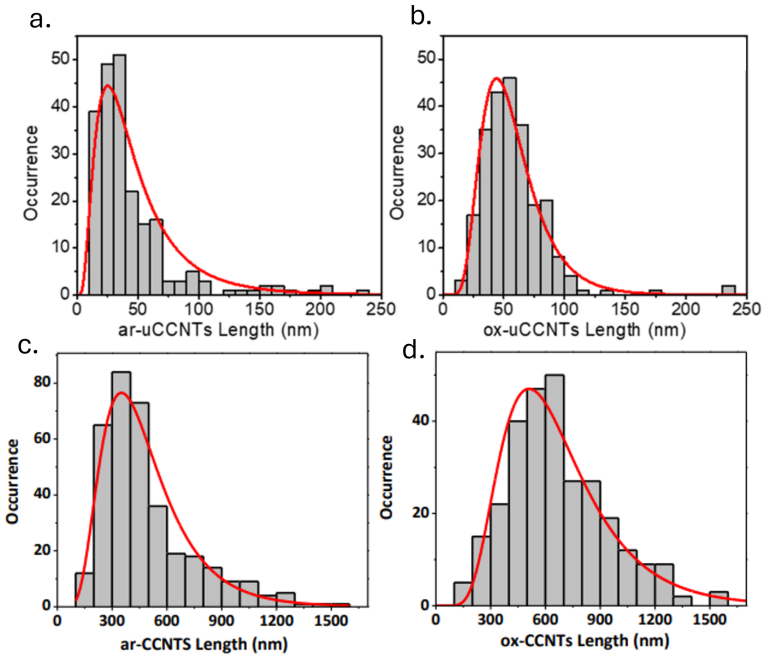

Figure 3.10: Length distribution of uCCNTs and CCNTs with different color centers The length distribution of the two color center SWCNTs measured using an Atomic Force Microscope shows ultrashort CCNTs of aryl- and oxygen- groups with a mean length of a. $53 \pm 40nm$ and b. $58 \pm 27nm$ respectively, and c. $490 \pm 250nm$ and d.$674 \pm 280nm$ respectively (Adapted from [51]).

In our team, CCNTs have been created by independently adding aryl group defects and oxygen defects on (6, 5) chirality of SWCNTs (henceforth labelled ar-(u)CCNTs and ox-(u)CCNTs) [51]. Aryl defects are added using diazonium reactions on SWCNTs, followed by chemical cutting with hydrogen peroxide (H_2O_2) to obtain (6, 5) ar-uCCNTs. On the other hand, for achieving ox-uCCNTs, (6, 5) SWCNTs are first physically cut using tip sonication to first create ultrashort SWCNTs(which would no longer show PL), followed by a fenton reaction for the addition of oxygen defects to obtain (6, 5) ox-uCCNTs (Figure 3.10). These CCNTs and uCCNTs can be further modulated based on surfactant coating for biocompatibility or other applications. The lengths of the CCNTs and uCCNTs were measured using atomic force microscopy and the distribution of lengths revealed uCCNTs to be about 50 nm and CCNTs to be around 500 nm (Figure 3.10) Their ultrabright infrared emission proves useful for deep tissue imaging with high localization precision. By imaging single particles of uCCNTs and QDs (emitting at 655 nm) through different brain tissue slices of varying thickness, work from our group demonstrated the superior localization precision of uCCNTs upto depths of 100 µm that was not feasible with QDs (Figure 3.11) [51].

In general, SWCNTs have attracted significant interest across a wide range of fields owing to their unique combination of optical, electronic, mechanical, and chemical properties. Semiconducting SWCNTs are particularly valuable in photonics and bioimaging due to their near-infrared photoluminescence, high photostability, and sensitivity to their local environment. These properties have enabled applications in biological imaging, single-particle tracking, chemical and biological sensing, and environmental monitoring [124–126]. Beyond imaging, SWCNTs have also been explored in nanoelectronics, energy storage, composite materials, and optoelectronic devices, where their high aspect ratio, mechanical strength, and tunable electronic structure offer significant advantages over conventional materials [127–129].

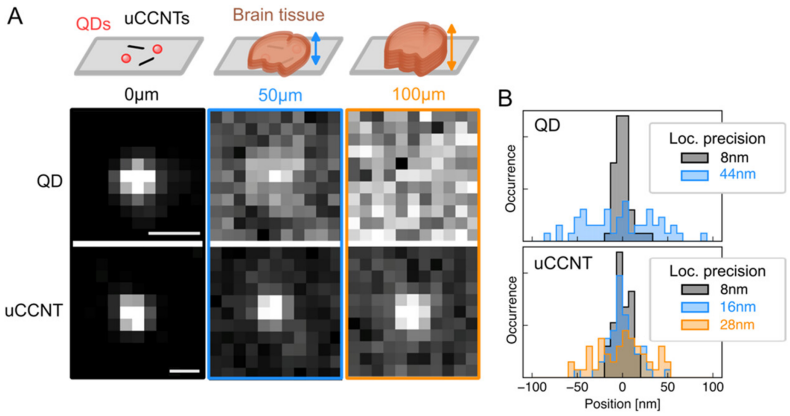

Figure 3.11: Single particle ex vivo imaging through organotypic slices a. Single particle imaging of quantum dots (QDs) and ox-uCCNTs through different thicknesses of brain tissues [0, 50, 100] µm b. Localization precision of QDs and uCCNTs as measured through different thicknesses of brain tissue showing the higher localization precision achieved from uCCNTs as opposed to QD. The QD is no longer detected at a thickness of 100 µm (Adapted from [51]).

Now that we have described the electronic and optical properties of SWCNTs and the chemical and physical tuning of SWCNTs to achieve CCNTs and uCCNTs, we will next look at our microsopy setup and methods to achieve 3D single particle localization of individual nanotubes in SWIR.

3.4 Presentation of the 3D single particle tracking setup

3.4.1 The setup

Our microscopy system, nicknamed "Montreal", was designed to incorporate a double helix PSF (DHPSF or DHPM for double helix phase mask) phase mask in the Fourier

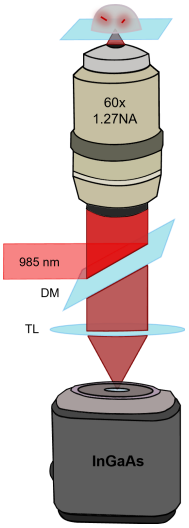

Figure 3.12: Schematic of the microscopy setup: A schematic representation of the microscopy setup used to study diffusing CCNTs and uCCNTs. The system uses a 985 nm for excitation, a dichroic mirror (DM) to reflect and filter excitation beam, an objective and a tube lens (TL). The image is captured on an InGaAs camera.

plane to modulate the emission of individual nanotubes to achieve 3D localization in the short wave infrared regime. The experiments and imaging conducted on this setup are described next. Videos of diffusing (6,5) CCNTs and uCCNTs were acquired in near-infrared range by exciting the sample at 985 nm (AeroDIODE) with an intensity of $\sim 4kW/cm^2$ through a 1000 nm dichroic mirror (DM) and detecting emission through a 1100 nm long-pass filter (Figure 3.12). A double helix phase mask (DHPM) was used for engineering the PSF to localize single particles in the lateral and axial directions. To maintain uniform excitation regardless of nanotube orientation, the laser beam was circularly polarized. Near-infrared acquisitions were made possible with the use of a C-RED2 InGaAs camera (First Light Imaging) at a frame rate of 30Hz. In the following sections, we will introduce the DHPM and its application to 3D-SPT.

3.4.1.1 PSF engineering for 3D tracking

While so far we have looked at the localization and tracking of single fluorophore molecules in 2D, we next consider the case of 3D microscopy of single point emitters. Given that the PSF changes only slightly around the focal plane before disappearing or spreading too thin, we consider a case of directly engineering the PSF to be sensitive to the axial direction or in other words focusing and defocusing.

However, the motion of the PSF in the axial domain, that shows up as focusing and defocusing directly influences the phase at the back focal plane of the microscope that can be modeled as follows:

$$P(\xi, \eta) = \exp\left(i\frac{2\pi}{\lambda}\frac{\mathrm{NA}^2}{2n}z\right) \tag{3.8}$$

where $P(\xi, \eta)$ is the complex propagation factor in the image plane, λ is the wavelength of the emitted light, NA is the numerical aperture of the objective lens, n is the refractive index of the imaging medium, and z is the axial propagation distance from the focal plane. The exponential term describes the phase accumulation associated with wave propagation in the imaging system.

A simple example of encoding the z position would be the use of a cylindrical lens. Indeed, passing the emission of single molecules through a cylindrical lens before the system allows for modulating the ellipticity (as a result of astigmatism) of the PSF as a function of axial position. Using least square fits, the ellipticity of the PSF can be determined to obtain nanoscale localization in all three directions [130].

There are multiple standardized phase masks to achieve this, such as the DHPSF and tetrapod PSF. In my experiments, I have used the DHPSF to achieve localizations in 3D. The functional basis for DHPSF are the Laguerre-Gaussian (LG) modes, whose linear combinations along a modal plane yields a PSF shape comprised of two bright lobes that encodes the axial position in the rotation of the lobes about their common center [54, 97, 131]. The rotation angle is fairly monotonic with the axial position of the particle and hence can be used as a measure of z-position reliably, allowing for z-range of almost 6 µm which is much larger than the one achieved using astigmatic lenses (around 1 µm).

3.4.1.2 Phase retrieval

Next we discuss how to retrieve localizations from the images obtained. Knowing that the axial position of the particle is encoded as the angle between rotation of the two lobes about a common center, we must therefore have a calibration of the angle against the z-position of the particle. Such a calibration can be obtained from a simple experiment. First, sparsely dispersed single particles (uCCNTs or CCNTs in our case) were immobilized in 5% agarose gel. A stack of images were procured with the stage coordinates incrementing in steps of 50 nm within a range of -3 µm to +3 µm (Figure 3.13). At each step, 50 images were acquired to average out the noise. Using the ZOLA plugin on Fiji (which banks on the use of Zernike polynomials), a calibration of the phase mask was retrieved. The PSF thus retrieved now acts as the benchmark in processes such as MLE. A simple autocorrelation of the calibration file with the experimental data set used for the calibration. The localization precision was determined to be $> 10\ nm$ in the lateral directions and $> 20\ nm$ in the axial direction. Localizations of diffusing single particles

in 3D could now be retrieved using the calibrations on the ZOLA plugin on Fiji [132].

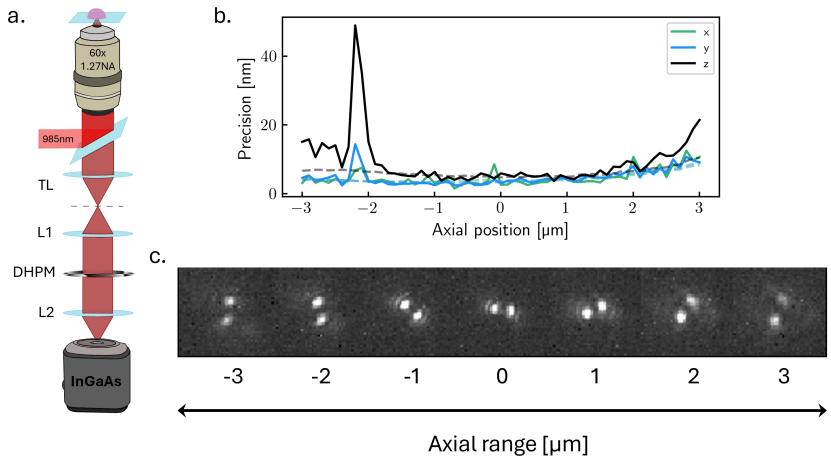

Figure 3.13: Axial range and localization precision of DHPSF: a. A schematic of the microscopy setup used for 3DSPT of (u)CCNTs in the short-wave infrared. b. The localization precision of the DHPSF measured across the full range of z positions is is below 10 nm along the lateral directions and below 20 nm along the axial direction. The kink seen between -2 and -3 µm can be explained by intermittent fluctuations and dimming of the CCNT. The dotted lines represent the Cramér-Rao lower bound, the theoretical minimum variance with the localization precision can be estimated for a given signal-to-noise ratio. c. A panel of images showing the DHPSF of a single CCNT across the full range of available axial positions.

3.4.1.3 The role of localization precision

Now that we have discussed the theoretical aspects of various estimators to study diffusion in the previous chapter, and the setup to achieve 3D SPT, we now look at how these translate to real SPT data. In experiments, all localizations have a corresponding static as well as dynamic localization errors. Both these errors are inherent to SPT experiments, since particle positions need to be extracted from images that have been recorded during a finite acquisition time. While the analysis of image stream is based on a strong assumption that particles only move between positions between frames, they continue diffusing within the acquisition window of a single frame. This results in the equivalent of a motion blur within an individual image, that is, the image represents the average of all the positions that have been visited by a particle during this acquisition time frame [66].

Even for immobile particles, finite image acquisition times influence localization accuracy. Single-particle imaging relies on detecting a finite number of photons emitted during the exposure time of each frame. This emission from a point source is recorded on the detector as the point spread function (PSF). At the diffraction limit, the PSF for a given

wavelength λ can be approximated by a Gaussian function, whose variance is given by:

$$\sigma_{PSF}^2 \sim \lambda^2 \tag{3.9}$$

where λ is the wavelength of the fluorescence photon.

The centre of this PSF is determined by the position of emitter. In general, the particle being tracked has a size smaller than the wavelength, which allows all the emissions to be viewed as a single point source. As a result, the position of the centre therefore yields the best estimate for the particle position, which we refer to as localization. Yet, from basic statistics it is known that the actual center of a Gaussian can only be determined with an accuracy that is given by the standard error that is mathematically determined as

$$\sigma = \sigma_{PSF}/\sqrt{n}_p \tag{3.10}$$

As a result, the fewer the photons collected, the worse is estimation of particle localization [65]. For a much larger photon budget, this static localization error is often in the range of a few nanometers which is at the origin of super-resolution techniques such as PALM and STORM.

Here, we consider the net consequence of noise in single molecule imaging to be variation of the localization precision. As expected, the localization precision plays a central role in how we interpret single-particle tracking observables such as the mean squared displacement (MSD) and velocity autocorrelation function (VACF) [133]. In experimental trajectories, the measured position can be written as the sum of the ground truth of the particle position and a localization error term, which is typically modeled as Gaussian noise with variance σ^2 [67]. This additive noise introduces a systematic bias in downstream analyses.

For the MSD, localization uncertainty leads to a positive offset. The measured MSD becomes:

$$\mathrm{MSD}(\Delta t) = 6D\Delta t - 2Dt_E + 6\epsilon^2 \tag{3.11}$$

where $\mathrm{MSD}(\Delta t)$ is the measured mean squared displacement, D is the diffusion coefficient, Δt is the lag time, t_E is the exposure time, and ϵ^2 is the variance of the localization error (*i.e.* the square of the localization uncertainty). The term $6\epsilon^2$ accounts for the contribution of uncorrelated Gaussian localization noise in three dimensions [134].

This offset is most significant at short lag times, where the true displacement is small and comparable to the localization noise. As a result, the MSD curve appears artificially elevated at small τ, which can bias the estimation of diffusion coefficients and anomalous exponents (α). In particular, it can make subdiffusive motion appear closer to Brownian

or even mask confinement effects if not corrected [67]. A simple correction technique involves the estimation of this localization precision and subtracting it, or more naturally, to fit data beyond the first two time points to avoid biasing the regression parameters.

Similarly, the VACF too is sensitive to localization noise. Here, the effect is more prominent as each successive position measurement contains independent noise, taking finite differences to compute velocities introduces anti-correlations. This leads to an artificial negative dip in the VACF at short lag times, even for purely Brownian motion where the true VACF should vanish beyond zero lag [66]. This effect can be mistakenly interpreted as physical backscattering, viscoelasticity, or confinement if localization error is not accounted for [67].

More generally, however, localization precision sets a fundamental resolution limit: dynamics occurring below the spatial scale σ or temporal scale where displacements are comparable to σ cannot be reliably resolved. In practice, careful calibration of localization precision (e.g., via immobile emitters), inclusion of noise models in fitting procedures, or use of methods that explicitly account for localization error (such as covariance-based estimators) are essential to extract unbiased physical parameters from trajectory data. In the following sections we will see how various experimental factors along with localization precision affect diffusion metrics for standard Brownian motion.

3.5 Diffusion of (u)CCNTs in a brownian fluid

First, we begin by studying the diffusion of nanotubes in a homogeneous fluid. In such a fluid, we expect the diffusion of CCNTs and uCCNTs to be purely Brownian. This would validate our experimental setup and analysis procedure while also providing for a useful control to study diffusion in more complex environments. To this end, CCNTs and uCCNTs were independently imaged in diffusing in a 10 mM SDS 1:1 water-glycerol (v/v). The choice of this homogeneous fluid is discussed in detail in Chapter 4.

3.5.1 Experimental constraints and measurement artefacts

Initial analysis of diffusion began with simply the time ensemble averaged and ensemble averaged MSDs which revealed non ergodic behavior at shorter time lags despite the diffusion occurring in homogeneous media. At longer time lags they seemed to converge to have more ergodic behavior. When the curves were linearly fitted in the log-log format, the slope revealed the scaling exponent α (Figure 3.14). Furthermore as shown in Figure 3.15, the MSD calculated along the x, y, z axes independently revealed that the MSD along the axial direction was significantly different from that of the lateral axes. This

resulted in the fit having a diffusion constant as well as the anomalous diffusion coefficient α in the axial direction being lower than the ones in the two lateral axes which converged well. To begin with, the intercept of the z axis is relatively higher than that of the x and y axes, indicating a larger localization error. While this is to be expected in 3D localization microscopy that the errors in localization are not homogenous in the lateral and axial directions [131], the extent of the errors in each direction needs to be determined to be corrected.

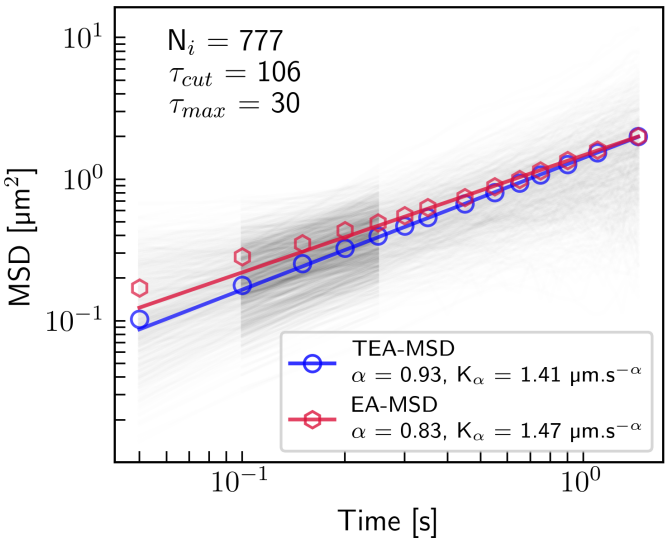

Figure 3.14: MSDs for CCNTs in bulk liquid: The EA-MSD and TEA-MSD as calculated for CCNTs diffusin in 1:1 water-glycerol solution shows non-ergodic behavior with the ensemble α significantly less than unity. At longer time lags the diffusion converges to ergodicity. N_i, τ_{cut}, and τ_{max} are the total number of trajectories, the number of timepoints in the smallest trajectory, and the number of timelags in frames the MSD was calculated for.

Using a power law fit with an offset, the intercept (offset) was determined in each direction. It was found that the intercepts in the x and y direction were fairly similar and much lower as compared to the z direction. The offset is comprised of two factors that determine localization error, the first being the localization error due to the point spread function, and the second is from the finite frame rate that creates a blur when the particle moves during acquisition of each frame. By substituting the acquisition rate of the camera in equation 3.10, the localization errors along the axes were determined independently to be 33 nm in the lateral direction and 59 nm in the axial direction. We then looked at several factors that could potentially add to this heterogeneity.

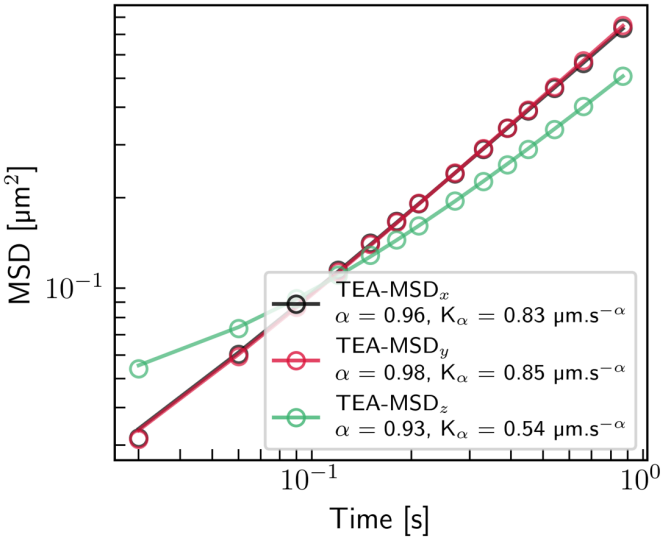

Figure 3.15: MSD for CCNTs in bulk liquid along independent coordinate axes: Ensemble MSD calculated independently along each of the coordinate axes reveals a heterogeneity between the lateral and axial axes. While the diffusion in x and y directions is Brownian in nature, the diffusion of particles in the axial region shows deviations from Brownian diffusion with large localization error as seen in the y-intercept.

3.5.1.1 Truncation of trajectories

A common challenge in analyzing 3D SPT data is that trajectories exhibit a broad distribution of lengths, such that ensemble quantifiers cannot be calculated over homogenous lengths of time. One common approach is to truncate all the trajectories to equal lengths and discard anything above this length. While this homogenizes the trajectories by length, we risk the loss of large amount of our data, especially at longer time scales. Moreover, as highlighted by Rehfeldt and Weiss, one could vary the truncation length of trajectories to yet again reveal systemic differences in the observables [66]. For example, longer trajectories may specifically be long simply due to confinement effects which faster particles do not experience. On the other hand, splitting long trajectories into multiple shorter segments can artificially increase the weight of the few long trajectories within the ensemble without accounting for the role of effects such as ageing. Lastly, the act of equalizing trajectory lengths also adds an artificial homogenizing bias, which could potentially mask other influences such as localization errors or even true phenomena involving heterogeneous diffusion along the axes.

Here, as an example, I discuss results of segmentation of the trajectories where each segment is considered as a new trajectory. Various segmentation lengths were tested, which achieved strong ergodic behavior and diffusion exponents closer to 1 occurring when the segments were 50 time points in length (Figure 3.16) and also largely homogenized

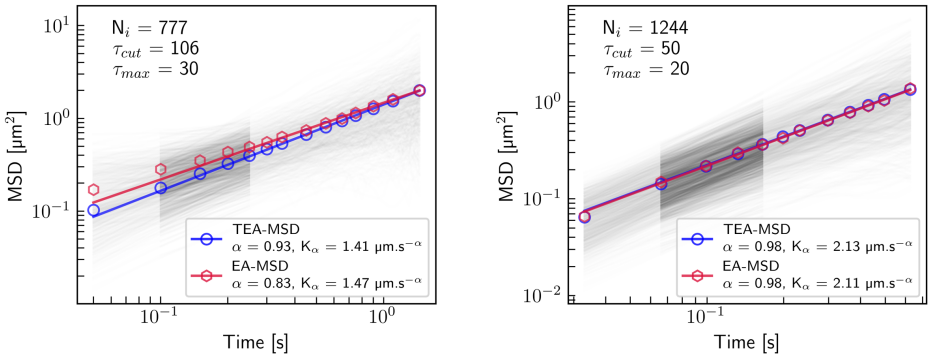

Figure 3.16: Effect of truncation of trajectories on MSD: The MSD calculated by truncating each trajectory to 50 time points and discarding the remainder of trajectories (right) shows strong ergodic Brownian behavior in bulk liquid as opposed to untruncated whole trajectories of variable lengths (left).

MSDs in the three axes (Figure 3.17), as well as a. This largely subsumed the localization error and caused the MSD curve along the z direction to align itself parallel to the MSD along the lateral directions. However, the diffusion coefficient remained smaller(Figure 3.17).

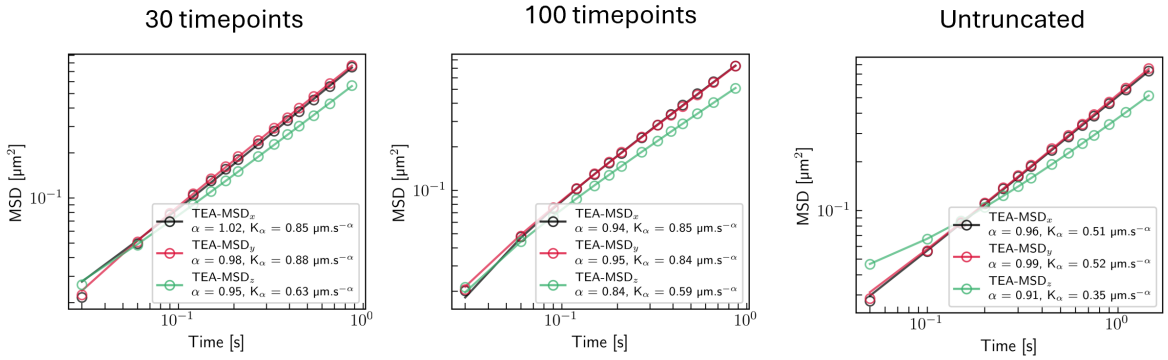

Figure 3.17: Effect of homogenizing trajectory lengths on MSD in the independent axis: Truncating the trajectories to equal lengths results in homogeneity in MSD along the coordinate axes, however the length of truncation introduces systemic biases in measuring scaling exponents and diffusion coeffecients. Here we see that equalizing the lengths to 30 time points(far left) as well as retaining the full length trajectories(far right) reveal fairly Brownian behaviors despite some residual heterogeneities. Parallelly, it is seen that equalizing the trajectory lengths to 100 time points(middle) reveals a subdiffusive behaviour in the axial axis as compared to the lateral directions.

In my work however, I retain trajectories to their full heterogeneous distribution of lengths and compute ensemble quantities using all available data at each lag time. Effectively, this corresponds to an effective ensemble size that decreases with increasing lag time, as shorter trajectories contribute less at longer time lags. As a result, ensemble averages are well sampled at short lag times but become progressively dominated by longer trajectories at larger time lags. Hence, for ensemble properties within the droplets structure, I have

chosen to work at low time lags to avoid such biases. To maintain statistics, very short trajectories, that is, shorter than 30 frames were excluded, avoiding biases arising from short tracks.

3.5.1.2 Effect of refractive index matching

Next, we look at the influence that the refractive index has on single particle localization in microscopy. A systematic bias arises from the refractive index mismatch between the objective immersion medium and the sample, leading to an underestimation of displacement along the axial (z) direction. As shown by the group of W. E. Moerner, this effect can be corrected for by a scaling factor equal to the ratio of the refractive indices of the sample and the immersion medium [135]. Accordingly, each localization in the z direction was corrected by multiplying by n_{sample} /n_{water} , where n_{sample} corresponds to the refractive index of the glycerol water solution used in the experiments. As shown in Figure fig:ricorrection, the corrections strongly curbed localization errors in the z direction and homogenized the diffusion along the three directions. While this correction does not

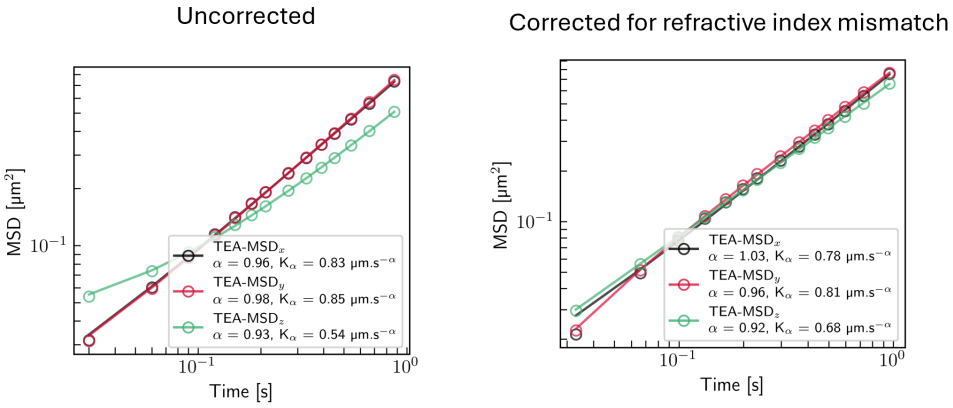

Figure 3.18: Effect of refractive index matching on axial MSD measurements: The mismatch in refractive index between the objective immersion medium (water in our case) and the sample shows deviations underestimates the size of steps taken by the particle taken in the z direction. A refractive index correction factor of ∼1.05 used to account for this mismatch strongly homogenizes the diffraction in the three axes revealing the true nature of Brownian diffusion.

fully eliminate axial distortions, it significantly reduces the anisotropy between spatial dimensions, improving the consistency with the isotropic behavior expected for Brownian diffusion.

3.5.2 True Brownian motion in bulk homogeneous liquid

After having accounted for possible factors that could bias data or create artefacts, we now look at the true nature of diffusing single particles in a bulk homogenous liquid (1:1 water-glycerol). Given the interstitial space is filled with the imaging buffer, we studied the brownian diffusion of nanoparticles in a 10mM SDS 1:1 water-glycerol solution, thus making this solution an ideal control. Additionally, given the low viscosity of water, the acquisition time must be fast enough to capture the motion of particles in order to minimize motion blur effects. However, fast acquisition time also compromises on photon budget especially with the DHPSF. Thus, we study diffusion of nanoparticles in bulk liquid by increasing the viscosity by adding glycerol. First, the ensemble MSD was

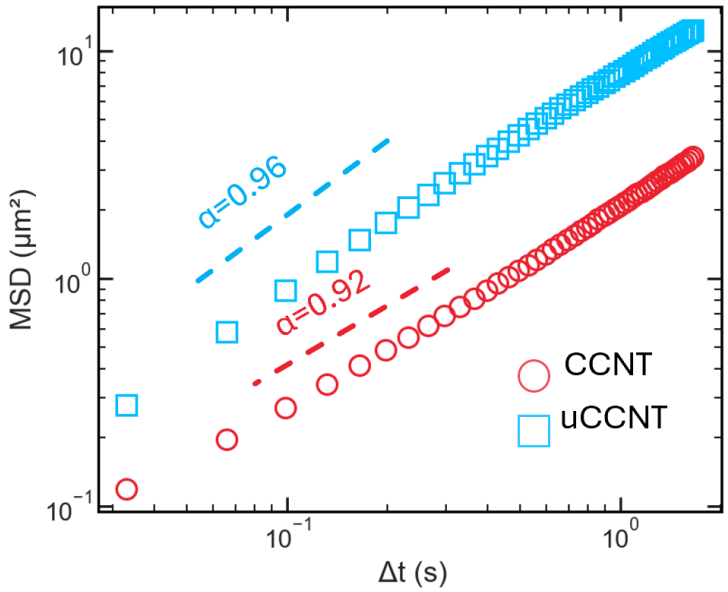

Figure 3.19: Mean squared displacement for CCNTs and uCCNTs in a homogeneous medium: The ensemble MSD of CCNTs and uCCNTs diffusing in bulk homogeneous liquid of 1:1 water-glycerol solution reveals Brownian motion with $\alpha = 0.92$ and $\alpha = 0.96$ for the CCNTs and uCCNTs. The slightly lower value obtained for the CCNTs reflects errors in localizing single particles that are close to or may even exceed the diffraction limit resulting the MSD being slightly sublinear at early time lags.

computed for both CCNTs and uCCNTs diffusing in a 1:1 water glycerol solutioin. The diffusion exponent, obtained via linear regression of the MSD curve, was found to be 0.92 for CCNTs and 0.96 for uCCNTs, in close agreement with the unitary exponent expected for ideal Brownian motion. Small deviations from ideal brownian behavior are attributed to experimentally finite statistics, motion blurring, and localization uncertainties. These effects are more relevant with the CCNTs, whose lengths approach or may even exceed the diffraction limit at an emission wavelength of 1140 nm, potentially introducing additional bias in position estimation. Nevertheless, considering these experimental limitations, the observed exponents remain in good agreement with brownian diffusion. The diffusion

coefficients in the were retrieved from the fit and were found to be 0.33 $\mu m^2/s$ and 1.41 $\mu m^2/s$ for the CCNTs and uCCNTs respectively (Figure 3.19).

Next, we look at the correlation between the displacements of the particle steps. The velocity autocorrelation function (VACF) was calculated for the trajectories of the CCNTs and uCCNTs. The uCCNTs showed purely uncorrelated steps. However, the steps taken by CCNTs showed slight anticorrelation or negative persistence, that rapidly converge to zero (Figure 3.20). Here again, we attribute this minor deviation from ideal random motion as an effect of motion blurring, and localization inaccuracies especially arising from the size of the nanotube.

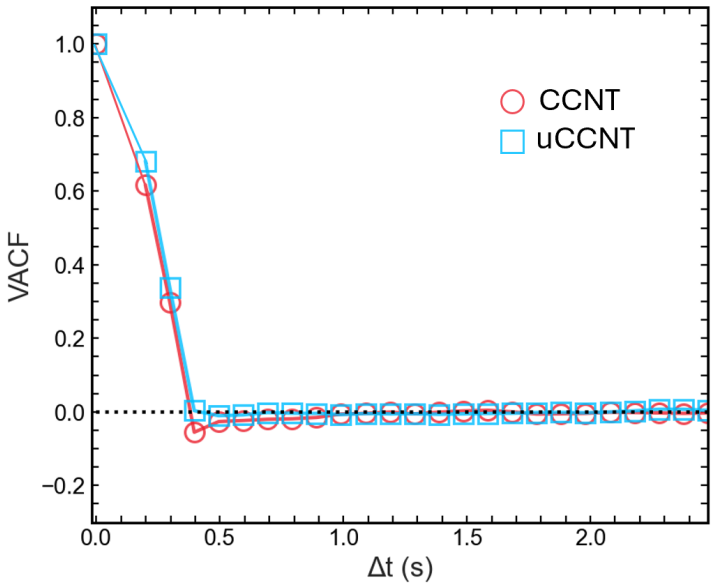

Figure 3.20: Velocity autocorrelation function of CCNTs and uCCNTs in a homgeneous medium: The ensemble VACF calculated reveals uncorrelated motion of uCCNTs in the water-glycerol solution, while the CCNTs show a slight anticorrelation at early time lags before converging to uncorrelated steps in argeement with Brownian motion. The slight deviation from ideal behavior is again a result of errors in localization precision.

Finally, we look at the distribution of the turning angles of CCNTs and uCCNTs in the bulk liquid. As discussed in the earlier chapter, in 3D, the Brownian statistics result in a positive cycle of a sinusoidal curve peaking at 90°(Figure 3.21). This was confirmed independently from our experiments for both the CCNTs and uCCNTs at various time lags.

We observed a slight leftward shift toward smaller turning angles for nanotubes diffusing in Brownian fluids at early time lags ($\Delta t = 1$), for both the CCNTs and the uCCNTs. This deviation disappears at higher time lags, even by $\Delta t = 2$. To rule out the role of particle anisotropy in these statistics, we performed the same experiments with spherical AuNPs, which exhibited similar deviations. While we have not been able to conclusively

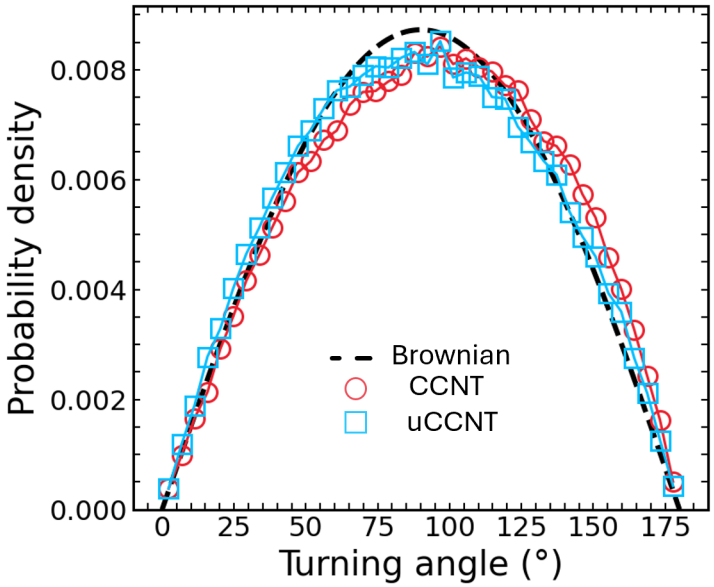

Figure 3.21: Distribution of turning angles of CCNTs and uCCNTs in a homogeneous medium: The distribution of turning angles reveals that both the CCNTs and uCCNTs closely follow the expected theoretical curve for Brownian motion with minimal deviations.

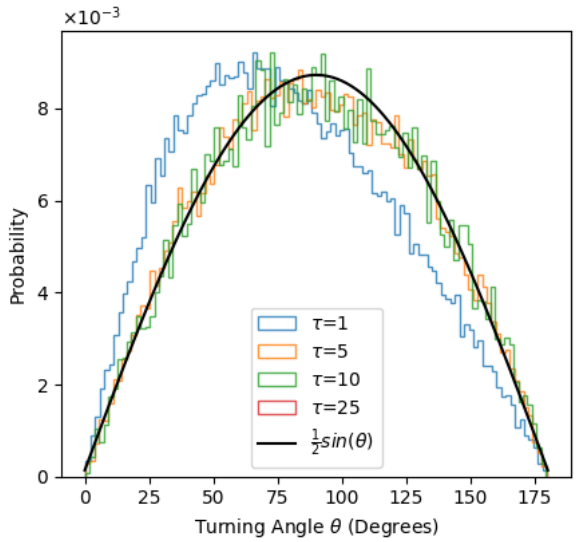

Figure 3.22: Distribution of turning angles at early timescales in Brownian fluids: At $\Delta t = 1$, the distribution shifts toward smaller turning angles before rapidly converging back to ideal Brownian behavior.

identify the source of this irregularity, it is most likely a systematic error arising from the fact that the particles explore regions very close to the focal plane at early time lags, effectively navigating a "flattened" narrow region and thereby skewing the distribution. At longer timescales, the exploration becomes more isotropic, resulting in classical Brownian statistics.

Having achieved 3DSPT using DHPSF of single ultrabright CCNTs and uCCNTs, followed by quantification and corrections of possible biases, we were able to characterize true Brownian motion of single CCNTs and uCCNTs, thus validating our setup and analysis pipeline. In the next chapter, we will look at the assembly and characterization of a complex soft matter system to study nanoscale diffusion in.

Chapter 4

Packed emulsion droplets: a novel diffusion landscape

In the previous chapter, we introduced three-dimensional single-particle tracking using localization microscopy, discussing the principles underlying our experimental setup as well as the challenges associated with achieving accurate localization and trajectory reconstruction. We also investigated the experimental constraints and potential sources of artefacts after which we characterizing the diffusion of CCNTs and uCCNTs in a homogeneous bulk medium. Building upon these results, this chapter turns to the central problem of diffusion in complex soft matter environments. We introduce biomimetic packed emulsion droplets as a tunable biophysical model of tissue-like confinement and describe the development and optimization of the experimental protocols used to prepare the system and incorporate carbon nanotubes. Finally, we characterize the physical architecture of the diffusion environment prior to investigating nanotube transport within it.

4.1 Packed emulsions as model systems

In recent years, concentrated emulsions have emerged as powerful model systems for exploring how complex, disordered soft matter materials organize and behave under confinement and compression [136–139]. Emulsions are primarily composed of stabilized liquid droplets in an otherwise immiscible liquid, the simplest example of which would be oil in water. Such systems, while mostly fluid at dilute concentrations, show unique mechanical and dynamic properties often associated with solids when densely concentrated. That is to say, as one increases the concentration of droplets in the fluid, droplets press up against each other and undergo physical deformation due to lack of free volume giving rise to crowded and jammed structures held together by interfacial tensions [140].

Furthermore, recent advances have allowed for the self-assembly of these droplets using programmable folding [141]. As a result, such densely packed emulsions act as a primary tool in studying soft matter that display collective bulk behavior akin to solids, such as elasticity, structural relaxation, and unique rheology and therefore form an interesting material for investigation in soft matter physics [142, 143]. A major experimental advan-

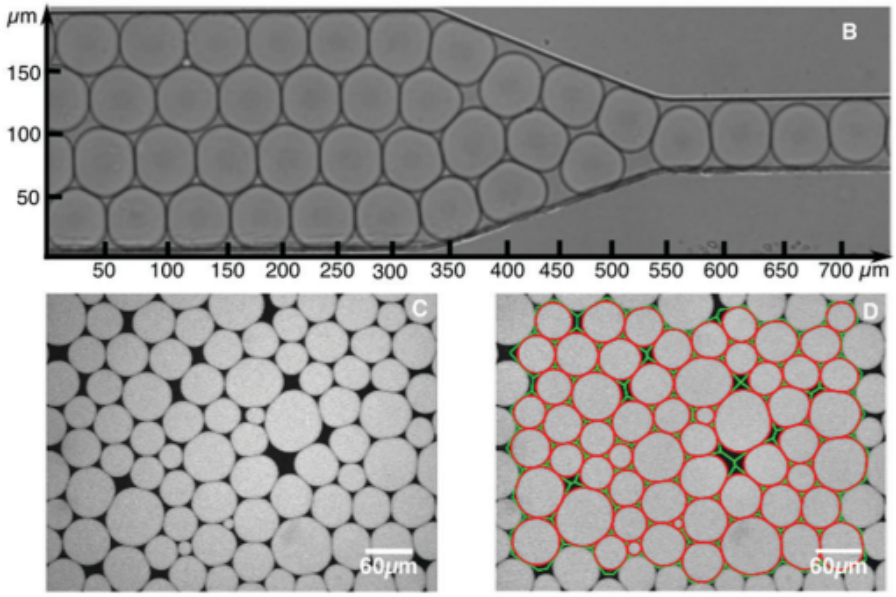

Figure 4.1: Packing and constrictions in emulsion droplets: A typical brightfield image of emulsion droplets flowing through constrictions (top). Typical confocal images with analysis of compressed droplets in 2D (bottom).(adapted from [138])

tage that arises from systems of jammed emulsions is the accesibility to their internal structure at the microscale. A series of experiments demonstrated measuring of quantifiers such as coordination, force bearing, and deformation of individual droplets using 2D and 3D confocal imaging of densely packed emulsions(Figure 4.1) [136, 144]. These studies provided experimental insight into organization of crowded and jammed soft matter at the microscopic scale, revealing that despite the apparent disorder of the packings, robust statistical and geometrical regularities emerge [145].

Beyond their role as model soft materials, emulsions have been shown to be powerful biomimetic systems for studying cellular organization and tissue mechanics [142, 145]. Using controlled attractive interactions through depletion forces, surfactant tuning, or more recently binding with biomolecular interactions, droplets can be engineered to mimic and investigate cell–cell adhesion [146]. This approach builds on the conceptual frameworks that describe tissues as effectively fluid-like assemblies governed by interfacial tensions. Furthermore, droplets in such a packed system have been interconnected through nanopores to understand cell to cell communication [27, 147]. In this context, emulsion droplets have been used to reproduce phenomena such as cell sorting, interface-driven organization, and the emergence of tissue-like mechanical properties. Thus, packed emul-

sion droplets embody systems that can be tuned to emulate multicellular assemblies, providing a fundamental and highly controllable platform to investigate how microscopic adhesion rules give rise to macroscopic structure and function [143].

A key advantage of such packed emulsion systems lies in their ability to provide direct insight into the forces and mechanical constraints that govern disordered packings. Using high-resolution imaging and reconstruction techniques, studies by the group of Lea-Laetitia Pontani [143, 148]have quantified the relationship between area of adhesion of particles and interparticle forces. Additionally, along with theoretical validation, these measurements reveal physical mechanisms of how forces and pressure influence adhesion in real cell-cell junctions [142]. The interplay between droplet geometry, force balance, and mechanical stability in these systems display direct experimental evidence of jamming theory and offers a framework for understanding how local constraints propagate to determine its bulk mechanical response [136] .

Given the extensive use of packed emulsion droplets to study tissue rheology, packing of soft matter, and their application as biomimetic systems, they form an interesting material to study diffusion in soft matter. Their general architecture combines disorder with local structural organization, producing environments that are neither fully random nor perfectly ordered. Their tightly packed structure allows for narrow interstitial regions between the droplets which is reminiscent of the structure of the extracellular space of tissues [145]. Furthermore, these interstitial regions between the packed droplets form a homogenous, continuous, intricate network for diffusion regulated solely by the geometry of the bounding walls of the droplets, unlike the ECS and other biologically relevant media that contain complexities such as extracellular matrices, non-specific binding and trapping sites, ionic gradients, biomolecular activity, and flows. Thus, a soft matter system of packed emulsion droplets was an ideal candidate for us to study the diffusion in complex biophysical models. To this end, we collaborated with the Pontani group to procure droplets to form biophysical models of the ECS.

4.2 Characterizing droplets packing: HiLo optical sectioning

Before introducing the preparation protocols for the droplet system, we first describe the imaging modality used to visualize the packed emulsion environment.

Biomimetic models of densely packed emulsion droplets are commonly imaged using confocal microscopy, where one of the two immiscible liquid phases is fluorescently labelled to provide strong contrast between droplets and their surroundings [142]. High image

quality is particularly important in such systems, as accurate determination of droplet morphology, deformation and rearrangement requires effective rejection of out-of-focus background fluorescence. To achieve optical sectioning while retaining the high acquisition speed and large field of view characteristic of widefield microscopy, we employed the SPARQ HiLo (High-pass Low-pass) optical sectioning system developed by the group of Jérôme Mertz and commercialized by Bliq Photonics [149,150]. A schematic of the setup adapted from [149] has been shown in Figure 4.2.

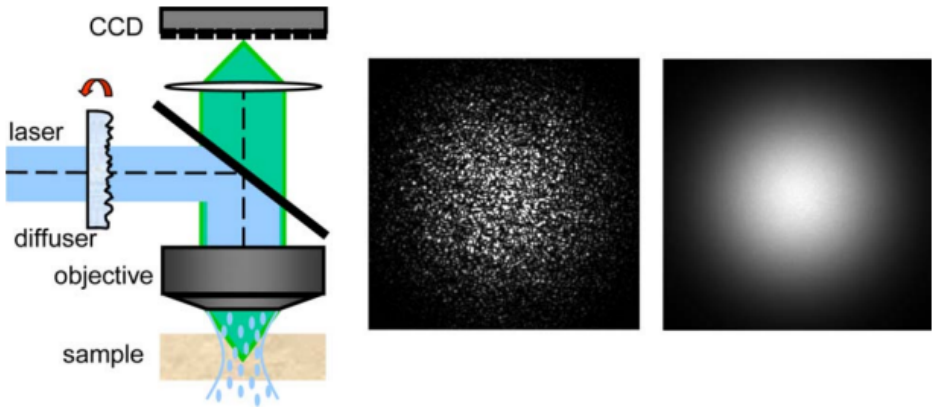

Figure 4.2: HiLo optical sectioning setup: Schematic of the optical sectioning microscope (far left). Speckle illumination (middle) is generated using a static diffuser element, while uniform illumination (right) is achieved using a rapidly rotating diffuser. Adapted from [149].

HiLo imaging achieves optical sectioning through the acquisition of two fluorescence images of the same field of view. The first image, denoted I_s, is obtained under speckle illumination achieved using a diffuser element that randomizes the laser's phase front. and therefore resembles a conventional widefield fluorescence image. The second image, denoted I_u, is acquired under uniform illumination generated by rapidly rotating the diffuser element to randomize the speckle pattern. Now, $I_s(\mathbf{r})$ and $I_u(\mathbf{r})$ can be described as follows:

$$I_s(\mathbf{r_d}) = \iint PSF(\mathbf{r_d} - \mathbf{r}, z)O(\mathbf{r}, z)S(\mathbf{r}, z)d^2\mathbf{r}dz \tag{4.1}$$

$$I_u(\mathbf{r_d}) = \iint PSF(\mathbf{r_d} - \mathbf{r}, z)O(\mathbf{r}, z)\langle S\rangle d^2\mathbf{r}dz \tag{4.2}$$

where $PSF(\mathbf{r}, z)$ is the 3D detection PSF, $O(\mathbf{r}, z)$ represents the object distribution in 3D, and $S(\mathbf{r}, z)$ is the speckle illumination intensity.

Next we take the difference of the two images which results in:

$$\delta I(\mathbf{r}) = \iint [PSF(\mathbf{r_d} - \mathbf{r}, z)\delta S(\mathbf{r}, z)]O(\mathbf{r}, z)d^2\mathbf{r}dz \tag{4.3}$$

Here, $\delta S(\mathbf{r}, z) = S(\mathbf{r}, z) - \langle S \rangle$. The terms in the square brackets as a whole now represents a weighting function that decays with defocusing. This decay can be further accelerated to zero by applying an additional bandpass filter to obtain:

$$\delta I(\mathbf{r}) = \iint [W(\mathbf{r_d} - \mathbf{r}')PSF(\mathbf{r}' - \mathbf{r}, z)\delta S(\mathbf{r}, z)]O(\mathbf{r}, z)\mathbf{r}'d^2\mathbf{r}dz \tag{4.4}$$

To understand the optical sectioning, we next evaluate the contrast of the speckle with reference to defocus. For this, let us consider a plane uniform object at a certain z (here $z = 0$ represents the focal plane). Now, the contrast achieved when illuminated by speckle illumination is defined by:

$$C_{\delta s} = \frac{\sigma_{\delta s(z)}}{\langle I_s \rangle} = \frac{\sigma_{\delta s}(z)}{\langle I_u \rangle} \tag{4.5}$$

where $C_{\delta s}(z)$ represents the contrast, and $\sigma_{\delta s}(z)$ denotes the standard deviation of the variations in fluorescence imaged.

Working in the frequency domain for ease, the optical transfer functions can be defined as:

$$OTF(\kappa_\perp, z) = \int PSF(\mathbf{r}, z)e^{-i2\pi\kappa_\perp \cdot \mathbf{r}}d^2\mathbf{r} \tag{4.6}$$

Applying the Fourier of the weight function ($\mathcal{W}$) to the above two equations, we derive:

$$C^2_{\delta s}(z) = A_s \int |\mathcal{W}(\kappa_\perp)|^2 |OTF_{det}(\kappa_\perp, z)|^2 OTF_{ill}(\kappa_\perp, 0)d_2\kappa_\perp \tag{4.7}$$

Thus $C_{\delta s}(z)$ itself can be interpreted as a weighting function that reaches a maxima when the object is in focus ($z = 0$) and decays to zero as z increases. Going back to the additional filter W added, we see that by adjusting the width of this filter we are essentially tuning the sectioning strength. In the ImageJ plugin, this parameter is labelled as the thickness weight factor.

We will next synthesize the final HiLo image. For this, we first reconstruct a low resolution estimate of the image in focus, we apply a lowpass filter (LP) to the weighted uniform image giving $I_{LP}(\mathbf{r}) = LP[C_{\delta s}(\mathbf{r})I_u(\mathbf{r})]$. Similarly, a complementary high resolution image is constructed using a high pass filter applied on the uniform illumination image given by $HP(\kappa_\perp) = 1 - LP(\kappa_\perp)$, that is, $I_{HP}(\mathbf{r}) = HP[I_u(\mathbf{r})]$. Fusing the LP and HP images, we arrive at:

$$I_{HiLo}(\mathbf{r_d}) = \eta I_{LP}(\mathbf{r_d}) + I_{HP}(\mathbf{r_d}) \tag{4.8}$$

Here, η is a scaling function used to transition between the low and high frequencies. where $C_N(\mathbf{r})$ is the local speckle contrast evaluated at the image coordinates $\mathbf{r}$, $\langle \sigma_n(\mathbf{r}) \rangle_A$ is the local standard deviation of the difference image intensity, and $\langle I_n(\mathbf{r}) \rangle_A$ is the corresponding local mean intensity, both computed over a neighborhood A with center at $\mathbf{r}$. The averaging region A is chosen to be large enough to contain several speckle grains, allowing a robust estimation of the local speckle contrast yet small enough to preserve spatial variations in the image.

To summarize, the HiLo image is obtained by first taking a difference image of the uniform illumination and speckle illumination images. Next, a bandpass filter is used to control the sectioning. This is followed by evaluating the contrast from the speckle and removal of noise induced biases. Ultimately, low pass and high pass filters are constructed based on the weighting function, a scaling factor is evaluated, which are then applied to retrieve the HiLo image.

Unlike confocal microscopy, HiLo does not require point-by-point scanning and therefore allows optical sectioning at substantially higher acquisition speeds. This makes the technique particularly attractive for imaging dynamic systems and large fields of view. Furthermore, the images can be further enhanced through image processing algorithms such as Deblurring through Pixel Reassignment (DPR) or Super-resolution radial fluctuation (SRRF) [151] [152]. Figure 4.3 illustrates the improvement in image contrast obtained using HiLo imaging compared with conventional widefield microscopy in a 100 μm-thick eGFP-labelled mouse hippocampal tissue sample [150].

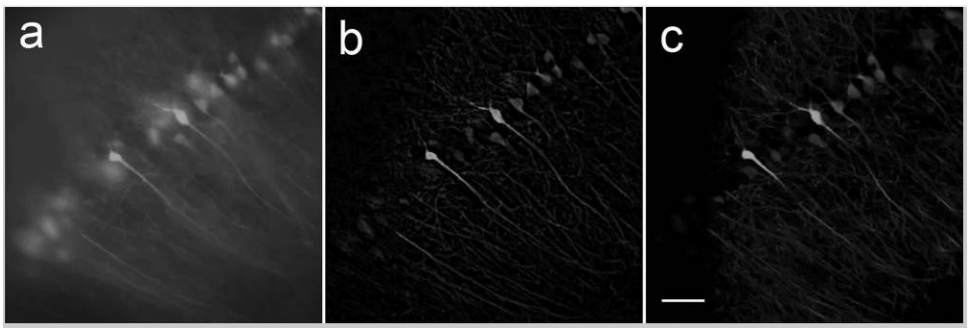

Figure 4.3: High-contrast imaging using HiLo. (a) Conventional widefield image of an eGFP-labelled mouse hippocampal slice. (b) Corresponding HiLo image showing substantial rejection of out-of-focus background fluorescence. (c) Confocal image of the same region for comparison. Adapted from [150].

4.3 Assembling the biophysical system for single particle studies

The emulsion droplets were synthesized and provided to us by our collaborator, Lea-Laetitia Pontani [145]. The following is a brief description of the synthesis procedure. The emulsion was synthetized by extrusion through Shirasu Porous Glass (SPG) membranes as follows: 5mL of silicone oil (viscosity = 50 cSt, Sigma Aldrich) was extruded into a solution of 10mM Sodium Dodecyl Sulphate (SDS) through a cylindrical SPG membrane with a mean pore size of 1.6 micrometers, using an Internal Pressure Micro Kit from SPG Technonolgy Co., Ltd. The droplets were then stored at room temperature. Their average diameter was 5 micrometers.

4.3.1 Index matching of droplets

Given that the droplets sample is fundamentally made of two liquids, silicone oil and a solution of SDS, the different refractive indices strongly affect the quality of imaging. Light refracts unevenly through the sample leading to scattering effects, distortions, aberrations, and a loss of resolution and localization accuracy. I decided to employ a refractive index matching technique to minimize such effects. To this end, the sample is prepared and stored in an index matching solution of 10mM SDS in 1:1 water:glycerol [142]. This protocol was established following a series of experiments in which parameters such as washing procedures, solvent composition, and ratios were varied to maximize imaging clarity. The final conditions were selected based on the quality of the acquired images and the resulting localization performance. Additionally, to label the droplets for imaging, Nile red dye was used. A saturated solution of nile red in the index matching buffer is used for labelling. The preparation involves adding around 5mg of nile red powder in 5 mL of 20mM SDS solution in water and stirring for several hours or overnight. 5 mL of glycerol is added to this solution, mixed and centrifuged at 5000g to recover the labelling solution without disturbing the sediments. This solution acts as the stock labelling solution and is diluted as per experimental requirements. The sample was pipetted onto a coverslip and imaged under whitelight and under illumination by a 568 nm laser (Figure 4.4). The whitelight image showed multiple droplets floating in the SDS buffer, similarly, under laser illumination, the nile red was excited to image the boundaries of single droplets.

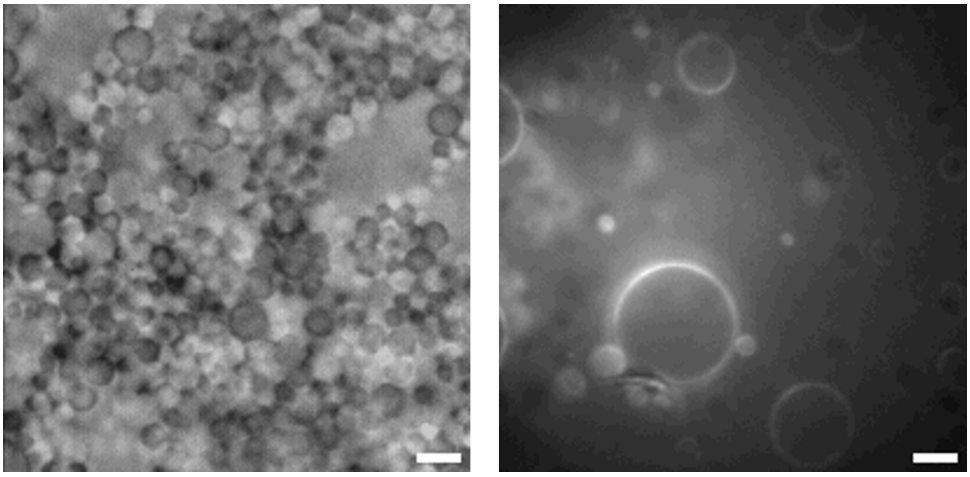

Figure 4.4: Visualisation of emulsion droplets: A typical widefield whitelight image of stock emulsion droplets as received (left), and a single large emulsion droplet in a dilute solution under fluorescence. The fluorophore nile red marks the interface of the droplet(right). The scale bar represents 5 µm.

4.4 Packing of droplets

To prepare the biophysical model, emulsion droplets of diameter 5 µm were labelled and index matched by diluting them in a 1:4 volume ratio (100 µL : 400 µL) of Nile red labelled index matching solution. Emulsions were incubated in this solution for several days to allow complete phase separation between the emulsion and aqueous phases. To obtain a packed system, the sample was centrifuged at 3000 g in a filter tube, facilitating packing of the emulsions and separating the liquid phase from the emulsions (Figure 4.5).

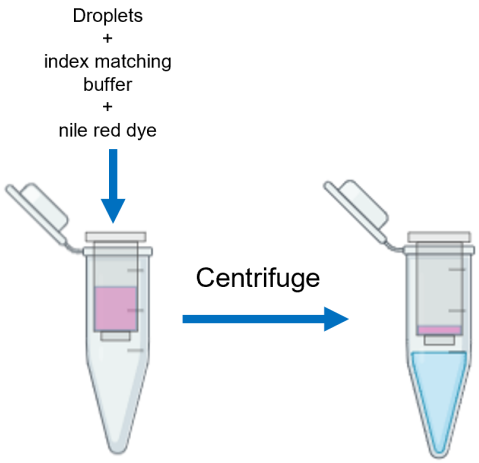

Figure 4.5: Packing of droplets: Schematic representation of the protocol to prepare packed droplets. The emulsion is mixed the index matching buffer and nile red dye solution in a filter tube and centrifuged at 3000 g in a fixed rotor centrifuge upto 1 hour. The filter phase contains the packed droplets that were pipetted out for imaging.

4.4.1 Preparation of samples for imaging

Samples were then prepared onto slides. A 50 µm deep imaging spacers (double sided) from SunJin/Nikon were used to form a well into which 2-2.5 μL of the prepared droplet was pipetted. A coverslip was placed over it and sealed along the edges of the imaging spacer. These samples remain in good condition for long periods of time and can be repeatedly imaged over the course of a few days to a few weeks.

4.4.2 Sample imaging

The prepared emulsion droplet samples were imaged under white light at first (as shown in Figure 4.4) and then illuminated with lasers either at 488 nm or 568 nm to excite the Nile red dye. This technique allowed us to visualize the droplets structure even at low powers. Next, the HiLo setup was used to image the sampling with optical sectioning. Several imaging tests were conduct sequentially to understand and optimize the HiLo imaging. The imaging was repeated with several samples, varying parameters such as centrifugation speed, centrifugation time, andlabelling concentration to achieve standardized, reliable and repeatable sample preparation methods. The quality of droplet images required for analysis was found to be dependent on the interplay of the frequency filter parameters for optical sectioning, and the Nile red concentration. The droplets were found to have a tolerance of upto 3000 g force beyond which the droplets seemed to degrade over time if not immediately. This optimization procedure has been discussed in detail in the following section.

4.4.3 Optimizing imaging conditions for the biophysical model

Whe had to optimize the imaging of the packed droplet structure to retrieve high contrast images for quantification of the droplets as well as the interstitial space that would act as the biophysical landscape for diffusion. In this regard, we decided to label the droplets with the Nile red dye. Nile red has a wide excitations spectrum of the Nile red dye, however, owing to its solvatochromic nature, the 568 nm excitation was best suited for illumination at the oil-water interface [153]. Next, to optimize the Nile red concentration used in the preparation, I tested and imaged a series of concentrations between 0.2x to 1x the stock concentration (Figure 4.4). We found that the best contrast and highest resolution of images were obtained at 0.4 times the stock concentration of the labelling solution(Figure 4.6).

The optimized labelling and HiLo imaging parameters allowed for sharp, high resolution and high contrast images, with strong background rejection allowing for imaging of single

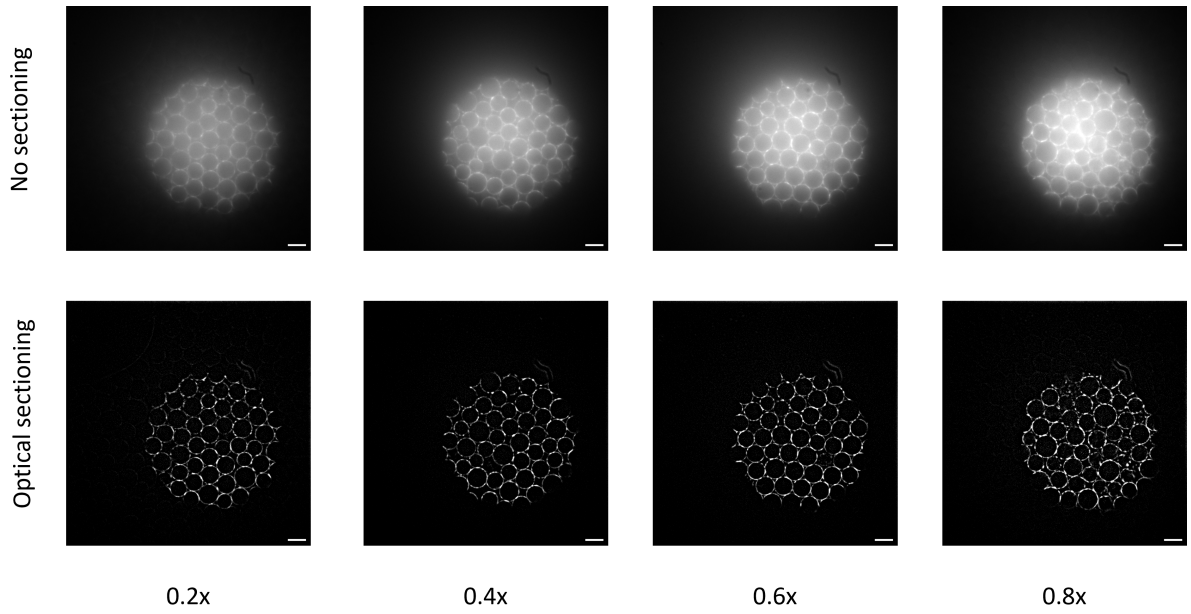

Figure 4.6: Optimizing droplet labelling for optical sectioning: A panel of images showing the effect of nile red labelling concentration on imaging with(bottom panel) and without the HiLo optical sectioning (top panel) The scale bar represents 10µm.

layers of droplets (Figure 4.7).

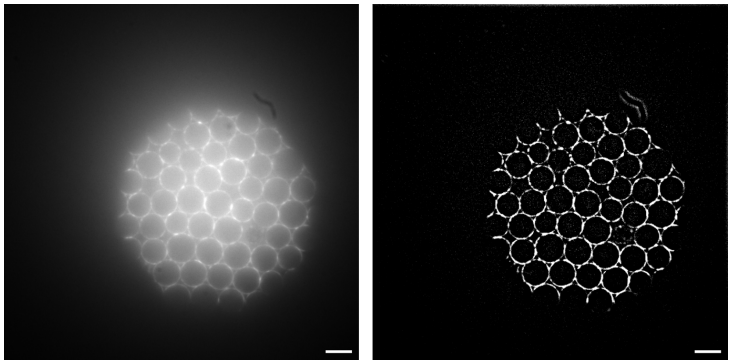

Figure 4.7: Optimizing labelling and HiLo parameters: Fluorescence images with and without HiLo optical sectioning on optimally labelled samples shows strong background rejection in case of sectioning allowing for high speed high contrast imaging (right). The scale bar represents 10 µm.

Similarly, to optimize the optical sectioning, images of the packed droplets were obtained by varying the HiLo parameters, Sparq Weight Factor (SWF) and Target Thickness Factor (TWF) independently. The optimal parameters for achieving high contrast and high resolution optically sectioned were found to be with a SWF of 0 and a TTF of 0.5 µm. Theoretically, this would correspond to an optical sectioning thickness of 500 nm. At these values, the droplets showed the highest contrast of fluorescence between the boundaries and the bulk of the droplets. To further validate this optimization, we imaged droplets at several depths, starting from the layer closest to the coverslip. Such imaging

also allowed us to visualize the projection of the 3D structure of the material in 2D using a 3 color RGB scheme, where the colors red, green, and blue represent successive layers starting from the bottom as shown in Figure 4.8.

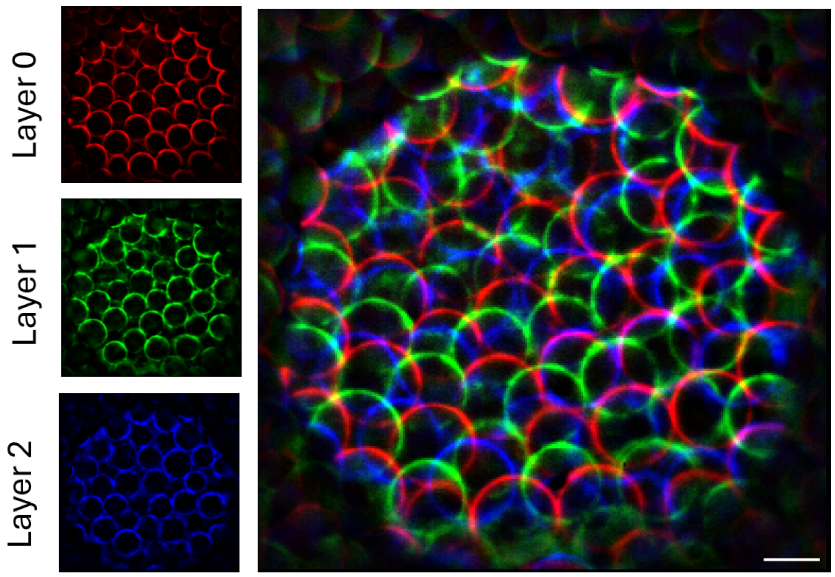

Figure 4.8: 2D projection of 3D droplet structure: 3 consecutive layers of the packed droplets were imaged using HiLo optical sectioning. With the z-recording of each layer, the layers were stacked in 3 color channels to project the 3D structure in 2D.

4.5 Segmentation of droplets and interstitial spaces

The optically sectioned images were then segmented to extract the droplet regions and the interstitial spaces. First, 100 frames of optically sectioned images of the same field of view were acquired and averaged. The average image was thresholded to create a binary mask of the droplet boundaries, and the *Ridge Detection* Plugin on Fiji ImageJ was used to recover the boundaries of the droplets. Segmentation of the droplets and interstitial spaces was carried out on the CellPose software [154]. CellPose is a deep learning based software with a python backend specifically built for image analysis of biological relevance. Using a pre-trained network called *Tissue Network* available directly on the software, we segmented the droplets making up the biophysical model. With yet another pre-trained model sensitive to shapes resembling live cells *Live Cell*, we were able to segment the space between the droplets. These masks were then used to retrieve the areas of the corresponding regions on Fiji (Figure 4.9 and 4.10). Using these methods, we were able to independently verify the sizes of 112 droplets and 182 interstitial voids between them. The droplet size distribution follows a Gaussian distribution resulting in a median area with standard deviation of $75 \pm 14\mu m^2$ correlating to droplet diameters of about $8.5\mu m$. The voids showed a median area of $16 \pm 6m^2$. However, with the voids, two distinct

populations of void sizes are seen. The smaller voids are around 4 μm^2 and the larger voids are around 20 μm^2 (Figure 4.11, 4.12). Segmentation and sizes estimated here prove useful in understanding the effect of centrifugation on packing.

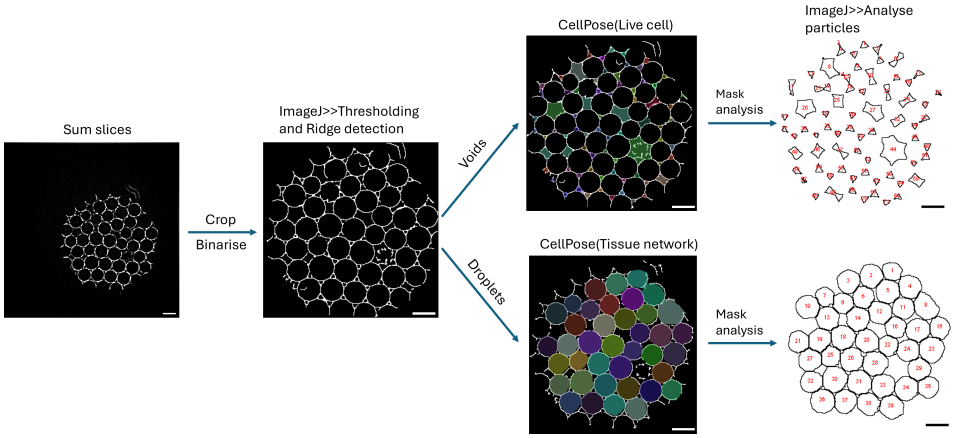

Figure 4.9: Segmentation of droplets and interstitial spaces A panel of images demonstrating the use of CellPose to segment the droplets and interstitial spaces for spatial analysis.

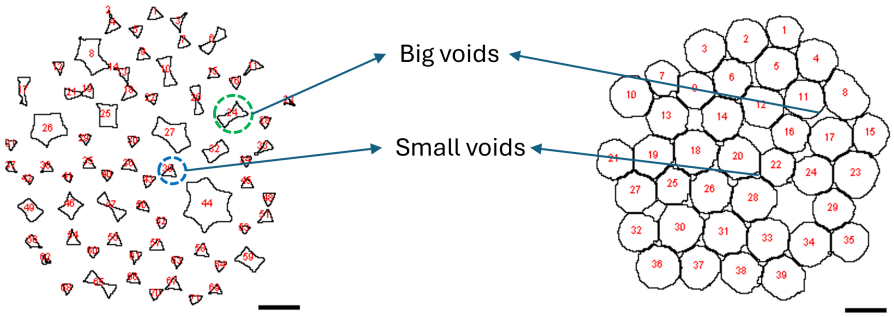

Figure 4.10: Segmented mask showing complementary regions Masks as extracted from CellPose reveal the shape and size of the droplets(left) and interstitial spaces(right)

Finally, Hough Circle transform was performed on three layers of the prepared biophysical model to retrieve the radii and centres of the droplets. Knowing the distance between the focal planes of the three layers, a model of the packed droplets was reconstructed (Figure 4.13).

4.6 Introduction of CCNTs in the biophysical model

The carbon nanotubes were introduced into the sample simply by pipetting about 1 µL of a known concentration of carbon nanotubes into the droplets before centrifugation. Initial experiments were conducted with long SWCNTs excited at 568 nm and imaged

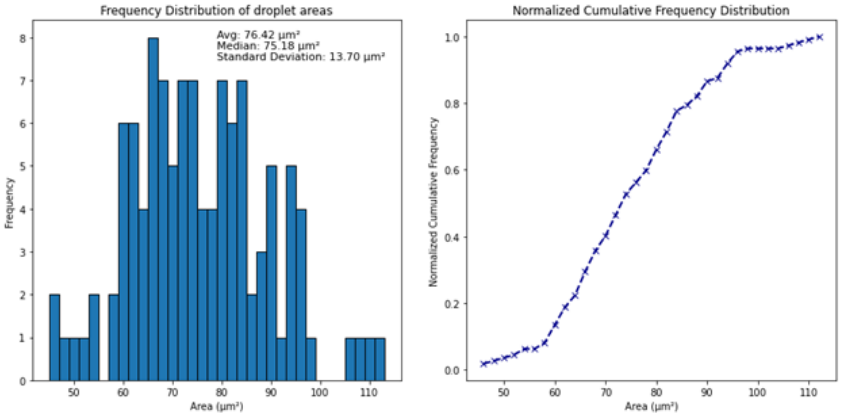

Figure 4.11: Distribution of droplet sizes in packed emulsions: The distribution and cumulative distribution of the areas of the packed droplets as calculated from the masks extracted using CellPose shows a median area of $75 \pm 14 \mu m^2$. 112 droplets were used to extract this distribution.

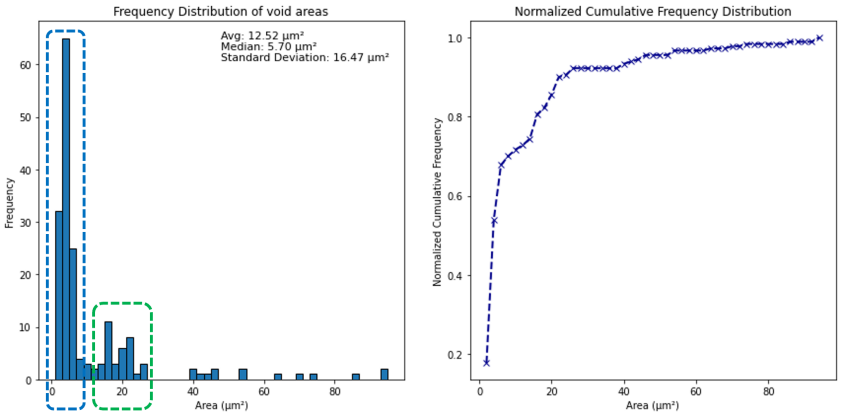

Figure 4.12: Distribution of interstitial space area: The distribution and cumulative distribution of the interstitial areas as calculated from the masks extracted using CellPose shows a median area of $6 \pm 16 \mu m^2$. Furthermore the distribution showed two subpopulations, while most of the interstitial spaces were small, a small subpopulation were larger interstitial regions. A total of 182 interstitial spaces were analyzed.

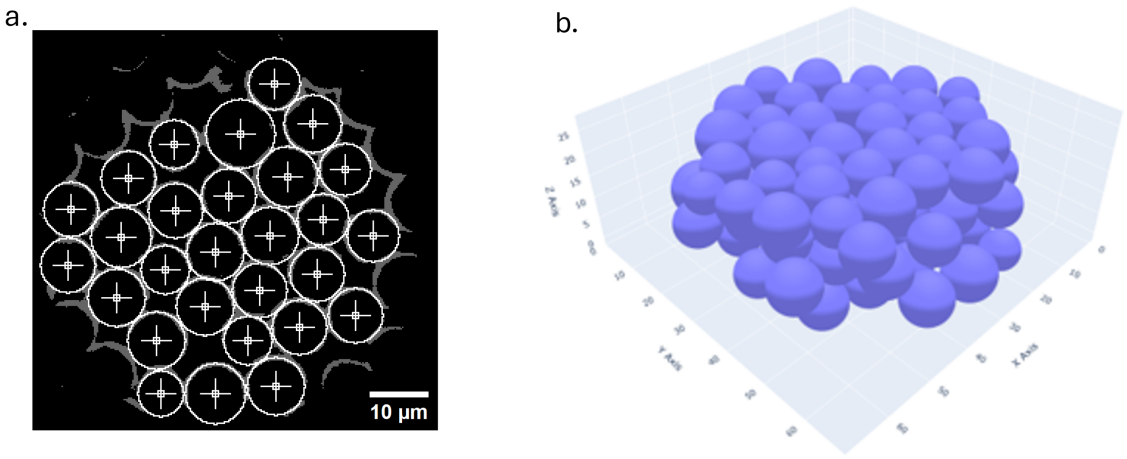

Figure 4.13: Reconstruction of the droplet structure: a. Extraction of droplet sizes using Hough circle transform and b. Reconstruction of multilayered packed droplet structure.

through a 900 longpass filter. Very soon, however, with the work of Nandi *et. al.* [51], we were able to produce ultrabright and highly photostable CCNTs and uCCNTs with much higher signal-to-noise statistics. After this, all diffusion experiments were carried out with CCNTs or uCCNTs as required. The particles were initially localized and tracked using the Fiji Plugin *TrackMate*. A cumulative representation of all the trajectories on the same image clearly revealed the interstitial structure created by the droplets (Figure 4.14).

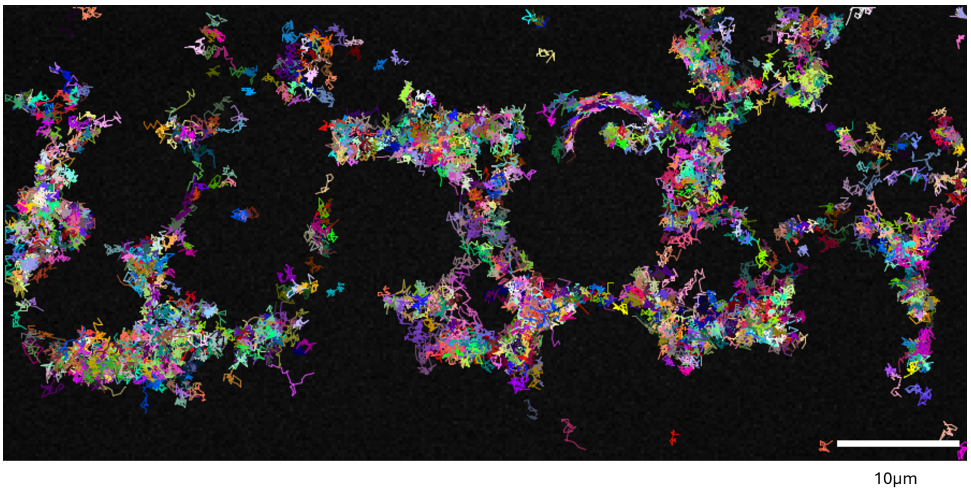

Figure 4.14: 2D trajectories of diffusing CCNTs in packed droplets: 2D trajectories of nanotubes diffusing in the interstitial regions of packed droplets reveals the structure of the packing.

4.7 Role of nanotube surfactants

SWCNTs are coated with surfactants to enable stable dispersion in aqueous environments, as bare nanotubes have a strong tendency to aggregate due to their hydrophobic nature [155]. In our study, we looked at the effect of two different surfactant coatings-phospholipid-PEG (PLPEG) and deoxycholate (DOC) [156]. Independently, PLPEG coated CCNTs and DOC coated CCNTs were introduced into two different samples of packed droplets (diameter = $10\mu m$) samples. The diffusing particles were localized and trajectories were reconstructed in 2D and 3D. In case of PLPEG coated CCNTs it was visually clear that the diffusion trajectories formed a curved surface. The trajectories were then fit with the equations of spheres, and the diameters of the fitted spheres were retrieved (Figure 4.15 a, b). The distribution of these diameters revealed that the particles were indeed sticking to and diffusing solely on the surface of the droplets (Figure 4.15 c).

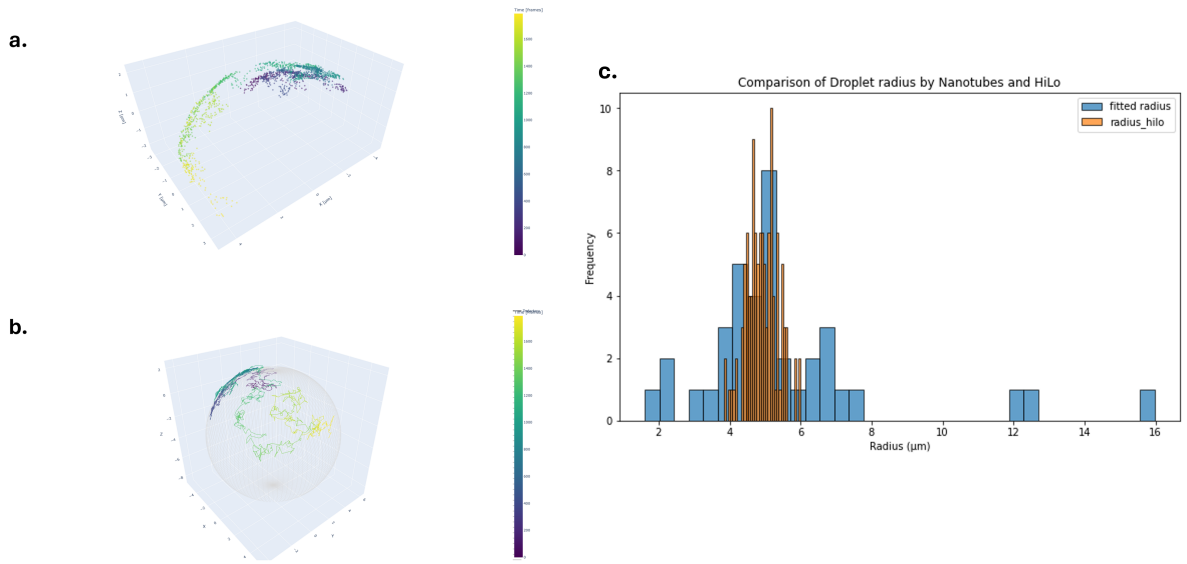

Figure 4.15: Optimizing CCNT surface chemistry: The choice of surfactant used to coat the CCNT allowed us to tune the diffusion of the nanotubes to the surface (left top-PLPEG) or to the interstitial spaces (left bottom-DOC). Using sphere fits on CCNTs diffusing on the surface of the droplets, we measured the size of the droplets, and this was in agreement to the sizes estimated from optically sectioned fluorescence images (right).

On the contrary, DOC coated nanotubes diffused in the interstitial spaces of the packed droplets structure. While the DOC nanotubes frequently collided with the boundary walls, there was no strong interactions or "sticking" to the droplet surface observed. 2D and 3D trajectories were reconstructed to visualize the shape of the droplets and the interstitial spaces (Figure 4.14 and 4.15).

4.8 Optimizing packing of droplets

Optical sectioning followed by segmentation and analysis of the dimensions of the interstitial spaces were key experiments to ensure a dense packing of droplets such that the interstitial dimensions approached the dimensions of extracellular spaces in tissues [47]. Primarily, the packing of droplets was carried out by centrifugation of droplets around 3000g for anywhere between 15 minutes to an hour in filter tube using a fixed angle rotor.

While the early preparation methods were useful in creating a biophysical model structure of packed droplets, there were several drawbacks. The primary concern was that this method resulted in large interstitial spaces between the droplets, with interstitial dimensions spanning several microns, exceeding an order in magnitude in comparison to extracellular spaces in brain and other tissues [47]. To overcome this, a strategy was adopted to mix ratiometrically droplets of different sizes to allow for smaller droplets to "fill in" the voids, thus making the interstitial spaces smaller (Figure 4.16).

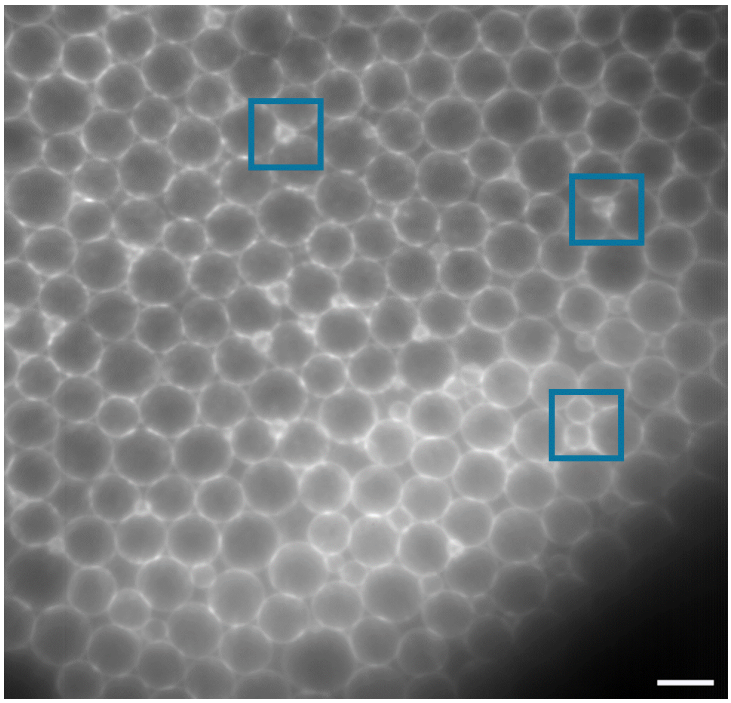

Figure 4.16: Reducing the intersitital space by mixing droplets: A fluorescence widefield image showing large(10 µm) and small(5 µm) droplets mixed ratiometrically in order to reduce the size of the interstitial space to approach extracellular space dimensions. Blue squares point to the smaller droplets "plugging" in larger voids.

While this method seemed to work, it was seen that the small and large droplets phase separated after some time with the smaller droplets residing at the bottom and the larger ones at top. This also proved that the packing structure was not dense enough, rendering fluidity to the droplets. Ultimately, the trajectories of the diffusing DOC-CCNTs also revealed that the extent of packing was low thereby resulting in larger interstitial spaces,

much larger than typical sizes found in tissues.

Furthermore, it was also found that the yield of the packed droplets was quite low, around 10µL for every 100µL of emulsion. Next, it was found that due to adhesive forces, plastic was not an optimal container for preparation. Additionally, the fixed angle rotor resulted in heterogeneous packing of the droplets, with the densest packing occurring at the edge of the filter, thereby making it difficult to retrieve the droplets. Ultimately, it was observed that even the act of pipetting the droplet resulted in vigorous vortices that could disperse the packed droplets.

To address these shortcomings, the protocol was optimized to improve the yield, packing, and quality of droplets. First, to increase the yield, the initial quantity of emulsion used in preparation of droplets was increased substantially from 0.1 mL to 0.5 mL. The plastic filter Eppendorf tubes were replaced with 2 mL glass vials, a material that was far more agreeable with the droplets. The preparation of the droplets was left unchanged. In addition, the samples prepared in the glass vials were left to rest for at least 2-3 days. After 2-3 days, the liquids had phase seperated, with the labelled emulsions (pink) forming the floating top phase, and the water:glycerol solution forming the bottom phase. Then, the vials were centrifuged at 4500g in a swing bucket rotor to avoid heterogenous packing (Figure 4.17). The use of glass vials during sample preparation, combined with centrifugation in swing-bucket rotors rather than fixed-angle rotors, proved essential for achieving dense and uniform packing while minimizing the accumulation of emulsion droplets along the walls of the container. Finally, the packed droplets were scooped onto a coverslip bounded by an imaging spacer using a spatula to avoid inducing vortices and flows from drawing.

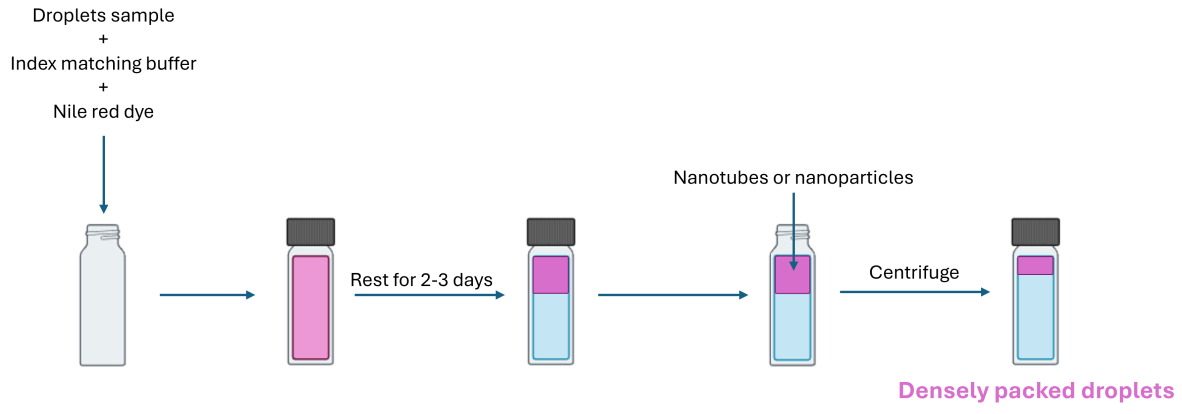

Figure 4.17: Optimized method of preparation of droplets: A panel of images showing the steps to prepare the optimized densely packed emulsion droplets representative of tissue-like material.

This protocol was confirmed to be optimal due to the thick "jelly-like" consistency after packing. Furthermore, imaging the prepared biophysical model showed strong deforma-

tions of the droplets from circular to polygonal shapes owing to the extensive shearing forces endured during centrifugation. This method also markedly reduced the dimensions of interstitial spaces. Finally, to achieve interstitial spaces approaching the dimensions oof the brain ECS, droplets of diameter 5 µm were used to prepare the biophysical model, resulting in a packing efficiency of 10% (Figure 4.18). Now, given that our preparation and imaging techniques were optimized, we once again characterize the dimensions of the optimized biophysical model.

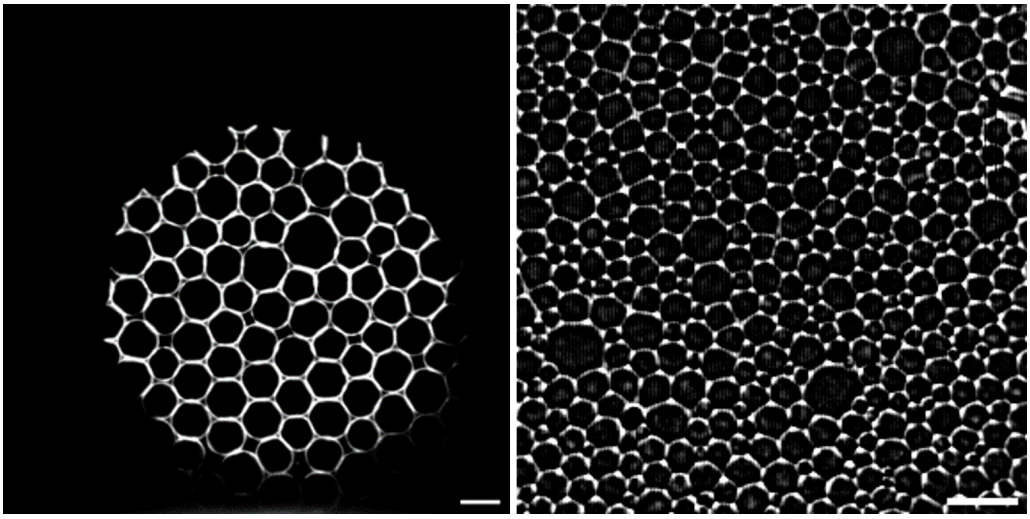

Figure 4.18: Optimized densely packed droplets: Optically sectioned widefield fluorescence images of densely packed droplets with optimized protocol clearly shows strong deformations in shape and sizes of the droplets. The representative images are of larger (10 µm) droplets (left) and smaller (5 µm) droplets (right). Size analyses revealed that the 5 µm droplets are ideal to achieve interstitial spaces in the order of the sizes of the brain ECS.

4.9 Characterization of local geometries

The high contrast images of the densely packed biophysical model shows almost a periodic pattern of triangular, voluminous voids or "chambers", that are interconnected by narrow channel-like passages or "tunnels". To understand the dimensions of these distinct geometries, these regions were now segmented by image thresholding on Fiji. Owing to the dense packing and therefore the small sizes of the interstitial spaces, it was not possible to reliably segment and retreiev physical dimensions from the image using methods described earlier in this chapter. The dimensions of the chambers were determined by inscribing a circle in each chamber, and the diameter of this inscription was considered as the characteristic dimension of the chamber. In case of the tunnels, the length of the tunnels were measured using a line scan. The mean dimension of the chambers was found to be $760 \pm 170nm$, and the mean tunnel length was $1.00 \pm 0.43\mu m$ (Figure 4.19).

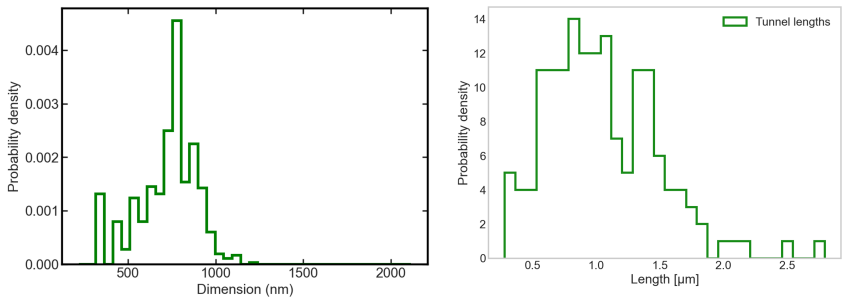

Figure 4.19: Characterizing the sizes of chambers and tunnels Optically sectioned widefield fluorescence images were segmented to extract chambers and tunnels independently. Using a circle fit into the 2D projections of the chambers, and a line scan on the tunnels, their dimensions and lengths were measured. The chambers had a mean dimension (diameter of the fitted circle) of $760 \pm 170nm$ (left), and the tunnels had a mean length of $1.00 \pm 0.43\mu m$(right).

To conclude, in this chapter we describe the methods and troubleshooting involved in assembling a tightly packed and labelled emulsion droplet system to form a biophysical model to study diffusion in ECS like complex environments. Additionally, we implemented the HiLo modality to have rapid high contrast optically sectioned images of the droplets. Finally, using these images we characterized the packing efficiency to be 10% and also the sizes of local microenvironments that we segmented as chambers and tunnels.

Chapter 5

Obstructed diffusion of nanoparticles in a liquid labyrinth

Having optimized the multimodal microscope to perform 3D SPT and HiLo of the biophysical method, as well as the preparation of the biophysical model and introduction of nanotubes into the sample, we were able to image and retrieve a large number of trajectories of diffusing single nanotubes in the biophysical structure. Together, about 2481 trajectories of the CCNTs and about 1564 trajectories of the uCCNTs were retrieved [157]. Most trajectories lasted from 2-5 s, however, we were also able to retrieve several trajectories that were upto 3 minutes long. An example each of a typical trajectory, and of a long trajectory are given below in Figure 5.1.

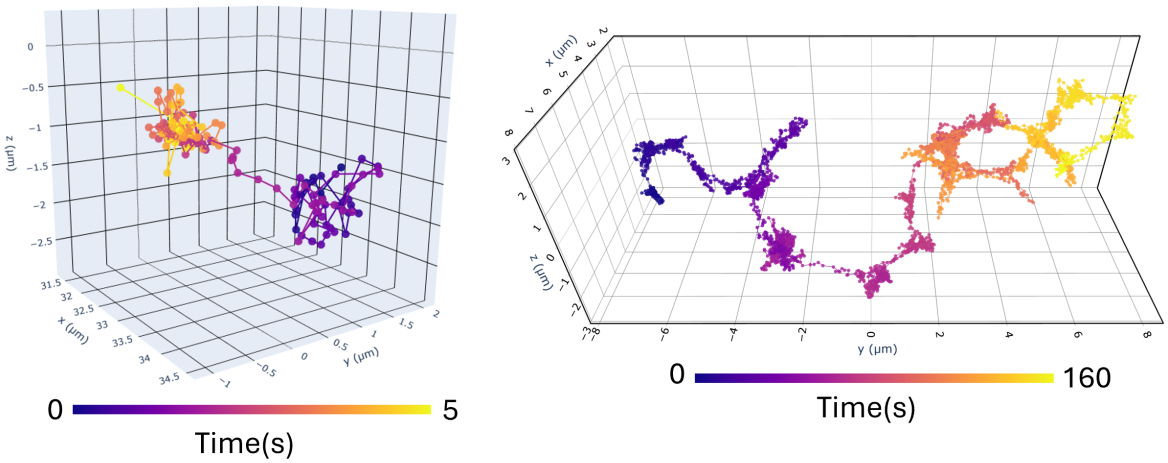

Figure 5.1: Visualisation of reconstructed 3D trajectories: A typical trajectory (left) and a long trajectory (right) of a single CCNT diffusing in the biophysical model.

Before we analyze the diffusive properties of single particle trajectories in the biophysical model, we first look at standard Brownian diffusion in simple bulk homogeneous liquid.

5.1 Ensemble diffusion in the biophysical model

5.1.1 Anomalous subdiffusive scaling of MSD

Having standardized and optimized the retrieval of diffusion analysis parameters (as shown in Chapter 3), we now analyze the trajectories of the nanotubes diffusing in the biophysical model. The simplest characterization of diffusion in the droplets structure was procured by the ensemble MSD. To maintain fidelity of the calculations, the MSD

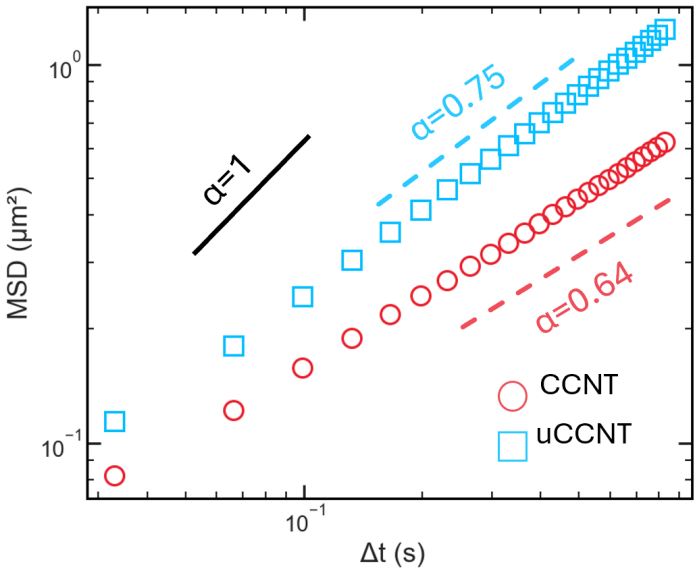

Figure 5.2: Mean squared displacement of CCNTs and uCCNTs in the biophysical model The ensemble MSDs of CCNTs and uCCNTs diffusing in the biophysical model reveals anomalous subdiffusion for both lengths of particles with the CCNTs experiencing a greater degree of subdiffusivity as compared to the uCCNTs.

was calculated only up to 25 time points in order to avoid biases by extremely long datasets which would otherwise dominate the diffusive properties especially at the longer timescales. The ensemble MSD clearly exhibits a subdiffusive scaling with time lag for both, CCNTs as well as uCCNTs (Figure 5.2). Such sublinear scaling denotes a subdiffusive exploration, *i.e*, the particles face hindrances in exploring their immediate environment through random walks (as discussed earlier in Chapter 2). The scaling exponent α was found to 0.75 in the case of the uCCNTs and 0.64 in the case of CCNTs delineating that the increased length of the nanotube increased the hindrances to diffusion it faced in the medium. Additionally, the sublinear nature of scaling even at very early timescales is evidently a reflection of the tightness of packing showing that the diffusing nanoparticles quickly encounter hindrances with minimal free diffusion time. The generalized diffusion coefficients were determined as K_α=1.43 ± 0.01 $\mu m^2/s^\alpha$ for uCCNTs and K_α=0.70 ± 0.01 $\mu m^2/s^\alpha$ for the uCCNTs and CCNTs respectively in the biophysical model. Due to the unconventional units of the generalized coefficients arising from the scaling exponent

here, it would not be entirely valid to compare the generalized coefficients of uCCNTs and CCNTs or to derive inferences from the same.

5.1.2 Anticorrelated dynamics reveal memory effects

Now, given the subdiffusive nature of nanoparticles in the droplets structure it is important to ascertain the source of hindrances, and more importantly how the hindrances are affecting the nanoparticle motion. For this, now we look again at the VACF (refer to Chapter 2), a quantifier that determines the tendency of a particle's motion to continue in the same direction, or for a reversal of direction in subsequent steps, or a completely random uncorrelated wall. The VACF of the uCCNTs and CCNTs both show a negative

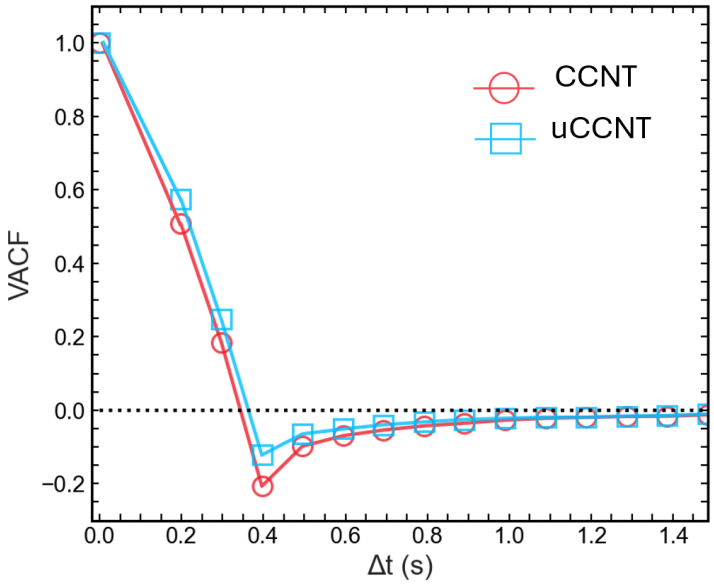

Figure 5.3: Velocity autocorrelation function of CCNTs and uCCNTs in the biophysical model: The VACF of CCNTs and uCCNTs diffusing in the biophysical model reveals strong anticorrelated steps as demonstrated by the negative dip before converging to uncorrelated steps over longer time scales. The CCNTs show stronger antipersistence in motion as compared to the uCCNTs in the biophysical model demonstrating a stronger hindrance to motion.

correlation in consecutive steps with time signifying that there is indeed a "pushback" or antipersistence from the medium. The extent of this antipersistence is stronger for the CCNTs as compared to uCCNTs, however interestingly, approximately between 0.4 to 1.0 s the negative autcorrelation relaxes back to zero in both cases (Figure 5.3). This relaxation time determines the timescale in which the steps no longer remain correlated.

5.1.3 Particle wall interactions skew Brownian statistics

Next, we look at the distribution of turning angles as a directional quantifier of the diffusive process. While brownian processes are truly random and explore homogeneously in all directions, structured environments often bear signatures of non-brownian statistics. Diffusing uCCNTs in the biophysical model showed a progressive right shift in turning angles with increasing time lag. Given that we measure the exterior angles of the vectors, persistence in transport, this right shifted distribution represents particles colliding against or "bouncing" against the walls. The systematic shift toward large turning angles reflects repeated wall-mediated deflections (Figure 5.4). In the case of the CCNTs diffusing in the biophysical model, we observe a stronger shift towards large turning angles as opposed to the uCCNTs. The stronger shift for CCNTs demonstrates that increasing particle length amplifies geometric frustration and the frequency of boundary interactions. Together, these observations strongly suggest that subdiffusive anomalous diffusion in the biophysical model arises from geometric frustration and are consistent with the obstructed diffusion model.

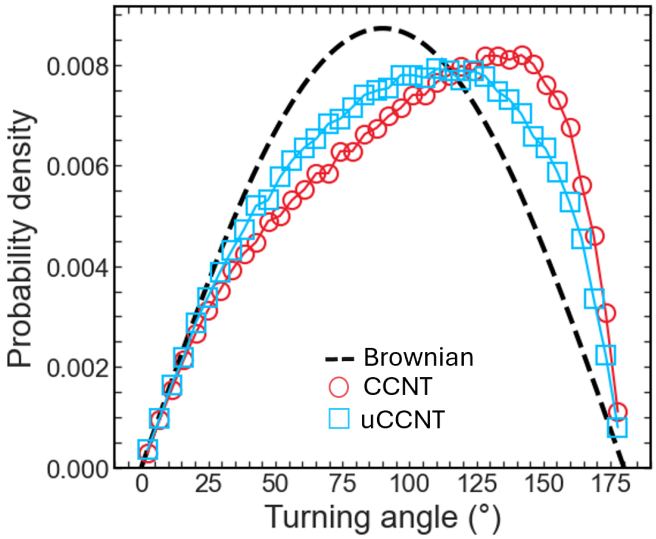

Figure 5.4: Distribution of turning angles of CCNTs and uCCNTs in the biophysical model: The distribution of turning angles of CCNTs and uCCNTs demonstrates the effects of collisions of the particles with the boundary walls seen as a right shifted distribution towards larger angles with respect to Brownian motion. The CCNTs show a larger degree of shift due to more frequent collisions with the boundaries.

5.1.4 Non-gaussianity validates obstructed diffusion

Finally, we look at the non-gaussian parameter (NGP) as a quantification of the evolution of the shape of trajectories over time. As discussed earlier, the NGP acts as a strong discriminator of stochastic processes, especially for recognizing diffusion models of

obstructed diffusion models from fractional brownian models. Figure 5.5 demonstrates the sustained and increasing non-gaussianity of diffusion shape in the biophysical model with the non-gaussianity increasing more sharply for the CCNTs as compared to uCCNTs. The decreasing non-gaussianity in early time scales is attributed to the nearly free exploration of the local environment at early time lags. In comparison, the nanotubes exploring isotropically in a brownian liquid quickly decay and converge to strongly gaussian statistics, as demonstrated by the low non-gaussianity. Three-dimensional fractional Brownian motion (FBM) trajectories with $\alpha = 0.7$ were generated to serve as a reference or baseline for subdiffusive dynamics. For each trajectory, displacements over increasing lag times were computed and used to evaluate the non-Gaussian parameter (NGP) from ensemble-averaged second and fourth displacement moments. This serves as a benchmark for identifying non-Gaussian behavior in the experimental data.

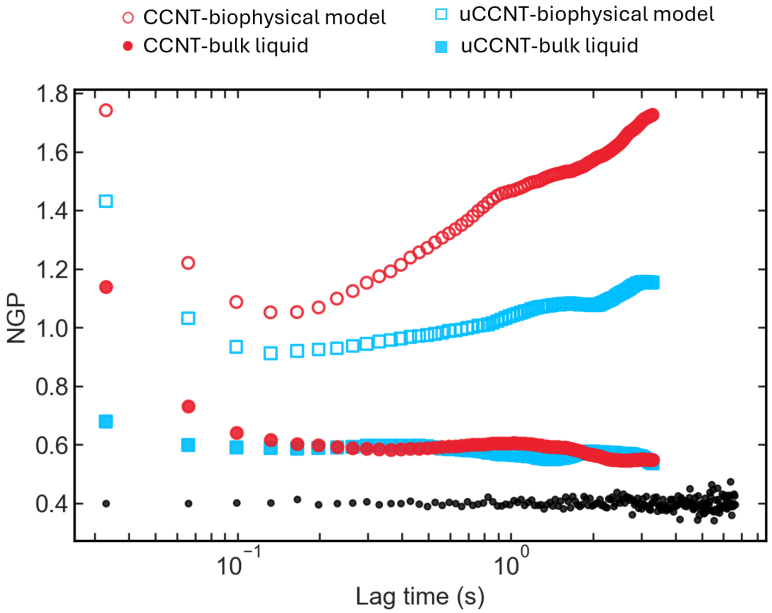

Figure 5.5: Non-Gaussianity parameter of diffusing nanotubes: The NGP of nanotubes diffusing in Brownian fluid (filled markers) and in the biophysical system (hollow markers) displayed strong divergences. The CCNTs and uCCNTs diffusing in the biophysical model show strong non-gaussian behaviors. CCNTs and uCCNTs diffusing in Brownian liquid however quickly converge to gaussian statistics. The NGP of a simulated fractional Brownian system has been shown as a reference.

5.2 Geometric characterization of the interstitial space

While so far, we have studied the ensemble properties of SPT in our biophysical model, we next look at statistics of individual particle diffusion. To this end, we first look at the MSDs of individual long trajectories. The individual MSDs of long trajectories were investigated for both uCCNTs and CCNTs which clearly resolved three distinct

dynamical regimes of diffusion. Figure 5.6 shows the MSDs of a single long trajectory of each uCCNT and CCNT. The diffusion curve, at short timescales, both lengths of nanotubes show nearly Brownian diffusion. At intermediate timescales, both uCCNTs and CCNTs show subdiffusive exploration with the subdiffusivity being much stronger in the case of CCNTs. At longer timescales, both lengths of nanotubes regain their diffusive ability due to long scale explorations. Such three regime diffusion mechanisms is consistent with literature, exhibiting near linear growth in the first regime or early timescales, followed by sublinear or near plateau-like behavior in the second regime, and finally, near linear growth again indicating free diffusion at longer time scale (∼1s) [36]. These diffusion properties are not reflected in the ensemble averaging simply due to the variance in particle size as well as size of the local environment explored.

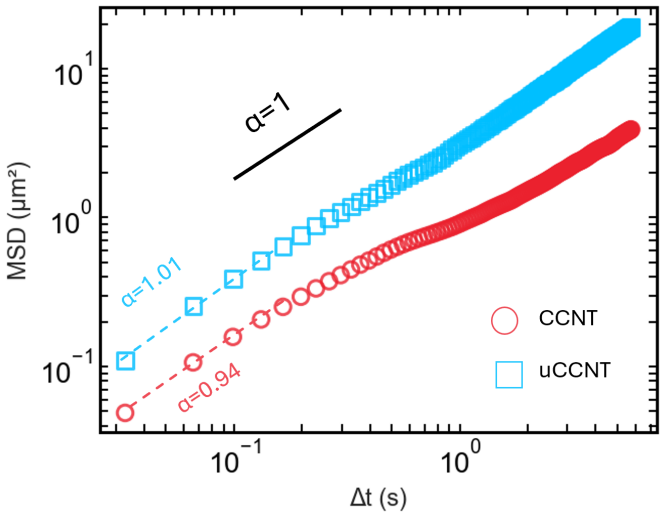

Figure 5.6: MSDs of single long trajectories: The MSD of single long trajectories of nanotubes diffusing in the biophysical model reveals a three regime transient trapping phenomena with strong subdiffusivity at intermediate time scales.

Additionally, when individual CCNTs and uCCNTs were imaged for long timescales in the range of 1 to 3 minutes, we were able to retrieve the network structure of the interstitial regions of the biophysical model clearly outlining two distinct geometries being explored 5.1. Interestingly, the projection of these long trajectories also resembled the interstitial shapes as visualized by the optically sectioned images of the packed droplet structure (Figure 5.7). Given the clear demarcations in geometries visually as well as analytically, we next look at the segmentation and characterization of the interstitial spaces by geometry.

5.2.1 Segmentation and characterization of the interstitial space from trajectories

To study the physical dimensions of local geometries explored by the nanoparticles, the trajectories were first segmented manually using the CloudCompare software. Two primary geometries were considered, the first being voluminous zones called *chambers* which are typically bound by the packing of generally four droplets. The second primary geometry are long channel-like structures that we named *tunnels* which are formed at the interface of three droplets (Figure 5.7). The entry and exit of the chambers and/or tunnels were evaluated as the point at which the tunnel first reaches the minimum width. Tunnels and chambers that had truncated trajectories were not used in this analysis. Typically, the overall structure is made of alternating chambers and tunnels with the tunnels acting as connectors between consecutive chambers.

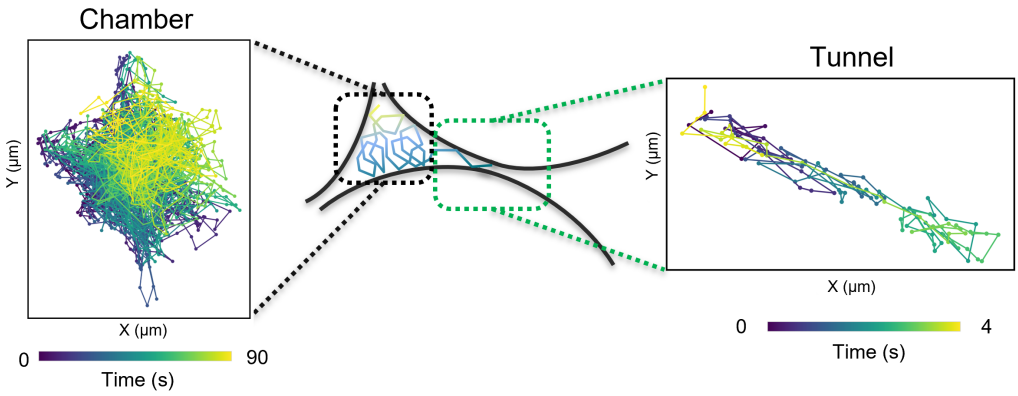

Figure 5.7: Segmentation of interstitial spaces into chambers and voids: The interstitial spaces between the droplets show two distinct local environments, that are, the voluminous regions called chambers and the narrow passages called tunnels.

5.2.1.1 Size characterization of chambers

The sizes of the chambers were estimated using convex hulls. For this, each segment of the trajectory representing a chamber was fitted using a convex hull. A convex hull is defined as the smallest polyhedron (or polygon in 2D) that encloses a given set of points (Figure 5.8). For each trajectory segment corresponding to a chamber explored, the convex hull of the localizations was computed, and its volume was used as an estimate of the accessible chamber size. Then, the distance from the centroid of the localizations to each face of the hull was calculated. The mean of these distances from the centroid to the face of the hull defines the characteristic dimension of the chambers. The distribution of this characteristic dimension was plotted for both CCNTs and uCCNTs and compared with the dimensions retrieved from the optically sectioned images of the packed droplets

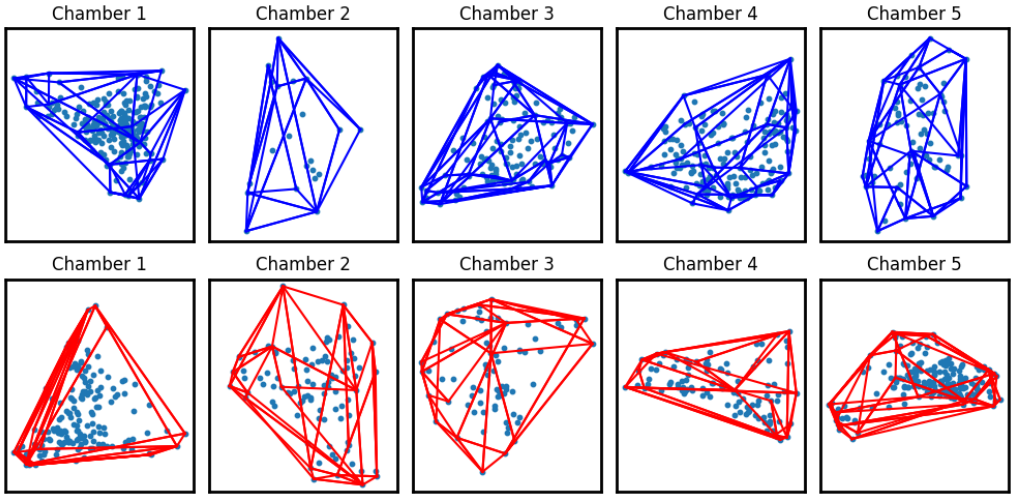

Figure 5.8: Examples of convex hulls with the CCNTs and uCCNT: The chamber trajectories were fitted with convex hulls to determine a characteristic dimensions. A panel of example fitted convex hulls have been shown for the CCNTs (below, red), and uCCNTs (above, blue).

5.9. The distribution of dimensions of the chambers shows a median dimension of 640 ± 290 nm when measured from CCNT trajectories, 860± 330 nm from uCCNT trajectories, and 760 ± 170 nm from segmentation of the HiLo images (Figure 5.9).

5.2.1.2 Size characterization of tunnels

Next, the dimensions of the tunnels were characterized. The radius was calculated using Principle Component Analysis (PCA) based ellispoid fit. First, each segment of the trajectory representing a tunnel was fitted with an ellipsoid. The radius of the tunnel was calculated as the geometric mean of the two semi-minor axes. That is, for an ellipsoid with axes represented by a, b, c, with a being the longest axes, the radius was determined as $r = \sqrt{bc}$. For a section of the ellipsoid representing an ellipse, the area is given by $A = \pi ab$, the case $a = b = r$, representing a circle. As such, the equivalent radius is considered to be geometric mean of the two semi-minor axes. The distribution of tunnel radius provides a median radius of 70 ± 20 nm with the CCNT trajectories and 110 ± 30 nm with the uCCNT trajectories (Figure 5.10). From the same fitted ellipsoids, the complete major axis a was used to calculate the tunnel length. This was further compared to the length as measured by line scans on optically sectioned images on Fiji. The median length of the tunnels was found to be 990nm with a standard deviattion of 440 nm from optically sectioned images. The median length from trajectories of CCNTs was found to be 900nm with a standard deviation of 420 nm, and from trajectories of uCCNTs it was found to be 1140nm with a standard deviation of 620 nm (Figure 5.10 right).

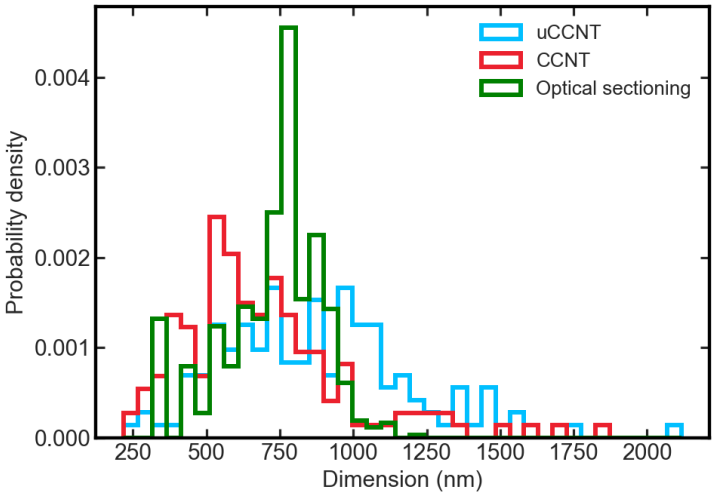

Figure 5.9: Size characterization of the chambers: The sizes of the chambers were measured for the trajectories by fitting convex hulls into each chamber segment, and twice the mean distance from the centroid of the hull to the face of the hulls is considered as the dimension of the chamber. The median distribution of chambers as measured by CCNT and uCCNT trajectories were 640 ± 290 nm and 860 ± 330 nm. For optically sectioned images, the chambers were thresholded from the image and a circle was inscribed into it, the diameter of this fitted circle defines the dimension of the chamber. The median dimension retrieved for the HiLo iamges was 760 ± 170 nm

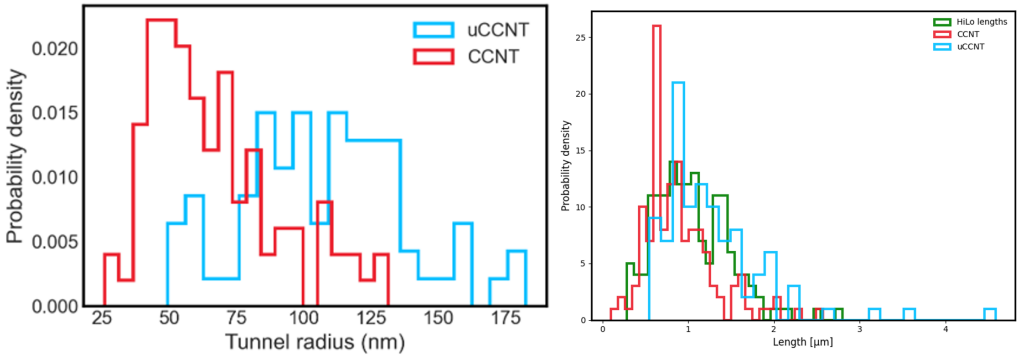

Figure 5.10: Size characterization of the tunnels: The radii and the length of the tunnels were retrieved by an ellipsoid fit with the geometric mean of the two smallest semiminor axes representing the radius. The lengths were defined by the length of the major axes. For the optically sectioned images, the length was measured using a line scan on thresholded images.

5.2.2 Local geometry governs diffusion of nanotubes

This segmentation also now enables a topology-resolved analysis, allowing the dynamical behavior of particles to be probed in relation to the local structural constraints of the environment. Following this classification, the MSD and turning angle distributions were computed independently for trajectories within each topology, providing insight into how confinement and connectivity influence transport.

5.2.2.1 Diffusion in Chambers

Within chambers, the MSD of uCCNTs exhibits an initial regime of near-linear growth with time, characteristic of quasi-Brownian motion in a relatively unconstrained space. This regime persists up to approximately 330 ms, beyond which the MSD transitions to a sublinear scaling. This crossover reflects the finite size of the chambers: at short timescales, the nanotubes explore their immediate surroundings with minimal hindrance, while at longer timescales, repeated interactions with the chamber boundaries and local

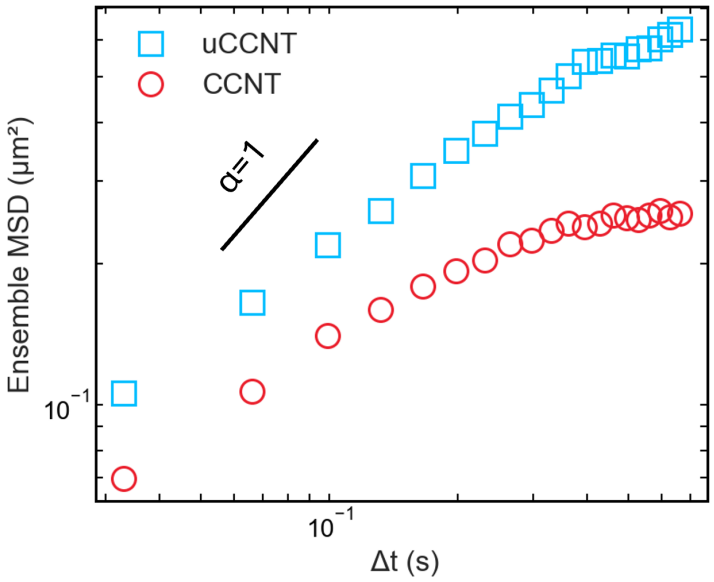

Figure 5.11: Mean squared displacement of nanotubes in the chambers: The ensemble MSD of the uCCNTs in the chambers reveals near Brownian exploration at early timescales suggesting a regime of exploration before interactions with bounding walls whereas the CCNTs show hindered diffusion even at early timelags due to their length. At longer timescales, the diffusion of uCCNTs is hindered and turns subdiffusive while for the CCNTs, the diffusion gets severely hindered as represented by the plateau delineating a transient trapping in the chambers.

crowding effects increasingly restrict their motion (Figure 5.11). In line with this, the turning angle distributions for uCCNTs are close to Brownian at the shortest time lag ($\Delta t = 1$), indicating largely uncorrelated step directions during the initial exploration

phase. However, at longer time lags ($\Delta t = 10$ and $\Delta t = 25$), the distributions exhibit pronounced shifts toward larger turning angles, reflecting frequent directional reversals consistent with interactions with confining boundaries. Correspondingly, the progressive bias toward larger angles highlights the growing influence of geometric confinement on particle trajectories(Figure 5.12).

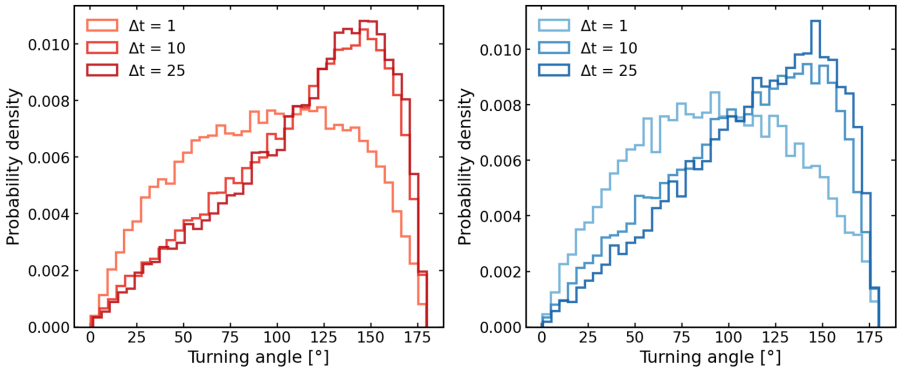

Figure 5.12: Distribution of turning angles of CCNTs(left) and uCCNTs(right) in the chambers The distribution of turning angles at short timescales show nearly isotropic diffusion in the chambers with a slight shift towards larger angles seen in the CCNTs. At larger timescales, both CCNTs and uCCNTs see a strong shift towards large angles demonstrating the confining properties of the boundary walls of the chambers.

In contrast, long CCNTs display significantly different dynamics within the same chamber environments. Their MSD is already sublinear at short timescales, indicating that their motion is hindered even during the initial exploration phase. This behavior can be attributed to their extended geometry approaching the dimensions of the chambers, which enhances steric interactions with the surrounding structure and reduces their ability to reorient freely. At longer timescales (around 200 ms), the MSD approaches a plateau, suggesting transient trapping or localization within confined regions of the chamber. This plateau-like behavior indicates that the nanotubes repeatedly revisit the same spatial region, consistent with strong geometric constraints and limited escape pathways. The turning angle behavior further supports this interpretation, as the enhanced probability of large-angle reorientations at increasing time lags reflects persistent encounters with structural boundaries.

Overall, these observations highlight the interplay between particle geometry and environmental topology: while chambers provide relatively open spaces that permit initial free exploration for uCCNTs and sublinear exploration for CCNTs, the onset of confinement effects, and extent of confinement and trapping are strongly modulated by the size and shape of the diffusing object.

5.2.2.2 Diffusion in tunnels

Now, when we look at diffusion through the tunnels, the MSD alone suggests nearly Brownian transport for both particle lengths (Figure 5.13). While this suggests equivalent explorations in the tunnels by the two sizes of particles, the differences in the distribution of tunnel radii already suggest distinct mechanisms in traversing the tunnels (Figure 5.10). With regard to this, we will see below, a more detailed picture emerging from the distribution of turning angles from the tunnel regions. These statistics reveal qualitatively that distinct transport mechanisms occur depending on particle length.

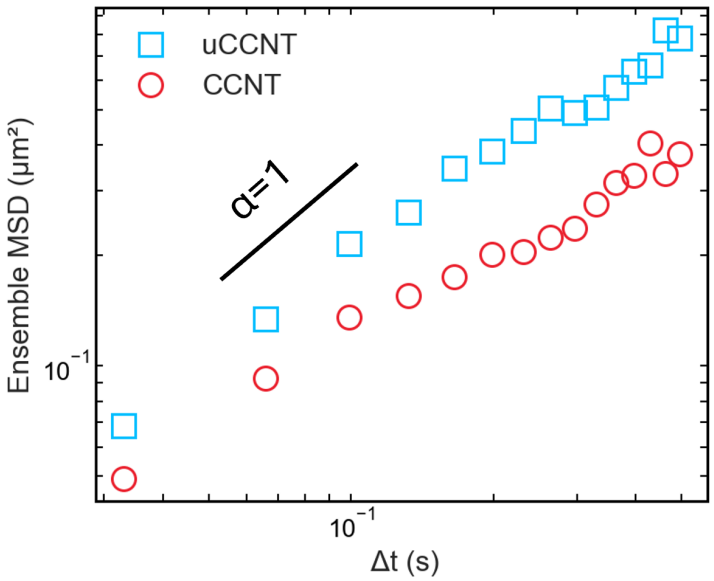

Figure 5.13: Mean squared displacement of nanotubes in the biophysical model The ensemble MSD of the CCNTs and uCCNTs reveal that both lengths of particles show a near linear growth in the tunnels.

For long CCNTs, the turning angle distribution evolves from an approximately Brownian-like distribution at early time scales ($\Delta t = 1$) toward a clear bimodal distribution at longer time lags ($\Delta t = 25$). This bimodality is characterized by pronounced peaks at small turning angles, corresponding to persistent forward motion along the axis of the tunnel, and at large turning angles, indicative of antipersistent, reversal-like steps. Such a distribution reflects a coupling between particle orientation and the tunnel geometry, where motion becomes effectively constrained along the tunnel axis, leading to alternating sequences of aligned (forward) and anti-aligned (backward) displacements. This behavior suggests that long CCNTs experience a form of geometrically induced guidance, where confinement promotes directionality and quasi-one-dimensional transport along the tunnel (Figure 5.14 left).

However, such a bimodal signature is absent for diffusing uCCNTs. While their turning angle distribution is almost Brownian at the shortest time lag ($\Delta t = 1$) reflecting the

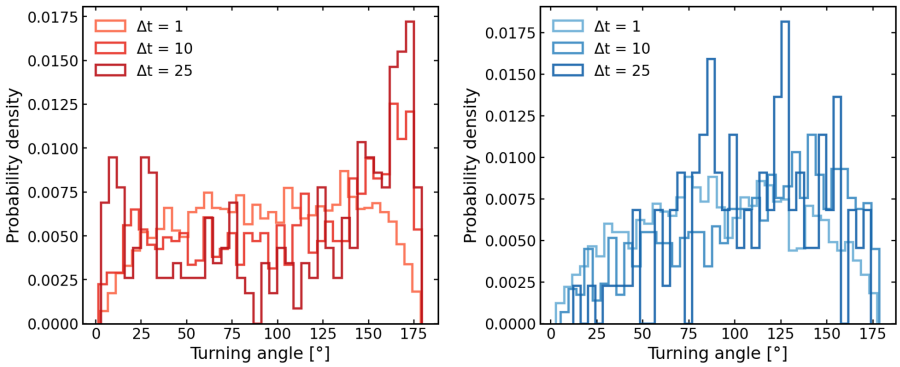

Figure 5.14: Distribution of turning angles of CCNTs (left) and uCCNTs (right) in the tunnels: While at early time lags both CCNTs and uCCNTs show nearly isotropic exploration within the tunnels, the distribution of turning angles diverges significantly at long timescales between the two lengths of the particles. For the CCNTs (left), the distribution progressively turns bimodal signifying aligned and antialigned motion along the tunnels representing a forward and backward exploration. The uCCNTs on the contrary show an exploration ridden with frequent collisions with the walls of the tunnel as demonstrated by the right shift in the distribution.

smaller size more easily exploring its surroundings, it progressively shifts toward larger angles at longer time lags ($\Delta t = 10$ and $\Delta t = 25$), indicative of increasing antipersistence as it encounters the boundaries. This trend reflects frequent interactions with the tunnel walls, leading to repeated directional reorientations and loss of directional memory, essentially reducing their diffusion in a manner that they do not "see" the shape of the tunnel (Figure 5.14 left). Unlike long CCNTs, the motion of the uCCNTs do not experience strong alignment with the tunnel axis. Instead, their motion remains comparatively isotropic within the tunnel geometry, with wall collisions dominating their trajectory evolution.

These observations demonstrate that particle length plays a central role in determining how geometric frustration is resolved within confined, anisotropic environments. While uCCNTs explore the tunnel space in a largely isotropic manner, continuously perturbed by boundary interactions, long CCNTs adapt to the confinement by aligning with the tunnel axis, effectively converting geometric constraints into a mechanism for guided transport. This distinction highlights that similar MSD scaling can arise from fundamentally different microscopic dynamics, highlighting the importance of the application of other statistical measures, such as turning angle distributions, in fully characterizing diffusion in complex environments.

5.3 From local to global transport

5.3.1 Distribution of escape time from chambers

Transient trapping and confinement act as a bottleneck for local exploration to transcend into long range transport. To better understand this process, we studied the distribution of escape times, defined as the duration a particle remains within a chamber before exiting through a connecting channel. Experimentally, this corresponds to the temporal length of a trajectory segment confined within a chamber prior to escape.

Importantly, the escape time serves as a key link between local and global transport. While MSDs and turning angles characterize how particles explore a given chamber, the escape time quantifies how quickly they transition between compartments [83]. As such, it captures the scaling of influence from short scale diffusion to long range diffusion as the escape time and mechanism acts as a bottleneck between local and global diffusion.

Escape times, denoted as τ_{long} and τ_{short} for long CCNTs and uCCNTs respectively, were extracted from a statistically significant number of independent events across 150 chambers and 148 chambers, respectively. By looking at the distribution, we obtain the complete picture of variability arising from differences in local geometry, connectivity, and particle–boundary interactions Figure 5.15). Strikingly, despite an approximately tenfold difference in nanotube length, the ratio of escape times scales relatively weakly, with $\tau_{long}/\tau_{short} \approx 1.4$.

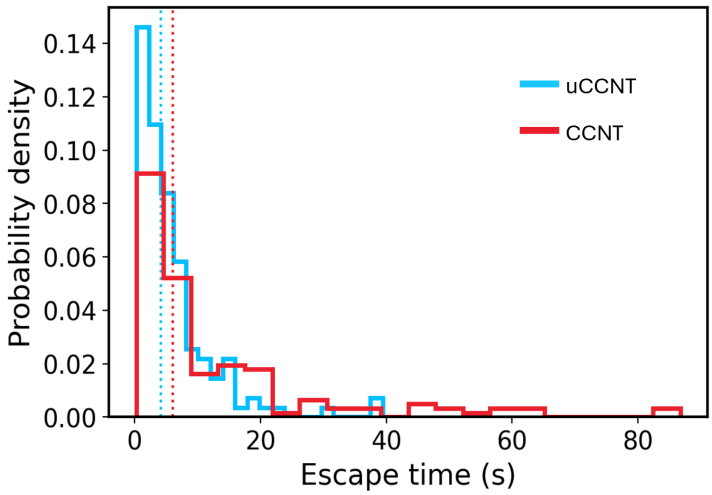

Figure 5.15: Escape time distribution of nanotubes from the chambers: The distribution of time taken by the CCNTs and uCCNTs to escape from the chambers reveals that the median escape time (represented by dotted lines) scales weakly with length (~ 1.4)

We then verified the statistical validity of our analysis. For this, we used a bootstrap resampling procedure (N = 100,000) to account for the finite sampling heterogeneity

of chambers. Bootstrapping is a statistical resampling technique in which datasets are repeatedly sampled with replacement to estimate the confidence intervals. This analysis yields a 95% confidence interval of [1.04, 1.85], with a median value of 1.38 (Figure 5.16). The confidence range reinforces the conclusion that the observed ratio is statistically valid and reflects an intrinsic property of transport in this system.

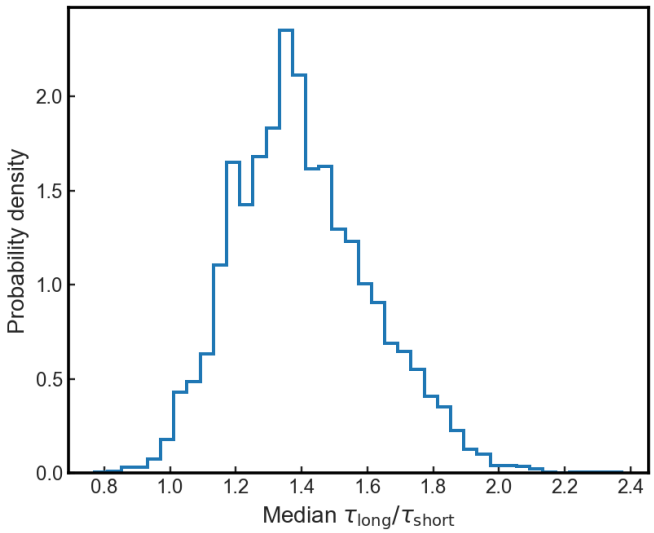

Figure 5.16: Bootstrap sampling of escape time ratios: A boostrap resampling method was used to achieve the confidence intervals of the median of escape time ratios of the CCNTs to the uCCNTs and was found to be [1.04, 1.85] with a median of 1.38

The weak dependence on particle length is somewhat counterintuitive given the pronounced differences observed in their local dynamics, particularly the stronger confinement and alignment effects exhibited by long CCNTs [78, 158]. The result suggests that while particle geometry significantly alters how motion occurs within a chamber (as reflected in MSD and turning angles), the overall timescale required to locate and traverse an exit is only weakly affected.

5.3.2 Simulating Brownian escape of anisotropic particles

To understand theoretical predictions on the diffusive escape of anisotropic molecules in the context of my work, we next quantitatively compared our experimental results to a simple analytical framework derived by Doi and Xu [81], which describes the Brownian escape of anisotropic, needle-like particles from a confined concave region through a narrow opening. In their model, they propose escape mechanisms of anisotropic particles is achieved in two distinct regimes, namely a free phase, in which the particle explores the chamber with full translational and rotational freedom, and a capture phase, in which one end of the particle enters the opening, significantly constraining its rotational degrees of freedom [158, 159]. The relative contribution of these two phases depends strongly on

the particle length relative to the chamber dimensions.

For long CCNTs, the lengths of the particles are comparable to the size of the chambers that they explore. Thus, escape is dominated by the captured phase: one end of the nanotube encounters and is captured by the opening. Once engaged, the particle's dynamics is governed by slow reorientation under strong geometric constraints [80]. As a result, the escape process is no longer limited by free exploration but by the dynamics within this rotationally restricted configuration. Accordingly, the escape time for long CCNTs can be expressed by the following derived expression as modeled by Doi and Xu:

$$\tau_{\text{long}} = \frac{2VL}{3\sqrt{3}\,a^2 D_t} \tag{5.1}$$

wherein V is the volume of the chamber, L is the length of the nanotube, a is the radius of the escape opening, and D_t is the translational diffusion coefficient.

On the other hand, for uCCNTs, whose lengths are much smaller than the chamber dimensions, escape is primarily governed by the free phase. These particles explore the chamber more isotropically, with weaker coupling between their orientation and the geometry, although boundary interactions still play a role. In this case, escape is predominantly dependent on searching for and locating the opening but without the strong rotational trapping characteristic of long CCNTs. The escape time τ_{short} is therefore described by (as earlier shown in Chapter 1):

$$\tau_{\text{short}} = \frac{V\left(1 + \frac{4aLD_r}{9D_t}\right)}{2\pi D_t\, a\left(1 + \frac{L^2 D_r}{6D_t}\right)} \tag{5.2}$$

where D_r is the rotational diffusion coefficient. The translational and rotational diffusion coefficients themselves are described by the following equations:

$$D_t = \frac{k_B T}{3\pi\eta L}(ln(p) + X_T(p)) \tag{5.3}$$

and

$$D_r = \frac{k_B T}{3\pi\eta L^3}(ln(p) + X_R(p)) \tag{5.4}$$

where k_B is the Boltzmann constant, T is the absolute temperature, η is the fluid viscosity, and p is the aspect ratio of the particle. The terms $X_T(p)$ and $X_R(p)$ account for finite length corrections.

Substituting the equations for the translational and rotational diffusion in the escape time

equations, we derive an escape time ratio τ_{long}/τ_{short} that can be analytically written as follows:

$$\frac{\tau_{\text{long}}}{\tau_{\text{short}}} \approx \frac{\left(L_{\text{long}} \ln\left(\frac{2L_{\text{short}}}{d}\right)\right)\left(\frac{L_{\text{long}}}{a}\right)}{L_{\text{short}} \ln\left(\frac{2L_{\text{long}}}{d}\right)\left(1+\frac{4L_{\text{short}}}{a}\right)} \tag{5.5}$$

where L_{long} and L_{short} represent the length of the CCNTs and uCCNTs respectively (measured using Atomic Force Microscopy, see Chapter 1) [51], a is the escape radius determined as the radius of the tunnels as observed by the uCCNTs, and d is the diameter of the nanotubes. The ratio of escape times between the CCNTs and uCCNTs were estimated using a Monte Carlo parameter sweep of the analytical model derived above. Parameters were randomly sampled from experimentally constrained ranges ($L_{long} = 200-1000nm, L_{short} = 30-150nm, a = 70-270nm$) with distributions centered on their respective mean values. The diameter was fixed at d=3nm. For each realization, the escape time ratio was computed, and a total of N=10000 samples were generated. The resulting distribution of escape time ratios was skewed with a tail towards large ratios. The median ratio was 10.19 with a standard deviation of 8.6, much higher than the values found experimentally.

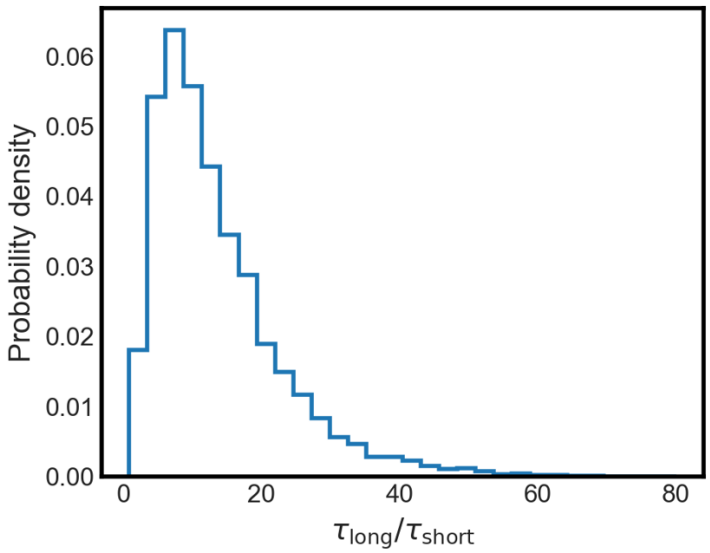

Figure 5.17: Monte Carlo parameter sweep of escape time ratios: A Monte Carlo parameter sweep of the analytical equation derived (Equation 5.5) results in a near linear tenfold increase in escape time for a tenfold increase in particle length, for a Brownian escape.

This prediction stands in stark contrast to our experimental observations, where escape times increase only weakly with particle length despite a tenfold difference in length (Figure 5.17). Thus, we cannot address this discrepancy completely using the translational degrees of freedom allowed for a rigid rod. Instead, the results of escape times point to an additional mechanism that penalizes the CCNTs less for the increased length.

We hypothesize that confinement and funneling induces a geometric frustration of rotational dynamics, which alters the escape mechanism. For uCCNTs, this manifests as frequent wall interactions, however, maintaining quasi-isotropic motion. For long CCNTs, however, confinement promotes alignment with the tunnel axis, effectively reducing the hindrance to escape. This alignment induced by geometry mediated orientational frustration facilitates entry into and traversal through tunnel openings, thereby mitigating the expected slowdown associated with increased particle length. Thus, the weak scaling of escape times, along with the distribution of turning angles observed in both chambers and tunnels, points to interplay between particle geometry and environmental structure.

5.4 Rotational diffusion explains anisotropic escape

To directly probe and confirm the orientational mechanism underlying transport of the nanotubes, we performed Single Particle Orientation Tracking (SPoT) on long CCNTs, which enabled us to simultaneously track the position in 2D and orientation in 3D using dipole spread function (DSF) engineering [52].

Due to their characteristic 1D shape, CCNTs and uCCNTs act as emitting dipoles along the nanotube's longitudnal axis, whose direction can be used to retrieve their orientation. The orientation of these dipoles can be mathematically written as a unit vector as follows:

$$\mu(\theta, \phi) = [\mu_x, \mu_y, \mu_z]^T = [sin\theta cos\phi, sin\theta sin\phi, cos\theta]^T \tag{5.6}$$

where z is the optical axis, θ is the polar angle and ϕ is the azimuthal angle.

In order to extract the instantaneous three-dimensional orientation (θ, ϕ) together with the two-dimensional position (x, y) of individual CCNTs along diffusive trajectories in real time, we implement a radially and azimuthally polarized (raPol) microscope operating in the SWIR regime. The method is based on a widefield single molecule epifluorescence configuration, in which circularly polarized excitation is used and the emitted fluorescence is analyzed in the back focal plane (BFP) of the objective using polarization-resolved detection.

The BFP is relayed onto an intermediate optical plane where a vortex half wave plate converts radially and azimuthally polarized emission components into two orthogonal linear polarization states [160, 161]. A polarizing beam splitter then separates these components, generating two distinct images that are projected side-by-side onto an InGaAs camera (Ninox, Raptor Photonics), enabling single CCNT detection in the SWIR spectral range.

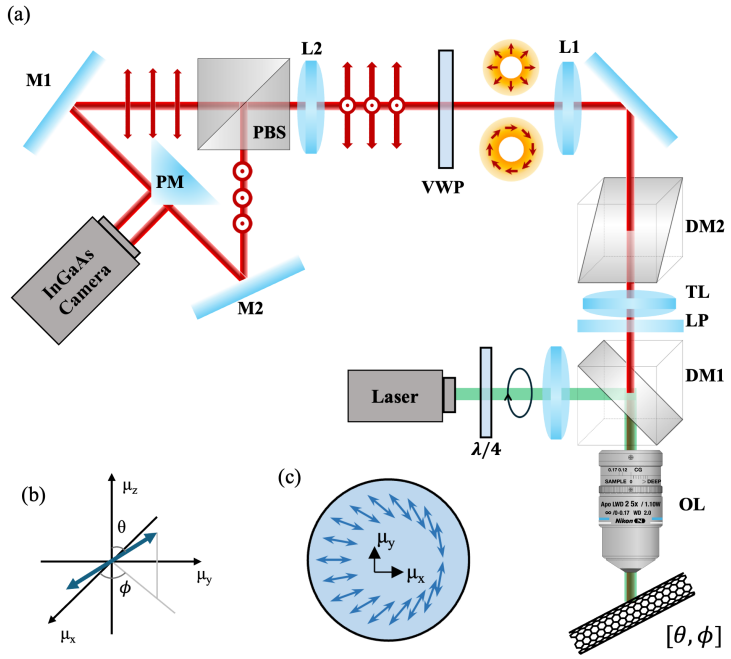

Figure 5.18: Single particle orientation tracking microscopy setup A schematic representation of the SPoT microscopy setup used to study orientations of diffusing nanotubes (Adapted from [52])

The two resulting images contain the information about the emitter orientation. An emitter oriented close to the optical axis primarily contributes to the radial channel, whereas an emitter lying in the transverse plane produces diffraction spot patterns in the azimuthal channel that exhibit a characteristic bilobed DSF. In this case, the orientation within the imaging plane is given by the line connecting the two intensity maxima. For an arbitrary orientation, both detection channels contribute simultaneously, encoding complementary information about the emission pattern. By jointly analyzing the intensity distribution across both channels and the shape of the resulting diffraction patterns, the full 3D orientation together with subdiffraction localization of individual CCNTs can be retrieved. Figure 5.19 shows the DSF of a single CCNT diffusing in the droplets (visualized using whitelight).

However, this method is sensitive to inherent abberations of the optical assembly. Experimental DSFs differ from the exact theoretical DSFs. Thus, in order to account for all possible abberations and distortion, a vectorial phase retrieval method is used to retrieve the birefringent distribution at the pupil plane (BDPP). By using immobilized SWIR active spherical 100 nm diameter AuNPs and a nonlinear optimization algorithm, we can extract the experimental BDPP.

The 3D orientations and 2D localization of single CCNTs were retrieved using the deep learning technique Deep-SMOLM [52, 162]. Briefly, based on the experimental BDPP retrieved, about 2000 simulated images were used as training for the neural network. Each

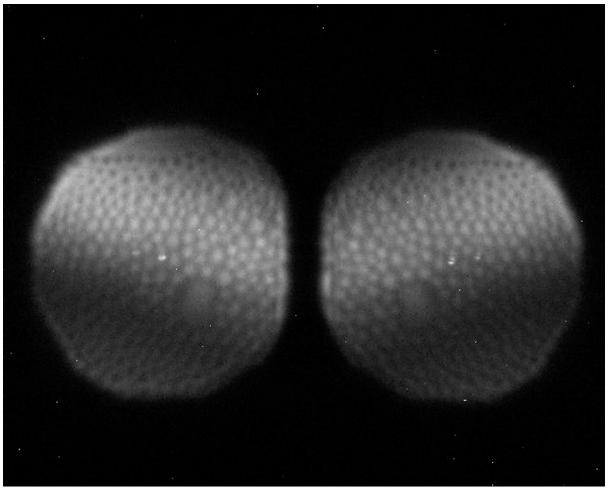

Figure 5.19: DSF of a single CCNT using SPoT microscopy Representative images of single CCNT DSF on two side-by-side images. The CCNT is diffusing in the packed droplets structure as visualized in whitelight.

training image contained 5-10 CCNTs with randomized 2D position, 3D orientations and emitter intensities with signal to noise ratios matching experimental conditions. The focal plane position was varied over a range of z $\sim$ [-500nm, 500nm]. The emitter intensities were set to follow a Poissonian distribution with Gaussian noise. Additionally, uniform background noise and Poissonian noise was added to the images.

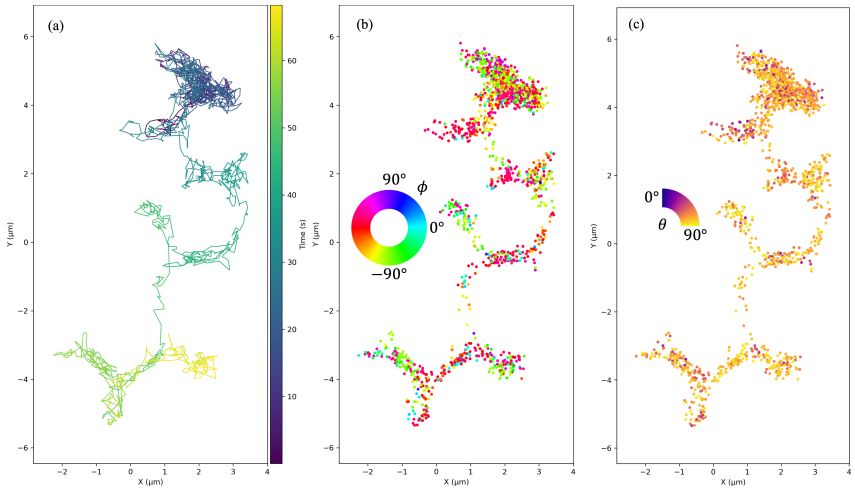

Figure 5.20: Representative trajectories of single CCNT A long trajectory of a single CCNT diffusing in the biophysical model shows a. diffusion in time (color scale in seconds) b. the in-plane angle ϕ and c. polar angle θ

Given that diffusion in our 3D biophysical model chambers and tunnels extend beyond the focal plane, particles frequently diffuse along the axial direction. This limits the number of trajectories exploring multiple chambers and tunnels. Despite this experimental constraint we were able to obtain orientational data from both chambers and tunnels from SPoT measurements consistently. We segmented 14 tunnels and 17 chambers which

proved sufficient sampling to resolve distinct rotational dynamics across the two environments. A single long trajectory of a CCNT diffusing in the droplets structure is visualized in Figure 5.20.

5.4.1 The mean square angular dispacement

To quantify rotational dynamics, we computed the mean square angular displacement (MSAD), defined as:

$$MSAD(\Delta t) = 4D_r\Delta t \tag{5.7}$$

where D_r is the rotational diffusion coefficient. The extracted values reveal a strong suppression of rotational motion within tunnels ($D_r = 0.4rad^2/s$), compared to significantly higher rotational freedom in chambers ($D_r = 1.4rad^2/s$). This pronounced reduction in D_r directly indicates orientational hindrance imposed by the anisotropic confinement of the tunnels, consistent with the alignment effects inferred from turning angle statistics (Figure 5.21).

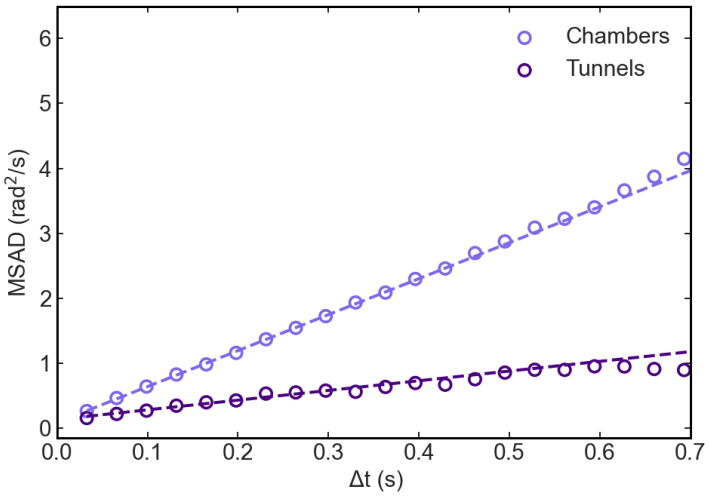

Figure 5.21: Mean squared angular displacement of CCNTs: The MSAD of the CCNTs in the chambers and tunnels show a marked difference in the rotational rate clearly demarcating the strong rotation hindrance suffered by the CCNTs in the tunnels.

5.4.2 Local geometry influences orientational memory

To further characterize orientational memory, we evaluated the reorientation time correlation function (RTF):

$$RTF(\Delta t) = Se^{\frac{-\Delta t}{\tau}} \tag{5.8}$$

where S is a constant, Δt is the time lag, and τ represents the characteristic timescale of orientational memory. Here, the RTF is a measure of how quickly an anisotropic molecule loses it's memory of orientation. In chambers, the RTF decays continuously, indicating that CCNTs progressively lose memory of their initial orientation due to relatively unconstrained rotational diffusion. In contrast, within tunnels, although a slight initial decay is observed, the correlation rapidly reaches a plateau, demonstrating persistent orientational memory over extended timescales. The initial decay is attributed to the narrow degree of rotational freedom allowed inside the tunnel. The plateau behavior, on the other hand, reflects confinement-induced stabilization of particle orientation, consistent with alignment along the tunnel axis (Figure 5.22).

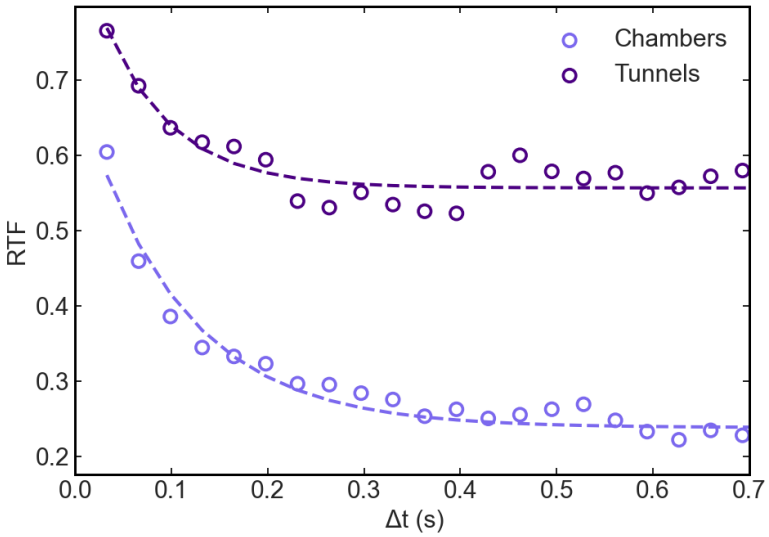

Figure 5.22: Reorientation time correlation function of CCNTs: The RTF of CCNTs diffusing in chambers shows a decaying curve representing the quick reorientation and thus loss of memory of early orientations. However, in the tunnels despite early decay, the curve quickly plateaus demonstrating the persistence in directionality maintained in line with the tunnel axis with a small "wiggle room".

5.4.3 Alignment induced escape of CCNTs

To compare orientation across the two distinct regions, we introduced a circularly normalized azimuthal orientation parameter. For each chamber or tunnel, the azimuthal angle distribution was recentered by subtracting its mean orientation, effectively setting the local preferred direction to zero. The angles were then wrapped to a common interval (-90° to 90°), and the normalized distributions were pooled across all regions to yield a centered angular distribution, denoted ϕ. This is done in order to remove geometric biases while preserving relative alignment, given that different chambers (and tunnels) are oriented in different directions. The resulting distribution shows strong orientational alignment in tunnels, in contrast to the nearly isotropic angular distribution observed

in chambers. This provides us with direct experimental evidence of geometry induced alignment. In the chambers, the rotation of the CCNTs allows for attaining all available orientations almost in an isotropic manner. When fitted with a Lorentzian, we retrieved a SD of 67°. Furthermore, we also observe three minor peaks at 60°, 0°, and -60° in an almost uniform distribution, suggesting that these peaks are geometrically relevant preferred angles and related to the triangular shape of the confining chambers. In the tunnels, the distribution takes the form of a narrow Gaussian peak centered at zero with a SD of 17°, implying the strong alignment of the nanotubes to the axis of the tunnels. Here, we find that the width of the distribution of angles in the tunnels determines small orientational shifts or "wiggles" as the nanotubes traverse the tunnels (Figure 5.23).

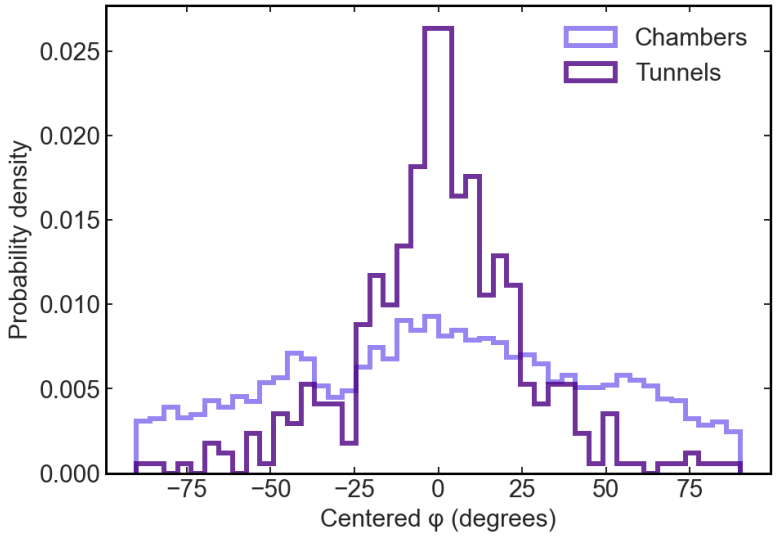

Figure 5.23: Normalized distribution of azimuthal orientations of CCNTs: The normalized distribution of the azimuthal orientations in the chambers and tunnels reveals a strong orientational conformity in the tunnels. Whereas in the chambers, the particles explore the full spectrum of angles to orient themselves in.

In comparison, while we could orientationally resolve the rotational as well as translational diffusion of the CCNTs, SPoT measurements could not resolve the orientations of uCCNTs in the same environment. Due to their small size, uCCNTs undergo extremely rapid rotational diffusion, with a characteristic timescale of ∼0.002 ms, much below the camera integration time (33ms) required for SPoT acquisition. As a result, their orientation effectively averages out within a single exposure, and the recorded PSF corresponds to an average projection over the acquisition window rather than a well-defined orientational signature, thus disallowing for reliable retrieval or interpretation of nanotube orientation. For long CCNTs, however, the characteristic rotational diffusion timescale (∼12 ms), combined with the subdiffusive constraints imposed by the environment, ensures that their orientation evolves slowly enough to be captured within the acquisition window, enabling accurate reconstruction of orientational dynamics.

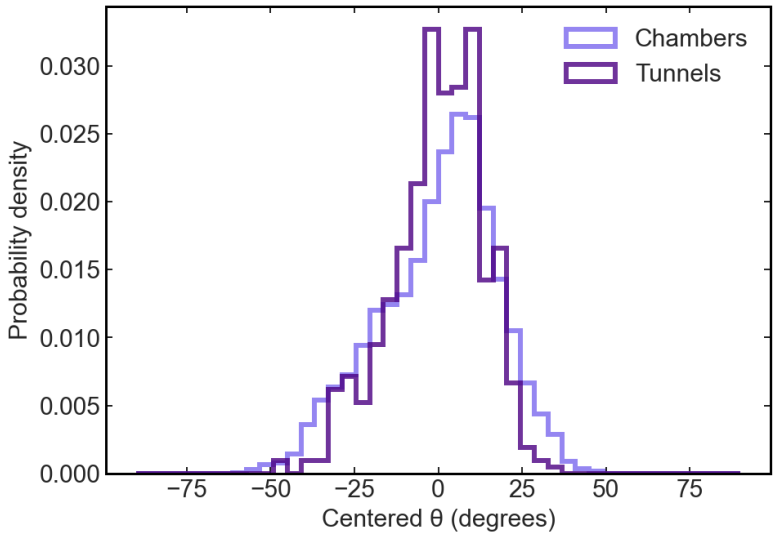

Figure 5.24: Normalized distribution of polar orientations of CCNTs: The normalized distribution of the polar orientations in the chambers and tunnels reveals an almost equal and narrow spread of the orientations. This validates our notion that for SPoT which allows for 2D localization and 3D orientations, the tunnels and chambers explored need to be in the focal plane.

In contrast to the azimuthal orientations, the cicularly normalized polar orientation parameter displays equivalent distribution in both the chambers and the tunnels. Additionally, both distributions show a narrow distribution, which when fitted with Gaussian curves yielded a SD of 17° and 13° for the chambers and tunnels respectively (Figure 5.24). This validates that for SPoT microscopy in 2D with 3D orientations, the particles were diffusing and explored in-plane chambers and tunnels.

Taken together, SPoT analysis reveals that long CCNTs experience significant rotational frustration within confined geometries, particularly in tunnels where orientational degrees of freedom are strongly restricted. Importantly, this orientational frustration due to the bounding walls of the chamber is not purely inhibitory, instead, it enhances alignment of nanotubes with the tunnel axis during transiently trapped states potentially through a funneling effect [80]. Such prealignment facilitates escape along preferred directions, which in turn effectively lowers the expected scaling of escape times with particle length. In contrast, uCCNTs, which lack such orientational coupling, rely on rapid diffusion and frequent boundary interactions, resulting in escape dynamics involving stochastic exploration and efficient spatial sampling or a simple "search and exit" rule. These findings provide direct experimental confirmation that geometry induced alignment is a key mechanism enabling efficient transport of elongated particles in complex, confined environments. Rather than just impeding transport, confinement reorganizes diffusion mechanisms depending on the length of the particle, allowing efficient escape and promoting connectivity between local compartments and global transport across the system

through funneling effects. The manuscript of this work has been submitted and is also available on ArXiv.

5.5 The effect of particle (an)isotropy on diffusion in the biophysical model: Preliminary results

While these experiments so far show the effect of length of the nanotubes on diffusion in complex convex environments, the true nature of particle anisotropy (or isotropy) in influencing diffusive processes has not yet been demonstrated. In this section, I have shown preliminary experimental results below.

For this, we next look at diffusion in the biophysical system with a more isotropic, spherical particle. To this end, after several attempts with various spherically shaped nanoparticles (quantum dots, Tetraspeck beads, etc), we settled on the HiQ Nano as the optimal choice of particles due to their isotropic shape and monodisperse size distribution. The particles are 25 nm in diameter.

We first determined the dimensions of the chambers as explored by the HiQ particles using convex hulls as before with the nanotubes. The resultant dimensions are in strong agreement with the sizes determined by the nanotubes as well as optically sectioned images, denoting that all particles explored similar geometries in the biophysical model(Fig. 5.25).

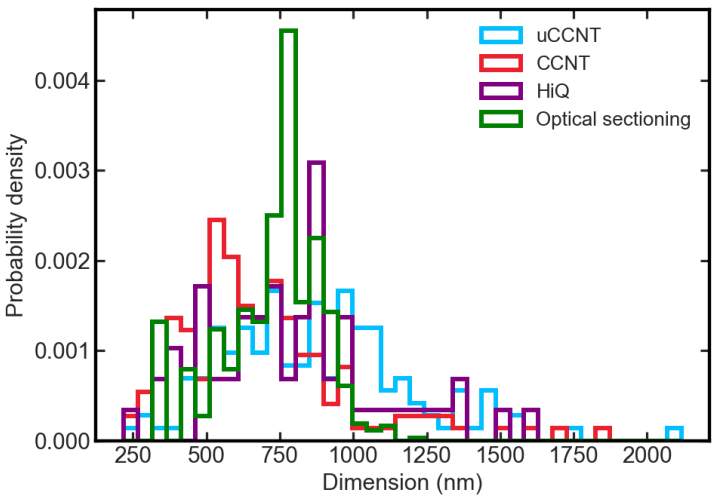

Figure 5.25: Chamber size characterization with isotropic HiQ nanoparticles: The sizes of the chambers were measured using the convex hull method as with the trajectories of the CCNTs and uCCNTs. The resulting dimensions were in close agreement with earlier measurements validating that the spherical particles also explored the same environments as the nanotubes.

5.5.1 Ensemble statistics of HiQ particles in the biophysical model

The ensemble averaged MSD of the HiQ particles were calculated against those of the nanotubes. The scaling exponent of the MSD was determined to be 0.57, below both the uCCNTs as well as the CCNTs. This reveals that the diffusion of the spherical particles is anomalous and subdiffusive. Furthermore, the diffusion is hindered more in the case of spherical particles than that of the nanotubes in the biophysical model (Figure 5.26).

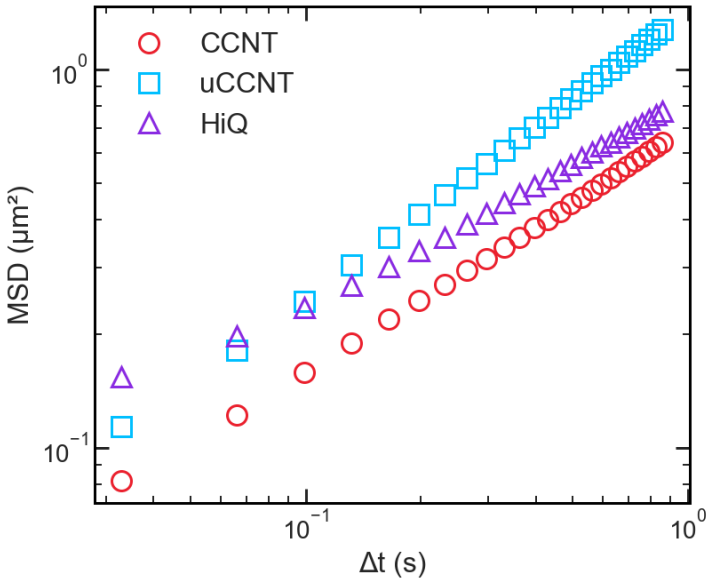

Figure 5.26: Mean squared displacement of spherical HiQ nanoparticles: The ensemble MSD was calculated and compared to those of CCNTs and uCCNTs showed that the scaling exponent $\alpha = 0.57$ is lower than both the CCNTs and uCCNTs signifying strong subdiffusivity.

Next, we look at the persistence of motion of the diffusive process of the HiQ particles in the biophysical model. Here again, the VACF displays anticorrelated steps taken by the HiQ particles, with the antipersistence being larger than both the CCNTs and uCCNTs (Figure 5.27). The negative correlation primarily demonstrates that the diffusion is still obstructed diffusion, and more importantly the interactions between the particles and the boundaries are strictly restricted to bouncing rather than binding or trapping through chemical interactions to the boundary (in these cases, the diffusion would no longer be obstructed diffusion but instead would demonstrate "stop and go" behavior that aligns with continuous time random walk with an uncorrelated VACF).

Finally, we complement the above results by looking at the distribution of turning angles of the HiQ particles. The distribution reveals a strong right shift of the angles, interestingly, stronger than both the uCCNTs and CCNTs (Figure 5.28). Apart from demonstrating the effect of the particle wall interactions and validating the antipersistence

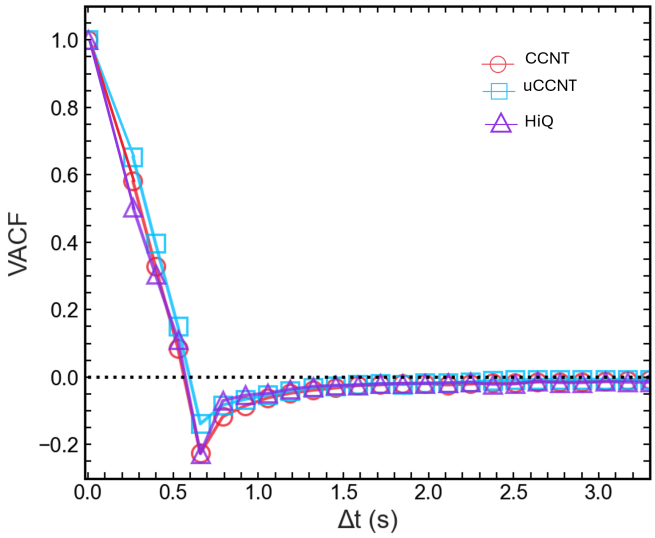

Figure 5.27: Velocity autocorrelation function of spherical HiQ nanoparticles: The VACF of HiQ particles shows strong antipersistence in it's steps on par with the CCNTs. The relaxation time to achieve uncorrelated steps is approximately the same for all three particles

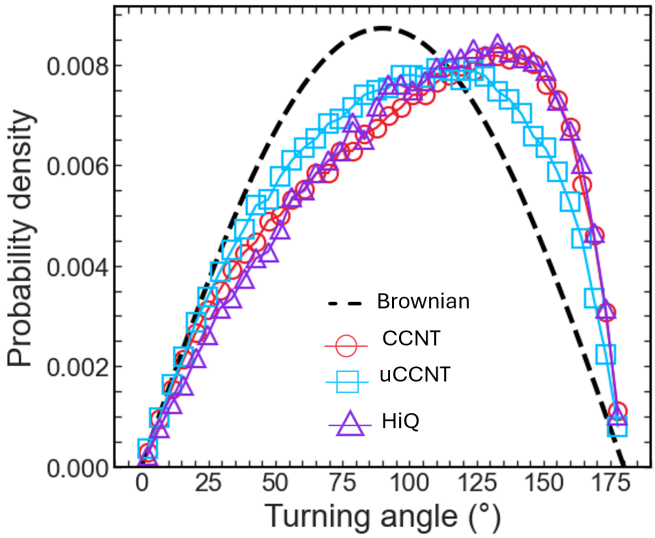

Figure 5.28: Distribution of turning angles for spherical HiQ particles: The turning angles distribution of HiQ particles shows strong shift towards higher angles on par with CCNTs and larger than uCCNTs denoting stronger interactions with the boundary walls.

behavior in the context of bounding walls, the increased right shift of the distribution also suggest that particles bounce back into the chamber, potentially being "contained" in the chambers rather than escaping quickly.

5.5.2 The effect of local geometry on diffusion of isotropic particles

Given the highly interesting nature of diffusion of isotropic particles in the biophysical model suggesting the increasing hindrance with respect to tracer isotropy, we consider the effect of the local geometry on diffusion statistics. As before, we segmented the trajectories into chambers and tunnels on CloudCompare. Due to the limited available data of this preliminary work, achieving clean statistics on the MSDs, especially in the tunnels was difficult. Instead, we looked purely at the distribution of turning angles at higher time scales (Δt =25) in comparison to those of the uCCNTs and CCNTs as shown in Figure 5.29 . A kernel density estimation was used to smoothen the curves to improve

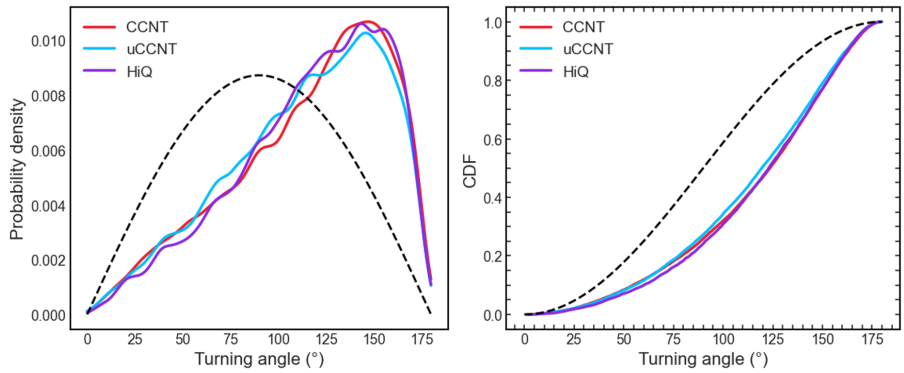

Figure 5.29: Distribution of turning angles of HiQ nanoparticles in chambers: The turning angle distribution of and cumulative distributive function of the HiQ particles and the nanotubes at $\Delta t = 25$ demonstrates the containing effects of the chambers and boundary walls.

visual representation. In the chambers, the distribution of angles show a strong right shift in all three types of particles indicating the confining effects in the chambers, which is also represented using the cumulative distribution function (CDF).

On the contrary, in the tunnels, the three types of particles engage in different modes of diffusion at these time scales (Δ t =25). As shown before, the CCNTs, which are long 1D particles, show a bimodal distribution with a back and forth motion aligned to the axis of the tunnels. The uCCNTs, representing the short 1D particles, follow a near homogeneous (slightly right shifted) diffusive search that is affected by frequent collisions against the bounding walls. Surprisingly, for the spherical HiQ nanoparticles, the distribution of turning angles is strongly right shifted signifying strong containment even within the

tunnels (Figure 5.30) which is to be further confirmed with larger statistics.

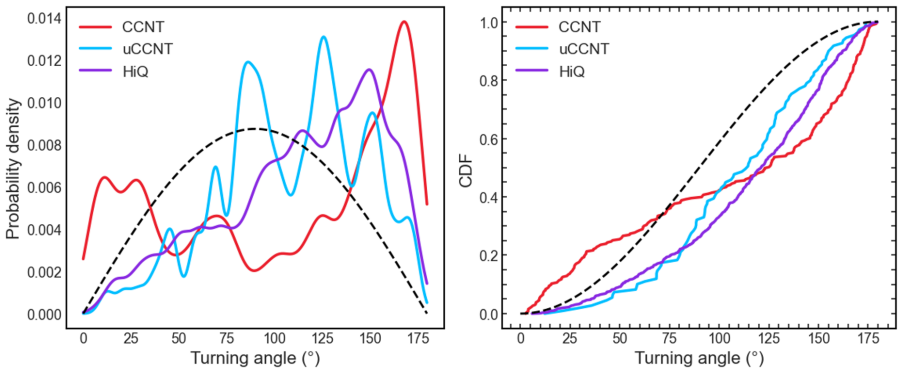

Figure 5.30: Distribution of turning angles of HiQ nanoparticles in tunnels: The turning angle distribution and the cumulative distribution function of the HiQ particles and nanotubes demonstrate varied mechanisms of traversing the tunnel at longer timescales ($\Delta t = 25$). The CCNTs as discussed before take an aligned approach to diffuse through the tunnels. The uCCNTs diffuse efficiently despite frequent collisions with the walls. The HiQ nanoparticles experienced much stronger hindrances as reflected in the strong right shifted angles.

To understand the transient nature of trapping, the trajectories were segmented as before into chambers and tunnels. The temporal residence length of trajectories in each chamber was analyzed to determine the escape time, and the distribution of escape times was plotted alongside the escape time distributions of the CCNTs and uCCNTs. It is interesting to note that the escape time of the isotropic particle was in fact slightly longer than that of both sizes of nanotubes, despite their lengths being about twice the diameter of the spherical particles (in case of uCCNTs) on the lower end and around twenty times the diameter of the particles as an upper bound (in case of CCNTs). These results alone suggest the importance of shape and not just the size of the particle with regard to diffusion in complex environments. Nanoparticle anisotropy would thus provide mechanistic advantages for diffusion in complex environments(Fig. 5.31).

In order to explain our observations, we suggest that the chamber's ability to contain particles via repeated collisions is far greater for isotropic particles as opposed to anisotropic particles, likely due to their ability to reorient themselves under confinement. We propose that the anisotropic particles due to wall mediated interactions and rotation constraints can align along the walls and towards the escape openings while isotropic particles collide with the bounding walls to be restricted to the chambers given their isotropic nature. Furthermore, one-dimensional particles exhibit anisotropic diffusion, with distinct diffusion coefficients along and perpendicular to the particle axis. In rod-like systems, the longitudinal diffusion is typically enhanced relative to the transverse component due to geometric constraints. As a result, alignment of the particle axis with an exit pathway can facilitate more efficient escape, in contrast to isotropic particles that explore config-

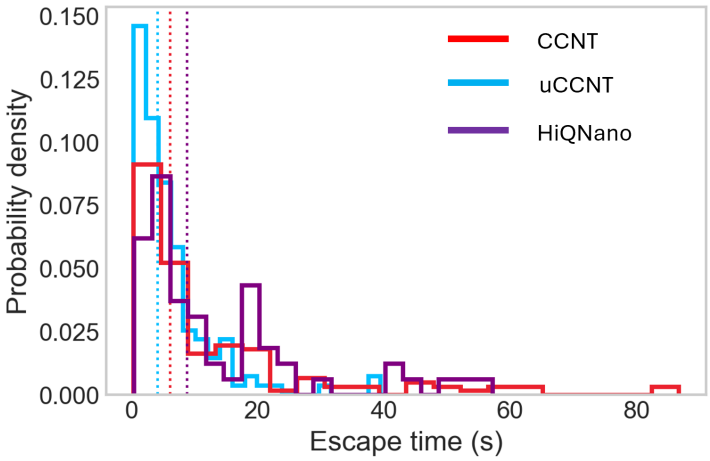

Figure 5.31: Distribution of escape times of HiQ nanoparticles: The escape time distribution of escape times of spherical particles as compared to CCNTs and uCCNTs showed the largest median time of escape demonstrating mechanistic advantages to anisotropic particles to diffuse in complex environments. The dotted vertical lines show the median escape time for each particle respectively.

uration space uniformly across all directions. More work will be needed to confirm the results and our hypothesis.

Chapter 6

Conclusion

In my work, I set up a multimodal correlative microscopy approach allowing for 3D-SPT in short-wave infrared window as well as high-resolution optical sectioning to achieve rapid high contrast images of the biophysical model approaching image qualities restricted to confocal microscopy. For optical sectioning, I implemented the HiLo system and optimized imaging and frequency filtering parameters to achieve background rejection and high contrast images with an axial sectioning of 500 nm. Using the double helix phase mask, we engineered the point spread function of single molecule emitters to achieve localization of the carbon nanotubes in 3D with an axial range of 6 µm. With this setup, we achieved a localization precision of under 10 nm in the lateral axes and under 20 nm in the axial direction at a wavelength above 1100 nm as shown in Chapter 3.

I have been able to optimally assemble and tightly pack emulsion droplets to form a biophysical model to study diffusion in complex soft matter environments. Next, I optimized and standardized the labelling of the droplets for optically sectioned images of the biophysical model which revealed interstitial geometries approaching typical sizes seen in the extracellular spaces of the mouse brain. Lastly, we tested the role of surfactants and identified the role of deoxycholate as a surfactant in tuning diffusion to the interstitial regions. With two distinct lengths of nanotubes differing by an order of magnitude, we investigated the effect of length in governing diffusion mechanisms in a complex environment. Finally, we also repeated these experiments with an appropriate isotropic particle to study the effect of particle shape on diffusion.

From the above experiments, we show that anisotropic particles with dimensions smaller than their surroundings undergo fast volumetric exploration, accompanied by frequent interactions with the confining boundaries, leading to highly efficient spatial sampling. At short timescales, their motion is effectively Brownian in nature, whereas at longer timescales, boundary interactions hinder isotropic exploration, giving rise to anomalous diffusion. Next, for the longer CCNTs, we showed that when the particle lengths approach

the characteristic dimensions of their local environment, spatial confinement strongly impacts diffusion even at short timescales, while still allowing efficient exploration. In this paradigm, escape from confined regions is facilitated by anisotropy of the particle, the particle frequently interacts with the boundaries that hinders rotation, this inturn prealigns the nanotube to the exit allowing quick exit. This causes a funneling effect which is reflected in the weak dependence of escape times on nanotube length. On the other hand, preliminary results indicate that isotropic particles, despite having small diameters, display exploration of their local environment that is strongly confined due to repeated collisions with the bounding walls which results in a containment effect where the particle is forced back into the chamber due to ballistic collisions. At short time scales this results in strong hindrance to the diffusion scaling.

Consequently, we identify geometric frustrations, arising from repeated wall-mediated collisions within a continuous, structured environment, is key to understanding anomalous diffusion and length-dependent escape dynamics of anisotropic particles. Furthermore, we infer that beyond the length of the particle, the shape or the anisotropy strongly influences diffusion in escape when compared to isotropic particles. In the absence of escape from binding or pore mediated escape, the convex architecture of interconnected chambers and tunnels suffices to provide for antipersistent and subdiffusive behavior that allow for rotational dynamics to dominate escape phenomena in nanotubes. On the contrary, isotropic particles that lack directionality then are penalized with stronger hindrances and trapping within chambers.

The anomalous transport of nanotubes however is not a result of strong trapping or persistent alignment, instead it emerges from navigating a heterogeneous environment via repeated collisions. These frequent boundary collisions and intermittent confinement progressively shape particle motion. Beyond this, the nanotube length dictates how this geometric frustration is resolved. Short nanotubes effectively combine the efficient, near-isotropic exploration associated with spherical particles with the orientational dynamics inherent to one-dimensional nanostructures. Consequently, they exhibit predominantly Brownian translational motion, while rotational diffusion is only transiently affected during collisions. Their escape is thus governed by first passage time dynamics which depends on the probability of reaching an opening through stochastic search. On the contrary, long nanotubes, wherein the dimensions of the particle are similar to those of the confining chambers, experience sustained rotational constraints. Their extended geometry then promotes alignment along available spatial directions, effectively pre-aligning them within tunnels and facilitating directional transport. Briefly, the interplay between the anisotropic nature of the particle and local architecture can enhance, rather than hinder, diffusion, giving rise to funneling effects driven by geometric effects. Thus, a particle that lacks these anisotropic and rotational dynamics does not gain any diffusive advantage and

therefore is penalized to remain trapped in the chamber for longer.

While the study here is restricted to a specific biomimetic system, the work has larger implications in the context of diffusion and transport of molecules in complex environments. Biomolecular activities in both intracellular and extracellular regions occur in complex, maze-like geometries with constrictions, trapping, and overall subdiffusive diffusion. Beyond the biophysical model, these findings may have broader implications for transport in heterogeneous environments. Biomolecular activity in intra- or extracellular spaces, filtration through porous materials, transport in crowded soft-matter systems, and heterogenous catalytic processes are all governed by hindered diffusion where confinement and topology can strongly modulate particle dynamics. By demonstrating that anomalous diffusion can be governed by funneling effects arising from the coupling between geometric constraints of the environment and particle anisotropy, we provide a physical framework for transport in complex systems, opening avenues for the design of materials and architectures with controlled diffusion properties.

Chapter 7

Perspectives

7.1 Novel single particle probes

7.1.1 Fluorescent worms

Beyond SWCNTs, recent work from the team of Chloe Grazon [163], on production of fluorescent polypeptide nanoparticles using a novel click chemistry based "Click'n ROPISA" (Ring-opening polymerization-induced self-assembly) technique have yielded ultrabright 1D nanoparticles using different fluorophores. Interestingly, given the soft matter components of the materials, the resulting nanoparticles are more "wormlike" than like rigid rods (like SWCNTs). Tunneling electron microscopy confirms their worm like shape and reveals a length of approximately 200 nm with a breadth of 10 nm. Fluorescence spectroscopy studies revealed such nanoparticles with Cy5 fluorophores (Cy5 NPs) continue to strongly maintain their spectral properties, with the added benefit that each nanoparticle has thousands of fluorophores, thereby with higher intensity per particle. This worm-like morphology, combined with exceptional brightness and photostable nature, make them an interesting probe to study diffusion of worms (as opposed to rigid rods) in complex soft matter.

Given the exceptional absorbance and brightness of the Cy5 NPs, as preliminary work, we imaged these particles at the single particle level. For this, we spin coated a dilute solution of the particles onto coverslip and imaged it under the microscope. The spincoating of particles ensures dispersion of particles in a homogeneous manner allowing for single particle detection.The particles were excited at 640 nm at a power density of $> 1kW/cm^2$. The particles were imaged on a ProEM EMCCD camera through a 698/70 bandpass filter. Their strong emission allowed us to localize individual Cy5 NPs below the diffraction limit (around 325 nm). Additionally, some of the images were further processed using deblurring by pixel reassignment (DPR) [151], a technique to improve resolution, which

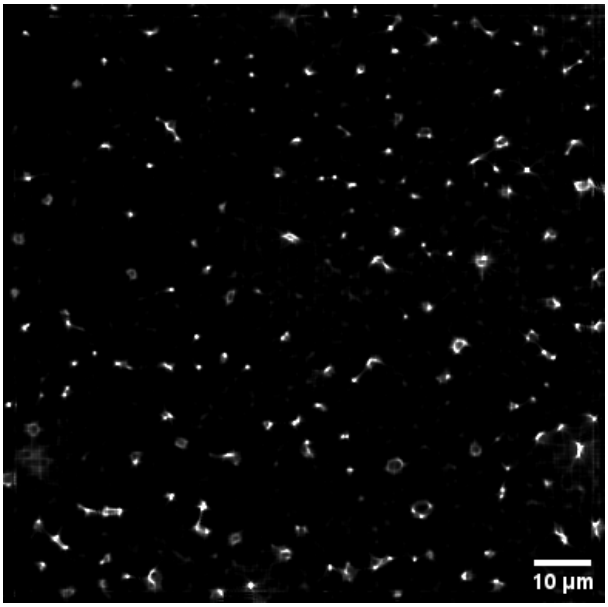

Figure 7.1: Single molecule reconstruction of Cy5 nanoparticles: High resolution reconstruction of Cy5 nanoparticles from a stack of images using deblurring by pixel reassignment (DPR) reveals the worm-like shapes of the particles.

reveals the worm-like morphology on optical microscopy. To further test their capacity as single molecule probes, we imaged them in a 1:1 water-glycerol solution to detect their diffusive motion. Using ThunderSTORM and home-built codes based on TrackPy we were able to superlocalize and reconstruct trajectories thereby tracking the diffusion of individual Cy5 NPs. The MSD obtained from around 200 of these trajectories yielded a linear increase ($\alpha = 1$), demonstrating Brownian motion as expected in a homogeneous and unrestricted fluid environment. Furthermore, using the known viscosity of water-glycerol solutions ($9.00 \pm 0.09 mPa.s$), we were able to calculate the diffusion coefficient of the particle to be $0.18 \pm 0.01 \mu m^2/s$. Applying the Stokes-Einstein relation, we were able to calculate the hydrodynamic radius of the particles to be $124 \pm 10 nm$. Finally, to understand the intensity characteristics of Cy5 NPs in the single particle regime for applications, we extracted the intensity distribution of about 2700 diffusing Cy5 NPs which resulted in a unimodal distribution with a median intensity of 752 photons detected per particle (Figure 7.2).

Given their aqueous and relative simplicity of "one-pot" synthesis coupled with their biological and biodregradable nature, Cy5 NPs will bridge the gap between molecular fluorophores and mesoscopic soft colloids. Combining NPs with suitable pairs of fluorophores, the particles have also shown to display FRET phenomena, exchanging energies between each other. Notably, their combination of brightness, deformability, and functionalizability positions them as promising tools for extending SPT probe toolbox. Their soft bodied nature could further allow them to interact with their surroundings in new ways leading to interesting viscoelastic behaviors with possible innovative escape-

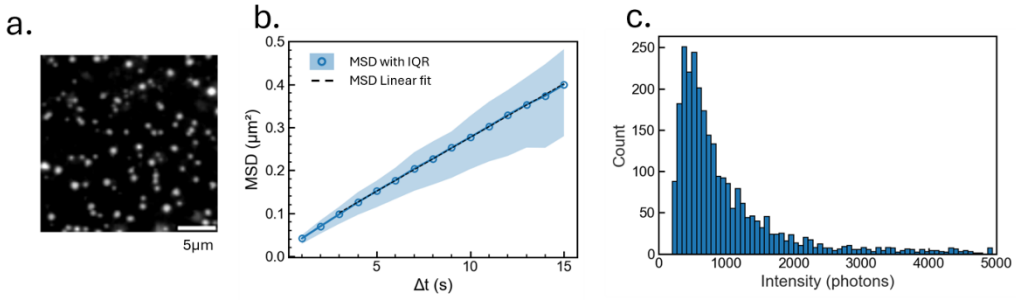

Figure 7.2: Single particle imaging and tracking: a. Representative image of Cy5 NPs dispersed on a coverslip. b. The ensemble averaged MSD of about 200 particles diffusing in a Brownian fluid shows normal diffusion with diffusion cefficient at $D = 0.18\mu m^2/s$ c. The distribution of intensities in photons of about 2700 single particles displays a median brightness of 752 photons (Adapted from [163]).

from-confinement mechanisms. Thus, worm-like Cy5 NPs synthesized using the Click'n ROPISA method are deemed to be excellent one-dimensional, soft, single particle tracers for studying biologically relevant regimes, including deep tissue environments and dynamically evolving soft matter systems, where both structural disorder and temporal fluctuations govern diffusive behavior.

7.1.2 Gold nanoparticles

Another direction of extending the palette of fluorophores is to assess the novel fluorophores or optically active nanoparticles in the infrared regime. As discussed previously through the thesis, the SWIR regime is an important spectral window signifying the range of wavelengths that show the least scattering as well as autofluorescence in biological tissue specimen. In this regard, gold nanoparticles (AuNPs) synthesized by the group of Xavier Le Guevel, have been shown to have unique photophysical properties in the SWIR and could be stabilized by RNA [164, 165].

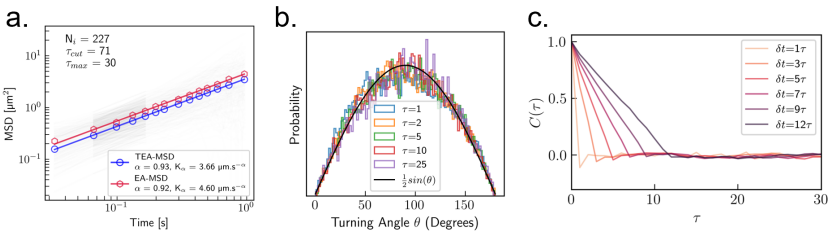

Figure 7.3: Brownian diffusion of AuNPs: Diffusing single AuNPs were tracked in 1:1 water:glycerol solution. a. The eaMSD and teaMSD both determine a nearly ergodic and Brownian motion. b. The distribution of turning angles across different time scales (given in terms of τ) displays distributions as expected for normal diffusion. c. The VACF calculated at varying time lags also confirms uncorrelated and therefore truly random steps with localization precision induced noise.

We first used AuNPs of 30-50 nm diameter, to study their diffusion properties in free solution of 1:1 water-glycerol. Due to their emission at around 1050 nm, it was also possible to track them in 3D using the phase mask we have in the setup. Their MSD showed a linear increase, confirming the Brownian nature of the particles. Additionally, the velocity autocorrelation as well as the turning angles also demonstrated uncorrelated Brownian behavior (Figure 7.3). Lastly, we introduced these particles into the packed droplet biophysical model. The complications arose when certain particles interacted strongly with the surface of the droplets, sticking indefinitely to them. This led to the complete immobilization of most of the AuNPs introduced. While other AuNPs diffused, the signal-to-noise and their fluorescence decay made localizing and reconstruction of trajectories challenging. However, it still remains a very promising candidate for a spherical probe in the SWIR for SPT objectives in tissue and tissue-like materials and further modifications of the particles would strongly influence their application in this field. Additionally, the size tunability of AuNPs would also make them an interesting control. The development of SWIR-active AuNPs continues through the ongoing collaboration between the two groups.

7.1.3 Nunchaku SWCNTs

So far, we have looked at the diffusion of spherical probes, ellipsoidal particles, and one-dimensional rigid anisotropic probes in both Brownian and complex (and sometimes biological) environments. Furthermore, studies on various filamentous systems, such as actin filaments and long SWCNTs, have revealed rich dynamical behaviors including continuous bending and reptation [58, 59]. In these systems, however, the deformation is distributed continuously along the entire length of the particle, making it difficult to isolate the role of bending itself in the overall dynamics.

To better understand the interplay between translational, rotational, and bending motions, it would be interesting to study particles that can bend at a single, well-defined location. A particle consisting of two rigid rods connected by a flexible joint would introduce a new degree of freedom, allowing the bending dynamics to be observed and quantified independently from the continuous flexibility seen in filamentous systems. Our collaborators, the group of Matteo Palma, have been able to realize such ”nunchaku” nanoparticles by joining two rigid rods together, creating a system that occupies an intermediate regime between fully rigid and continuously flexible particles. Working with our collaborators, we have been able to detect such particles formed by joining two SWCNTs through a molecular linker at their ends. While we have characterized these structures spectroscopically to confirm their chiralities and composition, single-particle tracking studies have yet to be performed (Figure 7.4). Exploring their dynamics could

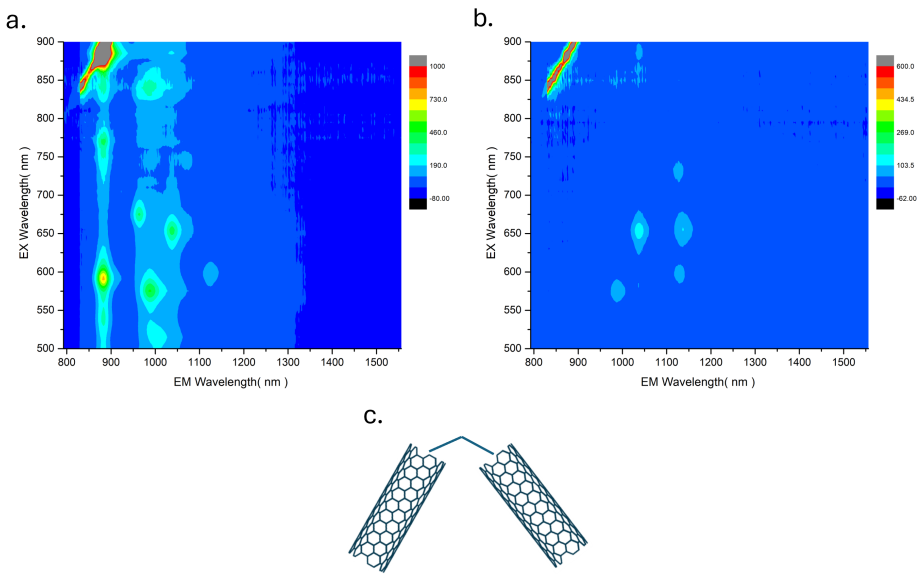

Figure 7.4: Photoluminiscence of PEG-junction SWCNTs The PL spectral maps of peg junctioned SWCNTs of a. (6,5) and b. (7,6) chiralities. c. Schematic representation of peg junctioned SWCNTs.

provide a unique opportunity to investigate how localized flexibility influences diffusion, potentially opening a new avenue for understanding the motion of anisotropic particles in complex environments.

7.2 Novel environments

7.2.1 Opallic structures

Tightly packed colloidal structures have already been shown to be interesting environments for studying diffusion [29]. Owing to their porous and confining geometry, the motion of particles is strongly influenced by the local structure they encounter. However, two factors that strongly distinguish packed silica opallic structures as compared to our packed droplets model. Firstly, the opallic structures are ”hard” structures giving rigidity to the walls as opposed to the droplets which are true soft matter environments with deformable walls. Previously, theoretical work has shown the variation in diffusion near soft or deformable surfaces [166], as such, it would be interesting to experimentally investigate diffusion in landscapes bounded by soft and hard material, independently. Another factor that is interesting to probe would be the homogeneity of the chamber sizes. Silica spheres are highly monodispersed as opposed to droplets. As a result, the opals formed from packing silica spheres form periodic strucutures with equidistant and equal sized chambers. Diffusion in periodic porous structures could yet unravel new understandings on mechanisms influencing the transition between nanoscale and micro to

macroscale diffusion.

Furthermore, compared to systems such as packed droplets or agarose gels, opal structures are composed of silica beads with rigid, non-deformable surfaces. This is an important distinction, as the nature of the confining boundaries can play a major role in determining diffusion statistics. The rigid surfaces of opals may therefore give rise to diffusive behaviors that differ from those observed in softer materials, where the environment itself can fluctuate, deform, or interact dynamically with the diffusing particles.

Additionally, the high monodispersity of the colloidal particles used to form opal structures results in a highly ordered, crystalline arrangement with pores that are nearly periodic in both size and spacing. Such a level of structural regularity is generally absent in complex soft matter or biological systems, which tend to exhibit greater disorder and heterogeneity. The presence of this periodic pore network provides a unique opportunity to investigate how ordered confinement influences diffusion and whether transport phenomena emerge that are not accessible in more disordered porous environments.

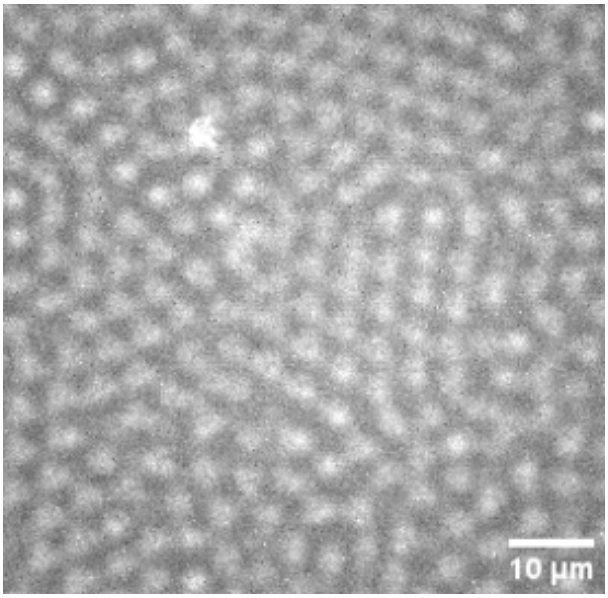

Figure 7.5: Single particle imagin of CCNT in opal Representative frame from a video displaying a CCNT exploring the interstitial network in an opal (seen as bright white spot)

By performing a series of washes with 2:3 water-glycerol mixture, followed by centrifugation, we have been able to pack $5\mu m$ diameter silica colloidal particles to form opals. Additionally, we were also able to introduce DOC coated CCNTs into the system and observe their diffusion (Figure 7.5). However, the experiments remain hard to replicate due to strong affinity of CCNTs (as well as other conventional nanoparticles), which resulted in the nanoparticles strongly "sticking" to the silica spheres rather than diffusing. As a result, we have been unable to extract the diffusive properties of CCNTs and uCCNTs in opal structures. However, efforts to mitigate these possible electrostatic interactions and

standardize such protocols in a reproducible manner continue.

7.2.2 Bottom up approach to building ECS environments

With the growing interest in the composition and function of the brain ECS, it would also be interesting to introduce crowding molecules and an analog of the extracellular matrix (ECM) into the system to mimic the dense and complex molecular environment present in the brain. This would be especially promising given that the sizes of the chambers and tunnels are approaching the sizes of ECS in brain tissues (Figure 7.6. Apart from brain tissues, structures closely resembling the chambers and tunnels influencing diffusion of single molecules have been demonstrated in the ECS of zebra fish embryonic tissues [167].

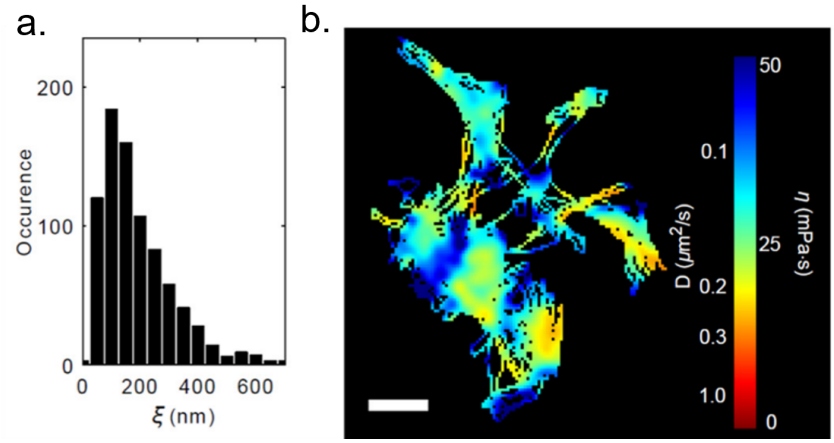

Figure 7.6: Heterogeneity in diffusion space and size in the ECS: a. Distribution of dimensions of the brain ECS b. Diffusion map in the brain ECS showing the heterogeneous diffusion and viscosity.

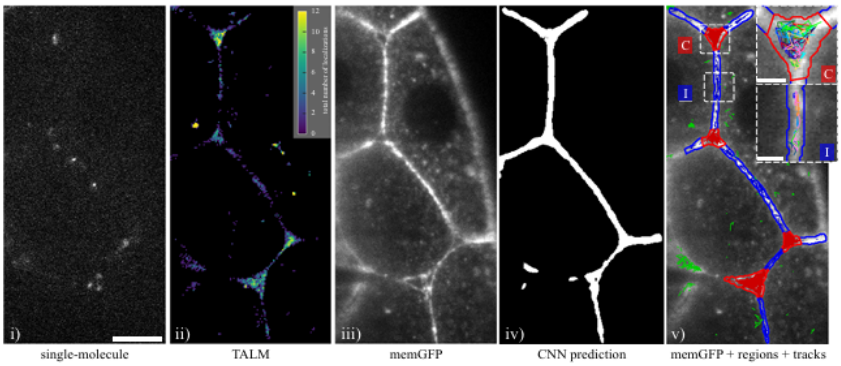

Figure 7.7: Distinct local geometries in the ECS of zebra fish embryo: A sequency of images from i to v showing SPT and segmentation based on local geometries. The shapes of local geometries segmented are reminescent of chambers and tunnels that we have seen in our own study (Adapted from [167]).

As discussed in earlier Chapter 4, it is well known that droplets can be functionalized with a range of biomolecules. In many cases, such functionalization is used to enhance interac-

tions between adjacent droplets through various "locking" mechanisms [142]. Beyond this, however, it would interesting to consider the possibility of introducing biomolecules that are more representative of proteins, receptors, and other components commonly found in biological environments. This would make the droplet system an attractive model for studying the diffusion of particles that not only experience geometric restrictions but also directly interact with the surrounding interfaces (Figure 7.8 a). Such modifications could provide insight into how diffusion is altered in the presence of biomolecular interactions that occur within the ECS [52]. Furthermore, the extracellular matrix, which serves as a structural scaffold in these environments, could potentially be incorporated through the addition of gel-like materials during droplet preparation and packing. This would allow the model to move beyond simple confinement and begin capturing some of the structural complexity that characterizes real biological systems.

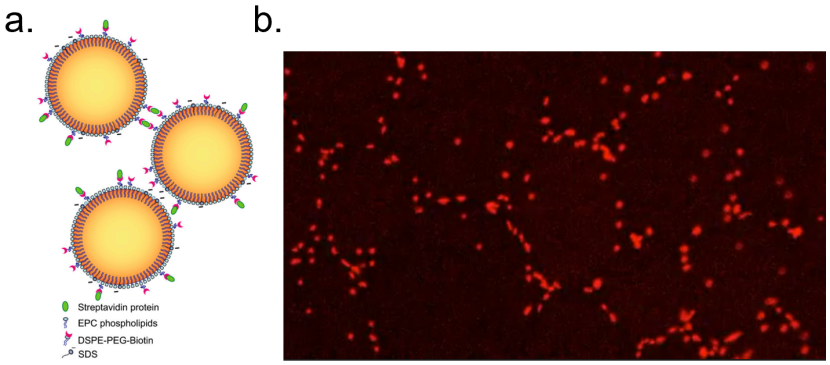

Figure 7.8: Towards a realistic artificial ECS: a. Emulsion droplets stabilized by phospholipids and SDS and functionalized with PEG biotin group. Adjacent droplets binding via biotin-streptavidin interactions (Adapted from [142]) b. Diffusion of fluorescent particles in a flow in the interstitial space between droplets.

Another potentially exciting direction comes from recent work demonstrating that microfluidic approaches can introduce controlled fluid flow through biomimetic tissues (Figure 7.8 b). Incorporating such flows into our model system would open the possibility of studying transport and diffusion under flow at the nanoscale, a topic where experimental observations are yet to validate theoretical predictions [148].

Together, these possibilities suggest a natural roadmap for future work; starting from geometry, then progressively introducing molecular crowding, extracellular matrix components, and fluid flows. In doing so, it may become possible to build increasingly realistic artificial ECS environments, while still retaining the control and simplicity needed to isolate the role of each of these factors. Ultimately, such a bottom-up method could allow for model systems to approach the complexity of living tissues while maintaining control and tunability, thus providing a framework for understanding transport in environments that are otherwise difficult to access experimentally.

Appendix A

Paper-I: Orientational frustration drives enhanced diffusion of anisotropic particles in a liquid labyrinth

Orientational frustration drives enhanced diffusion of anisotropic particles in a liquid labyrinth

Rohit Mangalwedhekar[1,2], Limeng Ruan[1,2], Somen Nandi[1,2], Quentin Gresil[1,2], Marc Tondusson[1,2], Stephane Bancelin[1,2], Lea-Laetitia Pontani[3,4], Laurent Cognet[1,2,*]

[1]*Laboratoire Photonique Numerique et Nanosciences, Université de Bordeaux, 33400 Talence, France,*
[2]*LP2N, Institut d'Optique Graduate School, CNRS UMR 5298, 33400 Talence, France*
[3] *Sorbonne Université, CNRS, Laboratoire Jean Perrin, LJP, F-75005 Paris, France*
[4] *Sorbonne Université, CNRS, Inserm, Institut de Biologie Paris-Seine, IBPS, F75005 Paris, France*

Keywords: *Carbon nanotubes, anisotropic diffusion, anomalous diffusion, 3D single-particle tracking, orientational tracking, confinement, transport in complex soft matter*

ABSTRACT

Transport of nanoscale objects in complex, structured environments plays a key role in a wide range of processes, from biomolecular dynamics in extracellular spaces to transport in porous materials such as filters and catalysts. While anomalous diffusion is well established, how particle anisotropy governs transport under geometric constraints remains unclear. Here we use 3D single-particle tracking to investigate the diffusion of stiff one-dimensional carbon nanotubes in a continuous soft matter network of interconnected chambers and constrictions. Transport is anomalous and antipersistent, with strong length dependent confinement and trapping, consistent with obstructed diffusion. Unexpectedly, however, escape from confinement is poorly sensitive to nanotube length as opposed to what would be expected of pore mediated transport. Despite a tenfold length increase and significantly enhanced trapping, escape time increased by only ~1.4×. Single-particle orientational tracking reveals the origin of this weak scaling. Indeed, long nanotube, i.e. those with length comparable to the chamber dimensions, dynamically align with constrictions enabling efficient, geometry-assisted escape that offsets increased confinement while shorter nanotubes need to screen the volume to find their escape path.

These results uncover an alignment-mediated transport mechanism that decouples confinement strength from escape kinetics, distinct from pore-mediated transport mechanisms, establishing a quantitative framework for anisotropic diffusion in complex environments.

Introduction

Diffusive processes in natural systems are generally described within frameworks that explain how stochastic motion evolves over time. While Brownian motion provides the simplest model for such processes[1,2], real-world environments often exhibit significant deviations from simple Brownian statistics[3]. The transport of nanoscale objects in many natural systems that have complex structures and confinements display such deviations from Brownian mechanics[4]. These processes range from biomolecular activity within cells or intercellular communications in the extracellular spaces (ECS) of tissues to the diffusion of fluids through filters, catalysts, and metalorganic frameworks and pose critical challenges and opportunities both for fundamental research and technological innovation[5–13].

In recent years, diffusion in confined and complex environments has therefore received widespread attention. This growing interest has been significantly advanced by breakthroughs in single-particle tracking (SPT) [14,15] and the development of environmental models as well as diverse fluorescent probes, which can passively or actively navigate confined spaces[7,16–22]. When applied to biological systems, single-molecule diffusion measurements have revealed anomalous diffusion patterns driven by local variations in viscosity, biomolecular crowding, and intrinsic fluxes within cellular and tissue architectures [6,23–27]. Understanding diffusion in such intricate environments, and unravelling the origins of anomalous behavior, is not only a fundamental scientific challenge but also essential toward advancing our knowledge of health, disease and treatment strategies.

Much of our current understanding of diffusion in complex systems has been established using spherical probes, such as small fluorescent molecules, quantum dots, or fluorescent beads[22,26,28]. In synthetic environments such as porous gels, packed colloids, and inverse

opals, these isotropic probes have been instrumental in demonstrating and characterizing how environmental heterogeneities give rise to anomalous behavior and non-Gaussian statistics[9,10,29–32]. In biological samples, diffusing entities often exhibit limited isotropy, leaving the influence of particle shape on transport, confinement, and escape mechanisms largely unexplored. Additionally, anisotropic particles may offer further insights by highlighting specific environmental features that govern diffusion, features that spherical particles might overlook[33]. Experiments on the free diffusion of anisotropic particles have demonstrated the coupling between orientational and translational diffusion[34].

In recent years, single-walled carbon nanotubes (CNTs) have successfully been used as single particle fluorescent probes to study diffusion in biological tissues. The combination of their bright and photostable luminescence in the short-wave infrared with their high 1D aspect ratio and tiny diameter indeed enables probing bioenvironments at depth inside preserved tissues. Notably, investigations of the brain ECS using CNTs of varying lengths ranging from 50 to several hundred nanometers have revealed anomalous diffusion while simultaneously enabling the mapping of intricate structures previously inaccessible to other techniques [16,35–37]. Recent work on the SPT of CNTs in the ECS of the brain has shown that hindered diffusion emerges as a result of geometry[38]. Similarly, CNTs exploring interstitial spaces in highly autofluorescent mouse liver tissues display pronounced variations in anomalous diffusion between healthy and fibrosed states[39].

Beyond biological tissues, the diffusion of rigid nanorods within crowded and cross-linked synthetic networks has been extensively studied in polymer physics. Notably, nanorods longer than the mesh size of entangled or cross-linked polymer networks have been shown to diffuse anomalously fast compared to the predictions of reptation or simple obstruction models, owing to a decoupling from polymer relaxation dynamics[40]. More recent work has directly linked this enhanced mobility to a coupling between rotational and translational dynamics, whereby nanorod reorientation facilitates passage through adjacent mesh openings[41], with the magnitude of the effect depending sensitively on nanorod length, rigidity, and surface roughness. These studies, conducted in mesh-like, effectively concave

confining geometries, provide an important point of comparison for the present work, which instead probes a continuous, convex landscape of interconnected chambers and tunnels.

Long CNTs have been used to study the reptation and elastic behavior of semiflexible filaments across diverse diffusing environments[42,43]. However, reports on the dynamics of rigid anisotropic diffusers in confined spaces remain limited. While theoretical studies have explored the diffusive escape of rigid rods within idealized confined geometries[44], experimental investigations into the diffusion of anisotropic rigid particles in complex environments is still poorly understood. Within this context, how rigid anisotropic particle geometry interacts with local architecture to shape diffusion, orientation dynamics, confinement and escape statistics in soft-matter environments appears as a timely and key question. Beyond biological environments, this question is also relevant to molecular movements in zeolites and porous media [8–10,29–31]. Addressing this question calls for well-defined model systems that decouple geometrical effects from, e.g. chemical content or biological complexities, enabling controlled investigation of transport mechanisms.

In this work, we demonstrate how the interstitial spaces within densely packed emulsion droplets can act as a biophysical model for studying 3D single-particle diffusive processes in complex soft matter environments as an idealized proxy of the ECS freed from complex molecular crowding. These densely packed droplets have already been instrumental to serve as model systems to explore the macroscopic response of tissues, particularly the roles of mechanical forces, rheology, and cell–cell contact interactions[45–48]. The intricate network of interstitial spaces between these droplets provides a unique landscape for investigating the diffusion of single molecules at the nanoscale. By introducing diffusing anisotropic CNTs, we examine how geometric frustration of their rotational motion within continuous convex confinements enhance the translational diffusion and escape dynamics of rigid anisotropic particles.

Within these environments we demonstrate the anomalous 3D diffusion of anisotropic particles due to purely geometrical effects. We further show how local geometries influence diffusion of these anisotropic particles depending on their length. Importantly, we reveal that

in such a convex landscape, the escape time of particles from local areas scales more weakly with particle length than expected in concave spaces. This effect is attributed to local alignment induced by frequent particle–wall interactions that pre-align particles and favor their escape. To validate this interpretation, we employ single-particle orientation tracking (SPoT), demonstrating how geometric frustrations differentially influence particle orientation depending on particle length. These interactions ultimately shape escape mechanisms and affect the scaling of escape times for anisotropic particles.

Results

We selected a soft matter system composed of densely packed emulsion droplets (~5 μm in diameter) whose interstitial spaces form a network of continuous convex architecture representative of a complex soft matter diffusion landscape such as the brain ECS. This intricate network of interstitial space serves as our biophysical model system used to challenge current diffusion models in complex soft matter.

We used (6,5) CNTs functionalized with quantum color centers (called as CCNTs) emitting at ~1140 nm based on an aryl substituent as the functional group[16]. This functionalization yields bright nanotubes at typical lengths of ~500 nm (mean), and further enables the production of ultrashort luminescent nanotubes (uCCNTs), with a mean length of about 50 nm[16] as measured using Atomic Force Microscopy (AFM) (Supplementary Figure 1). Consequently, both CCNTs and uCCNTs can serve as highly effective probes for deep-tissue imaging at depths exceeding 100 μm, highlighting the transformative potential of anisotropic probes in revealing the complexities of biological structures. Imaging was performed using a custom-built single molecule setup equipped with a double helix phase mask to engineers the point spread function (PSF), enabling 3D single-particle tracking (SPT) of (u)CCNTs in the near-infrared[49,16]. This approach allowed us to record ultra-long trajectories of CCNTs and uCCNTs within the emulsion droplets (Figure 1a).

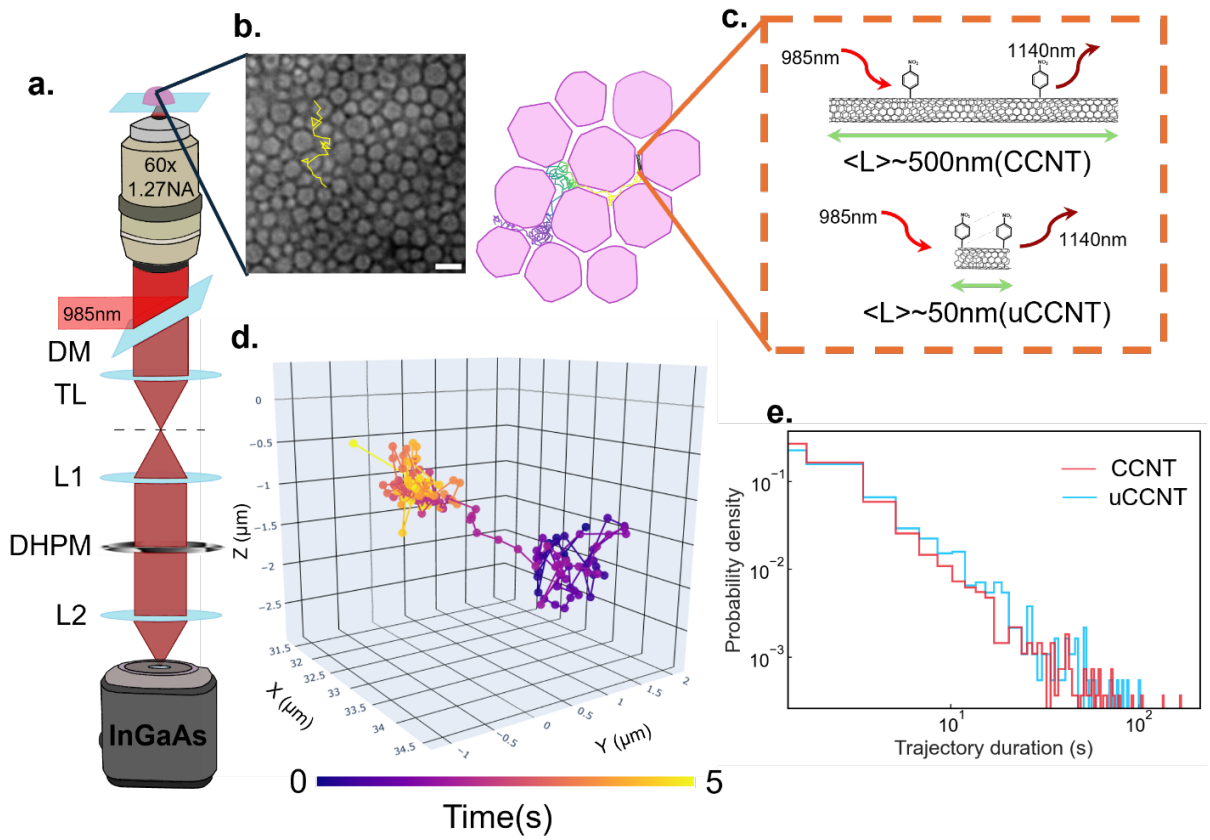

Figure 1 3D Single Particle Tracking of individual Carbon nanotubes in a biophysical model a. Schematic widefield microscopy setup equipped with a Double Helix Phase mask (DHPM) to achieve 3D single particle tracking of diffusing individual CNTs. b. An optically sectioned fluorescence image representative of the packed emulsion droplet structure as a biophysical model and a schematic representation of a CNT diffusing in interstitial regions. Scale bar: 5 μm. c. Schematic representation of the long CNTs (CCNTs) and ultra-short CNTs (uCCNTs) used to study the length dependence of diffusion in complex structures. Both types of CNTs were functionalized to fluoresce brightly with high photostability at ~1140 nm when excited at 985 nm. d. Typical 3D trajectory of a single CNT tracked while exploring the biophysical model. e. A histogram of acquired trajectory lengths. The median trajectory length is around 2s and the average trajectory length is about 5s for both CCNTs and uCCNTs.

The biophysical model exhibited a highly dense packing under white-light imaging (Figure 1b). To quantify its structure more precisely, we fluorescently labeled the droplet interfaces with Nile Red and implemented the HiLo modality (SPARQ, Bliq Photonics), which provides optical sectioning for imaging fluorescently tagged droplet surfaces[37,50] (see Droplets imaging under Materials and methods). Fluorescence images revealed a tight packing evidenced by the deformations of the individual droplets from nearly circular to polygon-like shapes[50]. The distribution of the packed droplets sizes (median diameter ~4.3 μm) was

estimated using the Hough Circle Transform in Fiji (Supplementary Figure 2a) from the optically sectioned 2D fluorescence images. The fraction of the space occupied by the interstitial spaces between droplets was quantified by thresholding optically sectioned images in Fiji. This analysis revealed that interstitial regions account for approximately 12 ± 1% of the total sectioned area. Next, the biophysical model was prepared with the inclusion of (u)CCNTs (Figure 1c). A total of 2481 and 1564 trajectories of CCNTs and uCCNTs were acquired respectively, providing statistically robust interpretations. In both cases, the median trajectory length was ~2 s corresponding to ~60 data points (Figure 1d, e), ensuring comparable temporal sampling across particle lengths. Some individual CCNTs were also imaged for longer timescales (up to 160 s, i.e. 4874 data points) allowing to retrieve the network structure of the interstitial regions between the emulsion droplets.

Diffusion of anisotropic particles was first analyzed by calculating the ensemble Mean Squared Displacement (MSD - $< r^2(\Delta t) >$) to understand the scaling of exploration in the structure[51].

$$< r^2(\Delta t) > = K_\alpha (\Delta t)^\alpha \quad (1)$$

where α is the anomalous diffusion exponent, Δt the lag time between two positions, and K_α the generalized diffusion coefficient.

The ensemble MSD exhibits clear sublinear scaling at short time lags, with diffusion exponents α = 0.75 ± 0.02 (uCCNTs) and α = 0.64 ± 0.01 (CCNTs), establishing that diffusion is anomalous for both particle lengths despite a tenfold size difference (Figure 2a). The generalized diffusion coefficients were determined as K_α=1.43 ± 0.01 μm^2/s$^\alpha$ for uCCNTs and K_α=0.70 ± 0.01 μm^2/s$^\alpha$. Next, we use the Velocity Autocorrelation Function (VACF) as a parameter that quantifies temporal correlations in particle displacements and reveals memory effects through interactions with the environment[51] (Figure 2b).

$$\tilde{C}_v(\Delta t) = \frac{\langle \boldsymbol{v}(t + \Delta t) \cdot \boldsymbol{v}(t) \rangle}{\langle \boldsymbol{v}(t)^2 \rangle} \quad (2)$$

where $\boldsymbol{v}(t)$ is the velocity component of the particle at time t and Δt is the time lag. The VACF calculated at the fourth time lag independently corroborates anomalous transport with antipersistent steps, displaying pronounced negative correlations from $\Delta t \approx 0.4 - 1.0$ s before returning to zero, with stronger antipersistence for CCNTs than for uCCNTs.

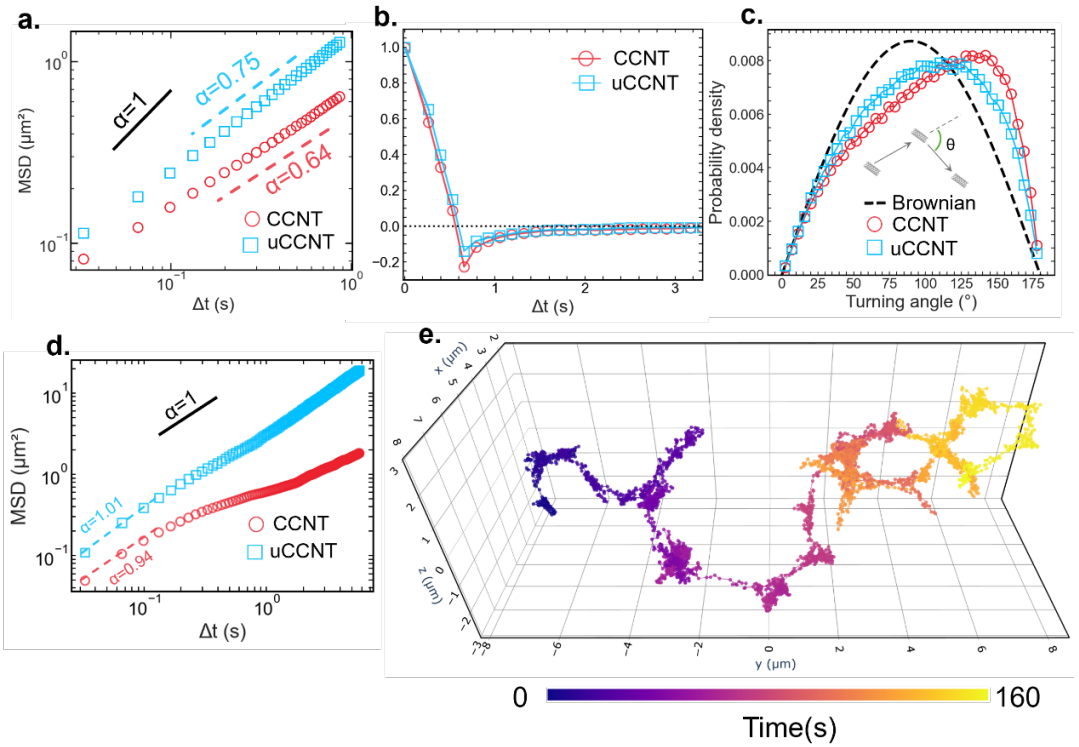

Figure 2 Diffusion analysis of 3D SPT of nanotubes reveals anomalous behaviour a. MSD versus lag time for CCNTs and uCCNTs in the biophysical model showing subdiffusive anomalous behaviour. b. The velocity autocorrelation function (VACF) exhibits a negative correlation, highlighting the restriction CNTs face when bouncing against the walls of the droplets. c. The right shifted nature of distribution of turning angle (measured as the exterior angles as shown in inset) confirms the increased interactions with the walls as compared to Brownian motion (black dotted line). d. MSD of single long trajectories of uCCNTs and CCNTs illustrating that within a single trajectory diffusion is complex and contains multiple regimes. e. Representations of the cartesian coordinates of a long single trajectory indicates the presence of local geometries of "chambers" and "tunnels".

Lastly, we choose to assess the distribution of turning angles as a direct probe of directional constraints in molecular motion[51] (Figure 2c). Here, we define the turning angle as the exterior angle between successive displacement vectors formed by three consecutive particles' localizations, quantifying the change in direction of motion independent of particle orientation (inset Figure 2c). The distribution from the trajectories of both the uCCNTs and

CCNTs exploring the biophysical model revealed a right shift towards large angles with a maximum at 110° and 142° respectively, as compared to distribution of standard Brownian motion (dashed black line, Figure 2c). The systematic shift toward large turning angles reflects repeated wall-mediated deflections. The stronger shift observed for CCNTs demonstrates that increasing particle length amplifies geometric frustration and the frequency of boundary interactions (Figure 2c). Together, these observations strongly suggest that subdiffusive anomalous diffusion in the biophysical model arises from geometric frustration and are consistent with the obstructed diffusion model[38]. As a control, the MSD, VACF, and distribution of turning angles were also calculated for Brownian diffusion in a homogeneous imaging buffer solution (Supplementary Figure 3).

Some individual CCNTs were also imaged for longer timescales to retrieve the network structure of the interstitial regions of the biophysical model. While ensemble averaging smooths out these features, individual long-trajectory MSDs clearly resolve three distinct dynamical regimes characteristic of transient trapping (Figure 2d), exhibiting a near linear growth in the first regime (α = 0.94 and 1.01 for CCNTs and uCCNTs respectively), followed by sublinear or near plateau-like behavior in the second regime, and finally, near linear growth again indicating free diffusion at longer time scale (~1 s). Interestingly, direct examination of the particle trajectories in the interstitial spaces clearly demarcates different geometries explored by the particles such as voluminous “chambers”, and channel like “tunnels” as will be discussed below (Figure 1d, 2e). Furthermore, these geometries were also visualized when the droplet environment was imaged with optical sectioning. This motivates a geometry-resolved analysis of particle motion as is discussed below.

To study the effect of local geometry on diffusion, the long trajectories were manually segmented into two main distinct topologies using the software CloudCompare: chambers and tunnels, connecting various chambers (Figure 3a). The MSD and turning angles of the particles in these two topologies were next studied separately. The MSD of uCCNTs in the chambers grow almost linearly before turning sublinear, indicating the time required for the

nanotubes to explore their local environment. Within chambers, uCCNTs initially exhibit near-linear MSD growth before transitioning to subdiffusion at ~330 ms, consistent with rapid free volume exploration followed by confinement-limited motion. In contrast, long CCNTs display sublinear MSD growth at lower time scales, evolving into a plateau indicative of transient trapping at ~200 ms (Figure 3b).

In the chambers, the distribution of turning angles for both ultrashort and long CCNTs is close to Brownian at the earliest time lag (Δt=0.033 s). However, at longer time lags (Δt=0.33 s, Δt=0.825 s) the strong shifts progressing towards large turning angles indicate prominent interaction with walls (Figure 3c, d).

Notably, within tunnels, while MSDs alone suggest nearly Brownian transport for both particle lengths (Figure 3e), turning-angle statistics reveal fundamentally different underlying dynamics. For long CCNTs, the turning-angle distribution evolves from homogenous (Δt=0.033 s) toward bimodal form (Δt=0.825 s), with peaks at small angles (persistent motion) and large angles (antipersistence), reflecting aligned (forward) and anti-aligned (backward) steps along the tunnel axis (Figure 3f). Such a bimodality is absent for uCCNTs, which retain progressively antipersistent turning statistics at longer time lags (Δt=0.33 s, Δt=0.825 s) due to repeated collisions with the boundary walls while showing nearly Brownian distributions at very early time lags (Δt=0.033 s) (Figure 3g). These length-dependent turning statistics indicate that particle length determines how geometric frustration is resolved: uCCNTs undergo near isotropic exploration with frequent wall interactions, whereas long CCNTs adopt alignment-assisted transport along tunnels.

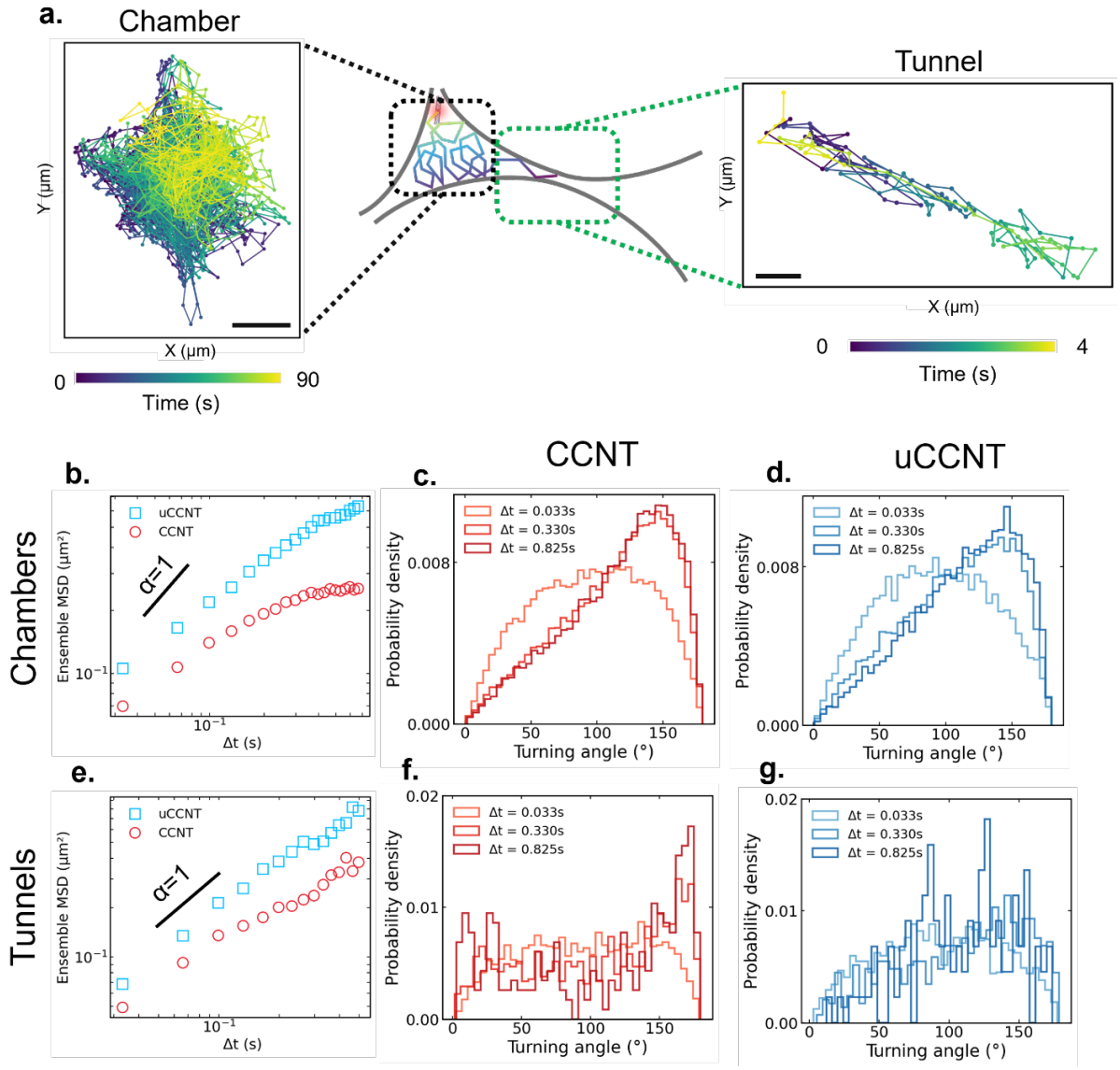

Figure 3 Diffusion of nanotubes is influenced by local geometry a. Schematic of a nanotube trajectory in the model system, displaying the two distinct environmental topologies, together with representative trajectories in chambers (Scale bar: 500 nm) and tunnels (Scale bar: 200 nm), manually segmented on CloudCompare. b. MSD versus lag time for CCNTs shows transient trapping in the chambers while the uCCNTs show strongly subdiffusive behaviour at longer lag times. c, d. Distribution of turning angles in the chambers shows near Brownian exploration in the first time lag but right shifted distributions at longer time lags, confirming strong subdiffusive behavior for both CCNTs and uCCNTs. e. MSD versus lag time for both CCNTs and uCCNTs reveals nearly Brownian diffusivity in the tunnel regions. f, g. Distribution of turning angles in tunnels is strongly parallel or anti-parallel with significant under-representation of intermediate angles owing to the geometric and steric constraints at higher time lags for long nanotubes. Conversely the ultra-short nanotubes continue to show right shifted angles at different time lags indicating obstructed yet Brownian diffusion.

Next, we studied the distribution of escape times, defined as the time taken by the nanotubes to exit a chamber. We determined the escape times, τ_{long} (for CCNTs) and τ_{short} (for uCCNTs), from 150 and 148 chamber-residency events respectively (Figure 4a, see Methods for extraction criteria and Supplementary Figure 2c for the resulting, overlapping chamber-size distributions of the two populations). Strikingly, despite a tenfold difference in nanotube length, we found the ratio $\tau_{long}/\tau_{short} \approx 1.4$ only. To estimate statistical uncertainty, we use a bootstrap resampling (N=100 000) that results in a 95% confidence interval range of [1.04, 1.85] with a median of 1.38 (Figure 4b).

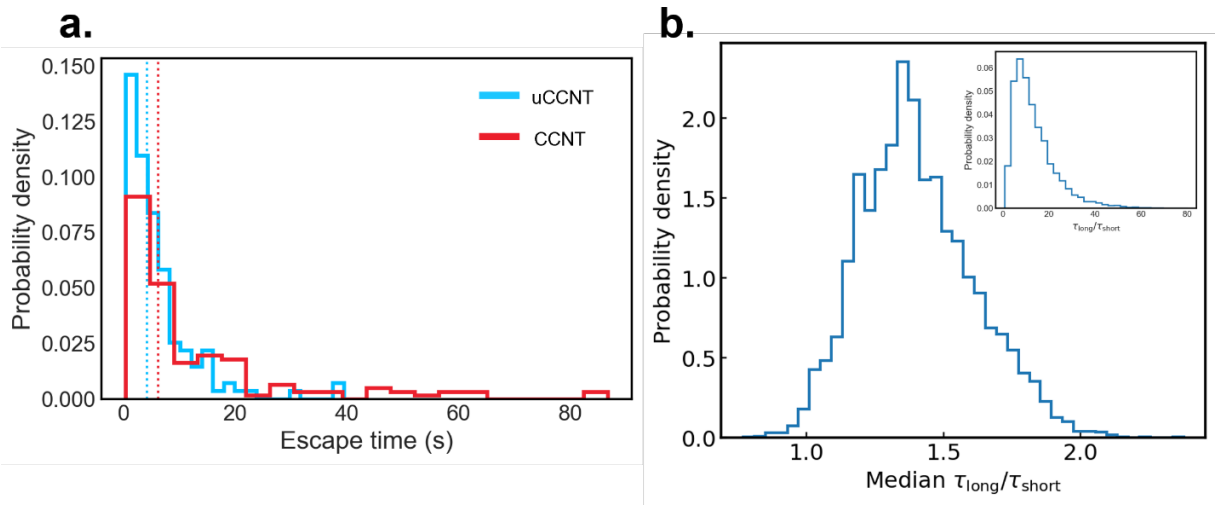

Figure 4 Length dependence on escape times from chambers a. The distribution of residency times of uCCNTs and CCNTs reveals a median escape time of around 3.3 s and 5 s, respectively. Thus, the escape time ratio for long and short particles is 1.38. b. A bootstrap resampling (N=100 000) was used to quantify the 95% confidence interval of the median escape time ratios to be [1.04, 1.85]. A Monte Carlo parameter sweep simulation was used to theoretically predict ratio of escape times by Brownian diffusion of anisotropic particles from confinement and the median value was found to be 11.28 ± 9.66 (inset).

To test whether this weak length-dependence is consistent with purely diffusive escape, we compared it to a quantitative model of Brownian escape for anisotropic particles from confinement (Doi and Xu model[44]), evaluated via a Monte Carlo parameter-sweep simulation built on our measured geometry (see Methods). This purely Brownian model predicts a linear scaling of escape time with particle length. For a tenfold increase in nanotube length, it predicts a median escape-time ratio of 11.28 ± 9.66 (Figure 4b, inset). This predicted ratio is

much larger than the ~1.4-fold increase we measured experimentally. We examine the physical origin of this deviation in the Discussion.

The striking reduction in length sensitivity reveals that escape is not limited by translational or rotational diffusion alone. Instead, based on the length of the particle, we hypothesize the confinement induces a geometric frustration of rotational dynamics that adjusts escape mechanisms for the uCCNTs and CCNTs and compensate for the increased length of the particle. This reduced scaling of escape times along with the distribution of angles in the chambers and tunnels points to geometry-induced alignment of long anisotropic particles to the tunnels that mitigate rotational constraints and facilitate escape.

We next place this interpretation on a more quantitative aspect by characterizing the geometry of the biophysical model itself. For a statistically homogeneous and locally isotropic medium such as our densely packed droplet network, the area fraction measured on a random 2D section is, by the classical Delesse stereological principle, an unbiased estimator of the corresponding 3D volume fraction[52,53]. The interstitial area fraction reported above (12 ± 1%) therefore provides a direct estimate of the 3D porosity of the biophysical model, $\phi \approx 12 \pm 1\%$ (Table 1a in Supplementary Information).

Independently of this porosity estimate, the chamber and tunnel dimensions define the dimensionless confinement ratios (Table 1b in Supplementary Information): for CCNTs, $L/D_c \approx 0.6\text{-}0.8$ and $L/a \approx 4.5\text{-}7.1$, placing the long nanotube length within a factor of ~1.5 of the chamber size and several tunnel diameters. For uCCNTs, $L/D_c \approx 0.07$ and $L/a \approx 0.45\text{-}0.71$, an order of magnitude smaller on both confinement scales. These same quantities (chamber volume V, nanotube length L, tunnel radius a) are the direct inputs to the Doi-Xu escape-time model (Eqs. 3-6) and to the Monte Carlo parameter-sweep simulation below (Figure 4b inset): the theoretical comparison presented in this work is therefore calibrated directly by our own measured geometry.

The tunnel and radius distributions obtained independently from CCNT and uCCNT trajectories (Supplementary Figure 2d) further indicate that the escape mechanism is constrained on purely steric grounds: all the tunnels have a radius smaller than half the

CCNT length (a < 250 nm), meaning CCNT passage requires substantial reorientation in virtually every escape event; by contrast, all of the same tunnels are wider than half the uCCNT length (a > 25 nm), consistent with the near-isotropic, alignment-free passage inferred for uCCNTs from the turning-angle statistics (Figure 3g). This purely geometric analysis provides independent quantitative support for the length-dependent escape mechanism proposed above.

To probe and confirm directly this orientational mechanism underlying length-dependent transport, we performed Single Particle orientation Tracking (SPoT) on long CCNTs, enabling simultaneous tracking of position in 2D and orientation in 3D[54–56] (Figure 5a). Notably, SPoT lacks the extended depth-of-focus capability of the double-helix SPT approach used above. As a result, in the 3D biophysical model where chambers and tunnels extend beyond the focal plane, recording long trajectories becomes challenging since particles may diffuse along the optical axis, thereby reducing the number of trajectories that can be reliably analyzed. Despite the limited number of trajectories accessible to SPoT, we obtained consistent and robust orientational signatures. More precisely, after segmentation of the trajectories, we retrieved 14 tunnels and 17 chambers. The orientational dynamics were quantitatively analyzed by calculating the Mean Square Angular Displacement (MSAD):

$$MSAD(\Delta t) = 4D_r\Delta t \quad (3)$$

The resulting values show a strong orientational hindrance in the tunnels (D_r= 0.4 rad^2/s), while in the chambers, CCNTs have a much higher rotational freedom in the chambers (D_r= 1.4 rad^2/s) (Figure 5b).

Furthermore, the persistence of an anisotropic particle's initial orientation quantified by the Reorientation Time correlation Function (RTF) was evaluated:

$$RTF(\Delta t) = Se^{\frac{-\Delta t}{\tau}} \quad (4)$$

where S is a constant, Δt is the time lag, and τ gives the characteristic length of orientational memory.

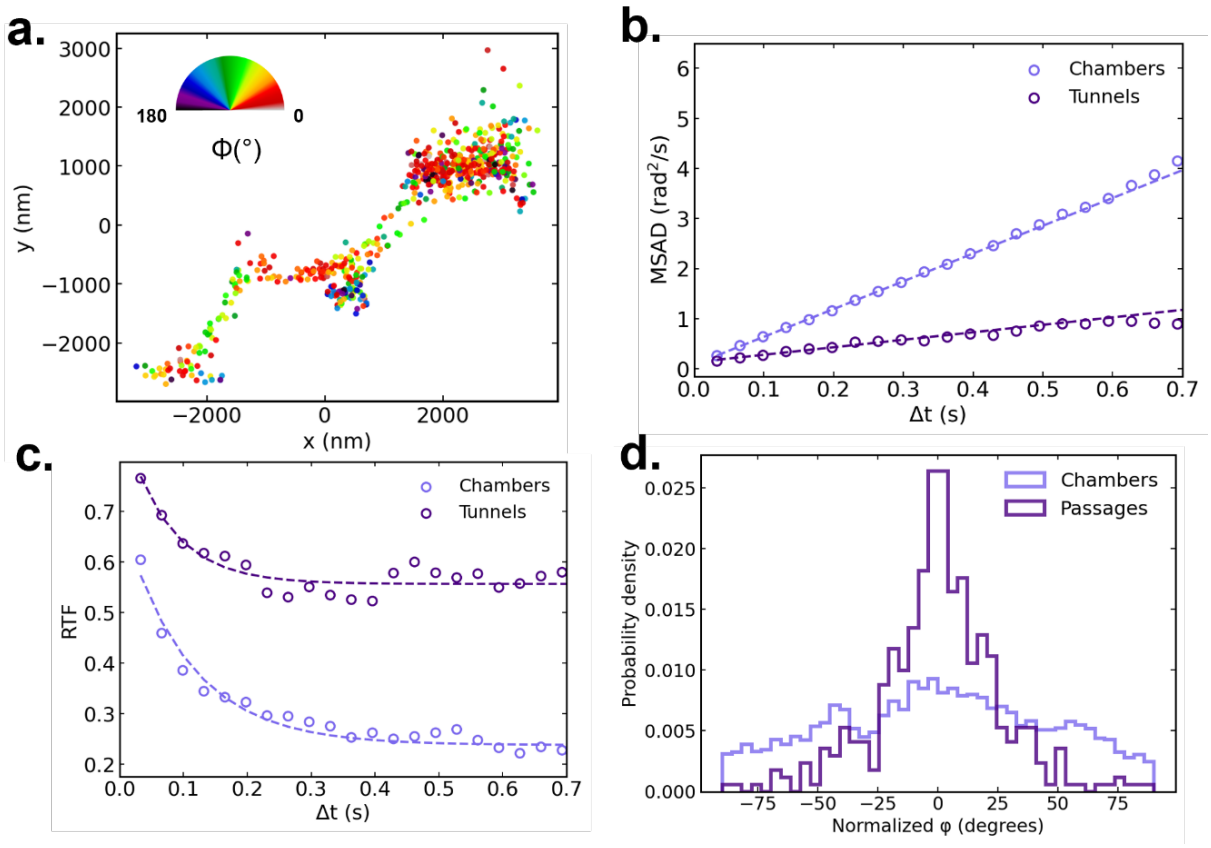

Figure 5 Geometrically frustrated diffusion induces facilitated escape a. The spatial distribution of the planar angle (Φ) of a representative trajectory of a CCNT exploring the chambers and tunnels in the biophysical model reveals spatial heterogeneities in particle orientation. b. The Mean Squared Angular Displacement (MSAD) further confirms the hindered rotation of the particles in the tunnels as opposed to the chamber exploration. c. The Reorientation Time correlation Function (RTF) shows longer memory of the initial orientation in the tunnels, while in the chambers, the particles quickly "forget" them. d. The normalized distribution of the angles in the chambers and tunnels reveals a strong orientational conformity in the tunnels. Whereas in the chambers, the particles explore the full spectrum of angles to orient themselves in.

The RTF shows that in the chambers, CCNTs almost completely lose "memory" of their initial orientation over time with a small residual plateau probably due to their length being comparable to the chamber dimensions, whereas in the tunnels, despite a slight initial loss of orientational memory, the correlation quickly plateaus without dropping further,

indicating orientational persistence (Figure 5c). We next define a circularly normalized azimuthal orientation parameter to enable comparison across geometrically distinct regions. For each chamber or tunnel, the azimuthal angle distribution is recentered by subtracting its mean orientation, thereby setting the local average direction to zero. The angles are subsequently wrapped to a common interval (−90° to 90°), and the normalized distributions are aggregated across all regions as the Centered ϕ. This pooled distribution highlights strong alignment in tunnels, in contrast to the nearly isotropic angular freedom observed in chambers (Figure 5d). Some slight preferential orientations are observed due to the mean CCNT lengths being of the order of the chamber dimensions. Similarly, the distribution of circularly normalized polar angles ("Centered θ") displays nearly similar spread in both, the chambers and the tunnels (Supplementary Figure 4), confirming that only in-plane trajectories could be imaged and tracked. In contrast, for uCCNTs diffusing in the biophysical model, SPoT was unable to resolve the orientations of the particles. Given their small dimensions, uCCNTs can undergo fast rotational diffusion within the chamber, with a characteristic timescale of ~0.002 ms, much shorter than the camera integration time (33 ms) required for SPoT. As a result, their orientation averages out within a single exposure such that the recorded PSF corresponds to a time-averaged projection rather than a well resolved orientation PSF, precluding reliable extraction of particle orientation. Conversely, the characteristic timescale for free rotational diffusion of CCNTs is on the order of ~12 ms. Combined with the anomalous subdiffusion imposed by the biophysical model, an acquisition time of 33 ms is sufficient to capture and resolve particle orientations from the recorded PSFs. Analysis via SPoT indicates that CCNTs undergo rotational frustrations that correlate with transient trapping. Within this trapped state we observe a tendency for CCNT prealignment to the tunnels facilitating escape along these preferred orientations as indicated by a substantial lowering of the escape time scaling. In contrast, uCCNTs are characterized by rapid diffusion and frequent boundary interactions, suggesting escape dynamics based on efficient spatial sampling and stochastic exploration.

To further probe the geometric origin of this escape behavior, we tested whether it is governed by nanotube length relative to confinement size, rather than by either one alone,

by repeating our measurements in a second, smaller droplet environment. Small droplets (SD, diameter 1.4μm (Supplementary Figure S5)) give rise to smaller chambers (SC, characteristic chamber length measured from trajectories, $D_c \approx 250$ nm) which we compare here with the larger chambers (LC) used throughout the rest of this work. As the two confinement conditions differ in volume by a factor of ~24 (Supplementary Figure 6a), we first rescaled the escape time by the characteristic chamber volume to allow direct comparison. However, normalized escape times remained distinct for nanotubes of identical length in the SC and LC conditions (Supplementary Figure 6b), indicating that confinement volume alone does not account for the observed escape dynamics.

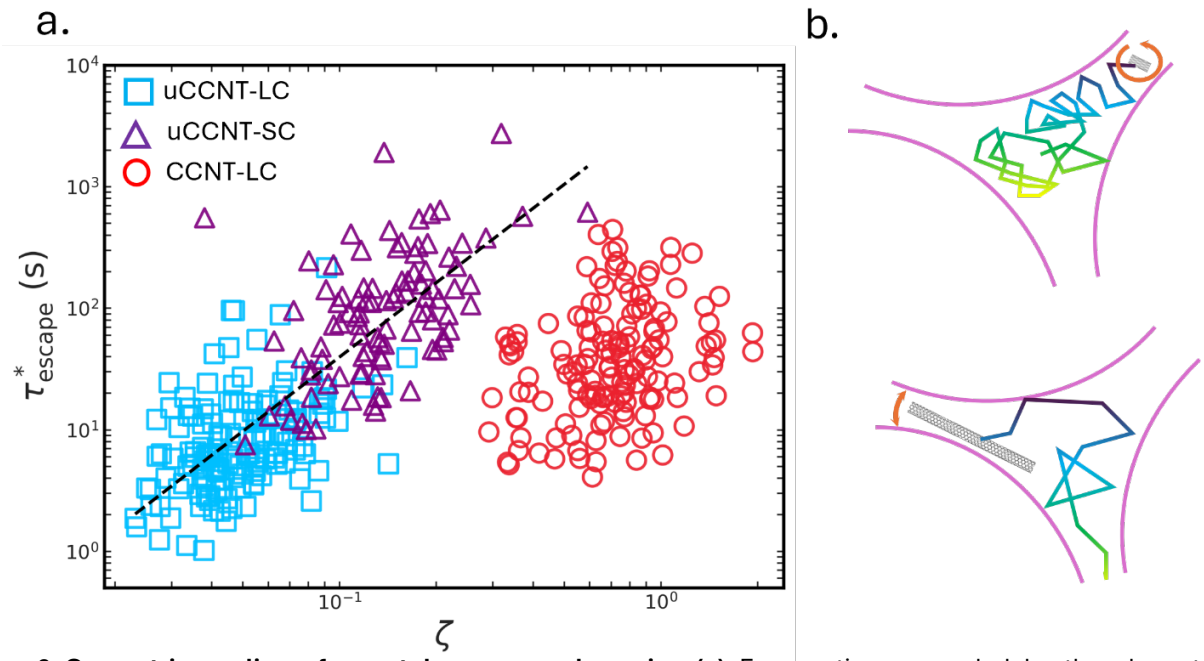

Figure 6 Geometric scaling of nanotube escape dynamics (a) Escape times rescaled by the characteristic confinement volume scale, $\tau^*_{esc} = \tau_{esc}/{D_C}^3$, are plotted as a function of the dimensionless nanotube-to-confinement size ratio, $\zeta = L/D_C$, for the different experimental conditions (LC and SC correspond to chambers in large and small droplets respectively). The data exhibit a common power-law scaling (exponent ≈ 2.13) over the low-ζ regime, while a systemic deviation emerges above a characteristic ζ, marking a crossover to a distinct escape regime. **b.** Schematic representations of nanotube escaping from chambers through connecting tunnels. For uCCNTs, whose dimensions are small relative to the chambers and tunnels, the nanotubes retain substantial rotational freedom (top). In contrast, the CCNTs experience restricted rotational freedom and preferentially align with the available exit pathway, facilitating escape through the connecting tunnels (bottom).

We therefore considered instead the dimensionless ratio $\zeta = L/D_C$ which directly compares nanotube length to the chamber dimension. Plotting the volume-normalized escape time

$\tau^*_{esc} = \tau_{\mathrm{esc}}/\mathrm{V}$, where V represents the volume of the convex hull used to characterize the chamber trajectory, against ζ reveals a common power law scaling, $\tau_{\mathrm{esc}} \sim \zeta^{2.13}$ across the low ζ regime (Figure 6a). Despite spanning distinct ranges of ζ, the uCCNT data from the SCs and LC conditions collapse onto this same scaling relationship, showing that the escape dynamics are governed by nanotube length relative to the chamber dimension rather than by the confinement volume or nanotube length alone. At larger ζ, the CCNT-LC data systematically deviate above this scaling, marking a crossover to a distinct escape regime. This regime is consistent with the restricted rotational freedom and preferential tunnel-alignment of the longer CCNTs independently observed by SPoT microscopy (Figure 6b).

Discussion

Our work indicates that anisotropic particles with dimensions smaller than their surroundings exhibit rapid volumetric diffusion together with frequent boundary interactions, resulting in highly efficient spatial sampling. At short timescales, they exhibit rapid diffusion, while at longer times, interactions with spatial boundaries induce confinement-driven hindrance, resulting in anomalous diffusion.

Conversely, as particle lengths approach the characteristic dimensions of the environment, spatial confinement strongly impacts diffusion even at short timescales, while still allowing efficient motion. Across two confinement regimes differing in chamber volume by a factor of ~28, we find that the normalized escape time follows a common power-law scaling with the dimensionless length-to-confinement ratio $\zeta = L/D_C$ (exponent ≈ 2.13, low-ζ regime), rather than with nanotube length or chamber dimension independently. This directly confirms that it is this ratio, and not particle length alone, that governs escape dynamics. At larger ζ, however, the CCNT-LC data systematically depart from this scaling: escape from confined regions is instead facilitated by the probe geometry as frequent interactions with the boundaries hinder rotational diffusion and effectively pre-align the particles along available pathways, promoting funneling[57,58] and increasing the escape probability (i.e., reducing

residence times) compared to a pore-like geometry. This effect is reflected in the weak dependence of escape times on nanotube length.

We further examine the theoretical basis for this weak length-dependence. We compare our escape-time measurements to a quantitative model derived by Doi and Xu[44]. This model describes the Brownian escape of 1D, needle-like objects through a narrow opening. It treats escape as a two-stage process: a free phase and a capture phase. In the free phase, the particle retains full translational and rotational freedom within the chamber; in the capture phase, one end of the particle enters the opening, imposing strong constraints on its rotational motion. For CCNTs, whose length is comparable to the chamber dimensions (Supplementary Figure 2b), escape is strongly dominated by the capture phase, so that their escape time (τ_{long}) can be expressed as[44] :

$$\tau_{long} = \frac{2VL}{3\sqrt{3}a^2 D_t} \tag{5}$$

where V, L, a , and D_t represent the bounding volume, the nanotube length, the radius of the escape hole and the translational diffusion coefficient, respectively. For uCCNTs, whose length is much smaller than the chamber dimensions, escape is instead governed by the free-exploration regime:

$$\tau_{short} = \frac{V\left(1 + \frac{4aLD_r}{9D_t}\right)}{2\pi D_t a\left(1 + \frac{L^2 D_r}{6D_t}\right)} \tag{6}$$

with D_r, the rotational diffusion coefficient. Here D_t, and D_r are given by[44]:

$$D_t = \frac{kT}{3\pi\eta L}\left(\log p + X_T(p)\right) \tag{7}$$

$$D_r = \frac{3kT}{\pi\eta L^3}\left(\ln p + X_R(p)\right) \tag{8}$$

where k, T, η and p represent the Boltzmann's constant, the absolute temperature, the viscosity of the fluid, and the aspect ratio of the anisotropic particle, respectively. The terms $X_T(p)$ and $X_R(p)$ are finite length correction terms.

While these expressions assume purely Brownian translational and rotational dynamics, they provide a useful geometric baseline for how escape times are expected to scale with particle length in the absence of tube-wall memory effects. To take those into account, we performed a Monte-Carlo parameter sweep simulation based on these equations and investigated the length dependent scaling of escape times. The values of particle lengths and escape-hole radii were drawn from our own measured distributions (Supplementary Figures 1, 2c, see Methods). We find that a tenfold increase in nanotube length predicts an approximately tenfold increase in escape time (median ratio 11.28 ± 9.66, Figure 4b inset). Hence, even purely Brownian theory predicts a linear length dependence on the scaling of escape times. This result strongly deviates from our experimental observation.

This deviation can be placed in the broader context of escape-time theories for confined diffusion. Geometry-controlled reaction kinetics frameworks predict that the mean first-passage time to a small target scales primarily with the ratio of confining volume to target size, with only weak (logarithmic) dependence on the diffusing particle's own dimensions once orientational degrees of freedom are accounted for[58,59]. Our results are qualitatively consistent with this picture, but go further by showing that anisotropy itself, through wall-induced pre-alignment, actively suppresses the residual length-dependence expected even from these frameworks.

This behavior also contrasts with escape-time scalings reported for spherical or near-isotropic nanoparticles escaping rigid porous cavities, where escape time typically scales more strongly with the size of the diffusing probe relative to the pore throat[29–31]. The comparatively weak length-dependence we observe for anisotropic 1D nanotubes therefore appears to be a distinct signature of orientational degrees of freedom coupling to escape kinetics, rather than a generic feature of confined diffusion in interconnected pore networks.

A relevant question is whether the softness of the emulsion interfaces, in contrast to solid porous media, affects the observed dynamics. To address this, we estimated the characteristic amplitude of thermally-driven interfacial fluctuations using classical capillary wave theory, $l_T = SQRT(k_BT/\gamma)$. Using an interfacial tension representative of silicone-oil-in-water, SDS-stabilized emulsions such as used here[60] ($\gamma \approx 10$ mN/m), we obtain $l_T \approx 0.6$ nm at room temperature, and $l_T \approx 2$ nm even under a conservative order-of-magnitude lower bound for γ. This thermal roughness is one to two orders of magnitude smaller than the confinement length scales relevant to nanotube transport (tunnel radius 70-110 nm; chamber size 640-860 nm), and the conclusion is insensitive to the exact value of γ within this range. We therefore conclude that, on the length scales governing nanotube confinement and escape, the droplet interfaces behave as effectively rigid boundaries, consistent with the faceted, polygonal droplet morphology observed under compression (Figure 1b, Supplementary Figure 2a) and with the absence of measurable coalescence or ripening over the imaging timescale.

This conclusion is independently corroborated by the analysis of nanotube dynamics. A mechanically soft, viscoelastic confinement is a classic physical origin of fractional Brownian motion (fBm) and related generalized-Langevin descriptions of anomalous diffusion[3,61], which would be expected to produce a scale-free, persistent VACF, a single spatially homogeneous anomalous exponent, and turning-angle statistics independent of tracer length. Chiefly, it would also show gaussian statistics, with a consistently low non-gaussianity parameter (NGP) converging to zero over long timescales[62]. None of these signatures is observed: the VACF (Figure 2b) relaxes to zero after a finite decorrelation time (1.03 s for CCNTs and 0.95 s for uCCNTs), the MSD of long trajectories (Figure 2d) resolves discrete dynamical regimes that map directly onto independently visualized chamber and tunnel geometries (Figure 2e, Figure 3a), turning-angle peak shifts systematically with nanotube length (110° for uCCNT vs. 140° for CCNT, Figure 2c) and the NGP of both uCCNTs and CCNTs are divergent with increasing timescales (Supplementary Figure 7). These are the classic signatures of obstructed diffusion by rigid-like boundaries, not of fBm[38]. These two independent lines of evidence show that our system therefore already operates in the

geometrically "hard" regime relevant to nanotube transport, despite the physically deformable nature of the droplet. Systematically tuning the interfacial tension to explore a genuine soft-to-hard transition remains an interesting avenue for future work.

Our results reveal that geometric frustration, arising from repeated wall-mediated collisions within a continuous, structured environment, is key to understanding anomalous diffusion and length-dependent escape dynamics of a rigid 1D tracer. In the absence of pore-mediated trapping, wall deformation or binding interactions, the convex architecture of interconnected chambers and tunnels alone is sufficient to generate antipersistent and subdiffusive behavior of the nanotubes. This anomalous transport does not rely on strong trapping or persistent alignment, but instead emerges from interactions with a heterogeneous geometry, where boundary collisions and intermittent confinement progressively shape particle motion. Nanotube length dictates how this geometric frustration is resolved. Short nanotubes primarily undergo near-isotropic, Brownian-like exploration of the volume, with rotational diffusion that may only be transiently affected during collision events. Their escape is thus governed by a first-passage process, dependent on the probability of reaching an opening through stochastic search. In contrast, longer nanotubes, whose dimensions approach those of the confining chambers, experience sustained rotational constraints. Their extended geometry promotes alignment along available spatial pathways, effectively pre-aligning them within tunnels and facilitating directional transport. Overall, the interplay between particle anisotropy and local architecture can enhance, rather than hinder, transport, giving rise to geometry-driven funneling effects.

The weak length-dependence of escape times reported here is conceptually related to, yet mechanistically distinct from, the enhanced nanorod mobility documented in entangled and cross-linked polymer networks[40,41]. In those systems, rod reorientation facilitates hopping between adjacent, effectively concave mesh openings, and the resulting diffusion enhancement is often understood as a decoupling from local polymer relaxation. In our convex, wall-dominated architecture, no such mesh-hopping occurs; instead, repeated collisions with continuously curved boundaries progressively pre-align the nanotube with

the escape pathway itself, so that the same rotational-translational coupling that speeds up mesh traversal in network systems here suppresses the length-dependence of escape from a single confining chamber. This distinction highlights that anisotropy-mediated enhancement of transport can arise from at least two distinct geometric mechanisms (mesh-hopping in concave network topologies, and wall-induced pre-alignment in convex, continuous landscapes) both converging on a weaker-than-expected dependence on particle length.

These confinement ratios can be placed in the context of related systems. In entangled polymer melts, nanorods diffuse anomalously fast once their length exceeds the entanglement mesh size while their diameter remains below it ($L/\xi \approx 5.4$, $d/\xi \approx 0.6$ for TiO_2 nanorods in polystyrene[40], a confinement ratio remarkably close in magnitude to L/a_{tunnel} reported here for CCNTs, despite the absolute length scales differing by more than an order of magnitude). Within our own prior work on the brain extracellular space using the similar CNT probes, extracellular width was found to vary down to ~40 nm[37], which is directly comparable to the tunnel radii reported here (70-110 nm), supporting the relevance of this biophysical model as a geometric proxy for that biological system.

Beyond the specific system studied here, these findings may have broader implications for transport in heterogeneous environments. Biomolecular activity in continuous intra- or extracellular spaces (as opposed to pore mediated transport e.g. through nuclear pores), filtration through continuous porous materials, transport in crowded soft-matter systems, and heterogenous catalytic processes are all governed by hindered diffusion where confinement and topology can strongly modulate particle dynamics. By demonstrating that anomalous diffusion can be governed by funneling effects arising from the coupling between geometric constraints of the environment and particle anisotropy, we provide a physical framework for transport in complex systems, opening avenues for the design of materials and architectures with controlled diffusion properties.

Materials and Methods

Droplet preparation

The emulsion was synthetized by extrusion through Shirasu Porous Glass (SPG) membranes as follows: 5mL of silicone oil (viscosity = 50 cSt, Sigma Aldrich) was extruded into a solution of 10mM SDS through a cylindrical SPG membrane with a mean pore size of 1.6 micrometers, using an Internal Pressure Micro Kit from SPG Technonolgy Co., Ltd. The droplets were then stored at room temperature. Their average diameter was ~5 μm.

To prepare the biophysical model, 5 μm diameter emulsion droplets were labelled and index-matched by diluting them at a 1:4 volume ratio in a combined labelling and index-matching solution. The index-matching buffer consisted of a 10 mM solution of sodium dodecyl sulfate (SDS) in a 1:1 (v/v) mixture of water and glycerol. For fluorescent labelling, a saturated solution of Nile Red in the index-matching buffer was used. Depending on the desired labelling intensity, the Nile Red solution was further diluted in the index-matching buffer prior to use.

Emulsions were incubated in this solution for several days to allow complete phase separation between the emulsion and aqueous phases. Once phase separation was achieved, CCNTs were introduced by gently pipetting 1 μL of the CCNTs (diluted to 1:20,000 in the index matching buffer) directly into the emulsion phase only, taking care not to disrupt the phase boundary. To obtain a densely packed droplet system, the sample was centrifuged at 4500 g, facilitating close packing of the emulsions. This configuration allows the CCNTs to explore the extracellular regions between droplets. The final sample was carefully scooped onto a coverslip with an imaging spacer (50 μm thickness) for imaging with the spatula. A similar procedure was used to prepare packed droplets with uCCNTs.

The 2 μm diameter droplets were obtained through emulsification in a Couette apparatus as described by Brujić J, et al.[63]. Briefly, a coarse emulsion is first obtained by manually mixing 18 ml Silicone oil 50 cSt in 30 ml aqueous phase containing 3% w/w Tergitol (Type 15-S-7, Sigma-Aldrich) and 3% w/w alginate (Alginic acid from brown algae, Sigma-Aldrich). This solution was then injected inside a narrow gap Couette mixer (gap size = 100 μm) and

sheared at 50 rpm. The resulting emulsion was finally washed three times in 500 ml of aqueous solution containing 10 mM SDS, using a separating funnel.

Droplet Imaging

Prepared biophysical model samples containing CCNTs were imaged using a Nikon Eclipse Ti inverted microscope equipped with a Nikon Plan Apo 60× IR water-immersion objective (NA 1.27) and a double-helix phase mask (Fig 1a). White-light imaging was used to visualize the overall droplet morphology (Fig 1b).

For fluorescence imaging of the biophysical model environment, excitation was performed using a 568 nm laser at an intensity of 0.14 kW/cm^2 at the focus of the objective. Emission was collected using a 655 nm long-pass filter and recorded with a Teledyne ProEM electron-multiplying CCD camera. Optical sectioning was achieved using the Sparq module (Bliq Photonics), which enabled axial resolution down to ~500 nm.

For the SD, the characteristic chamber dimensions (~250 nm median) approached the diffraction-limited length scale, precluding reliable resolution of the chamber-tunnel geometry by fluorescence/HiLo imaging. Droplet sizes were therefore determined from white light images. From the uCCNT trajectories, chambers could be identified based on the trajectory geometry; however, uCCNTs typically spent only 3-5 time points within the tunnels, making their segmentation and quantitative characterization unreliable. Consequently, only the chamber regions were segmented and analyzed for the smaller droplets.

3D SPT imaging and localization

Videos of diffusing (6,5) CCNTs and uCCNTs were acquired in the near-infrared range by exciting at 985 nm (AeroDIODE) with an intensity of ~4 kW/cm^2 and detecting emission through a 1100 nm long-pass filter (Fig 1c). A double helix phase mask was used for engineering the PSF to localize in the lateral and axial directions. To maintain uniform excitation regardless of nanotube orientation, the laser beam was circularly polarized. Near-infrared acquisitions were made possible with the use of a C-RED2 InGaAs camera (First

Light Imaging) at frame rate of 30Hz. Localization of single particles in 3D based on the double helix PSF was achieved using the ZOLA plugin on Fiji. First, a calibration of the phase mask was performed by acquiring a Z-stack of stationary nanotubes around the focal plane, with 50 nm steps. At each step, 50 images were recorded and averaged before moving to the next step. The full range of PSFs was monitored by acquiring images in the range -3 μm to +3 μm. The ZOLA plugin on Fiji was used for phase retrieval of the double helix phase mask and to calibrate it for further localizing single particle trajectories[49]. Linking of these localizations into trajectories were carried out using home-built python codes using the trackpy library[64].

SPoT imaging and localization

CCNTs orientation were detected using SPoT, a single-particle tracking epi-fluorescence microscopy technique based on dipole spread function (DSF) engineering[33] . A vortex half-wave plate placed at the objective's back focal plane converts radially and azimuthally polarized components of the emitted fluorescence into two orthogonal linear polarization states. These components are then separated by a polarizing beam splitter, producing two spatially distinct images that are projected side-by-side onto an InGaAs camera. The 3D orientations and in-plane localization of single CCNTs were retrieved using the deep learning technique Deep-SMOLM[65] as described in details in Ruan et. al[33]. In short, the neural network was trained on a dataset of 2000 simulated images. Each training image contained 5-10 CCNTs with randomized 2D position, 3D orientations and emitter intensities with signal to noise ratios matching experimental conditions. The focal plane position was varied over a range of z ~ [-500nm, 500nm].

Trajectory Analysis

Diffusion analysis of MSD, MSAD, VACF, distribution of turning angles, RTF and normalized orientations of centered azimuthal and polar angles were carried out with home-built python codes. The trajectories were segmented manually into chambers and tunnels using the CloudCompare software based on the local geometry of the point cloud: chambers were identified as regions where the trajectory point cloud extended comparably in all directions (quasi-isotropic, compact convex hull), whereas tunnels were identified as elongated,

quasi-one-dimensional segments with a large aspect ratio between their principal and secondary extents. Segment boundaries were placed at the visually identified transition between these two point-cloud geometries, consistent with the independent chamber and tunnel dimensions obtained from HiLo images of the droplet packing (Supplementary Figure 2).

Escape-time extraction

Escape (residency) times reported in Figure 4a were extracted from approximately 80-90 independent long trajectories per nanotube population (N_{CCNT} = 82, / N_{uCCNT}= 91). Within each trajectory, every complete chamber residency (defined as a continuous dwell beginning with the particle's entry into a chamber from a connecting tunnel and ending with its exit into a - possibly different - connecting tunnel) was retained as one independent residency-time sample, with escape time taken as the elapsed time between these two events. A single trajectory could therefore contribute more than one residency event. Truncated dwells, i.e. those for which recording began or ended while the particle was already inside a chamber, were excluded from the analysis. No explicit chamber-size selection criterion was applied meaning that all valid, non-truncated chambers were retained, yielding the final pool of 150 (CCNT) and 148 (uCCNT) residency-time events reported in the manuscript. Similarly for the uCCNTs diffusing in the SD, 97 non truncated chambers were extracted. The resulting distributions of chamber sizes for the two nanotube populations, which overlap substantially, are shown in Supplementary Figure 2c.

Quantification of local geometry

To independently quantify the dimensions of the chambers and tunnels, optically sectioned images of the biophysical model obtained by HiLo were analyzed using Fiji. A threshold was applied to segment the chambers, and their dimensions were estimated by the diameter of the inscribed circle into each chamber (Supplementary Figure 2), resulting in a mean chamber dimension of 760 ± 170 nm. These values are consistent with those obtained from segmented trajectories, where a convex hull was fitted to each trajectory to estimate an

effective diameter, defined as twice the distance from the centroid to the nearest point on the hull. For the long CCNTs, this resulted in a mean chamber dimension of 640 ± 290 nm whereas for the uCCNTs, the mean chamber dimension was found to be 860 ± 330 nm (Supplementary Figure 2b). For the tunnels, due to the limited resolution of HiLo images, their radii were determined only from trajectories. The radius was calculated as the geometric mean of the two smaller semi-minor axes from an ellipsoid fit onto each tunnel trajectory[36]. The mean radius of the tunnels from long CCNTs was determined to be 70 ± 20 nm while the uCCNT trajectories gave 110 ± 30 nm (Supplementary Figure 2c). The differences in estimated dimensions obtained from HiLo imaging and from nanotube trajectories arise intrinsically from the nature of the measurement techniques. SPT relies on localizing particles via their center of mass and therefore does not account for their full spatial extent or the steric constraints they experience. Due to their larger length, CCNTs interact more frequently with confining boundaries and experience stronger geometric hindrance than uCCNTs. As a result, trajectories of longer CCNTs tend to underestimate the true dimensions of the environment.

Simulations

Escape-time ratios between long and short nanotubes were estimated using a Monte Carlo parameter sampling of the analytical model derived from equations 3, 4, 5, and 6:

$$\frac{\tau_{\mathrm{long}}}{\tau_{\mathrm{short}}} \approx \frac{\left(L_{\mathrm{long}}\ln(2L_{\mathrm{short}}/d)\right)(L_{\mathrm{long}}/a)}{L_{\mathrm{short}}\ln(2L_{\mathrm{long}}/d)(1+4L_{\mathrm{short}}/a)} \quad (9)$$

where L_{long} and L_{short} are nanotube lengths for the CCNTs and uCCNTs respectively, a is the escape hole radius determined as the radius of the tunnels as observed by the uCCNTs, and d is the nanotube diameter. Parameters were randomly sampled from experimentally constrained ranges ($L_{\mathrm{long}} = 200$–1000 nm, $L_{\mathrm{short}} = 30$–150nm, $a = 70$–270nm), with

distributions centered on their respective mean values. The diameter was fixed at $d = 3\text{nm}$. For each realization, the escape-time ratio was computed, and a total of $N = 10000$ independent samples were generated.

Acknowledgments

The authors thank Jacques Fattaccioli for the use of the Couette apparatus. This work received financial support from the European Research Council Synergy grant (951294), Agence Nationale de la Recherche (ANR-24-CE09-2351-01), EUR Light&T (PIA3 Program, ANR-17-EURE-0027), the France-Bioimaging National Infrastructure (ANR-10-INBS- 04-01), and the Idex Bordeaux (Grand Research Program GPR LIGHT). LR is financially supported by the China Scholarship Council (Grant No. 202208330010). L.L.P acknowledges financial support from Agence Nationale de la Recherche (ANR-23-CE13-0025-02, ANR-23-CE13-0023-02, ANR-25-CE30-2977-01).

Supporting information

Quantification of droplet structure; Nanotube length to chamber and tunnel size ratios; Distribution of lengths of CCNTs and uCCNTs; Estimation of dimensions of the biophysical model; Diffusion analysis in bulk liquid ; Distribution of normalized polar angles; Distribution of normalized escape; Non-gaussianity confirms obstructed diffusion.

References

1. Einstein, A. Über die von der molekularkinetischen Theorie der Wärme geforderte Bewegung von in ruhenden Flüssigkeiten suspendierten Teilchen. *Ann. Phys.* **4, t. 17**, (1905).
2. Perrin, J. Mouvement brownien et réalité moléculaire.
3. Metzler, R. & Klafter, J. The random walk's guide to anomalous diffusion: a fractional dynamics approach. *Phys. Rep.* **339**, 1–77 (2000).

4. Saxton, M. J. Anomalous diffusion due to obstacles: a Monte Carlo study. *Biophys. J.* **66**, 394–401 (1994).
5. Sokolov, I. M. Models of anomalous diffusion in crowded environments. *Soft Matter* **8**, 9043–9052 (2012).
6. Syková, E. & Nicholson, C. Diffusion in Brain Extracellular Space. *Physiol. Rev.* **88**, 1277–1340 (2008).
7. Lin, Y., Lin, H. & Welsher, K. D. Super-Resolving Particle Diffusion Heterogeneity in Porous Hydrogels via High-Speed 3D Active-Feedback Single-Particle Tracking Microscopy. *Small* **21**, e05319 (2025).
8. Maris, J. J. E., Fu, D., Meirer, F. & Weckhuysen, B. M. Single-molecule observation of diffusion and catalysis in nanoporous solids. *Adsorption* **27**, 423–452 (2021).
9. Skaug, M. J. & Schwartz, D. K. Tracking Nanoparticle Diffusion in Porous Filtration Media. *Ind. Eng. Chem. Res.* **54**, 4414–4419 (2015).
10. Wu, H. & Schwartz, D. K. Nanoparticle Tracking to Probe Transport in Porous Media. *Acc. Chem. Res.* **53**, 2130–2139 (2020).
11. Kärger, J. & M. Ruthven, D. Diffusion in nanoporous materials: fundamental principles, insights and challenges. *New J. Chem.* **40**, 4027–4048 (2016).
12. Vincent, C. *et al.* Probing and modeling cell–cell communication in 2D biomimetic tissues. *Soft Matter* **22**, 2321–2328 (2026).
13. Valet, M., Pontani, L.-L., Voituriez, R., Wandersman, E. & Prevost, A. M. Diffusion through Nanopores in Connected Lipid Bilayer Networks. *Phys. Rev. Lett.* **123**, 088101 (2019).
14. Manley, S. *et al.* High-density mapping of single-molecule trajectories with photoactivated localization microscopy. *Nat. Methods* **5**, 155–157 (2008).

15. Jaqaman, K. *et al.* Robust single-particle tracking in live-cell time-lapse sequences. *Nat. Methods* **5**, 695–702 (2008).
16. Nandi, S. *et al.* Ultrashort Carbon Nanotubes with Luminescent Color Centers Are Bright NIR-II Nanoemitters. *ACS Nano* **19**, 19818–19830 (2025).
17. Danné, N. *et al.* Ultrashort Carbon Nanotubes That Fluoresce Brightly in the Near-Infrared. *ACS Nano* **12**, 6059–6065 (2018).
18. Ayed, Z. *et al.* Self-Assembled Small Interfering RNA-Gold Supraclusters Detected at the Single-Molecule Level in the Near-Infrared-II Window. *Small Struct.* **6**, 2500381 (2025).
19. Bechinger, C. *et al.* Active Particles in Complex and Crowded Environments. *Rev. Mod. Phys.* **88**, 045006 (2016).
20. Bruchez, M., Moronne, M., Gin, P., Weiss, S. & Alivisatos, A. P. Semiconductor Nanocrystals as Fluorescent Biological Labels. *Science* **281**, 2013–2016 (1998).
21. Fu, A., Gu, W., Larabell, C. & Alivisatos, A. P. Semiconductor nanocrystals for biological imaging. *Curr. Opin. Neurobiol.* **15**, 568–575 (2005).
22. Luo, H.-Y., Jiang, C., Dou, S.-X., Wang, P.-Y. & Li, H. Quantum Dot-Based Three-Dimensional Single-Particle Tracking Characterizes the Evolution of Spatiotemporal Heterogeneity in Necrotic Cells. *Anal. Chem.* **96**, 11682–11689 (2024).
23. Mastro, A. M., Babich, M. A., Taylor, W. D. & Keith, A. D. Diffusion of a small molecule in the cytoplasm of mammalian cells. *Proc. Natl. Acad. Sci.* **81**, 3414–3418 (1984).
24. Höfling, F. & Franosch, T. Anomalous transport in the crowded world of biological cells. *Rep. Prog. Phys.* **76**, 046602 (2013).
25. Nicholson, C. & Syková, E. Extracellular space structure revealed by diffusion analysis. *Trends Neurosci.* **21**, 207–215 (1998).

26. Saxton, M. J. & Jacobson, K. SINGLE-PARTICLE TRACKING:Applications to Membrane Dynamics. *Annu. Rev. Biophys.* **26**, 373–399 (1997).
27. Tardin, C. Direct imaging of lateral movements of AMPA receptors inside synapses. *EMBO J.* **22**, 4656–4665 (2003).
28. Betzig, E. *et al.* Imaging Intracellular Fluorescent Proteins at Nanometer Resolution. *Science* **313**, 1642–1645 (2006).
29. Wang, D., Wu, H., Liu, L., Chen, J. & Schwartz, D. K. Diffusive Escape of a Nanoparticle from a Porous Cavity. *Phys. Rev. Lett.* **123**, 118002 (2019).
30. Shi, A. & Schwartz, D. K. Bridging Macroscopic Diffusion and Microscopic Cavity Escape of Brownian and Active Particles in Irregular Porous Networks. *ACS Nano* **18**, 22864–22873 (2024).
31. Sarfati, R., Calderon, C. P. & Schwartz, D. K. Enhanced Diffusive Transport in Fluctuating Porous Media. *ACS Nano* **15**, 7392–7398 (2021).
32. Bouchaud, J.-P. & Georges, A. Anomalous diffusion in disordered media: Statistical mechanisms, models and physical applications. *Phys. Rep.* **195**, 127–293 (1990).
33. Ruan, L. *et al.* Nanoscale rheological heterogeneity revealed by Single Particle orientation Tracking (SPoT) of ultrashort carbon nanotubes in brain tissue. Preprint at https://doi.org/10.64898/2026.05.04.721587 (2026).
34. Han, Y. *et al.* Brownian Motion of an Ellipsoid. *Science* **314**, 626–630 (2006).
35. Paviolo, C. & Cognet, L. Near-infrared nanoscopy with carbon-based nanoparticles for the exploration of the brain extracellular space. *Neurobiol. Dis.* **153**, 105328 (2021).

36. Paviolo, C. *et al.* Nanoscale exploration of the extracellular space in the live brain by combining single carbon nanotube tracking and super-resolution imaging analysis. *Methods* **174**, 91–99 (2020).
37. Paviolo, C. *et al.* Near-Infrared Carbon Nanotube Tracking Reveals the Nanoscale Extracellular Space around Synapses. *Nano Lett.* **22**, 6849–6856 (2022).
38. Gresil, Q. *et al.* Scale-Dependent Emergence of Hindered Diffusion in the Brain Extracellular Space. Preprint at https://doi.org/10.48550/ARXIV.2603.18936 (2026).
39. Lee, A. *et al.* Identification of Early Stage Liver Fibrosis by Modifications in the Interstitial Space Diffusive Microenvironment Using Fluorescent Single-Walled Carbon Nanotubes. *Nano Lett.* **24**, 5603–5609 (2024).
40. Choi, J. *et al.* Fast Nanorod Diffusion through Entangled Polymer Melts. *ACS Macro Lett.* **4**, 952–956 (2015).
41. Zhang, X. *et al.* Unconventionally fast transport through sliding dynamics of rodlike particles in macromolecular networks. *Nat. Commun.* **15**, 525 (2024).
42. Tang, Z. *et al.* Single-walled carbon nanotube reptation dynamics in submicron sized pores from randomly packed mono-sized colloids. *Soft Matter* **18**, 5509–5517 (2022).
43. Fakhri, N., MacKintosh, F. C., Lounis, B., Cognet, L. & Pasquali, M. Brownian Motion of Stiff Filaments in a Crowded Environment. *Science* **330**, 1804–1807 (2010).
44. Doi, M. & Xu, X. Diffusion Limited Escape Rate of a Complex Molecule in Multi-dimensional Confinement. *J. Phys. Chem. B* **126**, 6171–6179 (2022).
45. Pontani, L.-L., Jorjadze, I., Viasnoff, V. & Brujic, J. Biomimetic emulsions reveal the effect of mechanical forces on cell–cell adhesion. *Proc. Natl. Acad. Sci.* **109**, 9839–9844 (2012).

46. Brujić, J. *et al.* Measuring the Coordination Number and Entropy of a 3D Jammed Emulsion Packing by Confocal Microscopy. *Phys. Rev. Lett.* **98**, 248001 (2007).
47. Montel, L. *et al.* Adhesion Percolation Determines Global Deformation Behavior in Biomimetic Emulsions. *Front. Phys.* **9**, (2021).
48. Guigue, Q. *et al.* Adhesion differentials control the rheology of biomimetic emulsions. *Biophys. J.* **125**, 1686–1700 (2026).
49. Aristov, A., Lelandais, B., Rensen, E. & Zimmer, C. ZOLA-3D allows flexible 3D localization microscopy over an adjustable axial range. *Nat. Commun.* **9**, 2409 (2018).
50. Lim, D., Chu, K. K. & Mertz, J. Wide-field fluorescence sectioning with hybrid speckle and uniform-illumination microscopy. *Opt. Lett.* **33**, 1819–1821 (2008).
51. Rehfeldt, F. & Weiss, M. The random walker's toolbox for analyzing single-particle tracking data. *Soft Matter* **19**, 5206–5222 (2023).
52. DELESSE, A. Procede mecanique pour determiner la composition des roches. *Ann Min* **13**, 379–388 (1848).
53. Underwood, E. E. *Quantitative Stereology*. (Addison-Wesley Publishing Company, 1970).
55. Brasselet, S. & Lew, M. D. Single-molecule orientation and localization microscopy. *Nat. Photonics* **19**, 925–937 (2025).
56. Zhang, O., Zhou, W., Lu, J., Wu, T. & Lew, M. D. Resolving the Three-Dimensional Rotational and Translational Dynamics of Single Molecules Using Radially and Azimuthally Polarized Fluorescence. *Nano Lett.* **22**, 1024–1031 (2022).
57. Bénichou, O., Chevalier, C., Klafter, J., Meyer, B. & Voituriez, R. Geometry-controlled kinetics. *Nat. Chem.* **2**, 472–477 (2010).

58. Holcman, D., Hoze, N. & Schuss, Z. Narrow escape through a funnel and effective diffusion on a crowded membrane. *Phys. Rev. E* **84**, 021906 (2011).
59. Bénichou, O., Chevalier, C., Klafter, J., Meyer, B. & Voituriez, R. Geometry-controlled kinetics. *Nat. Chem.* **2**, 472–477 (2010).
60. Brujic, J. & College, C. Experimental Study of Stress Transmission Through Particulate Matter.
61. Metzler, R., Jeon, J.-H., Cherstvy, A. G. & Barkai, E. Anomalous diffusion models and their properties: non-stationarity, non-ergodicity, and ageing at the centenary of single particle tracking. *Phys. Chem. Chem. Phys.* **16**, 24128–24164 (2014).
62. Metzler, R. & Weiss, M. Discriminating stochastic processes for the assessment of materials properties by diffusion measurements. *Phys. Chem. Chem. Phys.* **27**, 14350–14358 (2025).
63. Brujić, J. *et al.* 3D bulk measurements of the force distribution in a compressed emulsion system. *Faraday Discuss.* **123**, 207–220 (2003).
64. Allan, D. B., Caswell, T., Keim, N. C., van der Wel, C. M. & Verweij, R. W. soft-matter/trackpy: v0.7. Zenodo https://doi.org/10.5281/zenodo.16089574 (2025).
65. Wu, T., Lu, P., Rahman, M. A., Li, X. & Lew, M. D. Deep-SMOLM: deep learning resolves the 3D orientations and 2D positions of overlapping single molecules with optimal nanoscale resolution. *Opt. Express* **30**, 36761 (2022).

Supplementary Information

Orientational frustration drives enhanced diffusion of anisotropic particles in a liquid labyrinth

Rohit Mangalwedhekar[1,2], Limeng Ruan[1,2], Somen Nandi[1,2], Quentin Gresil[1,2], Marc Tondusson[1,2], Stephane Bancelin[1,2], Lea-Laetitia Pontani[3,4], Laurent Cognet[1,2,*]

[1] *Laboratoire Photonique Numerique et Nanosciences, Université de Bordeaux, 33400 Talence, France,*
[2] *LP2N, Institut d'Optique Graduate School, CNRS UMR 5298, 33400 Talence, France*
[3] *Sorbonne Université, CNRS, Laboratoire Jean Perrin, LJP, F-75005 Paris, France*
[4] *Sorbonne Université, CNRS, Inserm, Institut de Biologie Paris-Seine, IBPS, F75005 Paris, France*

Table 1a: Quantification of droplet structure.

Quantity	**Population / method**	**Value**
Droplet diameter	HiLo imaging, (particle-independent)	4.3 ± 1 μm
Chamber dimension D_c	HiLo imaging (particle-independent)	760 ± 170 nm
	CCNT-trajectory convex hull	640 ± 290 nm
	uCCNT-trajectory convex hull	860 ± 330 nm
Tunnel (constriction) radius a	CCNT-trajectory ellipsoid fit	70 ± 20 nm
	uCCNT-trajectory ellipsoid fit	110 ± 30 nm
Nanotube length L	CCNT (AFM)	500 ± 200 nm
	uCCNT (AFM)	50 ± 60 nm
Interstitial area fraction (2D) / Volume porosity ϕ (3D)	From HiLo imaging, particle-independent	12 ± 1 %

Table 1b: Nanotube length to chamber and tunnel size ratios. Both ratios are computed using the full range of chamber (640-860 nm) and tunnel-radius (70-110 nm) estimates in Table 1a (i.e. spanning the CCNT-derived, uCCNT-derived, and (for the chamber) independent HiLo values). The independent, particle-agnostic HiLo chamber estimate (760 nm) falls within the stated range in both cases.

Dimensionless ratio	**CCNT**	**uCCNT**
L / D_c	0.58 - 0.78	0.06 - 0.08
L / a	4.5 - 7.1	0.45 - 0.71

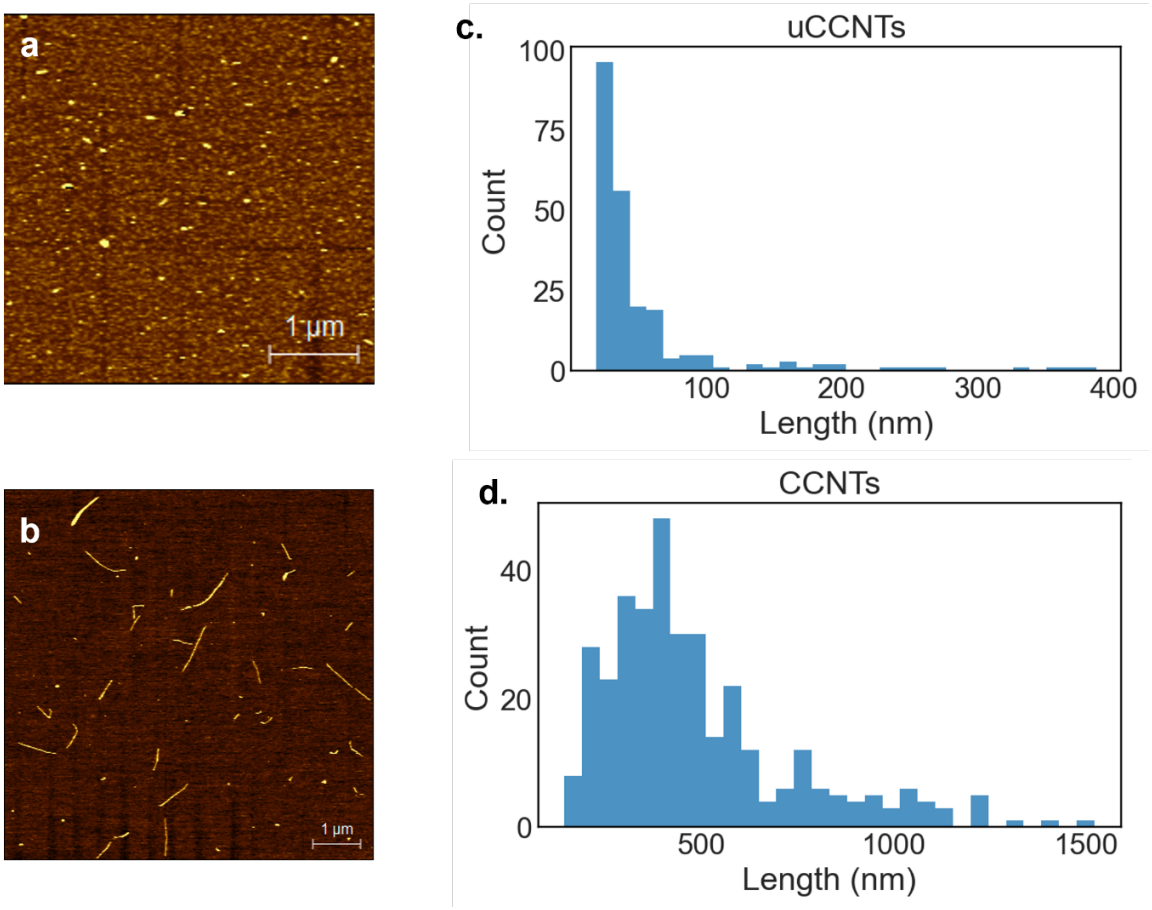

Figure S1 Distribution of lengths of CCNTs and uCCNTs Representative AFM images of a. uCCNTs and b. of CCNTs. Corresponding distribution of lengths of c. uCCNTs (mean length: 50 ± 60 nm) and d. CCNTs (mean length : 500 ± 200 nm), respectively.

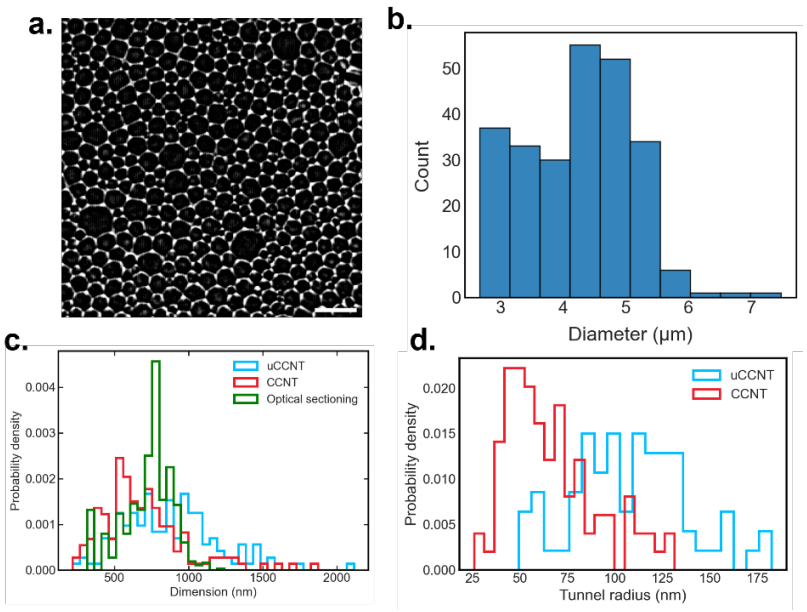

Figure S2 Estimation of dimensions of the biophysical model a. Representative optically sectioned fluorescence (HiLo) image of packed emulsion droplets (scale bar : 5 μm) b.The distribution of diameters of the droplets as measured by Hough circle transform on HiLo images using Fiji. The median diameter was 4.3 ± 1 μm. c. The distribution of dimensions of the chambers shows a median dimension of 640 ± 290 nm when measured from CCNT trajectories, 860± 330 nm from uCCNT trajectories, and 760 ± 170 nm from segmentation of the HiLo images. d. The distribution of tunnel radii estimated from the geometric mean of fitted ellipsoids provides a median radius of 70 ± 20 nm with the CCNT trajectories and 110 ± 30 nm with the uCCNT trajectories.

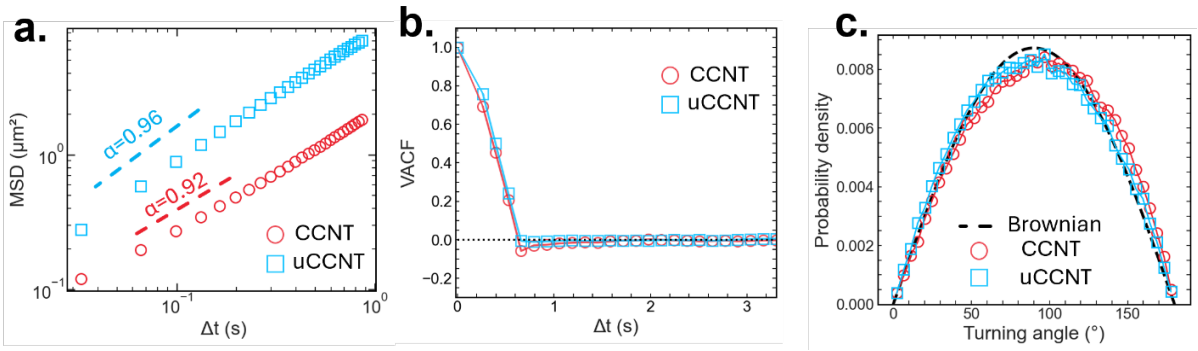

Figure S3 Diffusion analysis in bulk liquid a. MSD of CCNTs and uCCNTs in bulk liquid shows near Brownian diffusion for both CCNTs and uCCNTs. b. VACF of CCNTs and uCCNTs shows completely uncorrelated steps in Brownian motion in bulk liquid. c. The 3D distribution of angles closely follows the theoretical Brownian motion prediction (dashed black line).

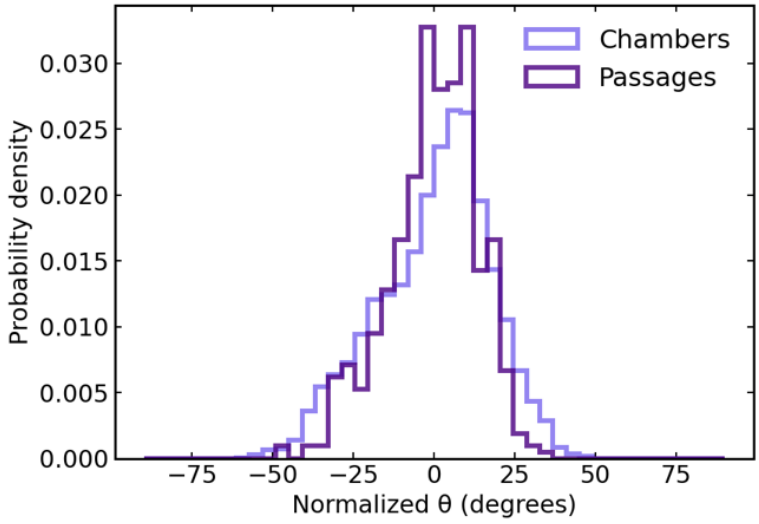

Figure S4 Distribution of normalized polar angles The normalized distribution of the polar angles in the chambers and tunnels reveals similar variance in both geometries since only in-plane trajectories can be imaged, tracked, and segmented.

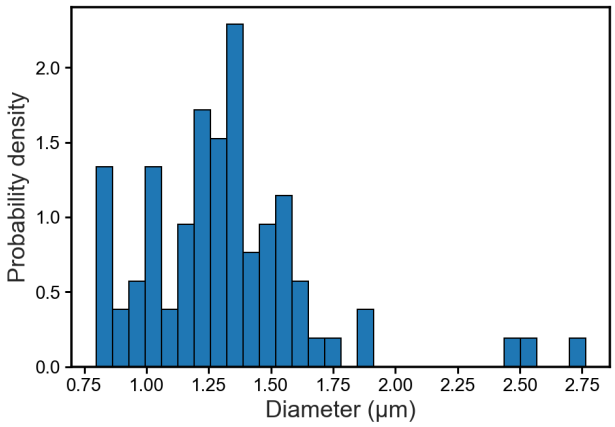

Figure S5 Size distribution of small droplets (SDs). Diameter distribution of SDs determined by threshold-based analysis of white-light microscopy images, yielding a mean diameter of 1.4 ± 0.5 μm.

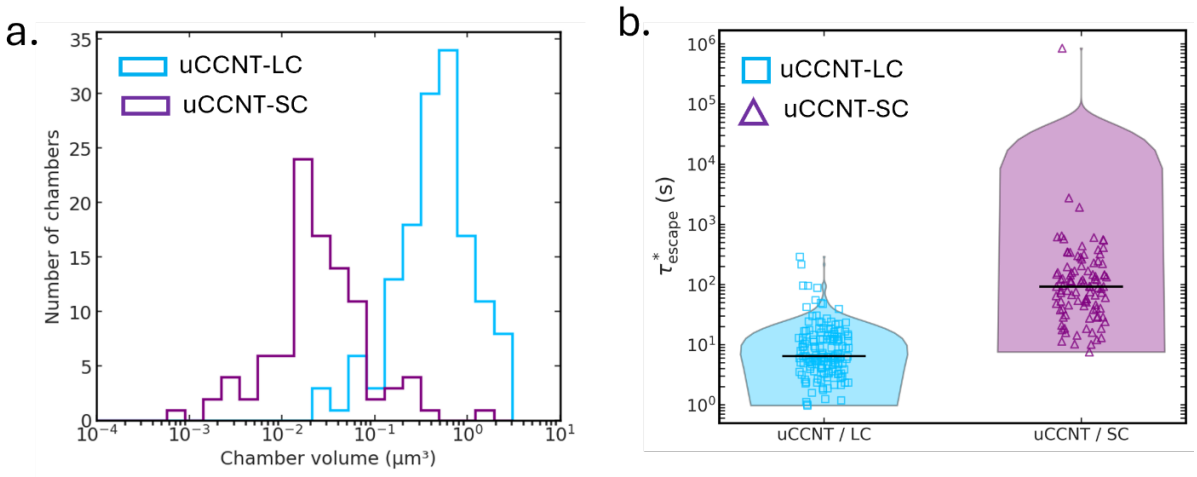

Figure S6 Distribution of normalized escape times a. Distribution of volumes of SC and LC obtained from diffusing uCCNTs b. Escape times of uCCNTs normalized by the characteristic volume scale. Despite this normalization, the escape times remain markedly different between LCs (median 7.28 s) and SCs (median 100.3 s).

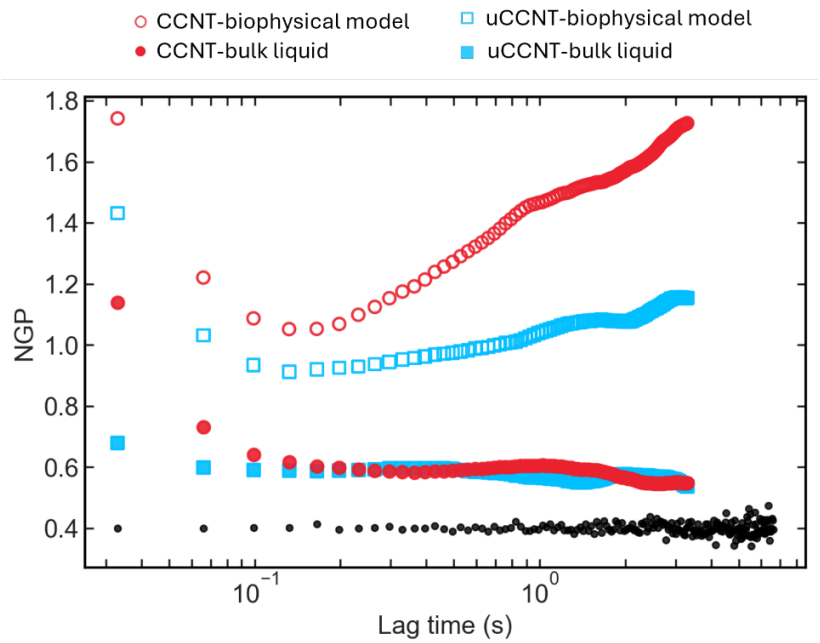

Figure S7 Non-gaussianity confirms obstructed diffusion The uCCNTs and CCNTs diffusing in the biophysical model show strong divergence with increased non gaussianity. The nanotubes diffusing in bulk Brownian fluid converge towards gaussianity. The NGP of a simulated fraction Brownian system has been shown as a reference (black).

Appendix B

Paper-II: Click'n ROPISA: One-pot synthesis of ultrabright fluorescent nanoparticles made of polypeptides

6 April 2026

Click’n ROPISA: One-pot Synthesis of Ultrabright Fluorescent Nanoparticles made of polypeptides

Amin El Jarroudi Hammou [1,2], Juliette Lavainne[1], Rohit Mangalwedhekar[3,4], Jyothis Devasia[1], Laurent Cognet[3,4], Sébastien Lecommandoux[2,5], Colin Bonduelle[2], Chloe Grazon

1. Univ. Bordeaux, CNRS, Bordeaux INP, ISM, UMR 5255
2. Univ. Bordeaux, CNRS, Bordeaux INP, LCPO, UMR 5629
3. Laboratoire Photonique Numérique et Nanosciences, Univ. Bordeaux
4. LP2N, Institut d’Optique Graduate School, CNRS – UMR
5. Institut Universitaire de France (IUF)

Abstract

Fluorescent nanoparticles are widely used in bioimaging and sensing, yet their preparation relies on multistep synthetic routes that limit scalability and structural control. Here we introduce a one-pot strategy that couples aqueous ring-opening polymerization-induced self-assembly (ROPISA) of γ-propargyl-L-glutamate N-carboxyanhydride with copper-catalyzed azide–alkyne cycloaddition (CuAAC) to produce fluorescent polypep- tide nanoparticles. This synchronized “Click’n ROPISA” process enables the si multaneous formation of polypeptide nano-objects and covalent incorporation of diverse azido-functionalized fluorophores. The resulting assemblies exhibit tunable emission across the visible spectrum and are accessible at high solids content while maintaining high brightness and structural uniformity. Dense fluorophore incorporation enables efficient Förster resonance energy transfer (FRET) both within the assemblies and with dye-labeled proteins, supporting sensing applications. The intense brightness of t he red-emitting nanoparticles further enables single-particle tracking in microscopy toward advanced bioimaging.

Keywords

Anisotropy, CuAAC, FRET, microscopy, N-carboxyanhydride, PISA

Posted on 6 April 2026 — CC-BY 4.0 — This is a preprint and has not been peer reviewed. Data may be preliminary. — https://doi.org/10.26434/chemrxiv.15001630/v1

Click'n ROPISA: One-pot Synthesis of Ultrabright Fluorescent Nanoparticles made of polypeptides

Amin El Jarroudi Hammou,[1,2] Juliette Lavainne,[1] Rohit Mangalwedhekar,[3,4] Jyothis Devasia,[1] Laurent Cognet,[3,4] Sébastien Lecommandoux,[2,5] Colin Bonduelle,[2] Chloé Grazon[1, 2]

1. Univ. Bordeaux, CNRS, Bordeaux INP, ISM, UMR 5255, F-33400 Talence, France
2. Univ. Bordeaux, CNRS, Bordeaux INP, LCPO, UMR 5629, F-33600 Pessac, France
3. Laboratoire Photonique Numérique et Nanosciences, Univ. Bordeaux, 33400 Talence, France
4. LP2N, Institut d'Optique Graduate School, CNRS – UMR 5298, 33400 Talence, France
5. Institut Universitaire de France (IUF)

KEYWORDS: Anisotropy, CuAAC, FRET, microscopy, *N*-carboxyanhydride, PISA

ABSTRACT: Fluorescent nanoparticles are widely used in bioimaging and sensing, yet their preparation relies on multistep synthetic routes that limit scalability and structural control. Here we introduce a one-pot strategy that couples aqueous ring-opening polymerization-induced self-assembly (ROPISA) of γ-propargyl-L-glutamate *N*-carboxyanhydride with copper-catalyzed azide–alkyne cycloaddition (CuAAC) to produce fluorescent polypeptide nanoparticles. This synchronized "Click'n ROPISA" process enables the simultaneous formation of polypeptide nano-objects and covalent incorporation of diverse azido-functionalized fluorophores. The resulting assemblies exhibit tunable emission across the visible spectrum and are accessible at high solids content while maintaining high brightness and structural uniformity. Dense fluorophore incorporation enables efficient Förster resonance energy transfer (FRET) both within the assemblies and with dye-labeled proteins, supporting sensing applications. The intense brightness of the red-emitting nanoparticles further enables single-particle tracking in microscopy toward advanced bioimaging.

INTRODUCTION

Self-assembly plays a central role in nanofabrication, enabling the production of nanomaterials with applications in fields ranging from biomedical engineering to electronics and fluorescence spectroscopy.[1–5] In particular, luminescent nanoparticles offer an attractive alternative to small organic dyes in modern bioimaging, which relies heavily on fluorescence-based techniques. Although molecular dyes remain the most widely used probes because of their small size and accessibility, their limited brightness prevents high image resolution in microscopy and the detection of analytes at sub-nanomolar concentrations.[6–8] In contrast, luminescent nanoparticles (NPs) offer enhanced brightness and improved photostability.[7,9,10] However, leading systems such as quantum dots (QDs)[11] and up-conversion NPs[12] are typically based on non-degradable matrices, require multistep fabrication, and raise concerns regarding long-term environmental persistence. Organic dye-doped polymer NPs are an emerging alternative.[13,14] In their simplest implementation, they are obtained via nanoprecipitation of a pre-synthesized amphiphilic polymer together with an organic dye encapsulated in the hydrophobic core.[15,16] However, the process requires multiple preparation steps and is limited to relatively low concentrations of nanoparticles (0.001-0.02 wt%[17,18]). Additionally, dye leakage from the hydrophobic core occurs when the fluorophores are not specifically modified or optimized for encapsulation.[19]

Polymerization-induced self-assembly (PISA) has emerged as a powerful method that enables the simultaneous polymerization and self-assembly of amphiphilic block copolymers in a single step and at high solid contents, leading to NPs with well-defined and homogeneous architectures.[20,21] Nevertheless, most PISA rely on controlled radical polymerization, yielding to non or only partially-degradable vinyl-based cores, while fully degradable systems remain comparatively underdeveloped.[22–25] Furthermore, the direct incorporation of fluorophores into purely aqueous PISA processes has, to the best of our knowledge, not yet been achieved. Beyond the limited water solubility of many organic dyes, this limitation likely arises from their sensitivity to radical conditions, particularly for red-emitting fluorophores, as well as from the incompatibility of reactive groups (e.g., maleimides, primary amines, phenols), with radical polymerization processes, especially alkyne/azido groups involved in click-type reactions such as the Meldal-Sharpless copper-catalyzed azide–alkyne cycloaddition (CuAAC).[26,27]

Herein, we overcome all these limitations through a simple one-pot process performed entirely in water: the aqueous ring-opening polymerization-induced self-assembly (ROPISA) of *N*-carboxyanhydrides.[28] In contrast to radical-mediated PISA approaches, we demonstrate that this system is fully compatible with CuAAC.[29] Using propargyl-functionalized L-glutamate *N*-carboxyanhydride (PLG-NCA)[30–32] and azido-dyes, the kinetics of polymerization and click functionalization could be synchronized in a rapid single-step process termed

ROPISA-CuAAC (Scheme 1). This strategy affords fluorescent nanoparticles with unprecedented tunable emission across the visible spectrum (from blue-emitting coumarins to red-emitting cyanine derivatives) including particularly bright cyanine-based NPs. The ROPISA-CuAAC approach accommodates fluorophores spanning a broad range of polarity, charge, and molecular weight, underscoring its generality. In addition, we demonstrate that this novel class of nanoparticles can mediate efficient Förster resonance energy transfer (FRET),[33] both internally and with dye-labeled proteins. The intense brightness of the cyanine nanoparticles further enables their individual localization and tracking using super-resolution imaging techniques. Collectively, these results establish ROPISA-CuAAC as a versatile platform for the one-step synthesis of ultra-bright, degradable, and addressable fluorescent nanoparticles suitable for dynamic imaging and biosensing applications.

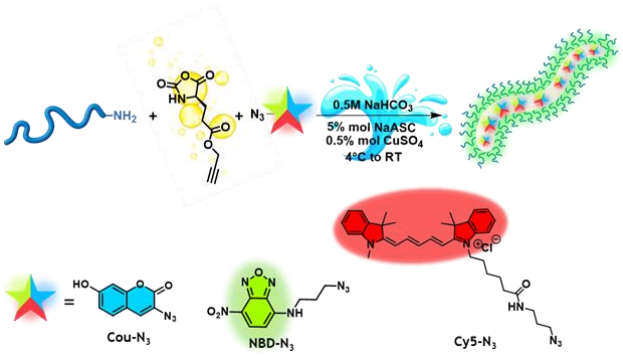

Scheme 1: One-step synthesis of fluorescent nanoparticles in water by ring opening polymerization induced by self-assembly (ROPISA) combined with copper-assisted azide alkyne cycloaddition (CuAAC): PEG-NH_2 initiates the polymerization of PLG-NCA and concomitantly an azido-dye (3-azido-7-hydroxycoumarin (Cou-N_3), *N*-(3-Azidopropyl)-7-nitro-2,1,3-benzoxadiazol-4-amine (NBD-N_3) and/or Cyanine 5-azide (Cy5-N_3) is grafted on the polymer backbone.

▪ RESULTS AND DISCUSSION

ROPISA. We first investigated the ability of γ-propargyl L-glutamate NCA (PLG-NCA) to undergo polymerization under ROPISA conditions.[28] This monomer presents a unique case, as it is a viscous liquid at room temperature, in contrast to the solid NCAs typically employed in previously reported ROPISA.[34] The synthesis of PLG-NCA is already described in the literature using different methods.[30,32,35] However, in this work, the synthesis was carried out using a phosgene-free method,[36] affording the monomer with a 43% molar yield after 3 preparation steps (Scheme SI 1, Figure SI 1-3). For the ROPISA process, the macroinitiator poly(ethylene glycol)-NH_2 (PEG-NH_2, M_n=5000g.mol^{-1}) was dissolved in bicarbonate buffer (0.05 M, pH 8.5) and introduced to PLG-NCA ([M]/[I] = 20) in a plastic microtube (Scheme SI 4). Efficient dispersion of the liquid monomer was achieved by brief vortexing followed by sonication in an ice-cooled bath. A yellowish dispersion was obtained after 10 min.

The crude product was purified by dialysis against ultrapure water for 2 days. Size exclusion chromatography (SEC) analysis revealed a leftward shift of the elution peak compared to the PEG initiator, confirming the successful formation of the block copolymer PEG-*b*-PPLG (Figure 1a). Following polymerization, the resulting nanoparticles were dialyzed and characterized by transmission electron microscopy (TEM, Figure 1c). Elongated objects with average dimensions of approximately 300 nm in length and 10 nm in width were observed. This finding confirms that, even when employing a liquid monomer, ROPISA exclusively yields elongated nanoparticles, a feature attributed to the intrinsic propensity of the polypeptide chains to adopt β-sheet secondary structures during self-assembly.[34,37,38]

ROPISA-CuAAC. A key methodology for introducing a fluorophore is the use of Meldal-Sharpless cycloaddition, a reaction that can be limited when carried out concomitantly with radical polymerization.[26,27] We anticipate that our alternative strategy, will unlock new opportunities in polymer synthesis and functional nanoparticle design. To first evaluate the potential interference of copper-based catalysts, the polymerization was conducted in the presence of copper and sodium ascorbate, hereafter referred as ROPISA-CuAAC. Remarkably, the reaction yielded a similar yellowish dispersion, and SEC analysis showed a comparable leftward shift relative to the initiator (Figure 1a). TEM analysis confirmed that the nanoparticles retained the same anisotropic morphology observed under standard ROPISA conditions (Figure 1d). In addition, the kinetic of the formation of the PPLG block during the ROPISA or ROPISA-CuAAc was monitored by SEC in DMF (Figure SI 7-8), following acid quenching.[39] Remarkably, kinetic monitoring revealed that the reaction reached completion within only 2 minutes (Figures 1b) with no detectable influence of copper on the polymerization rate. While sonication is known to accelerate NCA polymerization rates,[40] the process reported here proceeds very rapidly while maintaining excellent control over the polymer chains (M_n=8400g.mol^{-1} $Đ$=1.04). Overall, these results confirm the formation of the PEG-*b*-PPLG copolymer, indicating that CuAAC reagents did not interfere with the polymerization.

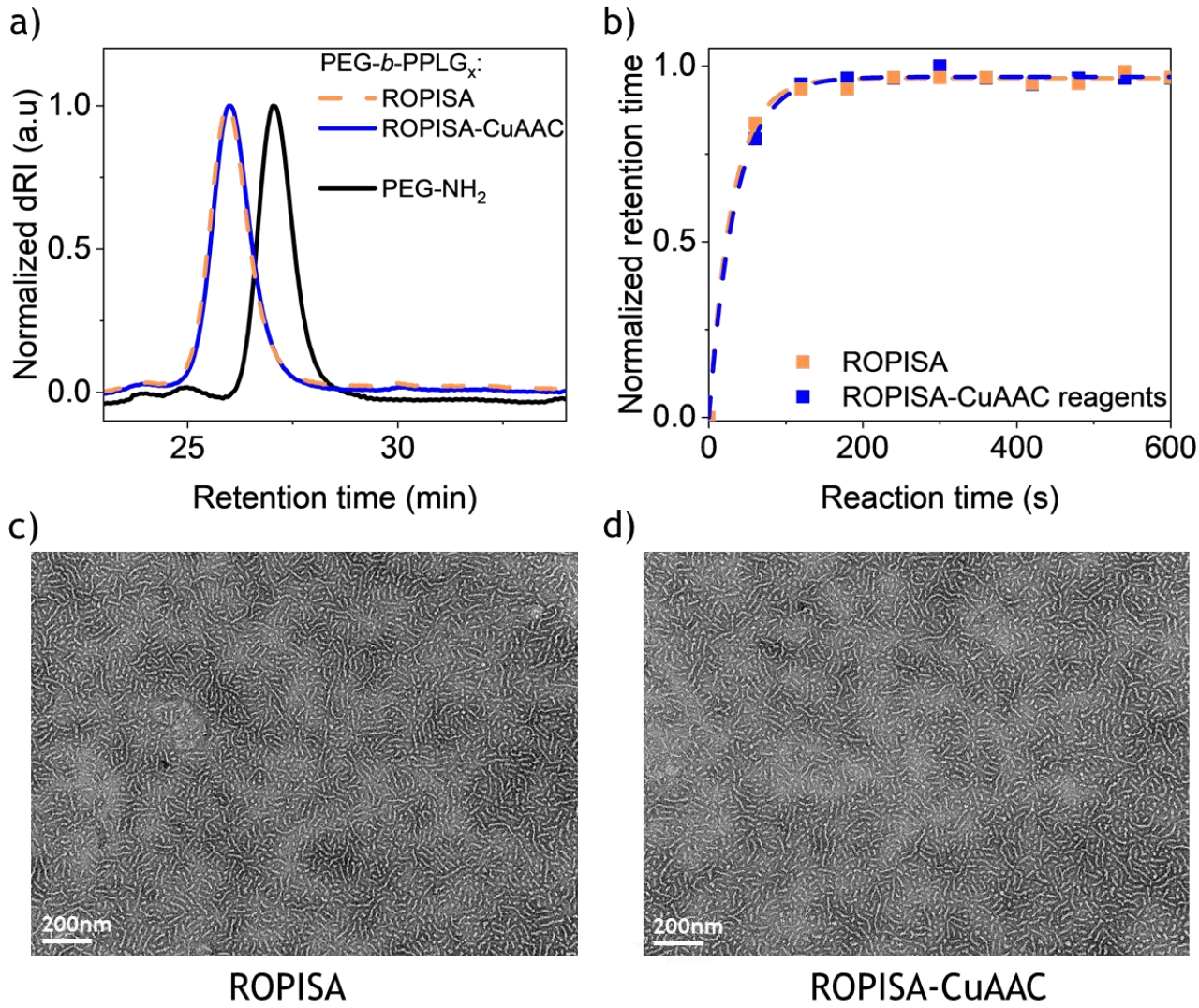

Figure 1: PEG_{113}-*b*-$PPLG_x$ NPs synthesized by ROPISA or in the ROPISA-CuAAC conditions a) Size-exclusion chromatograms of the polymers in DMF (+LiBr 1mg.ml^{-1}) b) Comparison of the normalized retention time (SEC) in function of the reaction time. c-d) TEM image of the NPs (scale bar = 200nm, stained using uranyl acetate) c) ROPISA. d) ROPISA-CuAAC.

Clicking fluorophores using ROPISA-CuAAC. Since ROPISA was found to be compatible with copper and ascorbate, we decided to incorporate a fluorophore into the ROPISA process to promote polypeptide grafting. The same protocol as described above was used, except that 3-azido-7-hydroxycoumarin (Cou-N_3, 5 % mol relative to PLG-NCA) was introduced at the beginning of the polymerization together with the other reactants (Scheme SI 5). After the synthesis, the dispersion was dialyzed to remove copper and other salts. SEC confirmed the formation of polymers with controlled molar mass (Figure 2a, M_n=7700g/mol, $Đ$=1.14) and the effective

incorporation of the dye into the polymer backbone (with the absorbance detector set to the characteristic wavelength of coumarin). In addition, absorption analysis of the purified samples allowed determination of the effective dye % in the final polymer chains (Eq. 5, Table 1). The experimental dye % is close to the theoretical value, confirming the efficiency of the synthesis. TEM and cryo-TEM images (Figure 2b-d) revealed elongated objects, once again, although a small fraction of spherical species was also observed in this case. The resulting nanoparticles absorbs at 350 nm and emit at 475 nm in water (figure 2c), with a fluorescence quantum yield of 6% associated with a lifetime of 3.3 ns (Table 1). Moreover, the brightness per volume was determined using equation (SI 6) leading to a value of 160 $M^{-1}cm^{-1}nm^{-3}$, ie in the same order of magnitude as BlueCy- doped in polymethacrylates NPs.[41]

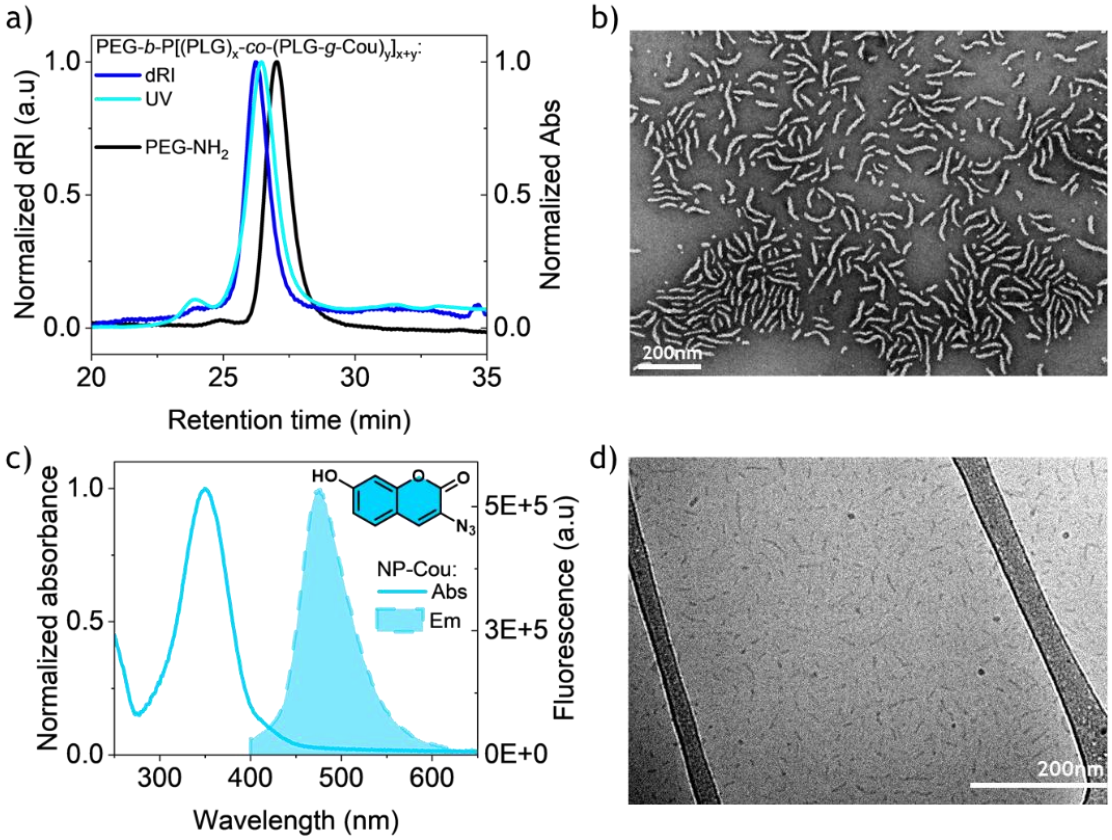

Figure 2: PEG_{113}-*b*-P[$(PLG)_x$ -*co*-$(PLG\text{-}g\text{-}Cou)_y]_{x+y}$ NPs synthesized by ROPISA-CuAAC a) Size-exclusion chromatograms of the polymers in DMF (+LiBr 1mg.ml^{-1}) RI detection, UV detection. b) TEM image of the NPs (scale bar = 200nm, stained using uranyl acetate) c) Absorption and florescence emission spectra (λ_{exc}=350 nm) of the NPs in water. d) Cryo-TEM image of the NPs in water (scale bar = 200 nm).

We then investigated the kinetics of both reactions by monitoring each process independently. Cou-N_3 is perfectly suitable for this purpose, as it is a fluorogenic probe that enables real-time monitoring of triazole formation by

fluorescence spectroscopy.[42] As shown in Figure SI 10, the reaction exhibited a gradual increase in blue fluorescence, plateauing after ~100 minutes. Comparative kinetic analysis of the ROPISA polymerization and the CuAAC click reaction were performed (Figure 3) and the kinetic profiles were fitted using a first-order exponential decay model. The CuAAC reaction displays a high-rate constant of k_{obs} = 925 s^{-1}. Since the click reaction follows a second-order rate law, from this pseudo-first-order rate constant (k_{obs}), a second-order rate constant of $k_2 = k_{obs} \times [cou\text{-}N_3]^{-1} \sim 6\times10^4\ M^{-1}.s^{-1}$ can be determined. This k_2 indicates that the CuAAC reaction is in the range of reported CuAAC kinetics in aqueous media ($k_2 \sim 10^2$-$10^4\ M^{-1}.s^{-1}$).[43–46] In opposition, the ROPISA process exhibited a significantly lower rate constant of k_1 = 34 s^{-1}. This stark contrast highlights the high efficiency of ROPISA, which reaches completion within 2 minutes, whereas the CuAAC reaction requires ~100 minutes under identical conditions. Importantly, although performed sequentially, the CuAAC click reaction does not interfere with the ROPISA process, as evidenced by the preservation of the expected polymerization behavior and particle morphology. This absence of cross-reactivity demonstrates the true orthogonality and robustness of the system, enabling temporal decoupling of polymerization and post-functionalization steps. Moreover, the invariance of the self-assembled structures during the slower CuAAC transformation suggests that the nano-objects are kinetically trapped on the experimental timescale, allowing for late-stage functionalization without structural reorganization. Collectively, these results establish a versatile platform for the controlled synthesis and modification of polymer nanostructures.

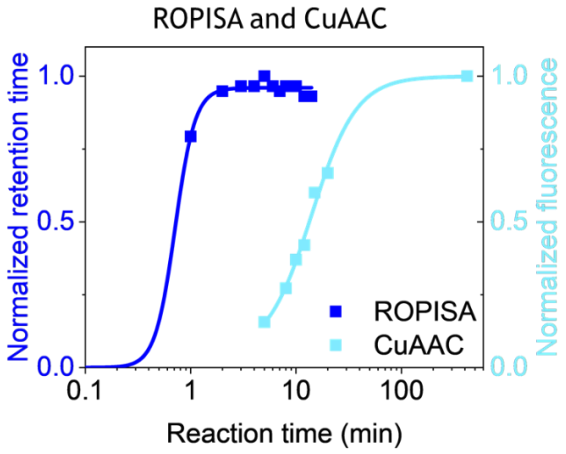

Figure 3: Comparison of the kinetics of the PPLG block formation (analyzed by size exclusion chromatography retention time) and the triazole formation (analyzed by fluorescence using the fluorogenic probe Cou-N_3, see figure SI 10). The kinetic profiles were fitted using a first-order exponential decay model.

Tuning NPs' fluorescence. For biological imaging, fluorescent probes emitting in the red or near-infrared (NIR) are highly advantageous due to deeper light tissue penetration and minimized background autofluorescence. Consequently, conventional blue-emitting dyes, such as Cou-N_3, being less suitable for *in vivo* applications. To expand the versatility of our system and enable the development of ratiometric fluorescent sensors, we incorporated multiple clickable dyes with distinct emission profiles: *N*-(3-Azidopropyl)-7-nitro-2,1,3-benzoxadiazol-4-amine (NBD-N_3, green-emitting) (Synthesis described in Scheme SI 2, Figure SI 4-5) and cyanine 5 (Cy5-N_3, red-emitting). Using NBD-N_3 (5 mol%)(Scheme SI 6), a yellow dispersion was obtained. SEC in DMF showed a shift to lower retention times, confirming copolymer formation (M_n=9500 g/mol, $Đ$=1.12). Absorption detection confirmed successful NBD incorporation into the polymer backbone. TEM revealed anisotropic nanoparticles (Figure 4b). Spectroscopic analysis indicated that the nanoparticles absorb at 470 nm and emit at 550 nm. Since NBD is a mildly solvatochromic dye, the positions of its absorption and emission bands provide information about its local environment. By comparing the spectra of the nanoparticles in water with the NBD in various solvents, we observed that the emission closely overlaps with that of propargyl alcohol (Figure SI 11), confirming that the dye is in the hydrophobic PLG environment rather in the aqueous phase. In addition, the nanoparticles present a quantum yield of 7% and a fluorescence lifetime of 2.6 ns (Figure 4c, Table 1). In addition, the brightness per volume was determined using equation (5), yielding B_v=340 $M^{-1}cm^{-1}nm^{-3}$ (Table 1). This value is consistent with literature reports for green-emitting nanoparticles. For instance, Z. Tian et al.[47] reported twisted perylene-based nanoparticles emitting at 550 nm with a comparable brightness per volume (B_v=310 $M^{-1}cm^{-1}nm^{-3}$), confirming that such polypeptidic nanoparticles fall within the same performance range, thought higher brightness values have been reported BODIPY-based nanoparticles.[14]

Finally, for Cy5 (used at 5 mol %) (Scheme SI 7), the reaction produced a blue dispersion. SEC analysis confirmed copolymer formation with M_n=8400 g/mol and $Đ$=1.14 with successful incorporation of the dye in the polymer chain (Figure 4d). Once again, TEM images showed the formation of anisotropic nanoparticles (Figure 4e). Spectroscopic characterizations in water revealed that the nanoparticles absorb at 650 nm and emit at 670 nm, similar to the isolated Cy5, with a quantum yield of 11% and a fluorescence lifetime of 0.8ns (Figure 4f, Table 1). Such NPs exhibit an exceptional B_v of 6700 $M^{-1}cm^{-1}nm^{-3}$ (Table 1), a value surpassing those reported in the literature for other red-emitting nanoparticles, especially Cy5-dopped poly(methyl methacrylate) NPs (B_v=4530 $M^{-1}cm^{-1}nm^{-3}$)[48]or Cy5-dopped in PLGA NPs (B_v=840 $M^{-1}cm^{-1}nm^{-3}$.).[49]

Table 1: Properties of the copolymers obtained by click'n ROPISA and of the corresponding fluorescent nanoparticles

Copolymer	Dye-N_3	% dye grafted			Theorical		SEC [b]		Spectroscopy				
		Theo.	exp[a]	exp	[M]/[I]	M_n	M_n	$Đ$	λ_{abs}^{max}	λ_{em}^{max}	ϕ_F [c]	τ [d]	$B_v \times 10^3$
		mol%	mol%	wt%		kg.mol.$^{-1}$	kg.mol.$^{-1}$		nm	nm	%	*ns*	M^{-1} cm^{-1} nm^{-3}
PEG_{113}-*b*-$PPLG_x$	-	-	-	-	20	8.4	8.8	1.1	-	-	-	-	-
PEG_{113}-*b*-P[$(PLG)_x$-*co*-$(PLG$-*g*-$Cou)_y]_{x+y}$	Cou-N_3	5%	4.8%	6%	20	8.6	7.7	1.1	350	475	6	3.3	0.16
PEG_{113}-*b*-P[$(PLG)_x$-*co*-$(PLG$-*g*-$NBD)_y]_{x+y}$	NBD-N_3	5%	5.2%	8%	20	8.7	9.5	1.1	470	550	7	2.6	0.34
PEG_{113}-*b*-P[$(PLG)_x$-*co*-$(PLG$-*g*-$Cy5)_y]_{x+y}$	Cy5-N_3	5%	4.4%	18%	20	9	8.4	1.1	650	670	11	0.8	6.7

a) Experimental mol% of dye grafted determined by absorption spectroscopy, using equation (5) and equation (7). b) Number-average molar mass (M_n) and molar-mass dispersity ($Đ$) determined by SEC in DMF (+1% LiBr), using polystyrene standards for calibration. c) Fluorescence quantum yield (ϕ_F), using the following references: Cou: quinine bisulfate (QBS, ϕ_F=0.546 in 0.5 M H_2SO_4),[50] NBD: 4-dicyanomethylene (DCM, ϕ_F=0.437 in EtOH)[51] and Cy5: Nile Blue (NB, ϕ_F=0.27 in EtOH).[52] d) Amplitude-weighted average fluorescence lifetime, measured at an excitation wavelength (λ^{exc}) and emission wavelength (λ^{em}) appropriate for each dye (Cou (λ^{exc}=370nm, λ^{em}=475nm), NBD (λ^{exc}=455nm, λ^{em}=560nm) and Cy5 (λ^{exc}=670nm, λ^{em}=680nm)) -based nanoparticles. e) Brightness per volume calculated using equation (6)

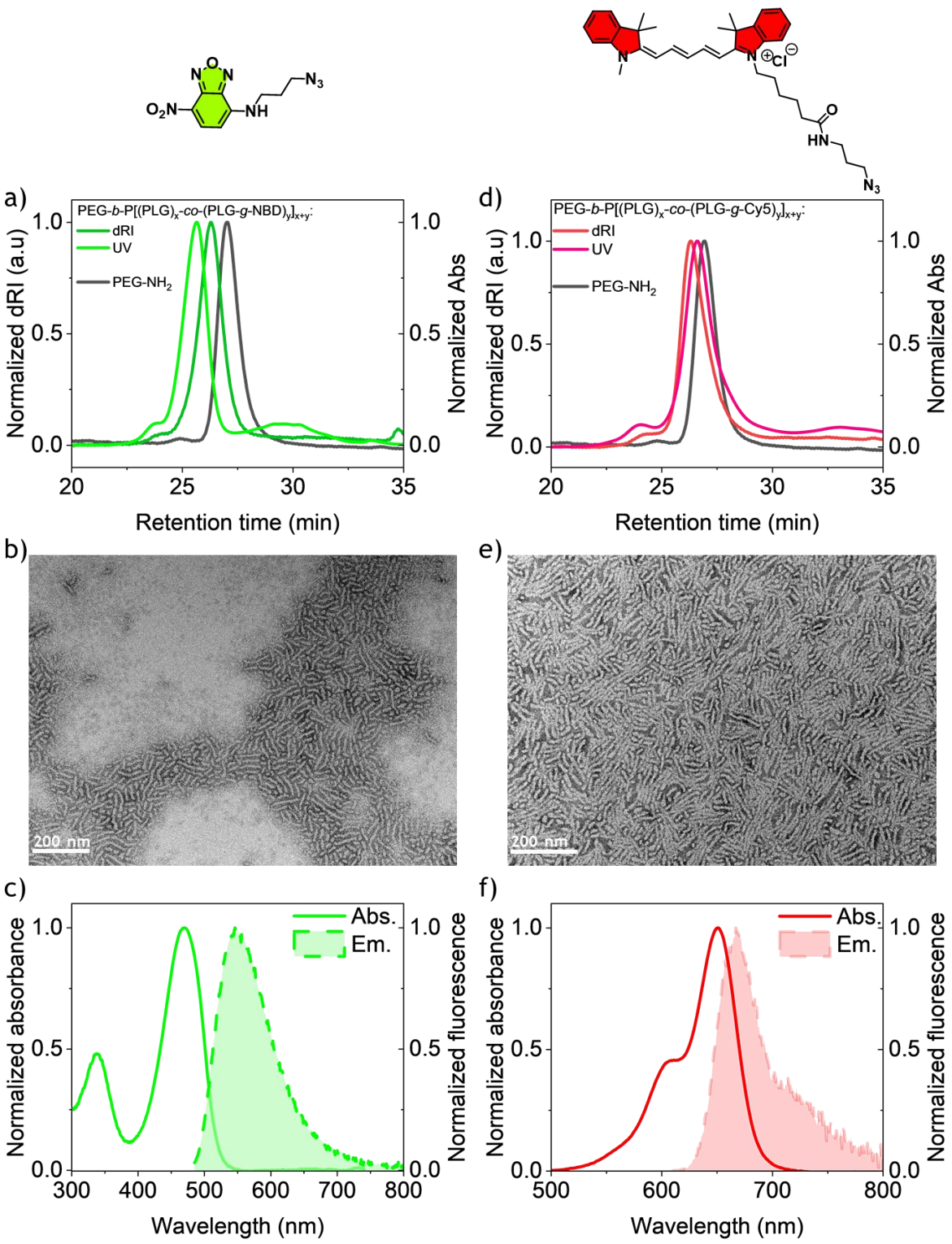

Figure 4: a-c) PEG_{113}-*b*-P$[(PLG)_x$-*co*-$(PLG$-*g*-$NBD)_y]_{x+y}$ NPs synthesized by ROPISA-CuAAC. a) Size-exclusion chromatograms of the polymers in DMF (+LiBr 1mg.ml^{-1}), RI detection, UV detection. b) TEM image of the NPs (scale bar = 200nm, stained using uranyl acetate) c) Absorption and florescence emission spectra (λ^{exc}=450nm) of the NPs in water. d-f) PEG_{113}-*b*-P$[(PLG)_x$-*co*-$(PLG$-*g*-$Cy5)_y]_{x+y}$ NPs synthesized by ROPISA-CuAAC. stained using uranyl acetate. e) TEM image of the NPs (scale bar = 200nm, stained using uranyl acetate). f) Absorption and florescence emission spectra (λ^{exc}=630nm) of the NPs in water.

This ability to incorporate molecules of diverse structures, polarities, charges, and molar masses into the PPLG chain highlights the versatility of the ROPISA approach. Importantly, the three types of nanoparticles can be freeze-dried for storage and subsequently redispersed in water without altering their morphology, demonstrating their practical stability and robustness for later applications (Figure SI 9,12,13,14).

FRET to study supramolecular copolymer assemblies (Intra-particle FRET) Förster resonance energy transfer (FRET) is widely used as a molecular nanoruler,[53] enabling the use of fluorescent probes to report on their local environment. Fluorescence spectroscopy thus affords a direct view of the molecular interactions within a single macromolecule or between different polymer chains.[54] To achieve FRET, a donor (D) and an acceptor (A) pair are required. In this work, two FRET pairs can be selected: Cou/NBD or NBD/Cy5. The Förster radius (R_0, SI eq. 8) of the Cou-NPs and NBD-NPs pair is 2.7 nm and of the NP-NBD and NP-Cy5 pair is as 4.2 nm. Therefore, the three types of fluorescent nanoparticles obtained here can, in principle, engage in pairwise FRET (D/A: Cou/NBD or D/A: NBD/Cy5). However, because the $S_0 \rightarrow S_1$ absorption band of coumarin overlaps with the $S_0 \rightarrow S_2$ band of NBD, selective excitation of the donor is not feasible. Accordingly, the NBD–NPs/Cy5-NPs pair was chosen as the most suitable FRET system. Using this FRET pair, we investigated the dynamics of polymer chain exchange within the nanoparticles. To this end, NBD–NPs and Cy5–NPs were mixed in pure water at C~0.02 mg. mL^{-1}, and the fluorescence emission ratio of acceptor to donor (upon selective excitation of the donor, i.e., NBD) was monitored over time. Samples were incubated at 4, 25, 37, or 50 °C for up to six days. At 4 °C, no spectral changes were detected, whereas at 50 °C, a pronounced Cy5 emission band progressively appeared, indicating the apparition of FRET. This observation demonstrates that polymer chains from NBD–NPs and Cy5–NPs come into close proximity through nanoparticle mixing and dynamic polymer chain exchanges, with maximum energy transfer reached after two days. Similarly, FRET was observed for samples at 25°C and 37 °C, with faster onset at higher temperatures. Fitting the experimental data with an exponential function enabled extraction of the characteristic relaxation time (τ_r) and construction of an Arrhenius plot (Figure 5c). Activation energy can be estimated from this plot, ie temperature dependence of the relaxation time (eq. SI 11,12,13) and is 70kJ.mol^{-1} for such NPs based on amphiphilic PEG-*b*-PPLG copolymers. To further elucidate this dynamic character, the glass transition temperature (Tg) of the PPLG hydrophobic core (Obtained by ROP in anhydrous conditions, Scheme SI 3) was determined by DSC analysis, yielding a value of approximately 16 °C (Figure SI 6), which is in good agreement with the literature value of ~20 °C,[55] consistent with the observed absence of exchange at 4 °C and the progressively faster dynamics at 25–50 °C. Without entering into detailed mechanistic studies, our findings

suggest that the polypeptidic nanoparticles are dynamic, with exchange processes slower than in surfactant micelles but faster than in frozen-core micelles made of block copolymers with high Tg.[56] By contrast, when the nanoparticles are mixed using ultrasonication, FRET occurs almost instantaneously and nearly reaches its maximum intensity (E~ 70%). This procedure enables the rapid formation of dual-colored NPs. Of note, the sonicated nanoparticles retain the same morphology as the original ones (Figure SI 14).

Finally, to confirm that our observations stemmed from chain exchange rather than non-specific interparticle interactions, we gradually titrated Cy5-labeled nanoparticles (Cy5-NPs) into NBD-labeled nanoparticles (NBD-NPs) and monitored the fluorescence quenching of NBD-NPs as a function of concentration (Stern-Volmer analysis, Figure SI 19c, SI eq. 10, data obtained after the deconvoluted fluorescence spectra Figure SI 16-18). The linear quenching profile obtained under static conditions indicated the occurrence of collisional quenching between nanoparticles, albeit minimal at working concentrations. By contrast, when the same experiment was performed under sonication, a bell-shaped quenching curve emerged, providing definitive evidence for the specificity of chain-exchange interactions.

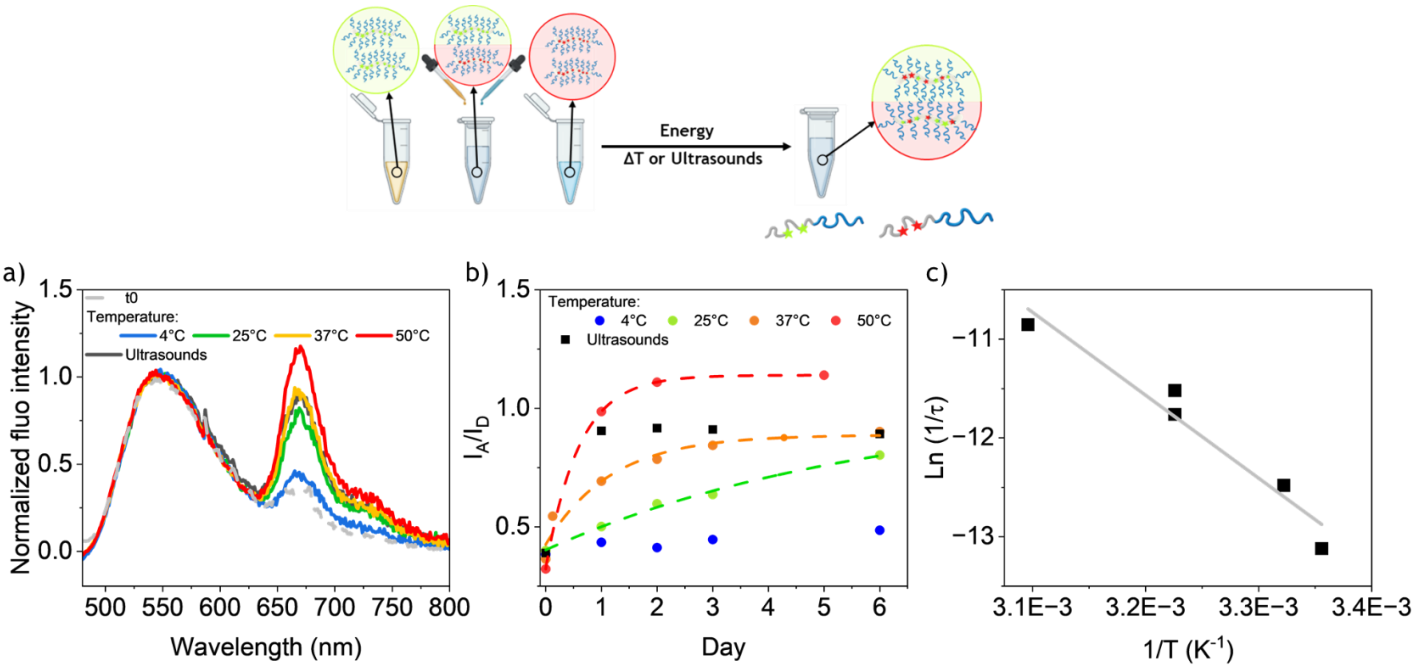

Figure 5: FRET to study chains exchange dynamics between donors PEG_{113}-*b*-P[(PLG)$_x$-*co*-(PLG-*g*-NBD)$_y$]$_{x+y}$ (D) and acceptors PEG_{113}-*b*-P[(PLG)$_x$-*co*-(PLG-*g*-Cy5)$_y$]$_{x+y}$ (A) in pure water at C~0.02mg.mL^{-1} a) Normalized fluorescence emission spectra of the donors and acceptors NPs in water, after reaching equilibrium (λ^{exc}=470nm) b) Fluorescence intensity (I_A@λ^{em}=670nm and I_D@λ^{em}=550nm) ratio of the acceptor and donor over time at different temperatures or after sonication (45°C). Experimental values (points) are fitted with Eq. 14 (dotted lines). c) Arrhenius plot.

FRET to study NP-ligand binding (core-shell FRET). To demonstrate the potential of these nanoparticles as FRET-based biosensors or biomarkers, we engineered biotin-functionalized core-shell nanoparticles (BtNBD-NPs). In this system, 10% of the macroinitiator consist of biotin-PEG-NH_2, while the remaining 90% is conventional PEG-NH_2. Synthesized under optimized ROPISA-CuAAC conditions using NBD-N_3, these nanoparticles formed a stable yellow/orange dispersion. SEC analysis in DMF confirmed the successful formation of the copolymer, as evidenced by a clear shift to higher molar masses compared to the initiator (Figure SI 15a). TEM imaging further revealed the formation of anisotropic nanoparticles (Figure SI 15b), consistent with our design.

To validate the biotin–streptavidin recognition capability, we performed a FRET binding assay using Texas Red–labeled streptavidin (TR-SA) as the acceptor (R_0 = 4.0 nm). Given the exceptionally high affinity of the biotin–streptavidin interaction ($K_d \sim 10^{-14}$ M), we anticipated robust FRET upon complex formation. Fluorescence spectroscopy confirmed this hypothesis: gradual addition of TR-SA to BtNBD-NPs resulted in quenching of the NBD emission band at 550nm, accompanied by a concomitant increase in TR-SA emission at λ^{em}= 615 nm (Figure 6a) (Figure SI 19a). This spectral shift is characteristic of FRET, demonstrating efficient energy transfer (E ~20%) (Figure 6b) (Figure SI 19d) between the NBD-NPs and TR-SA. Control experiments with biotin-free NBD-NPs showed no quenching (Figure SI 19b) (Figure SI 19c), further confirming the specificity of the interaction. Such FRET efficiencies are of the same order of magnitude as those reported for dye-labelled protein-coated with quantum dots[8] or pdots,[57] making it possible to envision similar types of FRET-based biosensing applications for these original nanostructures.

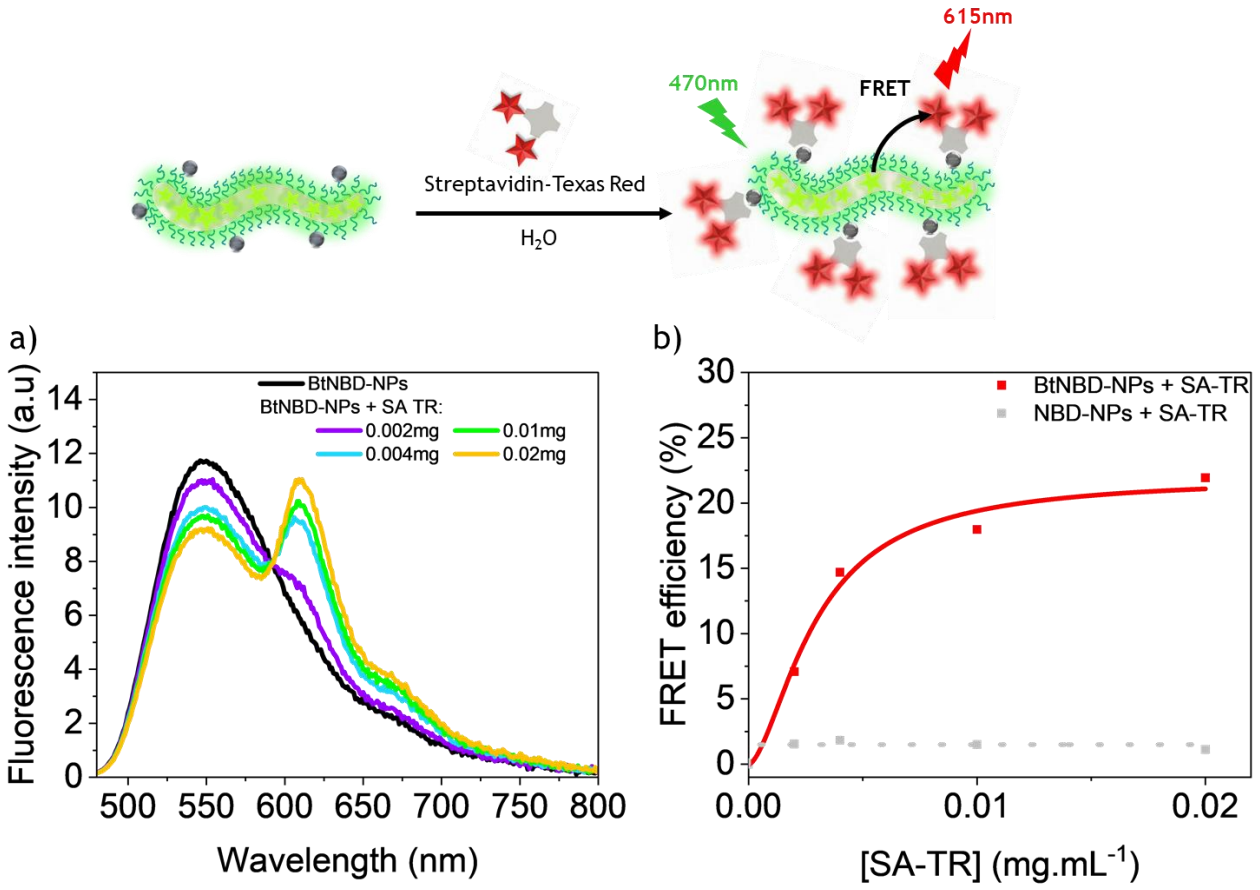

Figure 6: a) Fluorescence intensity of BtNBD-NPs excited at λ^{exc}=470nm upon addition of gradual concentrations of TR-SA b) FRET efficiency (E) of NBD-NPs and BtNBD-NPs with SA-TR. The red curve is fitted by a Hill function.

Single-particle Fluorescence Microscopy

Finally, given the exceptional absorbance and therefore brightness of the NPs-Cy5, we explored the possibility of imaging these nanoparticles at the single-particle level. Figure 7a presents a representative image of NPs-Cy5 immobilized on the surface of a glass coverslip, revealing nanoscale emitters with size below the diffraction limit (~325 nm). To further assess the detection of single particles, we analyzed 197 individual emitting nano-objects diffusing in an homogenous 1:1 water-glycerol solution (SI movie, accessible on Zenodo). After detection, we performed superlocalization of the emitters and reconstructed their trajectories.[58] This allowed calculating the evolution of the Mean Square Displacement (MSD) with lag time (Figure 7b). As expected for Brownian motion, a linear increase in MSD was observed. Using the known viscosity of 50% glycerol (9.00 ± 0.09 mPa·s)[59], we determined the diffusion constant of the particles to be 0.18 ± 0.01 $\mu m^2/s$. Applying the Stokes-Einstein relation, this value corresponds to a hydrodynamic radius of 124 ± 10 nm, consistent with the detection of single NPs-Cy5. Finally, from the trajectories, we extracted the intensity distribution of 2669 diffusing NPs-Cy5, yielding a nearly

unimodal distribution (median intensity of 752 detected photons), as anticipated for single-nanoparticle detection (Figure 7c).

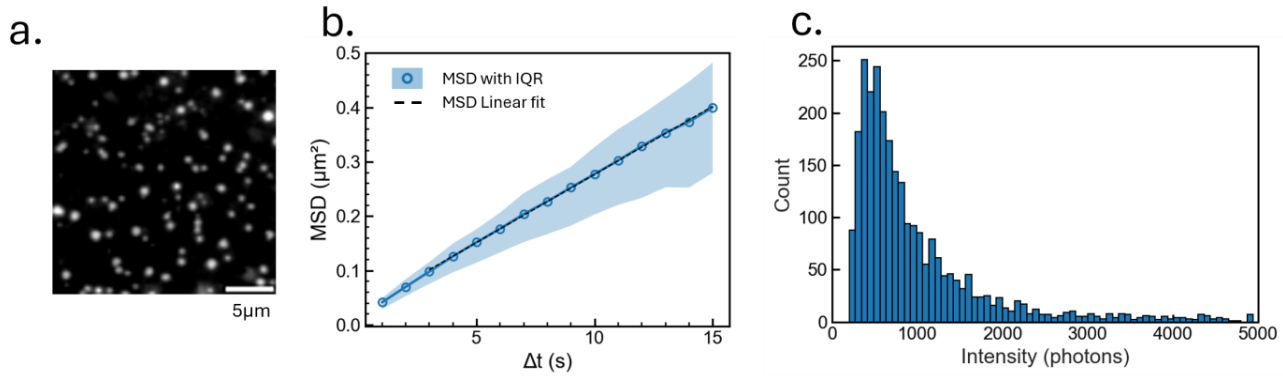

Figure 7: Single particle imaging and tracking: a) Representative image of single NPs-Cy5 in water dispersed on a coverslip b) The average MSD (with corresponding interquartile range (IQR)) of 197 individual particles diffusing in a 1:1 water-glycerol solution as a function of the lag time (Δt), reveals Brownian motion with a diffusion coefficient of D=0.18 $\mu m^2/s$ c) The intensity distribution of 2669 single particles is close to unimodal with a median intensity of 752 detected photons.

▪ Conclusion & perspectives

We report a one-pot, fully aqueous strategy combining ROPISA of PLG-NCA with CuAAC chemistry, enabling the direct formation of a unique class of anisotropic fluorescent polymer nanoparticles in a single step. This process operates at high solid contents (up to ~7 wt %), far exceeding those typically accessible by nanoprecipitation (<0.02 wt %),[17,18] highlighting both its efficiency and scalability. This versatile approach enables the controlled incorporation of fluorophores during nanoparticle formation, yielding blue (Cou), green (NBD), and red (Cy5) emitting nanoparticles and allowing a detailed investigation of their spectroscopic properties. The polypeptide nature of these nanoparticles makes them potentially degradable, in contrast to conventional fluorescent nanomaterials based on inorganic or organic semiconductors, or vinyl polymers.[11,14,17] In addition, the covalent incorporation of dyes within the polymer chains enables tracking of the polymer architecture throughout the nanoparticle, providing enhanced robustness and stability in biological environments.

Combining NBD- and Cy5-labeled nanoparticles reveals efficient FRET interactions driven by polymer chain exchange. This dynamic behavior provides a platform to probe energy transfer between anisotropic nano-objects[60] and to investigate temporal and structural aspects of interparticle interactions. Their versatility is further illustrated by straightforward functionalization (e.g., biotin), enabling responsive FRET sensors based on the biotin–streptavidin interaction with ~20% efficiency, comparable to established systems such as protein-coated quantum dots or polymer dots.

Cy5-labeled nanoparticles also exhibit exceptional brightness per unit volume, enabling detection as individual emitters. Combined with their red emission, this makes them well suited for biological applications such as deep-tissue imaging[61] and single-particle tracking[62,63]. More broadly, their combination of high brightness, aqueous single-step synthesis, high solid content, and soft anisotropic structure - typically achieved only in organic solvents[1,2,55,64] - opens new opportunities in super-resolution imaging[65,66], biological soft matter studies[67], and spectroscopy. Their flexibility and anisotropic shape also make them attractive for investigating transport in crowded and heterogeneous media[68].

Most notably, their high brightness and deformability make these nanoparticles particularly promising for extending single-particle tracking and diffusion studies to deep-tissue environments[67,69,70], where they could enable access to regions that remain inaccessible to conventional probes.

ASSOCIATED CONTENT

SUPPORTING INFORMATION.

Materials and methods, details on NCA synthesis including NMR spectra, FITR analysis, synthetic protocol of ROPISA-CuAAC polymerization, including additional data, SEC chromatograms, FITR analysis, TEM images, fluorescence spectra between NPs interactions, FRET deconvolution spectra and FRET efficiency spectra.

DATA AVAILABILITY STATEMENT.

The data that support the findings of this study are openly available in Zenodo at https://doi.org/10.5281/zenodo.19258603.

AUTHOR INFORMATION

Corresponding Authors

* Chloé Grazon – Univ. Bordeaux, CNRS, Bordeaux INP, ISM UMR 5255, F-33400 Talence, France; https://orcid.org/0000-0002-4564-8738; Email: chloe.grazon@u-bordeaux.fr

* Colin Bonduelle - Univ. Bordeaux, CNRS, Bordeaux INP, LCPO, UMR 5629, F-33600 Pessac, France; https://orcid.org/ 0000-0002-7213-7861; Email: colin.bonduelle@enscbp.fr

Authors

Amin El Jarroudi Hammou- Univ. Bordeaux, CNRS, Bordeaux INP, ISM UMR 5255, F-33400 Talence, France ; Univ. Bordeaux, CNRS, Bordeaux INP, LCPO, UMR 5629, F-33600 Pessac, France; https://orcid.org/0009-0003-1222-0772

Juliette Lavainne- Univ. Bordeaux, CNRS, Bordeaux INP, ISM UMR 5255, F-33400 Talence, France; https://orcid.org/0009-0006-8503-3814

Jyothis Devasia Univ. Bordeaux, CNRS, Bordeaux INP, ISM UMR 5255, F-33400 Talence, France

Rohit Mangalwedhekar Laboratoire Photonique Numérique et Nanosciences, Univ. Bordeaux, 33400 Talence, France; LP2N, Institut d'Optique Graduate School, CNRS – UMR 5298, 33400 Talence, France

Laurent Cognet Laboratoire Photonique Numérique et Nanosciences, Univ. Bordeaux, 33400 Talence, France; LP2N, Institut d'Optique Graduate School, CNRS – UMR 5298, 33400 Talence, France https://orcid.org/0000-0002-3573-5387

Sebastien Lecommandoux- Univ. Bordeaux, CNRS, Bordeaux INP, LCPO, UMR 5629, F-33600 Pessac, France; https://orcid.org/0000-0003-0465-8603

Author Contributions

The manuscript was written through contributions of all authors. / All authors have given approval to the final version of the manuscript.

Funding Sources

This study has mainly received funding from the European Research Council (ERC) starting grant (101077364) under European Union's Horizon Europe research and innovation program. It also received funding from the ERC synergy grant (951294), the Idex Bordeaux (Grand Research Program GPR LIGHT), the France-BioImaging National Infrastructure (ANR-10-INBS-04-01) the university of Bordeaux, Bordeaux-INP, CNRS and the LIGHT S&T Graduate Program (PIA 3 investment for the Future Program, ANR-17-EURE-0027). This work was also supported by a grant overseen by the French National Research Agency (ANR, Grant No. ANR-20-CE06-0020-01) and by the Horizon Europe research and innovation program under grant agreement No. 101079482 ("SUPRALIFE").

Acknowledgments

The authors thanks Antoine Tronnet for the training and tips on synthesis of NCA, Clara Catros for performing preliminary FRET-assays experiments, Jonathan Daniel for fruitful scientific discussions, Christophe Velours and Sylvain Bourasseau for the assistance with the size exclusion chromatography, Cedric Le Coz for the assistance with DSC and TGA analysis, Astrid Bergeat for kinetics discussions, and Sisareuth Tan for assistance with Cryo-TEM preparation and observation.

Abbreviations

ROPISA (Ring Opening Polymerization Induced by Self-Assembly), CuAAC (Copper Azide-Alkyne Cycloaddition), NCA (*N*-Carboxyanhydride), PLG-NCA (Propargyl-L-glutamate *N*-carboxyanhydride), PEG-NH_2 (Amino polyethylene glycol), Cou-N_3 (3-azido-7-hydroxycoumarin), NBD-N_3 (N-(3-Azidopropyl)-7-nitro-2,1,3-benzoxadiazol-4-amine), Cy5 (Cyanine 5), SEC (Size exclusion chromatography), PPLG (Polypropagryl-L-glutamate), TEM (Transmission electron microscopy), FRET (Förster resonance energy transfer), NPs (Nanoparticles), SA-TR (streptavidin Texas red), BtNBD-NPs (biotin 3-Azidopropyl)-7-nitro-2,1,3-benzoxadiazol-4-amine nanoparticles), R_0 (Förster radius), NMR (Nuclear magnetic resonance), FITR (Fourier-transform infrared spectroscopy), dRI (Refractive index), Abs (Absorbance), Tg (Glass transition temperature).

References

(1) Hoeben, F. J. M.; Jonkheijm, P.; Meijer, E. W.; Schenning, A. P. H. J. About Supramolecular Assemblies of π-Conjugated Systems. *Chem. Rev.* **2005**, *105* (4), 1491–1546. https://doi.org/10.1021/cr030070z.

(2) Maggini, L.; Bonifazi, D. Hierarchised Luminescent Organic Architectures: Design, Synthesis, Self-Assembly, Self-Organisation and Functions. *Chem. Soc. Rev.* **2012**, *41* (1), 211–241. https://doi.org/10.1039/C1CS15031F.

(3) Cabral, H.; Miyata, K.; Osada, K.; Kataoka, K. Block Copolymer Micelles in Nanomedicine Applications. *Chem. Rev.* **2018**, *118* (14), 6844–6892. https://doi.org/10.1021/acs.chemrev.8b00199.

(4) Beach, M. A.; Nayanathara, U.; Gao, Y.; Zhang, C.; Xiong, Y.; Wang, Y.; Such, G. K. Polymeric Nanoparticles for Drug Delivery. *Chem. Rev.* **2024**, *124* (9), 5505–5616. https://doi.org/10.1021/acs.chemrev.3c00705.

(5) Cummins, C.; Lundy, R.; Walsh, J. J.; Ponsinet, V.; Fleury, G.; Morris, M. A. Enabling Future Nanomanufacturing through Block Copolymer Self-Assembly: A Review. *Nano Today* **2020**, *35*, 100936. https://doi.org/10.1016/j.nantod.2020.100936.

(6) Grimm, J. B.; Lavis, L. D. Caveat Fluorophore: An Insiders' Guide to Small-Molecule Fluorescent Labels. *Nat Methods* **2022**, *19* (2), 149–158. https://doi.org/10.1038/s41592-021-01338-6.

(7) Ashoka, A. H.; Aparin, I. O.; Reisch, A.; Klymchenko, A. S. Brightness of Fluorescent Organic Nanomaterials. *Chem. Soc. Rev.* **2023**, *52* (14), 4525–4548. https://doi.org/10.1039/D2CS00464J.

(8) Grazon, C.; Chern, M.; Lally, P.; Baer, R. C.; Fan, A.; Lecommandoux, S.; Klapperich, C.; Dennis, A. M.; Galagan, J. E.; Grinstaff, M. W. The Quantum Dot vs. Organic Dye Conundrum for Ratiometric FRET-Based Biosensors: Which One Would You Chose? *Chem. Sci.* **2022**, *13* (22), 6715–6731. https://doi.org/10.1039/D1SC06921G.

(9) Stenspil, S. G.; Laursen, B. W. Photophysics of Fluorescent Nanoparticles Based on Organic Dyes – Challenges and Design Principles. *Chem. Sci.* **2024**, *15* (23), 8625–8638. https://doi.org/10.1039/D4SC01352B.

(10) Algar, W. R.; Massey, M.; Rees, K.; Higgins, R.; Krause, K. D.; Darwish, G. H.; Peveler, W. J.; Xiao, Z.; Tsai, H.-Y.; Gupta, R.; Lix, K.; Tran, M. V.; Kim, H. Photoluminescent Nanoparticles for Chemical and Biological Analysis and Imaging. *Chem. Rev.* **2021**, *121* (15), 9243–9358. https://doi.org/10.1021/acs.chemrev.0c01176.

(11) Martynenko, I. V.; Litvin, A. P.; Purcell-Milton, F.; Baranov, A. V.; Fedorov, A. V.; Gun'ko, Y. K. Application of Semiconductor Quantum Dots in Bioimaging and Biosensing. *J. Mater. Chem. B* **2017**, *5* (33), 6701–6727. https://doi.org/10.1039/C7TB01425B.

(12) Madirov, E.; Hildebrandt, N. FRET with Upconversion Nanoparticles. *Acc. Chem. Res.* **2026**, *59* (1), 114–125. https://doi.org/10.1021/acs.accounts.5c00670.

(13) Reisch, A.; Klymchenko, A. S. Fluorescent Polymer Nanoparticles Based on Dyes: Seeking Brighter Tools for Bioimaging. *Small* **2016**, *12* (15), 1968–1992. https://doi.org/10.1002/smll.201503396.

(14) Grazon, C.; Rieger, J.; Méallet-Renault, R.; Charleux, B.; Clavier, G. Ultrabright Fluorescent Polymeric Nanoparticles Made from a New Family of BODIPY Monomers. *Macromolecules* **2013**, *46* (13), 5167–5176. https://doi.org/10.1021/ma400590q.

(15) Reisch, A.; Didier, P.; Richert, L.; Oncul, S.; Arntz, Y.; Mély, Y.; Klymchenko, A. S. Collective Fluorescence Switching of Counterion-Assembled Dyes in Polymer Nanoparticles. *Nat Commun* **2014**, *5* (1), 4089. https://doi.org/10.1038/ncomms5089.

(16) Méallet-Renault, R.; Denjean, P.; Pansu, R. B. Polymer Beads as Nano-Sensors. *Sensors and Actuators B: Chemical* **1999**, *59* (2), 108–112. https://doi.org/10.1016/S0925-4005(99)00205-1.

(17) Lix, K.; Tran, M. V.; Massey, M.; Rees, K.; Sauvé, E. R.; Hudson, Z. M.; Algar, W. R. Dextran Functionalization of Semiconducting Polymer Dots and Conjugation with Tetrameric Antibody Complexes for Bioanalysis and Imaging. *ACS Appl. Bio Mater.* **2020**, *3* (1), 432–440. https://doi.org/10.1021/acsabm.9b00899.

(18) Andreiuk, B.; Reisch, A.; Lindecker, M.; Follain, G.; Peyriéras, N.; Goetz, J. G.; Klymchenko, A. S. Fluorescent Polymer Nanoparticles for Cell Barcoding In Vitro and In Vivo. *Small* **2017**, *13* (38). https://doi.org/10.1002/smll.201701582.

(19) Trofymchuk, K.; Valanciunaite, J.; Andreiuk, B.; Reisch, A.; Collot, M.; Klymchenko, A. S. BODIPY-Loaded Polymer Nanoparticles: Chemical Structure of Cargo Defines Leakage from Nanocarrier in Living Cells. *J. Mater. Chem. B* **2019**, *7* (34), 5199–5210. https://doi.org/10.1039/C8TB02781A.

(20) Penfold, N. J. W.; Yeow, J.; Boyer, C.; Armes, S. P. Emerging Trends in Polymerization-Induced Self-Assembly. *ACS Macro Lett.* **2019**, *8* (8), 1029–1054. https://doi.org/10.1021/acsmacrolett.9b00464.

(21) Charleux, B.; Delaittre, G.; Rieger, J.; D'Agosto, F. Polymerization-Induced Self-Assembly: From Soluble Macromolecules to Block Copolymer Nano-Objects in One Step. *Macromolecules* **2012**, *45* (17), 6753–6765. https://doi.org/10.1021/ma300713f.

(22) Galanopoulo, P.; Gil, N.; Gigmes, D.; Lefay, C.; Guillaneuf, Y.; Lages, M.; Nicolas, J.; D'Agosto, F.; Lansalot, M. RAFT-Mediated Emulsion Polymerization-Induced Self-Assembly for the Synthesis of Core-Degradable Waterborne Particles. *Angewandte Chemie International Edition* **2023**, *62* (16), e202302093. https://doi.org/10.1002/anie.202302093.

(23) Lei, L.; Nguyen, T. P. T.; Miménand, Y. de R. de; Grande, D.; Droumaguet, B. L.; Gnanou, Y.; Couturaud, B. PEG-Based Core-Degradable Nanoparticles via RAFT-Mediated Reverse-Sequence PISA. *Polym. Chem.* **2026**, *17* (8), 789–795. https://doi.org/10.1039/D5PY01119A.

(24) Neal, T. J.; Dalmasso, L.; Coumes, F.; Rieger, J. UV-Degradable Poly(Phenyl Vinyl Ketone) Particles Produced by Polymerisation-Induced Self-Assembly in Ethanol or Water. *Polym. Chem.* **2026**, *17* (3), 332–340. https://doi.org/10.1039/D5PY01020A.

(25) Zhang, S.; Li, R.; An, Z. Degradable Block Copolymer Nanoparticles Synthesized by Polymerization-Induced Self-Assembly. *Angewandte Chemie International Edition* **2024**, *63* (12), e202315849. https://doi.org/10.1002/anie.202315849.

(26) Ladmiral, V.; Legge, T. M.; Zhao, Y.; Perrier, S. "Click" Chemistry and Radical Polymerization: Potential Loss of Orthogonality. *Macromolecules* **2008**, *41* (18), 6728–6732. https://doi.org/10.1021/ma8010262.

(27) Geng, Z.; Shin, J. J.; Xi, Y.; Hawker, C. J. Click Chemistry Strategies for the Accelerated Synthesis of Functional Macromolecules. *Journal of Polymer Science* **2021**, *59* (11), 963–1042. https://doi.org/10.1002/pol.20210126.

(28) Grazon, C.; Salas-Ambrosio, P.; Ibarboure, E.; Buol, A.; Garanger, E.; Grinstaff, M. W.; Lecommandoux, S.; Bonduelle, C. Aqueous Ring-Opening Polymerization-Induced Self-Assembly (ROPISA) of N-Carboxyanhydrides. *Angewandte Chemie International Edition* **2020**, *59* (2), 622–626. https://doi.org/10.1002/anie.201912028.

(29) Proceedings of the Chemical Society. October 1961. *Proc. Chem. Soc.* **1961**, No. October, 357–396. https://doi.org/10.1039/PS9610000357.

(30) Engler, A. C.; Lee, H.; Hammond, P. T. Highly Efficient "Grafting onto" a Polypeptide Backbone Using Click Chemistry. *Angew Chem Int Ed* **2009**, *48* (49), 9334–9338. https://doi.org/10.1002/anie.200904070.

(31) Morton, S. W.; Zhao, X.; Quadir, M. A.; Hammond, P. T. FRET-Enabled Biological Characterization of Polymeric Micelles. *Biomaterials* **2014**, *35* (11), 3489–3496. https://doi.org/10.1016/j.biomaterials.2014.01.027.

(32) Nguyen, M.; Stigliani, J.-L.; Bijani, C.; Verhaeghe, P.; Pratviel, G.; Bonduelle, C. Ionic Polypeptide Polymers with Unusual β-Sheet Stability. *Biomacromolecules* **2018**, *19* (10), 4068–4074. https://doi.org/10.1021/acs.biomac.8b01084.

(33) Su, R.; Francés-Soriano, L.; Diriwari, P. I.; Munir, M.; Haye, L.; Sørensen, T. J.; Díaz, S. A.; Medintz, I. L.; Hildebrandt, N. FRET Materials for Biosensing and Bioimaging. *Chem. Rev.* **2025**, *125* (19), 9429–9551. https://doi.org/10.1021/acs.chemrev.5c00386.

(34) Beauseroy, H.; Salimi, F.; Aujard-Catot, J.; Alembik, L.; Lecommandoux, S.; Bonduelle, C. Aqueous Ring-Opening Polymerization-Induced Self-Assembly (ROPISA): Tailoring Anisotropic Nanoparticles through Amino Acid N-Carboxyanhydride (NCA) Monomer Selection. *Macromolecules* **2025**, *58* (13), 6466–6479. https://doi.org/10.1021/acs.macromol.5c01089.

(35) Nguyen, T. P.; Easley, A. D.; Kang, N.; Khan, S.; Lim, S.-M.; Rezenom, Y. H.; Wang, S.; Tran, D. K.; Fan, J.; Letteri, R. A.; He, X.; Su, L.; Yu, C.-H.; Lutkenhaus, J. L.; Wooley, K. L. Polypeptide Organic Radical Batteries. *Nature* **2021**, *593* (7857), 61–66. https://doi.org/10.1038/s41586-021-03399-1.

(36) Leuchs, H. Ueber Die Glycin-Carbonsäure. *Berichte der deutschen chemischen Gesellschaft* **1906**, *39* (1), 857–861. https://doi.org/10.1002/cber.190603901133.

(37) Spyridakou, M.; Tzourtzouklis, I.; Graf, R.; Beauseroy, H.; Bonduelle, C.; Lecommandoux, S.; Floudas, G. Multiple Levels of Organization in Amphiphilic Diblock Copolymers Based on Poly(γ-Benzyl-l-Glutamate) Produced by Aqueous ROPISA. *Biomacromolecules* **2025**, *26* (3), 1892–1903. https://doi.org/10.1021/acs.biomac.4c01657.

(38) Grazon, C.; Salas-Ambrosio, P.; Antoine, S.; Ibarboure, E.; Sandre, O.; Clulow, A. J.; Boyd, B. J.; Grinstaff, M. W.; Lecommandoux, S.; Bonduelle, C. Aqueous ROPISA of α-Amino Acid *N*-Carboxyanhydrides: Polypeptide Block Secondary Structure Controls Nanoparticle Shape Anisotropy. *Polym. Chem.* **2021**, *12* (43), 6242–6251. https://doi.org/10.1039/D1PY00995H.

(39) Hu, Y.; Tian, Z.-Y.; Xiong, W.; Wang, D.; Zhao, R.; Xie, Y.; Song, Y.-Q.; Zhu, J.; Lu, H. Water-Assisted and Protein-Initiated Fast and Controlled Ring-Opening Polymerization of Proline *N* -Carboxyanhydride. *National Science Review* **2022**, *9* (8), nwac033. https://doi.org/10.1093/nsr/nwac033.

(40) Liu, B.; Fang, R.; Li, W.; Wu, X.; Liu, T.; Lin, M.; Sun, J.; Chen, X. Fast Catalyst-Free Synthesis of Stereoselective Polypeptides via Hierarchical Chiral Assembly. *J. Am. Chem. Soc.* **2024**, *146* (24), 16558–16566. https://doi.org/10.1021/jacs.4c03281.

(41) Ashokkumar, P.; Adarsh, N.; Klymchenko, A. S. Ratiometric Nanoparticle Probe Based on FRET-Amplified Phosphorescence for Oxygen Sensing with Minimal Phototoxicity. *Small* **2020**, *16* (32), 2002494. https://doi.org/10.1002/smll.202002494.

(42) Sivakumar, K.; Xie, F.; Cash, B. M.; Long, S.; Barnhill, H. N.; Wang, Q. A Fluorogenic 1,3-Dipolar Cycloaddition Reaction of 3-Azidocoumarins and Acetylenes. *Org. Lett.* **2004**, *6* (24), 4603–4606. https://doi.org/10.1021/ol047955x.

(43) Luu, T.; Gristwood, K.; Knight, J. C.; Jörg, M. Click Chemistry: Reaction Rates and Their Suitability for Biomedical Applications. *Bioconjug Chem* **2024**, *35* (6), 715–731. https://doi.org/10.1021/acs.bioconjchem.4c00084.

(44) Nian, K.; Liu, Y.; Qiu, Y.; Zhang, Z.; Brigandi, L.; Wanunu, M.; Rouhanifard, S. H. inCu-Click: DNA-Enhanced Ligand Enables Live-Cell, Intracellular Click Chemistry Reaction with Copper Catalyst. *Nat Commun* **2025**, *16* (1), 4788. https://doi.org/10.1038/s41467-025-60143-3.

(45) Zhou, Z.; Fahrni, C. J. A Fluorogenic Probe for the Copper(I)-Catalyzed Azide–Alkyne Ligation Reaction: Modulation of the Fluorescence Emission via 3(n,Π*)–(π,Π*) Inversion. *J. Am. Chem. Soc.* **2004**, *126* (29), 8862–8863. https://doi.org/10.1021/ja049684r.

(46) Presolski, S. I.; Hong, V.; Cho, S.-H.; Finn, M. G. Tailored Ligand Acceleration of the Cu-Catalyzed Azide–Alkyne Cycloaddition Reaction: Practical and Mechanistic Implications. *J. Am. Chem. Soc.* **2010**, *132* (41), 14570–14576. https://doi.org/10.1021/ja105743g.

(47) Tian, Z.; Shaller, A. D.; Li, A. D. Q. Twisted Perylene Dyes Enable Highly Fluorescent and Photostable Nanoparticles. *Chem. Commun.* **2009**, No. 2, 180–182. https://doi.org/10.1039/B815507K.

(48) Egloff, S.; Melnychuk, N.; Cruz Da Silva, E.; Reisch, A.; Martin, S.; Klymchenko, A. S. Amplified Fluorescence in Situ Hybridization by Small and Bright Dye-Loaded Polymeric Nanoparticles. *ACS Nano* **2022**, *16* (1), 1381–1394. https://doi.org/10.1021/acsnano.1c09409.

(49) Wagh, A.; Qian, S. Y.; Law, B. Development of Biocompatible Polymeric Nanoparticles for in Vivo NIR and FRET Imaging. *Bioconjugate Chem.* **2012**, *23* (5), 981–992. https://doi.org/10.1021/bc200637h.

(50) Würth, C.; Grabolle, M.; Pauli, J.; Spieles, M.; Resch-Genger, U. Relative and Absolute Determination of Fluorescence Quantum Yields of Transparent Samples. *Nat Protoc* **2013**, *8* (8), 1535–1550. https://doi.org/10.1038/nprot.2013.087.

(51) Drake, J. M.; Lesiecki, M. L.; Camaioni, D. M. Photophysics and Cis-Trans Isomerization of DCM. *Chemical Physics Letters* **1985**, *113* (6), 530–534. https://doi.org/10.1016/0009-2614(85)85026-0.

(52) Sens, R.; Drexhage, K. H. Fluorescence Quantum Yield of Oxazine and Carbazine Laser Dyes. *Journal of Luminescence* **1981**, *24–25*, 709–712. https://doi.org/10.1016/0022-2313(81)90075-2.

(53) Algar, W. R.; Hildebrandt, N.; Vogel, S. S.; Medintz, I. L. FRET as a Biomolecular Research Tool — Understanding Its Potential While Avoiding Pitfalls. *Nat Methods* **2019**, *16* (9), 815–829. https://doi.org/10.1038/s41592-019-0530-8.

(54) Rajdev, P.; Ghosh, S. Fluorescence Resonance Energy Transfer (FRET): A Powerful Tool for Probing Amphiphilic Polymer Aggregates and Supramolecular Polymers. *J. Phys. Chem. B* **2019**, *123* (2), 327–342. https://doi.org/10.1021/acs.jpcb.8b09441.

(55) Lin, Y.-C.; Kuo, S.-W. Hierarchical Self-Assembly and Secondary Structures of Linear Polypeptides Graft onto POSS in the Side Chain through Click Chemistry. *Polym. Chem.* **2011**, *3* (1), 162–171. https://doi.org/10.1039/C1PY00381J.

(56) Nicolai, T.; Colombani, O.; Chassenieux, C. Dynamic Polymeric Micelles versus Frozen Nanoparticles Formed by Block Copolymers. *Soft Matter* **2010**, *6* (14), 3111–3118. https://doi.org/10.1039/B925666K.

(57) Lix, K.; Krause, K. D.; Kim, H.; Algar, W. R. Investigation of the Energy Transfer Mechanism Between Semiconducting Polymer Dots and Organic Dyes. *J. Phys. Chem. C* **2020**, *124* (31), 17387–17400. https://doi.org/10.1021/acs.jpcc.0c04983.

(58) Cognet, L.; Leduc, C.; Lounis, B. Advances in Live-Cell Single-Particle Tracking and Dynamic Super-Resolution Imaging. *Current Opinion in Chemical Biology* **2014**, *20*, 78–85. https://doi.org/10.1016/j.cbpa.2014.04.015.

(59) Volk, A.; Kähler, C. J. Density Model for Aqueous Glycerol Solutions. *Exp Fluids* **2018**, *59* (5), 75. https://doi.org/10.1007/s00348-018-2527-y.

(60) Madirov, E.; Catros, C.; Hildebrandt, N.; Grazon, C. Inter-Nanoparticle FRET for Biosensing: Photophysics Versus Size. *Angewandte Chemie International Edition* **2025**, *64* (39), e202510801. https://doi.org/10.1002/anie.202510801.

(61) Frangioni, J. V. *In Vivo* near-Infrared Fluorescence Imaging. *Current Opinion in Chemical Biology* **2003**, *7* (5), 626–634. https://doi.org/10.1016/j.cbpa.2003.08.007.

(62) Ruthardt, N.; Lamb, D. C.; Bräuchle, C. Single-Particle Tracking as a Quantitative Microscopy-Based Approach to Unravel Cell Entry Mechanisms of Viruses and Pharmaceutical Nanoparticles. *Mol Ther* **2011**, *19* (7), 1199–1211. https://doi.org/10.1038/mt.2011.102.

(63) Jin, D.; Xi, P.; Wang, B.; Zhang, L.; Enderlein, J.; van Oijen, A. M. Nanoparticles for Super-Resolution Microscopy and Single-Molecule Tracking. *Nat Methods* **2018**, *15* (6), 415–423. https://doi.org/10.1038/s41592-018-0012-4.

(64) Hudson, Z. M.; Lunn, D. J.; Winnik, M. A.; Manners, I. Colour-Tunable Fluorescent Multiblock Micelles. *Nat Commun* **2014**, *5* (1), 3372. https://doi.org/10.1038/ncomms4372.

(65) Szalai, A. M.; Siarry, B.; Lukin, J.; Giusti, S.; Unsain, N.; Cáceres, A.; Steiner, F.; Tinnefeld, P.; Refojo, D.; Jovin, T. M.; Stefani, F. D. Super-Resolution Imaging of Energy Transfer by Intensity-Based STED-FRET. *Nano Lett.* **2021**, *21* (5), 2296–2303. https://doi.org/10.1021/acs.nanolett.1c00158.

(66) Li, W.; Kaminski Schierle, G. S.; Lei, B.; Liu, Y.; Kaminski, C. F. Fluorescent Nanoparticles for Super-Resolution Imaging. *Chem. Rev.* **2022**, *122* (15), 12495–12543. https://doi.org/10.1021/acs.chemrev.2c00050.

(67) Estaun-Panzano, J.; Nandi, S.; Gresil, Q.; Doudnikoff, E.; Mazzocco, C.; Arotcarena, M. L.; Canron, M. H.; Dehay, B.; Cognet, L.; Bezard, E. Intracellular α-Synuclein Assemblies Are Sufficient to Alter Nanoscale Diffusion in the Striatal Extracellular Space. *npj Parkinsons Dis.* **2024**, *10* (1), 236. https://doi.org/10.1038/s41531-024-00850-8.

(68) Fakhri, N.; MacKintosh, F. C.; Lounis, B.; Cognet, L.; Pasquali, M. Brownian Motion of Stiff Filaments in a Crowded Environment. *Science* **2010**, *330* (6012), 1804–1807. https://doi.org/10.1126/science.1197321.

(69) Lee, A.; Simon, A. A.; Boyreau, A.; Allain-Courtois, N.; Lambert, B.; Pradère, J.-P.; Saltel, F.; Cognet, L. Identification of Early Stage Liver Fibrosis by Modifications in the Interstitial Space Diffusive Microenvironment Using Fluorescent Single-Walled Carbon Nanotubes. *Nano Lett.* **2024**, *24* (18), 5603–5609. https://doi.org/10.1021/acs.nanolett.4c00955.

(70) Godin, A. G.; Varela, J. A.; Gao, Z.; Danné, N.; Dupuis, J. P.; Lounis, B.; Groc, L.; Cognet, L. Single-Nanotube Tracking Reveals the Nanoscale Organization of the Extracellular Space in the Live Brain. *Nature Nanotech* **2017**, *12* (3), 238–243. https://doi.org/10.1038/nnano.2016.248.

Appendix C

Protocols for biophysical model with nanotubes

PROTOCOL FOR DROPLETS/NT PREPARATION

Preparation of dilute sp3 ultrashort nanotubes in water

- Pipette 1 µL of stock solution of sp3 ultrashort nanotubes into 99 µL of water and store in the refrigerator.
- This achieves a 1:100 solution of sp3 ultrashort nanotubes.

Preparation of dilute sp3 long nanotubes in water

- Pipette 1 µL of stock solution of sp3 long nanotubes into 99 µL of water and store in the refrigerator.
- This achieves a 1:100 solution of sp3 ultrashort nanotubes.

STEP 1. Index matching solution preparation

- A 10mM solution of Sodium Dodecyl Sulphate(SDS) in 1:1(volume) of water to glycerol acts as the index matching buffer solution.
- 28.8mg of SDS was dissolved in 5 mL of milliQ water using a magnetic stirrer. To this, 5mL of glycerol was added and stirred.
- The solution was centrifuged in a filter Tarson tube for 15 minutes at 5000g to remove particulate impurities.

STEP 2. Labelling solution preparation

- Prepare 5mL, 20mM solution of Sodium Dodecyl Sulphate(SDS) in water
- Add ~5mg of Nile red to the solution
- Stir for several hours
- Add 5mL of glycerol, this brings down the SDS concentration to 10mM
- Stir for hours(overnight)
- Centrifuge it without a filter at 4500g
- Carefully recover the labelling solution prepared without disturbing the sediments
- Consider this as stock solution, for general notes this has been named as 1M or 1xStock
- For dyeing at various concentrations, dilute the prepared stock nile red solution with index matching solution(from STEP 1)

STEP 3. Labelling the emulsion

- Prepare labelling solution of required concentration by diluting the saturated labelling solution in the index matching solution prepared in STEP 1. The ideal range is between 0.2x and 0.6x of the saturated labelling solution prepared in STEP 2.
- Add stock emulsion(5 micron droplets as given by Pontani Lab) and labelling solution in a 1:4 ratio
- The infusion takes about a few days(a minimum of 2-3 days); shake the solution a few times everyday to allow for better infusion. Preferably prepare the sample slide before 15 days of infusion.
- **NOTE:Prepare with 500 µL of droplets in 2.5 mL glass vials.**

STEP 4. Packed droplet preparation with nanotubes

- After labelling, the solution was allowed to phase separate with the labelled droplets at the top and uncoloured water phase at the bottom.

- 2.5 µL of 1:100 DOC ccNTs(ultrashort or long as required) was added carefully to 500 µL the prepared labelled droplets without disturbing the separated phases in order to achieve a 1:20000 concentration of nanotubes(to be adjusted as per nanoparticles used).
- This sample was placed in a 5 mL eppendorf and centrifuged at 4500g for 10 to 15 minutes in a swing bucket centrifuge.
- This yields up to 500µL of compact droplets that have been index matched.

STEP 5. Sample preparation

Samples were prepared by carefully scooping the top phase with a small spatula directly onto the coverslip.

STEP 6. Imaging of droplet sample

The prepared droplets with the nanotubes were imaged under white light using the Nikon Eclipse Ti Microscope(Montreal) using the 60x 1.27NA lens. The packed droplets(nile red) were imaged using a 568 nm laser at power of 140 mW at the source(reduced to ~70mW due to beam splitter) with the 655 nm filter. The ultrashort nanotubes were imaged using 985 nm with the 985 nm filter. The imaging was done using the InGaAs CRED 2 integrated with MM2.0. The gain factor has to be normalised. For this the following steps are taken:

1. Command prompt>> set aduoffset 0
2. Apply bias>> 0
3. Get bias>> 1
4. Apply bias>> 1
5. Command prompt >> set aduoffset 600

Bibliography

[1] Robert Brown. XXVII. *A brief account of microscopical observations made in the months of June, July and August* 1827, *on the particles contained in the pollen of plants; and on the general existence of active molecules in organic and inorganic bodies. The Philosophical Magazine*, 4(21):161–173, September 1828.

[2] Albert Einstein. Über die von der molekularkinetischen Theorie der Wärme geforderte Bewegung von in ruhenden Flüssigkeiten suspendierten Teilchen. *Annalen der Physik*, vol. 4, t. 17, 1905.

[3] Jean Perrin. Mouvement brownien et réalité moléculaire.

[4] Don S. Lemons and Anthony Gythiel. Paul Langevin's 1908 paper "On the Theory of Brownian Motion" ["Sur la théorie du mouvement brownien," C. R. Acad. Sci. (Paris) **146** , 530–533 (1908)]. *American Journal of Physics*, 65(11):1079–1081, November 1997.

[5] EL Hahn. Spin echoes phys rev 80: 580–594, 1950.

[6] Denis S Grebenkov. Nmr survey of reflected brownian motion. *Reviews of Modern Physics*, 79(3):1077–1137, 2007.

[7] TP Das and AK Saha. Mathematical analysis of the hahn spin-echo experiment. *Physical review*, 93(4):749, 1954.

[8] Donald E Woessner. Nmr spin-echo self-diffusion measurements on fluids undergoing restricted diffusion. *The Journal of Physical Chemistry*, 67(6):1365–1367, 1963.

[9] Chengqi Zhang, Zhicheng Jin, Birong Zeng, Wentao Wang, Goutam Palui, and Hedi Mattoussi. Characterizing the Brownian Diffusion of Nanocolloids and Molecular Solutions: Diffusion-Ordered NMR Spectroscopy vs Dynamic Light Scattering. *The Journal of Physical Chemistry B*, 124(22):4631–4650, June 2020.

[10] Jörg Stetefeld, Sean A. McKenna, and Trushar R. Patel. Dynamic light scattering: a practical guide and applications in biomedical sciences. *Biophysical Reviews*, 8(4):409–427, October 2016.

[11] Frédéric Pincet, Vladimir Adrien, Rong Yang, Jérôme Delacotte, James E. Rothman, Wladimir Urbach, and David Tareste. FRAP to Characterize Molecular Diffusion and Interaction in Various Membrane Environments. *PLoS ONE*, 11(7):e0158457, July 2016.

[12] Brian L. Sprague, Robert L. Pego, Diana A. Stavreva, and James G. McNally. Analysis of Binding Reactions by Fluorescence Recovery after Photobleaching. *Biophysical Journal*, 86(6):3473–3495, June 2004.

[13] Felix Höfling and Thomas Franosch. Anomalous transport in the crowded world of biological cells. *Reports on Progress in Physics*, 76(4):046602, March 2013.

[14] Samuel T Hess, Shaohui Huang, Ahmed A Heikal, and Watt W Webb. Biological and chemical applications of fluorescence correlation spectroscopy: a review. *Biochemistry*, 41(3):697–705, 2002.

[15] Miguel Angel Medina and Petra Schwille. Fluorescence correlation spectroscopy for the detection and study of single molecules in biology. *Bioessays*, 24(8):758–764, 2002.

[16] Suliana Manley, Jennifer M. Gillette, George H. Patterson, Hari Shroff, Harald F. Hess, Eric Betzig, and Jennifer Lippincott-Schwartz. High-density mapping of single-molecule trajectories with photoactivated localization microscopy. *Nature Methods*, 5(2):155–157, February 2008.

[17] E Van Craenenbroeck and Yves Engelborghs. Fluorescence correlation spectroscopy: molecular recognition at the single molecule level. *Journal of Molecular Recognition*, 13(2):93–100, 2000.

[18] Nancy L Thompson, Alena M Lieto, and Noah W Allen. Recent advances in fluorescence correlation spectroscopy. *Current opinion in structural biology*, 12(5):634–641, 2002.

[19] Catherine Tan, Michael C. Lanz, Matthew Swaffer, Jan Skotheim, and Fred Chang. Intracellular diffusion in the cytoplasm increases with cell size in fission yeast. *Molecular Biology of the Cell*, 36(4):ar51, April 2025.

[20] Iva Marija Tolić-Nørrelykke, Emilia-Laura Munteanu, Genevieve Thon, Lene Oddershede, and Kirstine Berg-Sørensen. Anomalous Diffusion in Living Yeast Cells. *Physical Review Letters*, 93(7):078102, August 2004.

[21] Jörg Kärger, Sergey Vasenkov, and Scott M Auerbach. Diffusion in Zeolites. 2003.

[22] Michael J. Skaug and Daniel K. Schwartz. Tracking Nanoparticle Diffusion in Porous Filtration Media. *Industrial & Engineering Chemistry Research*, 54(16):4414–4419, April 2015.

[23] Khuloud Jaqaman, Dinah Loerke, Marcel Mettlen, Hirotaka Kuwata, Sergio Grinstein, Sandra L. Schmid, and Gaudenz Danuser. Robust single-particle tracking in live-cell time-lapse sequences. *Nature Methods*, 5(8):695–702, August 2008.

[24] Eric Betzig, George H. Patterson, Rachid Sougrat, O. Wolf Lindwasser, Scott Olenych, Juan S. Bonifacino, Michael W. Davidson, Jennifer Lippincott-Schwartz, and Harald F. Hess. Imaging Intracellular Fluorescent Proteins at Nanometer Resolution. *Science*, 313(5793):1642–1645, September 2006.

[25] Yuxin Lin, Haoting Lin, and Kevin D. Welsher. Super-Resolving Particle Diffusion Heterogeneity in Porous Hydrogels via High-Speed 3D Active-Feedback Single-Particle Tracking Microscopy. *Small*, 21(40):e05319, 2025. _eprint: https://onlinelibrary.wiley.com/doi/pdf/10.1002/smll.202505319.

[26] Clemens Bechinger. Active particles in complex and crowded environments. *Reviews of Modern Physics*, 88(4), 2016.

[27] M. Valet, L.-L. Pontani, R. Voituriez, E. Wandersman, and A. M. Prevost. Diffusion through Nanopores in Connected Lipid Bilayer Networks. *Physical Review Letters*, 123(8):088101, August 2019.

[28] Jörg Kärger and Douglas M. Ruthven. Diffusion in nanoporous materials: fundamental principles, insights and challenges. *New Journal of Chemistry*, 40(5):4027–4048, 2016.

[29] Raphaël Sarfati, Christopher P. Calderon, and Daniel K. Schwartz. Enhanced Diffusive Transport in Fluctuating Porous Media. *ACS Nano*, 15(4):7392–7398, April 2021.

[30] Felix J. Meigel, Thomas Darwent, Leonie Bastin, Lucas Goehring, and Karen Alim. Dispersive transport dynamics in porous media emerge from local correlations. *Nature Communications*, 13(1):5885, October 2022.

[31] J. J. Erik Maris, Donglong Fu, Florian Meirer, and Bert M. Weckhuysen. Single-molecule observation of diffusion and catalysis in nanoporous solids. *Adsorption*, 27(3):423–452, April 2021.

[32] Charles Nicholson and Eva Syková. Extracellular space structure revealed by diffusion analysis. *Trends in Neurosciences*, 21(5):207–215, May 1998.

[33] Manuchehr Aminian, Francesca Bernardi, Roberto Camassa, Daniel M. Harris, and Richard M. McLaughlin. How boundaries shape chemical delivery in microfluidics. *Science*, 354(6317):1252–1256, December 2016.

[34] Brian Amsden. An Obstruction-Scaling Model for Diffusion in Homogeneous Hydrogels. *Macromolecules*, 32(3):874–879, February 1999.

[35] Sophie Marbach, David S. Dean, and Lydéric Bocquet. Transport and dispersion across wiggling nanopores. *Nature Physics*, 14(11):1108–1113, November 2018.

[36] Dapeng Wang, Haichao Wu, Lijun Liu, Jizhong Chen, and Daniel K. Schwartz. Diffusive Escape of a Nanoparticle from a Porous Cavity. *Physical Review Letters*, 123(11):118002, September 2019.

[37] Cheol Hee Lee, Alfred J Crosby, Todd Emrick, and Ryan C Hayward. Characterization of heterogeneous polyacrylamide hydrogels by tracking of single quantum dots. *Macromolecules*, 47(2):741–749, 2014.

[38] Charles Nicholson, Padideh Kamali-Zare, and Lian Tao. Brain extracellular space as a diffusion barrier. *Computing and Visualization in Science*, 14(7):309–325, 2011.

[39] Charles Nicholson and Sabina Hrabětová. Brain extracellular space: the final frontier of neuroscience. *Biophysical journal*, 113(10):2133–2142, 2017.

[40] Charles Nicholson and Eva Syková. Extracellular space structure revealed by diffusion analysis. *Trends in neurosciences*, 21(5):207–215, 1998.

[41] Chiara Paviolo, Federico N. Soria, Joana S. Ferreira, Antony Lee, Laurent Groc, Erwan Bezard, and Laurent Cognet. Nanoscale exploration of the extracellular space in the live brain by combining single carbon nanotube tracking and super-resolution imaging analysis. *Methods*, 174:91–99, March 2020.

[42] Charles Nicholson. Brain interstitial structure revealed through diffusive spread of molecules. In *Diffusive spreading in nature, technology and society*, pages 97–120. Springer, 2023.

[43] Federico N Soria, Chiara Paviolo, Evelyne Doudnikoff, Marie-Laure Arotcarena, Antony Lee, Noémie Danné, Amit Kumar Mandal, Philippe Gosset, Benjamin Dehay, Laurent Groc, et al. Synucleinopathy alters nanoscale organization and diffusion in the brain extracellular space through hyaluronan remodeling. *Nature communications*, 11(1):3440, 2020.

[44] Diego Grassi, Agata Idziak, Antony Lee, Ivo Calaresu, Jean-Baptiste Sibarita, Laurent Cognet, U Valentin Nägerl, and Laurent Groc. Nanoscale and functional heterogeneity of the hippocampal extracellular space. *Cell Reports*, 42(5), 2023.

[45] Ch Nicholson and JM1249623 Phillips. Ion diffusion modified by tortuosity and volume fraction in the extracellular microenvironment of the rat cerebellum. *The Journal of physiology*, 321(1):225–257, 1981.

[46] Eva Syková and Charles Nicholson. Diffusion in Brain Extracellular Space. *Physiological Reviews*, 88(4):1277–1340, October 2008.

[47] Antoine G. Godin, Juan A. Varela, Zhenghong Gao, Noémie Danné, Julien P. Dupuis, Brahim Lounis, Laurent Groc, and Laurent Cognet. Single-nanotube tracking reveals the nanoscale organization of the extracellular space in the live brain. *Nature Nanotechnology*, 12(3):238–243, March 2017.

[48] Chiara Paviolo and Laurent Cognet. Near-infrared nanoscopy with carbon-based nanoparticles for the exploration of the brain extracellular space. *Neurobiology of Disease*, 153:105328, June 2021.

[49] Chiara Paviolo, Joana S. Ferreira, Antony Lee, Daniel Hunter, Ivo Calaresu, Somen Nandi, Laurent Groc, and Laurent Cognet. Near-Infrared Carbon Nanotube Tracking Reveals the Nanoscale Extracellular Space around Synapses. *Nano Letters*, 22(17):6849–6856, September 2022.

[50] Antony Lee, Apolline A. Simon, Adeline Boyreau, Nathalie Allain-Courtois, Benjamin Lambert, Jean-Philippe Pradère, Frédéric Saltel, and Laurent Cognet. Identification of Early Stage Liver Fibrosis by Modifications in the Interstitial Space Diffusive Microenvironment Using Fluorescent Single-Walled Carbon Nanotubes. *Nano Letters*, 24(18):5603–5609, May 2024.

[51] Somen Nandi, Quentin Gresil, Benjamin P. Lambert, Finn L. Sebastian, Simon Settele, Ivo Calaresu, Juan Estaun-Panzano, Anna Lovisotto, Claire Mazzocco, Benjamin S. Flavel, Erwan Bezard, Laurent Groc, Jana Zaumseil, and Laurent Cognet. Ultrashort Carbon Nanotubes with Luminescent Color Centers Are Bright NIR-II Nanoemitters. *ACS Nano*, 19(21):19818–19830, June 2025.

[52] Limeng Ruan, Hanna Manko, Quentin Gresil, Luis A. Alemán-Castañeda, Morgane Meras, Finn L. Sebastian, Benjamin Flavel, Jana Zaumseil, Laurent Groc, Sophie Brasselet, Marc Tondusson, and Laurent Cognet. Nanoscale rheological heterogeneity revealed by Single Particle orientation Tracking (SPoT) of ultrashort carbon nanotubes in brain tissue, May 2026.

[53] Haichao Wu and Daniel K. Schwartz. Nanoparticle Tracking to Probe Transport in Porous Media. *Accounts of Chemical Research*, 53(10):2130–2139, October 2020.

[54] Hong-Yu Luo, Chao Jiang, Shuo-Xing Dou, Peng-Ye Wang, and Hui Li. Quantum Dot-Based Three-Dimensional Single-Particle Tracking Characterizes the Evolution of Spatiotemporal Heterogeneity in Necrotic Cells. *Analytical Chemistry*, 96(29):11682–11689, July 2024.

[55] A M Mastro, M A Babich, W D Taylor, and A D Keith. Diffusion of a small molecule in the cytoplasm of mammalian cells. *Proceedings of the National Academy of Sciences*, 81(11):3414–3418, June 1984.

[56] Francis Perrin. Mouvement brownien d'un ellipsoide - I. Dispersion diélectrique pour des molécules ellipsoidales. *Journal de Physique et le Radium*, 5(10):497–511, 1934.

[57] Y. Han, A. M. Alsayed, M. Nobili, J. Zhang, T. C. Lubensky, and A. G. Yodh. Brownian Motion of an Ellipsoid. *Science*, 314(5799):626–630, October 2006.

[58] Nikta Fakhri, Frederick C. MacKintosh, Brahim Lounis, Laurent Cognet, and Matteo Pasquali. Brownian Motion of Stiff Filaments in a Crowded Environment. *Science*, 330(6012):1804–1807, December 2010.

[59] Zhao Tang, Shannon L. Eichmann, Brahim Lounis, Laurent Cognet, Frederick C. MacKintosh, and Matteo Pasquali. Single-walled carbon nanotube reptation dynamics in submicron sized pores from randomly packed mono-sized colloids. *Soft Matter*, 18(29):5509–5517, 2022.

[60] M. J. Saxton. Anomalous diffusion due to obstacles: a Monte Carlo study. *Biophysical Journal*, 66(2):394–401, February 1994.

[61] Carlo Manzo and Maria F Garcia-Parajo. A review of progress in single particle tracking: from methods to biophysical insights. *Reports on Progress in Physics*, 78(12):124601, October 2015.

[62] Igor M. Sokolov. Models of anomalous diffusion in crowded environments. *Soft Matter*, 8(35):9043–9052, August 2012.

[63] Michael J. Saxton and Ken Jacobson. SINGLE-PARTICLE TRACKING:Applications to Membrane Dynamics. *Annual Review of Biophysics*, 26(Volume 26, 1997):373–399, June 1997.

[64] Jean-Philippe Bouchaud and Antoine Georges. Anomalous diffusion in disordered media: Statistical mechanisms, models and physical applications. *Physics Reports*, 195(4):127–293, November 1990.

[65] Ralf Metzler and Joseph Klafter. The random walk's guide to anomalous diffusion: a fractional dynamics approach. *Physics Reports*, 339(1):1–77, December 2000.

[66] Florian Rehfeldt and Matthias Weiss. The random walker's toolbox for analyzing single-particle tracking data. *Soft Matter*, 19(28):5206–5222, 2023.

[67] Stephanie C. Weber, Michael A. Thompson, W.E. Moerner, Andrew J. Spakowitz, and Julie A. Theriot. Analytical Tools To Distinguish the Effects of Localization Error, Confinement, and Medium Elasticity on the Velocity Autocorrelation Function. *Biophysical Journal*, 102(11):2443–2450, June 2012.

[68] Paweł Czajka, Jan M. Antosiewicz, and Maciej Długosz. Effects of Hydrodynamic Interactions on the Near-Surface Diffusion of Spheroidal Molecules. *ACS Omega*, 4(16):17016–17030, October 2019.

[69] Hongbo Chen, Jingrui Shi, Ming Hu, Anni Shi, Daniel K. Schwartz, and Dapeng Wang. Anomalous versus Fickian-but-Not-Gaussian Diffusion in Heterogeneous Systems Depends on the Time Scale of Observation. *The Journal of Physical Chemistry Letters*, 16(25):6259–6265, June 2025.

[70] Anomalous diffusion models and their properties: non-stationarity, non-ergodicity, and ageing at the centenary of single particle tracking - Physical Chemistry Chemical Physics (RSC Publishing).

[71] Stanislav Burov, S. M. Ali Tabei, Toan Huynh, Michael P. Murrell, Louis H. Philipson, Stuart A. Rice, Margaret L. Gardel, Norbert F. Scherer, and Aaron R. Dinner. Distribution of directional change as a signature of complex dynamics. *Proceedings of the National Academy of Sciences*, 110(49):19689–19694, December 2013.

[72] Bo Wang, Stephen M. Anthony, Sung Chul Bae, and Steve Granick. Anomalous yet Brownian. *Proceedings of the National Academy of Sciences*, 106(36):15160–15164, September 2009.

[73] The random walker's toolbox for analyzing single-particle tracking data - Soft Matter (RSC Publishing) DOI:10.1039/D3SM00557G.

[74] Ralf Metzler and Matthias Weiss. Discriminating stochastic processes for the assessment of materials properties by diffusion measurements. *Physical Chemistry Chemical Physics*, 27(27):14350–14358, 2025.

[75] Olivier Benichou, Thomas Guérin, and Raphaël Voituriez. Mean first-passage times in confined media: from markovian to non-markovian processes. *Journal of Physics A: Mathematical and Theoretical*, 48(16):163001, 2015.

[76] Thomas Guérin, M Dolgushev, O Bénichou, and R Voituriez. Imperfect narrow escape problem. *Physical Review E*, 107(3):034134, 2023.

[77] V Tejedor, O Bénichou, and R Voituriez. Global mean first-passage times of random walks on complex networks. *Physical Review E—Statistical, Nonlinear, and Soft Matter Physics*, 80(6):065104, 2009.

[78] O Bénichou and R Voituriez. Narrow-escape time problem: Time needed for a particle to exit a confining domain<? format?> through a small window. *Physical review letters*, 100(16):168105, 2008.

[79] O. Bénichou, C. Chevalier, J. Klafter, B. Meyer, and R. Voituriez. Geometry-controlled kinetics. *Nature Chemistry*, 2(6):472–477, June 2010.

[80] D. Holcman, N. Hoze, and Z. Schuss. Narrow escape through a funnel and effective diffusion on a crowded membrane. *Physical Review E*, 84(2):021906, August 2011.

[81] Masao Doi and Xianmin Xu. Diffusion Limited Escape Rate of a Complex Molecule in Multi-dimensional Confinement. *The Journal of Physical Chemistry B*, 126(33):6171–6179, August 2022.

[82] Anni Shi and Daniel K. Schwartz. Bridging Macroscopic Diffusion and Microscopic Cavity Escape of Brownian and Active Particles in Irregular Porous Networks. *ACS Nano*, 18(34):22864–22873, August 2024.

[83] Zeev Schuss, Amit Singer, and David Holcman. The narrow escape problem for diffusion in cellular microdomains. *Proceedings of the National Academy of Sciences*, 104(41):16098–16103, 2007.

[84] Nicolas Levernier, Olivier Bénichou, and Raphaël Voituriez. Mean first-passage time of an anisotropic diffusive searcher. *Journal of Physics A: Mathematical and Theoretical*, 50(2):024001, 2017.

[85] Matthias Weiss, Markus Elsner, Fredrik Kartberg, and Tommy Nilsson. Anomalous Subdiffusion Is a Measure for Cytoplasmic Crowding in Living Cells. *Biophysical Journal*, 87(5):3518–3524, November 2004.

[86] Maria Goiko, John R. de Bruyn, and Bryan Heit. Membrane Diffusion Occurs by Continuous-Time Random Walk Sustained by Vesicular Trafficking. *Biophysical Journal*, 114(12):2887–2899, June 2018.

[87] Andrew M. Edwards, Richard A. Phillips, Nicholas W. Watkins, Mervyn P. Freeman, Eugene J. Murphy, Vsevolod Afanasyev, Sergey V. Buldyrev, M. G. E. da Luz, E. P. Raposo, H. Eugene Stanley, and Gandhimohan M. Viswanathan. Revisiting

Lévy flight search patterns of wandering albatrosses, bumblebees and deer. *Nature*, 449(7165):1044–1048, October 2007.

[88] George Biddell Airy. On the diffraction of an object-glass with circular aperture. *Transactions of the Cambridge Philosophical Society*, 5:283, 1835.

[89] Ernst Abbe. Beiträge zur theorie des mikroskops und der mikroskopischen wahrnehmung. *Archiv für mikroskopische Anatomie*, 9(1):413–468, 1873.

[90] Raimund J. Ober, Sripad Ram, and E. Sally Ward. Localization Accuracy in Single-Molecule Microscopy. *Biophysical Journal*, 86(2):1185–1200, February 2004.

[91] Stefan W. Hell and Jan Wichmann. Breaking the diffraction resolution limit by stimulated emission: stimulated-emission-depletion fluorescence microscopy. *Optics Letters*, 19(11):780–782, June 1994.

[92] Anish V Abraham, Sripad Ram, Jerry Chao, ES Ward, and Raimund J Ober. Quantitative study of single molecule location estimation techniques. *Optics express*, 17(26):23352–23373, 2009.

[93] Russell E. Thompson, Daniel R. Larson, and Watt W. Webb. Precise Nanometer Localization Analysis for Individual Fluorescent Probes. *Biophysical Journal*, 82(5):2775–2783, May 2002.

[94] Kim I Mortensen, L Stirling Churchman, James A Spudich, and Henrik Flyvbjerg. Optimized localization analysis for single-molecule tracking and super-resolution microscopy. *Nature methods*, 7(5):377–381, 2010.

[95] J. Enderlein. Maximum-likelihood criterion and single-molecule detection. *Applied Optics*, 34(3):514–526, January 1995.

[96] Gabriella Gagliano, Tyler Nelson, Nahima Saliba, Sofía Vargas-Hernández, and Anna-Karin Gustavsson. Light sheet illumination for 3d single-molecule super-resolution imaging of neuronal synapses. *Frontiers in synaptic neuroscience*, 13:761530, 2021.

[97] Lexy von Diezmann, Yoav Shechtman, and WE Moerner. Three-dimensional localization of single molecules for super-resolution imaging and single-particle tracking. *Chemical reviews*, 117(11):7244–7275, 2017.

[98] Jennifer Lippincott-Schwartz and George H. Patterson. Development and use of fluorescent protein markers in living cells. *Science*, 300:87–91, 2001.

[99] Taekjip Ha and Philip Tinnefeld. Photophysics of fluorescent probes for single-molecule biophysics and super-resolution imaging. *Annual review of physical chemistry*, 63(1):595–617, 2012.

[100] Marcel Bruchez, Mario Moronne, Peter Gin, Shimon Weiss, and A. Paul Alivisatos. Semiconductor Nanocrystals as Fluorescent Biological Labels. *Science*, 281(5385):2013–2016, September 1998.

[101] Manoj Nirmal, Bashir O Dabbousi, Moungi G Bawendi, JJ Macklin, JK Trautman, TD Harris, and Louis E Brus. Fluorescence intermittency in single cadmium selenide nanocrystals. *Nature*, 383(6603):802–804, 1996.

[102] James Pawley. Fundamental limits in confocal microscopy. In *Handbook of biological confocal microscopy*, pages 15–26. Springer, 2006.

[103] Michael J Rust, Mark Bates, and Xiaowei Zhuang. Sub-diffraction-limit imaging by stochastic optical reconstruction microscopy (storm). *Nature methods*, 3(10):793–796, 2006.

[104] Sumio Iijima. Helical microtubules of graphitic carbon. *Nature*, 354(6348):56–58, November 1991.

[105] Noriaki Hamada, Shin-ichi Sawada, and Atsushi Oshiyama. New one-dimensional conductors: Graphitic microtubules. *Physical Review Letters*, 68(10):1579–1581, March 1992.

[106] Feng Wang, Gordana Dukovic, Louis E. Brus, and Tony F. Heinz. The Optical Resonances in Carbon Nanotubes Arise from Excitons. *Science*, 308(5723):838–841, May 2005.

[107] G Dresselhaus, Mildred S Dresselhaus, and Riichiro Saito. *Physical properties of carbon nanotubes*. World scientific, 1998.

[108] Physical Properties of Carbon Nanotubes.

[109] Carter T White and John W Mintmire. Fundamental properties of single-wall carbon nanotubes, 2005.

[110] Jean-Christophe Charlier, Xavier Blase, and Stephan Roche. Electronic and transport properties of nanotubes. *Reviews of Modern Physics*, 79(2):677–732, May 2007.

[111] Eric Chang, Giovanni Bussi, Alice Ruini, and Elisa Molinari. Excitons in Carbon Nanotubes: An *Ab Initio* Symmetry-Based Approach. *Physical Review Letters*, 92(19):196401, May 2004.

[112] Catalin D. Spataru, Sohrab Ismail-Beigi, Lorin X. Benedict, and Steven G. Louie. Excitonic Effects and Optical Spectra of Single-Walled Carbon Nanotubes. *Physical Review Letters*, 92(7):077402, February 2004.

[113] Min Ouyang, Jin-Lin Huang, and Charles M. Lieber. Fundamental Electronic Properties and Applications of Single-Walled Carbon Nanotubes. *Accounts of Chemical Research*, 35(12):1018–1025, December 2002.

[114] Tsuneya Ando. Theory of Electronic States and Transport in Carbon Nanotubes. *Journal of the Physical Society of Japan*, 74(3):777–817, March 2005.

[115] A. Grüneis, R. Saito, Ge. G. Samsonidze, T. Kimura, M. A. Pimenta, A. Jorio, A. G. Souza Filho, G. Dresselhaus, and M. S. Dresselhaus. Inhomogeneous optical absorption around the K point in graphite and carbon nanotubes. *Physical Review B*, 67(16):165402, April 2003.

[116] Francesco Mastrocinque, George Bullard, James A Alatis, Joseph A Albro, Animesh Nayak, Nicholas X Williams, Amar Kumbhar, Hope Meikle, Zachary XW Widel, Yusong Bai, et al. Band gap opening of metallic single-walled carbon nanotubes via noncovalent symmetry breaking. *Proceedings of the National Academy of Sciences*, 121(12):e2317078121, 2024.

[117] Michael Kasha. Characterization of electronic transitions in complex molecules. *Discussions of the Faraday society*, 9:14–19, 1950.

[118] Sergei M Bachilo, Michael S Strano, Carter Kittrell, Robert H Hauge, Richard E Smalley, and R Bruce Weisman. Structure-assigned optical spectra of single-walled carbon nanotubes. *science*, 298(5602):2361–2366, 2002.

[119] R. Bruce Weisman and Sergei M. Bachilo. Dependence of Optical Transition Energies on Structure for Single-Walled Carbon Nanotubes in Aqueous Suspension: An Empirical Kataura Plot. *Nano Letters*, 3(9):1235–1238, September 2003.

[120] Jana Zaumseil. Luminescent defects in single-walled carbon nanotubes for applications. *Advanced Optical Materials*, 10(2):2101576, 2022.

[121] Yong Piao, Brett Meany, Luke R. Powell, Natalie Valley, Hyeonggon Kwon, George C. Schatz, and Yuyang Wang. Brightening of carbon nanotube photoluminescence through the incorporation of sp3 defects. *Nature Chemistry*, 5(10):840–845, 2013.

[122] Flurin A. Mann, Nadine Herrmann, Felipe Opazo, and Sebastian Kruss. Quantum defects as a toolbox for the covalent functionalization of carbon nanotubes with

peptides and proteins. *Angewandte Chemie International Edition*, 56(17):4502–4505, 2017.

[123] Amit Kumar Mandal, Xiaojian Wu, Joana S. Ferreira, Mijin Kim, Lyndsey R. Powell, Hyejin Kwon, Laurent Groc, YuHuang Wang, and Laurent Cognet. Fluorescent sp3 Defect-Tailored Carbon Nanotubes Enable NIR-II Single Particle Imaging in Live Brain Slices at Ultra-Low Excitation Doses. *Scientific Reports*, 10(1):5286, March 2020.

[124] Zhenghong Gao. Advances in surface-coated single-walled carbon nanotubes as near-infrared photoluminescence emitters for single-particle tracking applications in biological environments. *Polymer Journal*, 50:589–601, 2018.

[125] Hannah M. Dewey, Ashley Lamb, and Januka Budhathoki-Uprety. Recent advances on applications of single-walled carbon nanotubes as cutting-edge optical nanosensors for biosensing technologies. *Nanoscale*, 16:16344–16375, 2024.

[126] Jing Pan, Feiran Li, and Jong Hyun Choi. Single-walled carbon nanotubes as optical probes for bio-sensing and imaging. *Journal of Materials Chemistry B*, 5:6511–6522, 2017.

[127] Kevin J Hughes, Kavita A Iyer, Robert E Bird, Julian Ivanov, Saswata Banerjee, Gilles Georges, and Qiongqiong Angela Zhou. Review of carbon nanotube research and development: materials and emerging applications. *ACS Applied Nano Materials*, 7(16):18695–18713, 2024.

[128] Michael FL De Volder, Sameh H Tawfick, Ray H Baughman, and A John Hart. Carbon nanotubes: present and future commercial applications. *science*, 339(6119):535–539, 2013.

[129] Gaurav Lalwani, Andrea Trinward Kwaczala, Shruti Kanakia, Sunny C Patel, Stefan Judex, and Balaji Sitharaman. Fabrication and characterization of three-dimensional macroscopic all-carbon scaffolds. *Carbon*, 53:90–100, 2013.

[130] Stefan Sokoll, Yury Prokazov, Magnus Hanses, Barbara Biermann, Klaus Tönnies, and Martin Heine. Fast three-dimensional single-particle tracking in natural brain tissue. *Biophysical Journal*, 109(7):1463–1471, 2015.

[131] Sri Rama Prasanna Pavani, Michael A Thompson, Julie S Biteen, Samuel J Lord, Na Liu, Robert J Twieg, Rafael Piestun, and William E Moerner. Three-dimensional, single-molecule fluorescence imaging beyond the diffraction limit by using a double-helix point spread function. *Proceedings of the National Academy of Sciences*, 106(9):2995–2999, 2009.

[132] Andrey Aristov, Benoit Lelandais, Elena Rensen, and Christophe Zimmer. ZOLA-3D allows flexible 3D localization microscopy over an adjustable axial range. *Nature Communications*, 9(1):2409, June 2018.

[133] Aishani Ghosal, Yu-Huan Wang, Nguyen Nguyen, Laura Troyer, and Sangjin Kim. Practical considerations for accurate estimation of diffusion parameters from single-particle tracking in living cells. *The Journal of Chemical Physics*, 163(13):134202, October 2025.

[134] Xavier Michalet. Mean square displacement analysis of single-particle trajectories with localization error: Brownian motion in an isotropic medium. *Physical Review E—Statistical, Nonlinear, and Soft Matter Physics*, 82(4):041914, 2010.

[135] Michael A Thompson, Matthew D Lew, Majid Badieirostami, and WE Moerner. Localizing and tracking single nanoscale emitters in three dimensions with high spatiotemporal resolution using a double-helix point spread function. *Nano letters*, 10(1):211–218, 2010.

[136] Jasna Brujić, Chaoming Song, Ping Wang, Christopher Briscoe, Guillaume Marty, and Hernán A. Makse. Measuring the Coordination Number and Entropy of a 3D Jammed Emulsion Packing by Confocal Microscopy. *Physical Review Letters*, 98(24):248001, June 2007.

[137] Ivane Jorjadze, Lea-Laetitia Pontani, Katherine A Newhall, and Jasna Brujić. Attractive emulsion droplets probe the phase diagram of jammed granular matter. *Proceedings of the National Academy of Sciences*, 108(11):4286–4291, 2011.

[138] Iaroslava Golovkova, Lorraine Montel, Elie Wandersman, Thibault Bertrand, Alexis Michel Prevost, and Lea-Laetitia Pontani. Depletion attraction impairs the plasticity of emulsions flowing in a constriction. *Soft Matter*, 16(13):3294–3302, 2020.

[139] Lea-Laetitia Pontani, Martin F Haase, Izabela Raczkowska, and Jasna Brujic. Immiscible lipids control the morphology of patchy emulsions. *Soft Matter*, 9(29):7150–7157, 2013.

[140] Nicolas Bremond and Jérôme Bibette. Exploring emulsion science with microfluidics. *Soft Matter*, 8(41):10549, 2012.

[141] Angus McMullen, Maitane Muñoz Basagoiti, Zorana Zeravcic, and Jasna Brujic. Self-assembly of emulsion droplets through programmable folding. *Nature*, 610(7932):502–506, 2022.

[142] Lea-Laetitia Pontani, Ivane Jorjadze, Virgile Viasnoff, and Jasna Brujic. Biomimetic emulsions reveal the effect of mechanical forces on cell–cell adhesion. *Proceedings of the National Academy of Sciences*, 109(25):9839–9844, June 2012.

[143] Lorraine Montel, Iaroslava Golovkova, Silvia Grigolon, Elie Wandersman, Alexis M. Prevost, Thibault Bertrand, and Lea-Laetitia Pontani. Adhesion Percolation Determines Global Deformation Behavior in Biomimetic Emulsions. *Frontiers in Physics*, 9, September 2021.

[144] Lang Feng, Lea-Laetitia Pontani, Rémi Dreyfus, Paul Chaikin, and Jasna Brujic. Specificity, flexibility and valence of DNA bonds guide emulsion architecture. *Soft Matter*, 9(41):9816, 2013.

[145] Quentin Guigue, Marc Besse, Raphael Voituriez, Alexis M. Prevost, Elie Wandersman, Matthias Merkel, and Lea-Laetitia Pontani. Adhesion differentials control the rheology of biomimetic emulsions. *Biophysical Journal*, 125(7):1686–1700, April 2026.

[146] Lea-Laetitia Pontani, Ivane Jorjadze, and Jasna Brujic. Cis and trans cooperativity of e-cadherin mediates adhesion in biomimetic lipid droplets. *Biophysical journal*, 110(2):391–399, 2016.

[147] C. Vincent, S. Ravindran, A. M. Prevost, L.-L. Pontani, O. Bénichou, and E. Wandersman. Probing and modeling cell–cell communication in 2D biomimetic tissues. *Soft Matter*, 22(11):2321–2328, 2026.

[148] Iaroslava Golovkova, Lorraine Montel, Franck Pan, Elie Wandersman, Alexis M Prevost, Thibault Bertrand, and Lea-Laetitia Pontani. Adhesion as a trigger of droplet polarization in flowing emulsions. *Soft Matter*, 17(14):3820–3828, 2021.

[149] Daryl Lim, Kengyeh K. Chu, and Jerome Mertz. Wide-field fluorescence sectioning with hybrid speckle and uniform-illumination microscopy. *Optics Letters*, 33(16):1819–1821, August 2008.

[150] Daryl Lim, Tim N Ford, Kengyeh K Chu, and Jerome Mertz. Optically sectioned in vivo imaging with speckle illumination hilo microscopy. *Journal of biomedical optics*, 16(1):016014–016014, 2011.

[151] Bingying Zhao and Jerome Mertz. Resolution enhancement with deblurring by pixel reassignment. *Advanced photonics*, 5(6):066004, 2023.

[152] Nils Gustafsson, Siân Culley, George Ashdown, Dylan M Owen, Pedro Matos Pereira, and Ricardo Henriques. Fast live-cell conventional fluorophore nanoscopy

with imagej through super-resolution radial fluctuations. *Nature communications*, 7(1):12471, 2016.

[153] Jerry F Deye, T Anderson Berger, and Albert G Anderson. Nile red as a solvatochromic dye for measuring solvent strength in normal liquids and mixtures of normal liquids with supercritical and near critical fluids. *Analytical chemistry*, 62(6):615–622, 1990.

[154] Carsen Stringer, Tim Wang, Michalis Michaelos, and Marius Pachitariu. Cellpose: a generalist algorithm for cellular segmentation. *Nature methods*, 18(1):100–106, 2021.

[155] Evgeniy E Tkalya, Marcos Ghislandi, Gijsbertus de With, and Cor E Koning. The use of surfactants for dispersing carbon nanotubes and graphene to make conductive nanocomposites. *Current Opinion in Colloid & Interface Science*, 17(4):225–232, 2012.

[156] Panagiotis Angelikopoulos and Henry Bock. The science of dispersing carbon nanotubes with surfactants. *Physical chemistry chemical physics*, 14(27):9546–9557, 2012.

[157] Rohit Mangalwedhekar, Limeng Ruan, Somen Nandi, Quentin Gresil, Marc Tondusson, Stephane Bancelin, Lea-Laetitia Pontani, and Laurent Cognet. Orientational frustration drives enhanced diffusion of anisotropic particles in a liquid labyrinth. *arXiv preprint arXiv:2605.23340*, 2026.

[158] O Bénichou, P Illien, G Oshanin, A Sarracino, and R Voituriez. Tracer diffusion in crowded narrow channels. *Journal of Physics: Condensed Matter*, 30(44):443001, 2018.

[159] M. Doi. Rotational relaxation time of rigid rod-like macromolecule in concentrated solution. *Journal de Physique*, 36(7-8):607–611, 1975.

[160] Sophie Brasselet and Matthew D Lew. Single-molecule orientation and localization microscopy. *Nature Photonics*, 19(9):925–937, 2025.

[161] Oumeng Zhang, Weiyan Zhou, Jin Lu, Tingting Wu, and Matthew D. Lew. Resolving the Three-Dimensional Rotational and Translational Dynamics of Single Molecules Using Radially and Azimuthally Polarized Fluorescence. *Nano Letters*, 22(3):1024–1031, February 2022.

[162] Tingting Wu, Peng Lu, Md Ashequr Rahman, Xiao Li, and Matthew D. Lew. DeepSMOLM: deep learning resolves the 3D orientations and 2D positions of overlapping

single molecules with optimal nanoscale resolution. *Optics Express*, 30(20):36761, September 2022.

[163] Amin El Jarroudi Hammou, Juliette Lavainne, Rohit Mangalwedhekar, Jyothis Devasia, Laurent Cognet, Sébastien Lecommandoux, Colin Bonduelle, and Chloe Grazon. Click'n ropisa: One-pot synthesis of ultrabright fluorescent nanoparticles made of polypeptides. 2026.

[164] Zeineb Ayed, Blanca Martín Muñoz, Catharina I. Vandekerckhove, Virginie Faure, Syed Nafis Shadman Ali, Jean-luc Coll, Laurent Cognet, and Xavier Le Guével. Self-Assembled Small Interfering RNA-Gold Supraclusters Detected at the Single-Molecule Level in the Near-Infrared-II Window. *Small Structures*, 6(11):2500381, 2025. _eprint: https://onlinelibrary.wiley.com/doi/pdf/10.1002/sstr.202500381.

[165] Apolline A Simon, Lucie Haye, Abdallah Alhalabi, Quentin Gresil, Blanca Martín Muñoz, Stéphane Mornet, Andreas Reisch, Xavier Le Guével, and Laurent Cognet. Expanding the palette of swir emitting nanoparticles based on au nanoclusters for single-particle tracking microscopy. *Advanced Science*, 11(24):2309267, 2024.

[166] Yilin Ye, Yacine Amarouchene, Raphaël Sarfati, David S Dean, and Thomas Salez. Brownian motion near a soft surface. *Comptes Rendus. Physique*, 26(G1):619–630, 2025.

[167] T Kuhn, AN Landge, D Mörsdorf, J Coßmann, J Gerstenecker, D Čapek, P Müller, and JCM Gebhardt. Single-molecule tracking of nodal and lefty in live zebrafish embryos supports hindered diffusion model. nat. commun. 13: 6101, 2022.

Diffusion de nanotubes de carbone unidimensionnels dans un environnement complexe de matière molle

Résumé : Le transport dobjets nanométriques dans des environnements structurés complexes est au cur de nombreux processus biologiques et physico-chimiques. Si la diffusion de particules sphériques est largement étudiée, le rôle de lanisotropie reste peu compris. Cette thèse examine la diffusion de nanotubes de carbone fonctionnalisés par des centres colorés émettant dans linfrarouge au sein dun modèle biophysique constitué de gouttelettes démulsion densément empilées, reproduisant les espaces extracellulaires. Grâce à une microscopie de particules uniques en trois dimensions dans le proche infrarouge, jai suivi des nanotubes de deux longueurs différant dun ordre de grandeur. Les deux populations présentent une diffusion sous-diffusive et anti-persistante. De manière inattendue, les nanotubes les plus longs séchappent de chambres confinées seulement 1,4 fois plus lentement que les plus courts, contrairement aux prédictions théoriques. La microscopie SPoT montre que le confinement aligne les nanotubes dans les canaux étroits, limitant leur liberté de rotation tout en facilitant leur transport. Ces résultats identifient la frustration géométrique comme un mécanisme fondamental du transport anormal dans les milieux structurés continus et établissent des principes physiques généraux gouvernant la diffusion dobjets anisotropes dans les systèmes biologiques, poreux et de matière molle.
Mots-clés : Microscopie optique, Biophotoniques, Super resolution, Nanotubes de carbone, Diffusion anormale, Matière molle

---

Diffusion of one-dimensional carbon nanotubes in a complex soft matter environment

Abstract: Transport of nanoscale objects through complex structured environments underlies processes ranging from biomolecular motion in tissues to transport in porous materials. While diffusion of spherical particles is well understood, the role of particle anisotropy remains largely unexplored. In this thesis, I investigate the diffusion of anisotropic carbon nanotubes functionalized with infrared-emitting color centers in a biophysical model consisting of densely packed emulsion droplets that mimic extracellular spaces. Using three-dimensional near-infrared single-particle microscopy, I tracked nanotubes differing by an order of magnitude in length. Both exhibit subdiffusive and antipersistent motion. Surprisingly, despite a tenfold increase in length, long nanotubes escape confined chambers only 1.4 times more slowly than short nanotubes, in contrast with theoretical expectations. Single Particle Orientation Tracking (SPoT) microscopy reveals that confinement aligns long nanotubes within narrow channels, reducing rotational freedom while facilitating transport. These results identify geometric frustration as a fundamental mechanism governing anomalous transport in continuous structured environments. Rather than simply impeding motion, confinement-induced alignment enables efficient escape of anisotropic particles. This work establishes general physical principles for diffusion in complex media and provides a framework for understanding transport in biological, porous, and soft matter systems.
Keywords: Optical microscopy, Biophotonics, Super resolution, Carbon nanotubes, Anomalous diffusion, Soft matter

---

Unité de recherche
UMR xxxx Université, 33000 Bordeaux, France.